

A CONTINUOUS ADJOINT FORMULATION FOR HYPERSONIC FLOWS IN  
THERMOCHEMICAL NONEQUILIBRIUM

A DISSERTATION  
SUBMITTED TO THE DEPARTMENT OF  
AERONAUTICS AND ASTRONAUTICS  
AND THE COMMITTEE ON GRADUATE STUDIES  
OF STANFORD UNIVERSITY  
IN PARTIAL FULFILLMENT OF THE REQUIREMENTS  
FOR THE DEGREE OF  
DOCTOR OF PHILOSOPHY

Sean R. Copeland  
February 2015

© 2015 by Sean Russell Copeland. All Rights Reserved.  
Re-distributed by Stanford University under license with the author.

This dissertation is online at: <http://purl.stanford.edu/cm664pb0182>

I certify that I have read this dissertation and that, in my opinion, it is fully adequate in scope and quality as a dissertation for the degree of Doctor of Philosophy.

**Juan Alonso, Primary Adviser**

I certify that I have read this dissertation and that, in my opinion, it is fully adequate in scope and quality as a dissertation for the degree of Doctor of Philosophy.

**Antony Jameson**

I certify that I have read this dissertation and that, in my opinion, it is fully adequate in scope and quality as a dissertation for the degree of Doctor of Philosophy.

**Robert MacCormack**

Approved for the Stanford University Committee on Graduate Studies.

**Patricia J. Gumpert, Vice Provost for Graduate Education**

*This signature page was generated electronically upon submission of this dissertation in electronic format. An original signed hard copy of the signature page is on file in University Archives.*



# Abstract

This thesis explores the formulation, derivation, and implementation of the continuous adjoint equations for hypersonic, nonequilibrium flow environments. The adjoint method is an efficient means for acquiring sensitivity information that can be used in a gradient-based framework to perform optimal shape design of aerospace systems. A solution to the adjoint system of equations carries a computational cost roughly equal to a single solution of the flow governing equations, regardless of the dimensionality of the design space. When compared to other gradient acquisition methods, where computational costs scale with design space dimensionality, the adjoint method is superior when the dimensionality is high and when solutions to the governing equations are expensive. Such conditions are often representative of most aerospace problems of practical interest. In addition to providing gradient information, solutions to the adjoint equations may be used as ‘sensors’ or ‘weighting factors’ to perform error estimation and adaptive mesh refinement.

Hypersonic systems operate in unique flow environments that are dominated by chemical and thermodynamic phenomena not observed at lower Mach numbers. Accurate simulations of these environments require sophisticated thermochemical models to resolve atomic-scale physical processes that have first-order effects on integrated vehicle performance metrics, including lift, drag, stability, controllability, and heat transfer. Because of the computational expense demanded by these high-fidelity tools, the conceptual vehicle design process often relies heavily on low- to medium-fidelity, correlation-based tools that are confined to narrow regions of applicability. As a consequence, the hypersonic vehicle design process has remained relatively static for the past several decades. The adjoint method enables the use of high-fidelity tools early in the design cycle of hypersonic systems, and is a transformative technology for the hypersonic community.

This work provides the first derivation, implementation, and verification of the continuous adjoint equations for hypersonic flow environments in thermochemical nonequilibrium. Appropriate boundary conditions and surface sensitivities are provided for both projected force and thermal objective functions for continuum, viscous, multi-component gas mixtures. The adjoint system is implemented in a second-order, unstructured, finite-volume-method (FVM) flow solver that is representative of the state-of-the-art in high-fidelity aerothermodynamic analysis for hypersonic entry systems. Gradients from the adjoint-derived surface sensitivities are verified against gradients calculated using a finite-difference methodology for several representative geometries relevant to ballistic and lifting-body entry vehicles.



# Acknowledgement

I consider myself very fortunate to have had an opportunity to pursue a graduate education at Stanford. Looking back on my experience, I will remember many friends, colleagues, and mentors who shaped my experience into some of the best years of my life. I would be remiss if I did not take this opportunity to thank a few of the individuals who made it possible.

As a student, I was supported primarily via the Stanford Graduate Fellowship (SGF) program. This support gave me total freedom to pursue a research project of my choosing, and provided an opportunity to explore a variety of fields in science and engineering. Such freedom is rare as a graduate student, and I am extremely grateful to the Christensen, Lillie, and Chiang families for their direct support of my education via their contributions to the SGF program.

I must thank my defense committee members: Prof. Mark Cappelli, Prof. Robert MacCormack, Prof. Antony Jameson, and Dr. Deepak Bose. Each of these individuals has had a profound impact on me, and it has been such a great honor to have studied and worked with them. Classroom experiences with Professors Cappelli and MacCormack sparked my interest in the numerical simulation of hypersonic flows, which I hope will be the subject of my career as a member of the scientific community. The theoretical foundation of this thesis is built upon the application of adjoint-methods to aerospace problems, pioneered by Prof. Jameson. I am truly honored to have his participation and contributions as part of this work. Dr. Bose is an expert on entry vehicle analysis and design and is also an excellent boss. I am grateful to have worked for him at NASA, and I hope that we will have many opportunities to collaborate together in the future.

The day-to-day research activities that led to this thesis were primarily directed by Dr. Francisco Palacios. I can say with a great deal of confidence that I would not have a thesis without him, and I am extremely thankful to have had his help and support. I am also grateful to have been supported by my advisor, Prof. Juan Alonso, during my time at Stanford. I appreciated the freedom that I had working in his lab group. Both Juan and Francisco managed me well, and I always left research meetings feeling more optimistic about solving the challenges that were ahead of me. Their enthusiasm is infectious, and I hope to remain friends and colleagues long into the future.

For the last six years, the Aerospace Design Laboratory has been my home, and I have shared it with great friends. I will remember the long hours, the conference trips, and non-academic activities that made it such a great place to be. In particular, I would like to thank Thomas Economou and Brendan Tracey for their research advice and for their friendship. To my greater community of

friends: I could not have come so far without you, thank you.

Finally, I would like to reserve a special thank you to my family. Throughout my life, my parents emphasized the importance of education and made great sacrifices to ensure that I had access to the best public schools and classes. My parents and grandparents saved funds, so that I could get a college education and escape, debt-free, to pursue my own life's ambitions without the burden of student loans. I cannot thank them enough for that gift, and I look forward to paying the debt forward. Beyond the opportunities I've been afforded, I am grateful to my family for inspiring me to seek to be a 'good man'. My brother has been the model of self-motivation and self-improvement during an incredibly tumultuous time in his career. I have always looked up to him, and I can only hope to show a fraction of his resolve through life's difficult times. My mother blazed a trail through the U.S. Navy, confronting an entrenched culture of sexism to achieve the rank of Navy Captain over a long, successful career. 'We can do it all' is the motto that she lives by, reminding me to work hard, but also to enjoy life to the fullest. My father, also a retired Navy officer, has the most integrity, the most patience, and the strongest work ethic of anyone I know. He is the best role model a son could ever ask for. I hope I have made them proud.

# Contents

<b>Abstract</b>	<b>v</b>
<b>Acknowledgement</b>	<b>vii</b>
<b>1 Introduction</b>	<b>5</b>
1.1 Motivation . . . . .	5
1.2 The Hypersonic Environment . . . . .	8
1.3 Computational Methods for Nonequilibrium Gases . . . . .	10
1.4 Entry Vehicle Design . . . . .	12
1.5 Adjoint Methods in Aeronautics . . . . .	14
1.6 Research Scope & Contributions . . . . .	15
1.7 Dissertation Layout . . . . .	15
<b>2 Modeling &amp; Governing Equations</b>	<b>17</b>
2.1 Formulation of the Conservation Equations . . . . .	17
2.1.1 Species Continuity . . . . .	19
2.1.2 Momentum . . . . .	20
2.1.3 Total Energy . . . . .	20
2.1.4 Vibrational-Electronic Energy . . . . .	21
2.1.5 Summary of the Governing Equations . . . . .	23
2.2 Two-temperature Thermodynamic Model . . . . .	24
2.3 Viscous Phenomena . . . . .	27
2.3.1 Viscous Terms . . . . .	28
2.3.2 Transport Coefficients . . . . .	28
2.4 Chemical Model . . . . .	30
2.5 Vibrational Excitation and Relaxation Model . . . . .	31
<b>3 Sensitivity Analysis Via the Adjoint Method</b>	<b>35</b>
3.1 Formulation of the Optimal Shape Design Problem . . . . .	35
3.2 The Adjoint Method for Design . . . . .	37
3.3 Definition and Variation of the Objective Functions . . . . .	39

3.3.1	Force-Based Functionals . . . . .	39
3.3.2	Thermal Functionals . . . . .	42
3.4	Variation of the Governing Equations . . . . .	43
3.5	The Adjoint Boundary Integrals . . . . .	47
3.5.1	Simplification of the First Adjoint Boundary Integral . . . . .	47
3.5.2	Simplification of the Second Adjoint Boundary Integral . . . . .	48
3.5.3	Simplification of the Third Adjoint Boundary Integral . . . . .	49
3.5.4	Summary of the Adjoint Boundary Integrals . . . . .	52
3.6	Linearized Boundary Conditions . . . . .	53
3.6.1	Dirichlet Boundary Conditions . . . . .	53
3.6.2	Neumann Boundary Conditions . . . . .	54
3.7	Adjoint Boundary Condition Assignment . . . . .	55
3.7.1	Boundary Conditions for the Projected Force Objective Function . . . . .	56
3.7.2	Boundary Conditions for the Thermal Objective Function . . . . .	64
<b>4</b>	<b>Numerical Implementation</b>	<b>69</b>
4.1	Discretization of the Flow Equations . . . . .	70
4.2	Flow Spatial Integration . . . . .	72
4.2.1	Convective Fluxes . . . . .	72
4.2.2	Viscous Fluxes . . . . .	75
4.2.3	Viscous Jacobians using the TSL Approximation . . . . .	76
4.3	Flow Boundary Conditions . . . . .	78
4.3.1	No-Slip Wall . . . . .	79
4.3.2	Flow Tangency . . . . .	80
4.3.3	Characteristic-Based Far Field . . . . .	81
4.4	Discretization of the Adjoint Equations . . . . .	81
4.5	Adjoint Spatial Integration . . . . .	83
4.5.1	Adjoint Convective Fluxes . . . . .	83
4.5.2	Adjoint Viscous Fluxes . . . . .	85
4.5.3	Adjoint Viscous Jacobians Using the TSL Method . . . . .	86
4.6	Adjoint Boundary Conditions . . . . .	88
4.6.1	Boundary Condition Enforcement: Projected Force Functional . . . . .	89
4.6.2	Boundary Condition Enforcement: Thermal Functional . . . . .	93
4.6.3	Boundary Condition Enforcement: Far Field Boundaries . . . . .	94
4.7	Temporal Integration . . . . .	94
4.7.1	Explicit Forward Euler Scheme . . . . .	95
4.7.2	Implicit Backward Euler Scheme . . . . .	96
4.8	Gradient Computation . . . . .	98
4.8.1	Green-Gauss . . . . .	98
4.8.2	Weighted Least Squares . . . . .	99

4.9	Flux Reconstruction and Limiters . . . . .	100
4.10	Shape Parametrization, Deformation, and Surface Sensitivity . . . . .	102
4.10.1	Projecting the Adjoint Surface Sensitivities onto the Design Space . . . . .	103
4.10.2	Surface Deformation . . . . .	104
4.10.3	Volumetric Deformation . . . . .	104
<b>5</b>	<b>Adjoint Gradient Verification</b>	<b>107</b>
5.1	RAM C-II Flight Test Article (Inviscid) . . . . .	107
5.2	Space Shuttle Wing Cross-Section (Viscous) . . . . .	116
<b>6</b>	<b>Conclusions &amp; Future Work</b>	<b>127</b>
<b>A</b>	<b>Thermochemical Parameters</b>	<b>131</b>
A.1	Species Properties . . . . .	131
A.2	Electronic Energy Parameters . . . . .	131
A.3	Reaction Rate Parameters . . . . .	134
A.4	Transport Coefficient Parameters . . . . .	135
<b>B</b>	<b>Jacobian Matrices</b>	<b>139</b>
B.1	Derivatives of the Primitive Variables . . . . .	139
B.2	Convective Flux Jacobian . . . . .	142
B.3	Viscous Flux Jacobians . . . . .	142
B.3.1	Diffusion . . . . .	143
B.3.2	Viscosity . . . . .	144
B.3.3	Translational-rotational Thermal Conduction . . . . .	145
B.3.4	Vibrational-electronic Thermal Conduction . . . . .	146
B.4	Eigenvalue-eigenvector Decomposition of the Convective Flux Jacobian . . . . .	147
<b>C</b>	<b>Details of Adjoint Derivation</b>	<b>151</b>
C.1	Variation of the Species Diffusion Flux . . . . .	151
C.2	Variation of the Trans.-Rot. Thermal Conduction . . . . .	153
C.3	Variation of the Vib.-El. Thermal Conduction . . . . .	154
<b>D</b>	<b>Solver Validation</b>	<b>157</b>
	<b>Bibliography</b>	<b>165</b>



# List of Tables

5.1	RAM C-II simulation free stream conditions.	108
5.2	RAM-C II geometry values	109
5.3	RAM-C II design variable definitions.	111
5.4	Corners of the FFD box surrounding the RAM C-II geometry.	111
5.5	$\nabla C_D$ values for the finite-difference and adjoint gradient methods.	116
5.6	Shuttle wing section free stream conditions.	117
5.7	Corners of the FFD box surrounding the Shuttle wing section.	119
5.8	Shuttle airfoil design variable definitions.	120
A.1	Species chemical properties.	131
A.2	$N_2$ electron energy data.	132
A.3	$O_2$ electron energy data.	132
A.4	$NO$ electron energy data.	133
A.5	N electron energy data.	133
A.6	O electron energy data.	133
A.7	Arrhenius parameters for the forward reaction rate coefficient.	134
A.8	Forward and backward reaction rate coefficient controlling temperature factors.	135
A.9	Parameters for the Park 1990 equilibrium reaction constants.	137
A.10	Blottner viscosity parameters	138
A.11	$\Omega_{i,j}^{(1,1)}$ collision integral correlation parameters.	138
D.1	70° blunted cone free stream conditions.	158
D.2	Mars entry vehicle model geometry.	158



# List of Figures

1.1	NASA crewed exploration systems (courtesy NASA) . . . . .	7
1.2	NASA Mars exploration systems (courtesy NASA) . . . . .	7
3.1	Infinitesimal surface perturbation in the local normal direction . . . . .	36
3.2	Assumed coordinate systems for the projected-force objective function. . . . .	40
4.1	Computational grid topologies . . . . .	70
4.2	Numerical and physical domains of dependence. . . . .	96
4.3	Sample computational mesh . . . . .	98
4.4	Hypothetical first- and second-order accurate spatial schemes with flux limiting. . .	101
4.5	Wing twist using FFD-based deformation. . . . .	104
5.1	RAM-C II vehicle definition . . . . .	109
5.2	Computational mesh for the RAM C-II test case. . . . .	109
5.3	Definition of the FFD box for the RAM-C II geometry. . . . .	110
5.4	Flow and adjoint field variables for the RAM C-II simulation . . . . .	112
5.5	Flow quantities on the stagnation line. . . . .	113
5.6	Surface sensitivity map for the RAM C-II. . . . .	114
5.7	A comparison of the drag coefficient gradient from the finite-difference and adjoint methods. . . . .	115
5.8	Shuttle wing cross-section. . . . .	117
5.9	Computational mesh for the Shuttle airfoil test case. . . . .	118
5.10	Definition of the FFD box for the shuttle airfoil verification test case. . . . .	119
5.11	Flow field solutions for Case 1 and Case 2 of the Shuttle airfoil. . . . .	121
5.12	Adjoint field solutions for Case 1 and Case 2 of the Shuttle airfoil. . . . .	122
5.13	Adjoint surface sensitivity maps for Case 1 and Case 2 of the Shuttle airfoil. . . . .	123
5.14	Case 1: Shuttle airfoil gradient verification. . . . .	125
5.15	Case 2: Shuttle airfoil gradient verification. . . . .	125
D.1	Schematic of the Mars entry vehicle model geometry. . . . .	159
D.2	Computational meshes for the Mars vehicle model. . . . .	160
D.3	Flow field solutions for the Mars vehicle model. . . . .	161

D.4 Surface heat transfer rates for the Mars vehicle model. . . . .	163
---	-----

# Nomenclature

## Roman Symbols

$\vec{a}$	Acceleration
$\vec{A}$	Flux Jacobian matrices, $\vec{A} = (\partial \vec{F} / \partial U) = \{A_x, A_y, A_z\}$
$B_k$	$k^{th}$ adjoint boundary integrand
$c$	Average molecular speed or local sonic speed
$C_v$	Specific heat at constant volume
$\vec{d}$	Force projection vector
$D$	Viscous Jacobian matrices, $\bar{D} = (\partial \vec{F} / \partial \nabla U)$ or diffusion coefficient
$e$	Average energy per unit mass, $e = \bar{\epsilon}$
$E^A$	Activation energy for the Arrhenius relation
$f$	Probabilistic species distribution function
$\vec{F}$	Flux vector, $\vec{F} = \{F_x, F_y, F_z\}$
$\hat{F}$	Numerical flux vector
$h$	Enthalpy, $h = (\rho e + p)/\rho$
$H_m$	Local mean curvature
$\bar{I}$	Identity matrix
$j$	Local scalar value on $S$
$J$	Scalar objective function
$\vec{J}$	Diffusion velocity, $\vec{J} = \{J_x, J_y, J_z\}$
$\mathcal{J}$	Objective function Lagrangian
$k$	Reaction rate coefficient
$k_B$	Boltzmann constant ( $1.3806488 \times 10^{-23} \frac{kg \cdot m^2}{s^2 \cdot K}$ )
$K$	Chemical reaction equilibrium constant
$m$	Molecular mass
$M$	Molar mass
$n$	Number density
$\vec{n}$	Local normal vector, $\vec{n} = \{n_x, n_y, n_z\}$
$N$	Number of species in the mixture
$\mathcal{N}$	Set of all species in the gas mixture

$\mathcal{N}_i$	Set of all neighboring nodes to $i$
$p$	Pressure
$p$	Norm p-value
$P$	Left eigenvector matrix
$\mathcal{P}$	Set of all polyatomic species in the gas mixture
$\vec{q}$	Thermal conduction
$q^x$	Vibrational-electronic relaxation source term
$Q$	Source terms
$R$	Universal gas constant ( $8.314 \frac{J}{mol \cdot K}$ )
$\mathcal{R}$	System of governing equations
$R_r^{f/b}$	Forward/backward reaction rate
$S$	Design surface
$S'$	Perturbed design surface
$t$	Time
$T$	Temperature
$\vec{u}$	Mixture velocity vector, $\vec{u} = \{u, v, w\}^\top$
$U$	Flow state vector of conserved variables
$\vec{v}$	Molecular velocity, $\vec{v} = \{v_x, v_y, v_z\}^\top$
$\bar{\vec{v}}$	Species average velocity
$\dot{w}$	Mass per unit volume produced by chemistry, $\dot{w}_s = m_s \dot{z}_s$
$\vec{x}$	Spatial location, $\vec{x} = \{x, y, z\}$
$X$	Mole fraction
$Y$	Mass fraction
$\dot{z}$	Rate of species production by chemistry per unit volume

### Greek Symbols

$\alpha$	Angle of attack or chemical reactant stoichiometric coefficient
$\vec{\alpha}$	Design variables
$\beta$	Angle of sideslip, constant in the thermal functional variation, or chemical product stoichiometric coefficient
$\epsilon$	Energy per unit mass of a particle
$\Gamma$	Domain boundary
$\kappa$	Thermal conductivity
$\lambda$	Eigenvalue
$\Lambda$	Diagonal eigenvalue matrix
$\mu$	Dynamic viscosity
$\Omega$	Volume domain
$\Omega_{ij}^{l,m}$	(l,m) collision integral between species $i$ and $j$
$\psi$	Scalar adjoint variable
$\Psi$	Vector of adjoint variables (Lagrange multipliers)
$\vec{\phi}$	Adjoint velocities

$\vec{\Phi}$	Adjoint flux vector
$\hat{\Phi}$	Numerical adjoint flux vector
$\rho$	Mass density
$\sigma$	Cross-section
$\bar{\bar{\sigma}}$	Shear stress tensor, $\mu\bar{\bar{\tau}}$
$\tau$	Vibrational relaxation time constant
$\bar{\bar{\tau}}$	Viscous strain rate tensor, $\bar{\bar{\tau}} = (1/2)(\nabla \vec{u} + \nabla \vec{u}^\top) - (2/3)\bar{\bar{I}}(\nabla \cdot \vec{u})$
$\xi$	Dummy variable or number of rotational modes
$\vec{\xi}$	Dummy vector
$\zeta$	Dummy variable

#### Subscripts

$D$	Drag
$i$	Node $i$
$ij$	Node $i$ to node $j$
$j$	Node $j$
$k$	Iterator
$L$	Lift
$L-T$	Landau-Teller
$n$	Normal
$p$	Park model
$r$	Reaction or species $r$
$s$	Species $s$
$S$	Surface-tangential
$\rho_s$	Species $s$ density
$\rho e$	Mixture total energy
$\rho e^{ve}$	Mixture vib.-el. energy
$\infty$	Far-field

#### Superscripts

$AUSM$	Advection Upstream Splitting Method
$b$	Backward
$c$	Convective or rate-controlling
$coll$	Collision
$D$	Diffusion
$el$	Electronic
$f$	Forward
$int$	Internal
$m$	Molecular
$MSW$	Modified Steger-Warming

<i>rot</i>	Rotational
<i>SW</i>	Steger-Warming
<i>tr</i>	Translational-rotational
<i>trans</i>	Translational
<i>TSL</i>	Thin Shear Layer
<i>v</i>	Viscous
<i>vib</i>	Vibrational
<i>vk</i>	$k^{th}$ viscous vector
<i>ve</i>	Vibrational-electronic
*	Optimal or equilibrium
○	Chemical

## Acronyms

AUSM	Advection Upstream Splitting Method
CAD	Computer-aided Drafting
CFD	Computational Fluid Dynamics
FVM	Finite Volume Method
GG	Green-Gauss
GMRES	Generalized Minimum Residual Method
HYPULSE	NASA Hypersonic Pulse Facility
IBVP	Initial Boundary Value Problem
LU-SGS	Lower-Upper Symmetric-Gauss-Seidel Method
PDE	Partial Differential Equation
RAM	Radio Attenuation Measurement
RANS	Reynolds Averaged Navier-Stokes
RRHO	Rigid-rotator-harmonic-oscillator
SU <sup>2</sup>	Stanford University Unstructured
TLNS	Thin Layer Navier-Stokes
TPS	Thermal Protection System
TSL	Thin Shear Layer
WLS	Weighted Least Squares

## Mathematical Notation

$$\begin{aligned}\partial_n \xi &= \nabla \xi \cdot \vec{n} \\ \nabla_S \xi &= \nabla \xi - \partial_n \xi \\ A : B &= \sum_i \sum_j A_{ij} + B_{ij} \\ s \in \mathcal{X} &= \{s | s \in \mathcal{X}\} \\ s \notin \mathcal{X} &= \{s | s \notin \mathcal{X}\} \\ \bar{x} &= \frac{1}{N} \sum_{j=1}^N x_j \quad \text{or} \quad \frac{1}{n_s} \int x f_s d\vec{v}_s\end{aligned}$$

# Chapter 1

## Introduction

This dissertation advances the field of engineering design for hypersonic aerospace systems by providing a detailed formulation and derivation of the continuous adjoint system of equations for high-enthalpy gas mixtures in thermochemical nonequilibrium. A solution of the adjoint problem provides sensitivity information that can be used in gradient-based analysis and design methodologies to perform optimal shape design. The adjoint solution may also be used in conjunction with additional mathematical operations to support error estimation, mesh adaptation, and uncertainty quantification, supporting design frameworks capable of delivering better performance with quantifiable reliability and robustness. This chapter discusses the motivation for the research project; reviews the canon of established literature on hypersonic numerical simulation, adjoint-based methods, and entry vehicle design; provides a detailed description of the research contributions of this work; and discusses the organization of the dissertation.

### 1.1 Motivation

In the last half-century, advances in computer technology have made truly awesome computing power available to scientists and engineers. In the aerospace community, discretized representations of nonlinear partial differential equations (PDEs) may be solved, using massively parallel computing architectures, to predict the performance of complex, interdisciplinary flight systems with great accuracy. Numerical simulation, in conjunction with traditional experimental methods, contribute to the development of new materials, propulsion systems, avionics, vehicle configurations, and operational procedures, playing a critical role in the design of nearly every major subsystem of modern aerospace vehicles.

The engineering design process in the aeronautics community is evolving to leverage the continuing growth and availability of computational power. Numerically predicted performance metrics may be used with tenets from optimization, surrogate modeling, reduced-order modeling, probability theory, Bayesian inference, machine learning, and other fields of science to address fundamental design engineering challenges, such as:

- Determining the ‘best’ configuration
- Assessing the accuracy of the simulations to identify and quantify sources of error
- Predicting the effect of random variability in the environment to vehicle performance
- Assessing the reliability and robustness of the design to known failure modes
- Understanding the effects of design decisions on performance, reliability, and safety

New design frameworks, driven by accurate predictive capabilities, are being constructed such that engineers can make informed vehicle configuration decisions, understanding the implications to performance, reliability, and safety simultaneously.

In particular, numerical simulation plays a key role in the analysis and design of hypersonic entry vehicles. Ground testing facilities, including arc-heaters, shock/expansion tubes, and ballistic ranges are unable to simultaneously match the free-stream dynamic pressures, shear stresses, and heat fluxes [12] experienced by trans-atmospheric vehicles during planetary entry, so high-fidelity simulation is often the best means of predicting the aerothermodynamic conditions in the flight environment. This environment, discussed more fully in Section 1.2, is very hostile, characterized by extreme temperatures, induced by strong shock waves that are a byproduct of the vehicle’s relative motion to the surrounding gas. As a consequence, vehicle survivability strongly depends on accurately predicting the force and thermal conditions imposed on the vehicle during entry.

In complex, multi-disciplinary engineering systems, design trades are often not obvious, and navigating the design space can be challenging, particularly when the dimensionality of the design space is large. Automated design techniques, using gradient-based or gradient-free algorithms, can be an effective means to arrive at optimal configurations in these cases. Gradient-free optimization methods, such as the Nelder-Mead simplex method [103] or genetic algorithms [54], rely on many repeated evaluations of the governing equations to guide the algorithm to a minimum solution. Gradient-based methods, on the other hand, use the gradient of the objective function to direct the algorithm in a search direction to find a local minimum. It can be computationally expensive to compute the gradient, but often this cost is offset by the improved efficiency in the optimization algorithm. For problems in the hypersonic regime, gradient-free methods are impractical, due to the significant computational investment necessary to acquire the individual solutions. However, acquiring accurate gradients from high-fidelity hypersonic simulation tools remains an open area of research. A variety of gradient computation methods are available, including finite-difference, complex-step, algorithmic-differentiation, symbolic manipulation, and adjoint approaches; each technique has its own inherent advantages and costs.

Despite a reliance on simulation-based predictions and the explosive growth in available computing power, the design process for hypersonic vehicles has remained largely the same since the Viking Mars missions of the 1970s. This is due, in part, to the greater computational expense and modeling challenges associated with simulating high-enthalpy gas mixtures in thermochemical nonequilibrium as compared to solving the Reynolds Averaged Navier-Stokes (RANS) equations for perfect gases. Atoms and molecules in high-temperature gas mixtures undergo chemical reaction, vibrational and

electronic excitation, and ionization as a consequence of high-energy collisional events, which must be modeled at the macroscopic level using expensive chemical, thermodynamic, and transport coefficient models. The resulting nonlinear system for the discretized governing equations is large and numerically stiff. As a byproduct of the increased computational cost of high-fidelity tools, many simple methods for computing gradients, such as the finite difference method, are too expensive to be employed in the conceptual design phase of most hypersonic entry systems, and the design process reverts to low-fidelity methods based on heritage vehicle configurations.



(a) Apollo Command Module (1968).

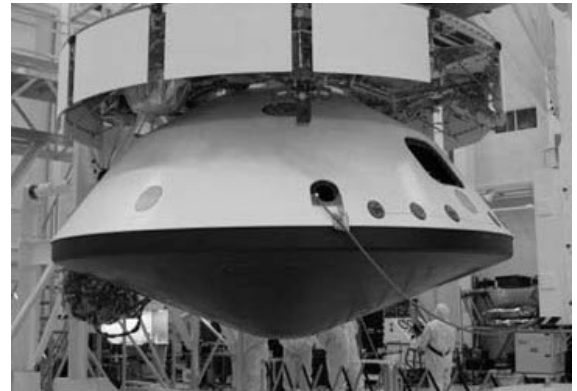


(b) Orion Multi-Purpose Crew Vehicle (2012).

Figure 1.1: NASA crewed exploration systems (courtesy NASA).



(a) Viking lander (1975).



(b) Mars Science Laboratory (2012).

Figure 1.2: NASA Mars exploration systems (courtesy NASA).

Moving forward, the existing hypersonic design methodology is not sustainable. Near-term exploration goals for NASA and the European Space Agency (ESA) cannot be supported using Viking-heritage entry descent and landing (EDL) architectures, and the success of the emerging commercial space industry is strongly dependent on safe and efficient vehicle designs to maximize profit margin and reliability. It is clear that new design methodologies must be explored to address the evolving

needs of the hypersonic community.

The purpose of this thesis is to deliver a powerful analysis and design technique for scientists and engineers in the hypersonic community via the formulation, derivation and implementation of the continuous adjoint system of equations for nonequilibrium hypersonic flows. The adjoint equations, when solved in conjunction with the flow governing equations, provides sensitivity information for a specified objective function, such as aerodynamic forces (e.g. lift, drag, static and dynamic stability) or thermal loads (e.g. peak heat flux and integrated heat load). Adjoint methods have applications including, but not limited to:

1. Uncertainty quantification to analyze system reliability and robustness
2. Goal-oriented adaptive mesh refinement for automated numerical error control
3. Surrogate modeling to mimic the output of expensive physics-based models
4. Optimal shape design using a gradient-based optimization framework

This sensitivity information is provided at a computational expense on the order of the solution to the flow equations, regardless of the dimensionality of the parameter space. This enables the use of high-fidelity analysis tools at all stages in the vehicle design process.

## 1.2 The Hypersonic Environment

The hypersonic flow regime is distinguished from other flow regimes by the onset of unique physical phenomena. These phenomena have first-order effects on vehicle stability, controllability, and integrated surface performance metrics including lift, drag, and heat transfer. An accurate predictive capability requires an understanding of the physical processes present in the flow environment, such that appropriate models can be constructed to faithfully represent the flow physics.

Fundamentally, the observable behavior of fluids is governed by interactions between particles at the atomic scale. As the ensemble of particles evolve in time, intermolecular interactions and collisional events transport mass, momentum, and energy throughout the domain. At the macroscopic scale, the observable advective and diffusive processes in gases and liquids represent the ensemble-averaged behavior of the particle system. In this way, we can represent the transport phenomena in fluids using *ab initio* principles from kinetic theory at the molecular scale [53, 144].

Energy can be stored in atoms and molecules in a variety of ways, depending on the structure of the particle. A particle's translational and rotational motion stores kinetic energy that may be transferred to other particles via collisional events. For polyatomic molecules, an electrostatic force between two positively charged nuclei and any shared electrons forms a chemical bond. The bond length is, nominally, at the potential energy minimum between the two atoms. However, collisional events may alter this spacing, instigating vibrational oscillations that store energy, analogous to the energy contained in an oscillating spring. Energy is also stored in the orbit of electrons that surround the nucleus. Energy transferred to and from the electrons may alter their orbital states.

The atomic system evolves in accordance with the Schrödinger equation. Solutions to this wave equation yield eigenvalues corresponding to the allowable, quantized energy states for translation, rotation, vibration, and electrons. Collisional and relaxation processes transfer energy between the different storage modes as each particle seeks its own minimum energy state. Using kinetic theory, the mean speed of a particle is related to its temperature as,

$$\bar{v} = \sqrt{\frac{8k_B T}{\pi m}}. \quad (1.1)$$

Consequently, the kinetic energy of collisional events scales as  $\bar{v}^2 \propto T$ .

In hypersonic flow fields, typically defined as  $M_\infty > 5$ , high temperatures are generated in the domain by strong compression waves and kinetic to thermal energy conversion within the boundary layer that surrounds the vehicle. These high temperatures, corresponding to high collisional energies at the molecular scale, are sufficient to excite molecules from the ground vibrational and electronic energy states. In some cases, the intermolecular interactions are energetic enough to break chemical bonds and eject electrons from their host nuclei.

Due to the high convective speeds within hypersonic flow fields, often the macroscopic fluid time scales are comparable to the microscopic energy exchange and chemical reaction time scales. In these cases, it becomes necessary to account for the finite-rate nature of the exchange processes that are occurring at the atomic level. Depending on the chemical constituents in the gas mixture, there may be many of these processes that must be accounted-for. Frequently, a full representation of all energy states and exchange mechanisms is too complex and expensive to resolve for general three-dimensional flow domains, so thermodynamic gas models are constructed by assuming equilibria between exchange processes with similar time-constants. Many such models of varying fidelity exist [77, 113, 40], and the particular model selected for this work is described in Chapter 2.

At the macroscopic scale, the hypersonic regime exhibits unique behavior. For very high Mach number flows, the lead shock wave is in close proximity to the vehicle surface. This is often referred to as the 'shock layer' since the proximity of the shock wave and growth of the boundary layer are strongly influenced by one another. Using perfect gas oblique shock theory, the following analytic expression relates the flow Mach number to the flow deflection angle,  $\theta$ , and the oblique shock angle,  $\beta$ ,

$$\frac{\tan(\beta - \theta)}{\tan \beta} = \left( \frac{(\gamma - 1)M_\infty^2 \sin^2 \beta + 2}{(\gamma + 1)M_\infty^2 \sin^2 \beta} \right). \quad (1.2)$$

As an illustrative example, consider a  $\theta = 10^\circ$  wedge in  $M_\infty = 15$  flow. Eqn. (1.2) predicts an oblique shock angle of  $\beta = 13^\circ$  at that condition. Real gas effects, including internal energy excitation and chemical reactions, further reduce  $\beta$ . As a result, the high-temperature, chemically reactive flow in the post-shock region is close to the vehicle surface and a variety of heat transfer mechanisms contribute to significant vehicle heating. Large temperature gradients in the boundary layer lead to considerable convective heat transfer while the high temperatures promote chemical reactions. Free radicals that diffuse to the wall often recombine, transferring energy catalytically from the flow environment to the wall. Also, the chemical, vibrational, and electronic state of the gas in the shock

layer may be conducive to radiative emission. Under some conditions, like those experienced by the Galileo probe during its entry to the Jovian atmosphere, radiation can be the dominant heat transfer mechanism. In all hypersonic systems, particularly entry vehicles, the thermal environment requires special consideration, and it is frequently the dominant design challenge.

Thick boundary layers are common in hypersonic flow fields. The laminar boundary layer thickness,  $\delta$ , on a flat plate grows proportionally [4] to,

$$\delta \propto M_\infty^2 / \sqrt{Re_x}, \quad (1.3)$$

where  $Re_x$  is the local Reynolds number. In high Mach number flows, the boundary layer can be many times larger than those seen in more conventional transonic or supersonic aerospace applications. The momentum deficit in the boundary layer significantly alters the apparent thickness of the vehicle, influencing the location and strength of the shock wave and the flow within the shock layer. In some cases, the boundary layer can be sufficiently thick to directly interfere with the shock system, leading to a merged shock-boundary layer. In all cases, the aerodynamic properties of hypersonic vehicles are significantly affected by the boundary layer thickness and its influence on the shock layer.

### 1.3 Computational Methods for Nonequilibrium Gases

Mathematical representations for nonequilibrium, multi-component gas mixtures and their solutions have been a topic of interest for more than 80 years. Significant global effort has been placed on accurate theoretical representations and numerical solutions of the complex, multi-physics flow environments surrounding hypersonic vehicles because of their implications on strategic national defense, fundamental science, and interplanetary exploration.

Early theoretical works on mathematical representations of multi-component gas mixtures in thermochemical nonequilibrium were derived from solutions to the Boltzmann equation, a seven-dimensional stochastic partial differential equation governing the evolution of a system of particles. By assuming small deviations from the equilibrium solution, Chapman and Cowling [15] provided a rigorous mathematical theory for viscosity, thermal conductivity, and diffusion in gas mixtures via Sonine polynomial expansions of the approximate solution to the Boltzmann equation. This work was later extended to a wider class of problems by Curtiss and Hirschfelder [20]. Theoretical approaches to quantifying stagnation-point heat transfer for engineering applications followed shortly after with contributions from Fay and Riddell [32] and Fay and Kemp [33]. In these works, a set of boundary layer equations were derived that included the effects of chemical reaction and catalytic wall recombination. It was shown that at the stagnation point, the equations are reduced to a set of nonlinear ordinary differential equations, even in the presence of chemical nonequilibrium. Fay and Riddell's stagnation-line theory is still commonly used as a low-order method for estimating stagnation point heating for modern entry vehicle design. Goulard's [44] work on wall catalycity quantified the overall contributions to wall heat transfer from surface chemical recombinations.

Goulard showed Fay and Riddell's work to be a limiting case for infinitely fast chemical recombination and expanded their stagnation-line method for finite catalytic rates by using a correction factor. These early works established the mathematical foundation for the practical analysis of engineering systems operating in the hypersonic flight regime.

As computing power grew in the middle of the 20th century, numerical methods were advanced to provide the first flow field simulations of the hypersonic aerothermodynamic environment. Early work by Moretti and Abbott [100] demonstrated a methodology for steady, inviscid, perfect gas problems around general bodies. Concurrently, Blottner [7] developed the numerical methods and algorithms for solving the chemically reactive boundary layer equations. The finite-difference based solution methodology enabled a full computation of the near-body flow field subject to specified boundary layer edge conditions. Blottner's approach was limited for this reason, as these edge conditions are not known *a priori* for general body geometries, requiring coupling to other numerical tools, like those of Moretti and Abbott. New spatial discretization methods in the early 1980s revolutionized computational fluid dynamics for supersonic and hypersonic configurations. Upwind flux methods by Steger and Warming [132] and Roe [120] were based on the characteristics of the hyperbolic Euler equations, propagating numerical fluxes in a physical way. These techniques provided good accuracy across strong shock waves within the computational domain. The first general CFD solvers to include the effects of thermochemical nonequilibrium began to appear in the mid- to late-1980s in support of several national initiatives to develop hypersonic vehicles. Different strategies for coupling the fluid and chemical systems were attempted, including the loosely-coupled approach of Gnoffo and McCandless [39], the tightly-coupled Eberhardt and Brown [27] methodology, and the explicit-implicit time marching of the flow and chemical systems by Bussing and Murman [11]. In 1988, Candler [12] demonstrated two-dimensional and axisymmetric solutions to chemically reacting, vibrationally relaxing, electronically excited, and weakly ionizing flows for general geometries. The tight coupling approach enabled Candler to include an unprecedented level of fidelity in the thermochemical modeling, while preserving numerical stability. The framework for modern computational aerothermodynamics was established during this time, and the methodologies, particularly Candler's, are still used today.

More recently, advances in solver technology and numerical methods have been the focus of research efforts. Advanced low-dissipation schemes, like Liou and Steffen's [83] advection upstream splitting method (AUSM), with follow on AUSM+ [82] and AUSMPW+ [68], have been specifically tailored for favorable numerical qualities in hypersonic flow regimes. Wright's Data-Parallel Line Relaxation Method (DPLR) [148] generalized the Gauss-Seidel line relaxation method for large, parallel computer architectures. Using this approach, the governing equations can be solved exactly along lines normal to vehicle surface, improving solution robustness and quality while accelerating convergence. Sheffer, Martinelli and Jameson [129] developed an efficient multigrid algorithm for inviscid and viscous chemically reacting flows on parallel computing architectures, enabling further convergence acceleration.

Most recently, real gas CFD solvers have leveraged unstructured mesh representations first pioneered by Thareja [135] and Mavriplis and Jameson [94] in the late 1980s and early 1990s. Nompelis

*et al.* [106], and Scalabrin [125] have developed parallel, unstructured, finite-volume, real-gas CFD solvers that include nonequilibrium thermochemistry for hypersonic applications. In both cases, these solvers utilize line-reconstruction methods to identify lines of cells in the wall-normal direction. With this wall-normal connectivity information, the linear system can be re-ordered such that line-implicit methods similar to DPLR and Gauss-Seidel can be used to solve the linear system. Despite these advanced numerical techniques, parallel, unstructured, real-gas solvers are still an area of active research. Strong shock waves with misaligned mesh connectivity greatly degrades the solution quality in unstructured finite-volume solvers. This is further aggravated by the additional thermochemical terms required to model hypersonic flow fields [43].

## 1.4 Entry Vehicle Design

Entry vehicle design is an inherently interdisciplinary process. Successfully delivering payload from space to a planets surface requires a synthesis of analyses to resolve the aerothermal environment, entry trajectory, structural loads, thermal protection system (TPS) performance, guidance protocols, and others. The aerothermodynamic environment plays a central role in the overall design process, as it directly influences the aerodynamic and thermal performance of the vehicle, which, in turn, influences the trajectory, TPS design, communications, and controllability of the system. Therefore, any advances in analysis and design that pertain to the nonequilibrium flow environment have a significant impact on the overall vehicle design process.

The most common design practice [42] is to begin with a broadly defined set of mission parameters that establish the requirements of the entry, descent, and landing (EDL) system. These mission requirements specify the landing accuracy, payload mass and volume, and set size limitations based on the launch vehicle payload fairing diameter. These parameters are used to specify an initial geometry that is used, in conjunction with the initial conditions at the entry interface, to establish an envelope of possible entry trajectories for the vehicle. Using low-fidelity tools [84, 71], like modified Newtonian aerodynamics and correlation-based stagnation point heat transfer, an aerothermodynamic database is generated across the preliminary flight envelope of the vehicle [72]. From this, a design trajectory is selected that meets all subsystem design constraints, such as payload acceleration loads and TPS maximum shear stress, heat flux, and heat load.

The design is matured by introducing higher-fidelity tools into the design environment that are tightly coupled to other subsystem analysis tools. As an example, changes to GN&C algorithms change the propulsion system requirements. The GN&C algorithms depend on the atmospheric flight characteristics of the vehicle, which are determined by the surface forces from the aerothermodynamic tools. The free stream conditions of the aerothermal environment are dictated by the trajectory analysis tools, which are, in turn, influenced by the packaging, C.G., and mass properties of the payload, TPS, and propulsion systems. The TPS is sized from the surface heat fluxes and heat loads predicted from the aerothermal environment. To capture the subsystem interdependencies and ‘close’ the design, an iterative process is used.

To reiterate, the design methodology establishes an envelope in the design space using low- to

medium-fidelity tools for an initial configuration that is selected from a heritage system, then procedurally refines the envelope around the optimal solution by injecting higher-fidelity tools into the design process. Unfortunately, this procedure is predicated on the assumption that the optimal configuration is captured by the initial envelope and remains within that envelope as it is refined by the use of more advanced analysis tools. In general, this is not guaranteed, as the low fidelity tools lack the necessary physical modeling to faithfully represent the vehicle and its environment. Moreover, the final vehicle configuration is strongly influenced by the selection of the initial configuration, which is set a point in the design process when the least amount of information is available about the aerothermodynamic environment.

To address this, many studies have been performed to determine entry vehicle designs that exhibit better performance than the heritage blunted sphere-cone geometry commonly used for ballistic entry vehicles. In 1968, Hankey [47] conducted a study to optimize an entry vehicle shape for maximum lift-to-drag ratio. Using simplified Newtonian theory and a laminar skin friction model he used a gradient-free numerical search algorithm to maximize vehicle performance under volumetric efficiency, nose heating, and skin friction constraints. Later, Lin [80] conducted a similar study to identify optimal re-entry configurations based on stability, boundary layer transition, and minimal reentry dispersion. More recently, techniques from multi-objective optimization were applied by Theisinger [136] to identify Pareto-optimal vehicle shapes with respect to multiple conflicting objectives derived from volumetric efficiency and aerodynamic performance metrics. In his study, the vehicle geometry was parameterized using B-splines and optimal configurations were determined using a genetic algorithm. He showed improvement over the baseline  $70^\circ$  sphere-cone initial geometry in all cases, demonstrating the utility of numerical optimization in shape design. Advances in symbolic manipulation enabled Grant [45] to explore the use of analytic methods to acquire gradient information to be used for entry vehicle shape optimization using Newtonian aerodynamics.

In the last decade, there has been great interest in the use of non-deterministic methods in the analysis and design process for hypersonic vehicles to quantify the effect of uncertainties in high-fidelity CFD and material response analysis tools. Bose, Wright and Gken [8] performed a detailed study on the effect of uncertainties in the thermochemical modes on laminar aeroheating predictions for Titan entry missions using a Monte Carlo method. A year later, Bose and Wright followed with a similar analysis for  $CO_2$ -based Martian atmosphere. For TPS response, studies by Wright, Bose, and Chen [149] and Copeland [17] used high-fidelity material response software in a stochastic analysis environment to propagate the effects of uncertainties in TPS material properties on the temperature distribution within the heat shield.

The works cited here demonstrate significant investment by the hypersonics community to develop and advance the state-of-the-art in hypersonic vehicle design and analysis methodologies. However, these studies, with few exceptions, continue to rely on low-fidelity, simplified aerothermodynamic models as the engine for the analysis. For the cited UQ works by Bose, Wright and Gken, many thousands of real-gas CFD simulations were necessary to acquire sufficient convergence in the statistics of the Monte Carlo method for their conclusions. Such an analysis is generally too-expensive to be employed in the design phase of most missions, though with the continuing growth

of computing resources this is likely to not always be the case. Nevertheless, studies [119, 123] point to the utility of CFD-driven, gradient-based design, and there is still no direct capability to apply high-fidelity analysis during the conceptual design phase at reasonable computational cost.

## 1.5 Adjoint Methods in Aeronautics

The adjoint method is a well-established procedure for providing accurate gradient information for shape design, error estimation, and uncertainty quantification using high-fidelity analysis tools. The methodology is based on optimal control theory and is typically described using the framework of Lagrange multipliers. Using the governing equations as constraints, the adjoint linear system is derived and boundary conditions are set in such a way that sensitivity information can be acquired using only one solution of the governing equations. In this way, the gradient to an objective function may be determined at the cost of one direct problem solution, and one adjoint problem solution, regardless of the dimensionality of the parameter space. This is a tremendous advantage for aerospace applications, where function evaluations are expensive, requiring solutions to the coupled partial differential equation system governing fluid flow, and when there are many design parameters. This adjoint approach to design enables the direct use of high-fidelity numerical simulations in a gradient-based optimization framework for optimal shape design of complex aerospace vehicles.

The earliest applications of the adjoint method to systems governed by partial differential equations were published by Lions [81] in 1971. Shortly afterward, Pironneau [117] applied variational principles from control theory for incompressible, laminar flows. Pironneau expanded upon his work [118], establishing much of the framework for analytic gradient calculations using the co-state, or adjoint vector. In this way, much of the theoretical basis for the adjoint method was established, including optimization techniques and optimality conditions. In his work, he also provided consideration for solving these equations on computers using finite-element methods. In the late 1980s, Jameson applied the adjoint method to design transonic aircraft design problems [60, 61], minimizing transonic shock-induced drag by automated shape design.

Advances in adjoint-based techniques for aerospace applications continued through the 1990s and 2000s. Jameson derived the adjoint equations and boundary conditions for the Euler [62] and Navier-Stokes [59] equations, demonstrating inviscid and viscous optimal shape design on wings and full aircraft configurations. Anderson and Venkatakrishnan [2] derived a surface formulation of the continuous adjoint system of equations for inviscid and viscous problems using unstructured mesh solvers. In their work, they cite implementation difficulties associated with the high-order derivative terms of the surface sensitivities on unstructured mesh topologies. Follow on work by Jameson [64, 63] presented a solution to this problem by reducing the order of the derivatives by inserting the governing equations written on the surface. Continued development by Castro *et al.* [14] provided a systematic approach to the derivation of the adjoint problem on unstructured meshes. Special emphasis was placed on gradient order reduction and simplifications for calculating viscous terms of the adjoint equations on unstructured grids using differential geometry and shape calculus. This approach was extended by Bueno-Orovio *et al.* [10] to include turbulence modeling in a Reynolds

Averaged Navier-Stokes solver, enabling turbulent viscous design of aerospace systems. Together, these methodologies alleviated many of the existing problems for calculating continuous adjoints on unstructured meshes and has been successfully applied to a variety of three-dimensional design problems [108, 126].

The adjoint method is an excellent means of communicating sensitivity information through complex systems. In addition to optimal shape design, adjoint gradient computations have been used for error estimation [37, 24, 34], adaptive mesh refinement [114, 79, 109, 16], and UQ [145, 23].

## 1.6 Research Scope & Contributions

This dissertation focuses on the mathematical formulation and derivation of the adjoint problem for viscous, laminar, high-enthalpy gas mixtures in thermochemical nonequilibrium. To the author's knowledge, it is the first time such a derivation has been performed for the nonequilibrium hypersonic flow environment. Specifically, this dissertation presents the adjoint formulation for a single-fluid, two-temperature, rigid-rotator-harmonic-oscillator (RRHO) gas model that includes finite-rate chemistry. Appropriate boundary conditions for the nonequilibrium adjoint problem are presented for projected-force and thermal objective functions for flow-tangency, no-slip, adiabatic, isothermal, non-catalytic, and catalytic wall boundaries. The derivation includes a formulation of the adjoint surface sensitivities to arbitrary shape perturbations using calculus of variations and identities from differential geometry, which enables optimal shape design in the nonequilibrium hypersonic environment. Furthermore, the derivation is presented in a systematic and general fashion, such that changes to the thermochemical modeling are contained and modularized to permit rapid reformulation of the adjoint problem under different modeling assumptions.

The flow and adjoint equations are implemented in a node-centric, edge-based, unstructured Finite Volume Method (FVM) solver that is representative of modern nonequilibrium solver technology. The numerical methods used to discretize and integrate the adjoint problem are discussed, including centered and upwind spatial integration schemes and simplifications to the adjoint surface sensitivities. Gradients computed from the adjoint surface sensitivities are compared against finite-difference gradients for the projected-force objective function for blunt-body and lifting-surface geometries.

## 1.7 Dissertation Layout

This dissertation is organized into six chapters, each discussing an important component of the research narrative. Chapter 1 discusses background material, the current status of the field, and the motivation for the selection of the research topic. It also defines the scope of the research project and enumerates the research contributions. Chapter 2 discusses the thermochemical model chosen to represent the hypersonic flow environment, establishing the governing equations that constitute the mathematical foundation upon which the adjoint framework is constructed. Chapter 3 contains the primary research contribution of this work, detailing the background, formulation, and derivation of

the adjoint system corresponding to the flow governing equations presented in the previous chapter. Appropriate boundary conditions and surface sensitivities for projected-force and thermal objective functions are provided for a variety of wall thermal and chemical conditions. Chapter 4 provides details on the numerical implementation of the flow and adjoint equations within the unstructured, FVM solver. Spatial and temporal integration schemes are presented for both equation sets alongside the surface and volume deformation schemes required for perturbing the surface topology and the computational mesh. Chapter 5 verifies the adjoint surface sensitivities presented in Chapter 3 by comparing projected force gradients against finite-difference computations for blunt body and lifting surface geometries for a variety of design surface boundary conditions. Some conclusions, assessments and clear future work to advance the topic are included in Chapter 6. Additional details regarding the thermochemical model parameters, the Jacobian matrices, detailed expansions on the adjoint derivation, and a solver validation case are provided in Appendices A, B, C, and D respectively.

## Chapter 2

# Modeling & Governing Equations

This chapter presents the mathematical model used to simulate the nonequilibrium, hypersonic flow environment. The PDE system governing viscous, continuum flows in thermochemical nonequilibrium is motivated by manipulations of the Boltzmann equation. A set of well-established simplifications and approximations are made to arrive at the two-temperature, rigid-rotator-harmonic-oscillator (RRHO) model [41, 77] used extensively in the hypersonic community. The narrative of this chapter is not intended to provide a rigorous derivation of the conservation equations from a particle system, many excellent references [15, 53, 133] are available for the interested reader, but rather, to provide motivation for the existence of the various physical terms present in the formulation. Additionally, models for the transport coefficients, finite-rate chemistry, and energy exchange processes are discussed in detail.

### 2.1 Formulation of the Conservation Equations

To derive the PDE system governing the hydrodynamics of viscous, continuum gas mixtures in thermochemical nonequilibrium, it is useful to return to a fundamental description of a particle ensemble. Consider a set,  $\mathcal{N}$ , consisting of  $N$  species distribution functions,

$$f_s = f_s(\vec{x}, \vec{v}_s, t), \quad \text{for } s \in \mathcal{N}, \quad (2.1)$$

that represent the probability of finding a molecule of component  $s$  at position  $\vec{x}$  and velocity  $\vec{v}_s$  at time  $t$ . These species distribution functions obey the Boltzmann equation,

$$\frac{df_s}{dt} = \frac{\partial f_s}{\partial t} + \vec{v}_s \cdot \nabla_x f_s + \vec{a}_s \cdot \nabla_v f_s = \left( \frac{\partial f_s}{\partial t} \right)^{coll}, \quad (2.2)$$

dictating the evolution of the probabilistic molecular states in phase space. Eqn. (2.2) is a seven-dimensional, stochastic partial differential equation, where  $\nabla_x$  denotes the gradient with respect to spatial coordinates,  $\vec{x}$ ,  $\nabla_{v_s}$  denotes the gradient with respect to species velocity components,

$\vec{v}_s$ , and  $(\partial f_s / \partial t)^{coll}$  denotes the probability of molecules entering a particular phase state through collisional interactions with other mixture constituents. The hydrodynamic conservation equations for mass, momentum, and energy can be derived directly from this complete description of a particle system. To do so, it is necessary to multiply Eqn. (2.2) by a scalar quantity associated with  $s$ ,  $\zeta_s$ , and integrate over species velocity space,

$$\int \zeta_s \left( \frac{\partial f_s}{\partial t} + \vec{v}_s \cdot \nabla_x f_s + \vec{a}_s \cdot \nabla_v f_s \right) d\vec{v}_s = \int \zeta_s \left( \frac{\partial f_s}{\partial t} \right)^{coll} d\vec{v}_s. \quad (2.3)$$

With some manipulation, it can be shown [53, 133] that Eqn. (2.3) simplifies to,

$$\frac{\partial(n_s \bar{\zeta}_s)}{\partial t} + \left( \frac{\partial}{\partial \vec{x}} \cdot n_s \zeta_s \bar{\vec{v}}_s \right) - n_s \left\{ \overline{\frac{\partial \zeta_s}{\partial t}} + \left( \bar{\vec{v}}_s \cdot \frac{\partial \zeta_s}{\partial \vec{x}} \right) + \left( \vec{a}_s \cdot \frac{\partial \zeta_s}{\partial \vec{v}_s} \right) \right\} = \int \zeta_s \left( \frac{\partial f_s}{\partial t} \right)^{coll} d\vec{v}_s, \quad (2.4)$$

where  $\bar{\zeta}_s = \int \zeta_s f_s d\vec{v}_s$  is the ensemble-averaged value of  $\zeta_s$  at  $\vec{x}$ . Eqn. (2.4) is known as Enskog's general equation of change, and provides a link between the processes occurring at the atomic scale and the observed behavior of the macroscopic fluid. Naturally, summing Eqn. (2.4) over all chemical constituents gives the equation of change for  $\zeta$  of the gas mixture.

Enskog's equation of change provides a common foundation for deriving the mass, momentum, and energy conservation equations. For these cases,  $\int \zeta_s (\partial f_s / \partial t)^{coll} d\vec{v}_s = 0$ , since these quantities are preserved through collisional events. When  $\zeta_s$  is not a collisional invariant, the details of the intermolecular interaction must be resolved over all possible orientations and trajectories for each binary interaction. In most cases, resolving the collisional term analytically is difficult and simplified, empirical models are introduced to arrive at a closed-form expression.

For chemically reactive, multi-component mixtures, there is additional complexity. Mass, momentum, and energy are conserved within the mixture, but not necessarily on a species-by-species basis. If a collision produces a chemical reaction, the participating species change 'classification' and the mass, momentum, and energy belonging to a particular species is transferred to a different species as a consequence of this classification change. Such changes are accommodated by defining

$$\dot{z}_s = \int \left( \frac{\partial f_s}{\partial t} \right)^{coll} d\vec{v}_s, \quad (2.5)$$

where  $\dot{z}_s$  is the total rate of production of  $s$  per unit volume due to collisional events with other molecules. For this work,  $\dot{z}_s$  is determined using a finite-rate chemical model described in Section 2.4.

It is useful to define some additional parameters to assist in the derivation of the conservation equations. The velocity of a molecule of  $s$  has already been defined as  $\vec{v}_s$ ; the average species velocity at a location,  $\vec{x}$ , is the expected velocity over all possible velocity states,

$$\bar{\vec{v}}_s = \int \vec{v}_s f_s d\vec{v}_s, \quad (2.6)$$

where  $n_s$  is the number-density of species  $s$ . The bulk motion of the gas mixture,  $\vec{u}$ , is determined by mass-averaging the contributions from each constituent,

$$\vec{u} = \frac{\sum_s \rho_s \bar{v}_s}{\sum_s \rho_s}, \quad (2.7)$$

where  $\rho_s$  is the mass per unit volume of species  $s$ . The motion of a particle relative to the mass-average mixture velocity is known as the peculiar velocity,  $\vec{v}_s^D$ . The average peculiar velocity tracks the mean transport of species  $s$  relative to the mass-average mixture velocity and is known as the diffusion velocity,  $\vec{u}_s^D$ ,

$$\vec{u}_s^D = \int \vec{v}_s^D f_s d\vec{v}_s = \int (\vec{v}_s - \vec{u}) f_s d\vec{v}_s = \bar{v}_s - \vec{u}. \quad (2.8)$$

By strategically inserting these velocity definitions into the equations that follow, it is possible to separate the molecular transport phenomena from the large scale convective behavior of the gas system such that a familiar extension to the Navier-Stokes equations appears.

### 2.1.1 Species Continuity

Let  $\zeta_s$  represent species molecular mass,  $m_s$ . Inserting this into Eqn (2.4), noting that  $m_s$  is constant, the Enskog equation of change for species mass is,

$$\frac{\partial(n_s m_s)}{\partial t} + \frac{\partial}{\partial \vec{x}} \cdot (n_s m_s \bar{v}_s) = m_s \dot{z}_s. \quad (2.9)$$

The bulk advective motion of the gas is separated from the species molecular processes by inserting the definition of the mass-averaged mixture velocity, Eqn. (2.7), and diffusion velocity, Eqn. (2.8) into Eqn. (2.9). The species molecular-scale mass transport is defined as the diffusion flux,  $\vec{J}_s$ ,

$$\vec{J}_s = n_s m_s \vec{u}_s^D. \quad (2.10)$$

Details of the diffusion model are provided in Section 2.3.1. By rewriting Eqn. (2.9) using mass density,  $\rho_s = n_s m_s$ , and inserting the definition of the diffusion flux, species continuity is expressed as,

$$\frac{\partial \rho_s}{\partial t} + \frac{\partial}{\partial \vec{x}} \cdot (\rho_s \vec{u}) + \frac{\partial}{\partial \vec{x}} \cdot \vec{J}_s = \dot{w}_s, \quad (2.11)$$

where  $\dot{w}_s = m_s \dot{z}_s$  is the mass per unit volume produced or destroyed via chemical processes, which is discussed in detail in Section 2.4. The continuity equation for the mixture is the sum of all species continuity equations,

$$\sum_s \left[ \frac{\partial \rho_s}{\partial t} + \frac{\partial}{\partial \vec{x}} \cdot (\rho_s \vec{u}) + \frac{\partial}{\partial \vec{x}} \cdot \vec{J}_s \right] = \sum_s \dot{w}_s \quad (2.12)$$

$$\frac{\partial \rho}{\partial t} + \frac{\partial}{\partial \vec{x}} \cdot (\rho \vec{u}) = 0. \quad (2.13)$$

Note, in Eqn. (2.12),  $\sum_s \dot{w}_s = 0$  because mass is conserved through chemical reactions in the mixture. Also, by the definition of  $\vec{u}_s^D$ , the diffusion fluxes in the mixture cancel, such that  $\sum_s \vec{J}_s = 0$ .

### 2.1.2 Momentum

To acquire the mixture momentum equations, let  $\zeta_s = m_s \vec{v}_s$  and sum the Enskog equation of change over all species,

$$\sum_s \left\{ \frac{\partial(n_s m_s \bar{\vec{v}}_s)}{\partial t} + \left( \frac{\partial}{\partial \vec{x}} \cdot n_s m_s \bar{\vec{v}}_s \bar{\vec{v}}_s \right) - n_s m_s \vec{a}_s \right\} = \sum_s \left\{ \int m_s \vec{v}_s \left( \frac{\partial f_s}{\partial t} \right)^{coll} d\vec{v}_s \right\}. \quad (2.14)$$

As before, the bulk fluid motion can be separated from the atomic-scale momentum transport processes by inserting the definitions of the peculiar, mixture, and diffusion velocities, such that

$$\begin{aligned} \sum_s \left\{ \frac{\partial[\rho_s(\vec{u} + \vec{u}_s^D)]}{\partial t} + \left( \frac{\partial}{\partial \vec{x}} \cdot \rho_s (\bar{\vec{u}} + \bar{\vec{v}}_s^D)(\bar{\vec{u}} + \bar{\vec{v}}_s^D) \right) - \rho_s \vec{a}_s \right\} &= \sum_s \int m_s \vec{v}_s \left( \frac{\partial f_s}{\partial t} \right)^{coll} d\vec{v}_s \\ \frac{\partial(\rho \vec{u})}{\partial t} + \frac{\partial}{\partial \vec{x}} \cdot (\rho \vec{u} \vec{u}) + \frac{\partial}{\partial \vec{x}} \cdot \left[ \sum_s \left( \rho_s \bar{\vec{v}}_s^D \bar{\vec{v}}_s^D \right) \right] - I \sum_s (\rho_s \vec{a}_s) &= 0 \\ \frac{\partial(\rho \vec{u})}{\partial t} + \frac{\partial}{\partial \vec{x}} \cdot (\rho \vec{u} \vec{u}) + \frac{\partial}{\partial \vec{x}} \cdot (p \bar{\vec{I}} - \bar{\sigma}) &= 0, \end{aligned} \quad (2.15)$$

where the term on the right hand side has been eliminated due to the collisional invariance of momentum within the mixture. In the absence of external forces,  $\sum_s \rho_s \vec{a}_s = 0$ , and is eliminated from Eqn. (2.15). The average molecular transport of momentum is captured by  $\sum_s (\rho_s \bar{\vec{v}}_s^D \bar{\vec{v}}_s^D)$ , which is redefined using the pressure and viscous shear stress tensors  $p \bar{\vec{I}}$  and  $\bar{\sigma}$ . Details pertaining to the viscous shear stress tensor are provided in Section 2.3.1.

### 2.1.3 Total Energy

To derive the species total energy equations, let  $\zeta_s$  represent the total energy of a particle of  $s$ , which includes translational kinetic energy, as well as internal energy from rotation, vibration, electronic excitation, and chemical potential. Explicitly,

$$\zeta_s = \frac{1}{2} m_s (\vec{v}_s \cdot \vec{v}_s) + m_s (\epsilon_s^{rot} + \epsilon_s^{vib} + \epsilon_s^{el} + \epsilon_s^\circ), \quad (2.16)$$

where  $\epsilon_s^k$  is the energy per unit mass in the  $k^{th}$  mode of a particle of  $s$ . It is assumed that the internal energy modes are not explicit functions of the particle's position or velocity and are described using only a temperature. The average particle energy is then,

$$\begin{aligned} \bar{\zeta}_s &= \frac{1}{2} m_s (\bar{\vec{v}}_s \cdot \bar{\vec{v}}_s) + m_s (\bar{\epsilon}_s^{rot} + \bar{\epsilon}_s^{vib} + \bar{\epsilon}_s^{el} + \bar{\epsilon}_s^\circ) \\ &= \frac{1}{2} m_s (\vec{u} \cdot \vec{u}) + m_s (\vec{u} \cdot \vec{u}_s^D) + m_s e_s^{int}, \end{aligned} \quad (2.17)$$

where the translational kinetic energy in the mean flow reference frame,  $\overline{\epsilon^{trans}} = \frac{1}{2}m_s \overline{\vec{v}_s^D \cdot \vec{v}_s^D}$ , has been included in the average molecular energy,

$$\epsilon_s^{int} = \epsilon_s^{trans} + \epsilon_s^{rot} + \epsilon_s^{vib} + \epsilon_s^{el} + \epsilon_s^\circ \quad (2.18)$$

and  $e_s^k = \overline{\epsilon_s^k}$ . Similarly, the average molecular transport of energy is given by,

$$\begin{aligned} \overline{\vec{v}_s \zeta_s} &= \vec{u} \left[ \frac{1}{2}m_s(\vec{u} \cdot \vec{u}) + m_s(\vec{u} \cdot \vec{u}_s^D) + \frac{1}{2}m_s(\overline{\vec{v}_s^D \cdot \vec{v}_s^D}) + m_s(\overline{\epsilon_s^{rot}} + \overline{\epsilon_s^{vib}} + \overline{\epsilon_s^{el}} + \epsilon_s^\circ) \right] \\ &\quad + \frac{1}{2}m_s(\vec{u} \cdot \vec{u})\vec{u}_s^D + m_s\overline{\vec{v}_s^D(\vec{u} \cdot \vec{v}_s^D)} + \frac{1}{2}m_s\overline{\vec{v}_s^D(\vec{v}_s^D \cdot \vec{v}_s^D)} + m_s(\overline{\vec{v}_s^D \epsilon_s^{rot}} + \overline{\vec{v}_s^D \epsilon_s^{vib}} + \overline{\vec{v}_s^D \epsilon_s^{el}} + \overline{\vec{v}_s^D \epsilon_s^\circ}) \\ &= \vec{u} [m_s e_s + m_s(\vec{u} \cdot \vec{u}_s^D)] + \frac{1}{2}m_s(\vec{u} \cdot \vec{u})\vec{u}_s^D + m_s \vec{u} \cdot (\overline{\vec{v}_s^D \vec{v}_s^D}) + m_s \overline{\vec{v}_s^D \epsilon^{int}}, \end{aligned} \quad (2.19)$$

where  $e_s$  is the average total energy per unit mass of species  $s$ ,

$$e_s = \overline{\epsilon_s^{int}} + \frac{1}{2}(\vec{u} \cdot \vec{u}) = \epsilon_s^{trans} + \epsilon_s^{rot} + \epsilon_s^{vib} + \epsilon_s^{el} + \epsilon_s^\circ + \frac{1}{2}(\vec{u} \cdot \vec{u}). \quad (2.20)$$

By inserting Eqns. (2.17) & (2.19) into Eqn. (2.4) and summing over all species, the mixture energy conservation equation can be derived,

$$\begin{aligned} \sum_s \left\{ \frac{\partial}{\partial t} [\rho_s e_s + \rho_s(\vec{u} \cdot \vec{u}_s^D)] + \frac{\partial}{\partial \vec{x}} \cdot \left[ \vec{u} \left( \rho_s e_s + \rho_s \vec{u} \cdot (\overline{\vec{v}_s^D \vec{v}_s^D}) + \rho_s \overline{\vec{v}_s^D \epsilon^{int}} \right) \right] \right\} \\ + \sum_s \left\{ \frac{\partial}{\partial \vec{x}} \cdot \left[ \rho_s(\vec{u} \cdot \vec{u}_s^D) + \frac{1}{2}\rho_s(\vec{u} \cdot \vec{u})\vec{u}_s^D \right] + \vec{a}_s \cdot m_s \vec{v}_s \right\} = 0 \\ \frac{\partial(\rho e)}{\partial t} + \frac{\partial}{\partial \vec{x}} \cdot [(\rho e + p)\vec{u}] - \frac{\partial}{\partial \vec{x}} \cdot \left[ \vec{u}^\tau \bar{\sigma} - q^{\vec{v}e} - \sum_s (\vec{J}_s h_s^{int}) \right] = 0. \end{aligned} \quad (2.21)$$

To arrive at Eqn. (2.21), several simplifying steps are performed simultaneously. First, all terms containing  $\sum_s \rho_s \vec{u}_s^D = 0$  are eliminated by definition. Second, the definition from Section 2.1.2 for the molecular transport of momentum,  $\sum_s \rho_s \overline{\vec{v}_s^D \vec{v}_s^D} = p \bar{I} - \bar{\sigma}$ , is inserted appropriately. Third, the molecular transport of energy,  $\rho_s \overline{\vec{v}_s^D \epsilon^{int}}$  is re-expressed as the sum of the thermal conduction,  $\vec{q}$ , within the mixture and energy transport via diffusion,  $\sum_s (\vec{J}_s h_s^{int})$ . Once again, the collisional contribution on the right hand side of Enskog's equation of change is omitted from the mixture energy equation since total energy is a collisional invariant.

#### 2.1.4 Vibrational-Electronic Energy

As discussed in Section 2.1.3, a particle of species  $s$  may store energy in the translational, rotational, vibrational, and electronic quantum states. The energy contained within each of these states changes due to intermolecular collisions and relaxation processes as each particle seeks its own minimum energy state. These excitation and relaxation processes require finite time, and, due to the high convective speeds in the flow domain, may lead to localized regions of thermal nonequilibrium.

To accommodate thermal nonequilibrium in the gas mixture, additional energy conservation equations are required. Recall the assumption made in Section 2.1.3 that the internal energy states are only dependent on an appropriately defined temperature. Therefore, an additional temperature conservation equation is required for each energy state considered to be out of equilibrium with any of the other energy states. In this manner, two-, three-, four-, or many-temperature models have been constructed [40] to provide varying levels of fidelity in the thermodynamic modeling of hypersonic nonequilibrium flows. However, increasing the number of temperatures in a model does not necessarily increase the fidelity of the simulation. As the number of temperatures grows by a factor of  $n$ , the number of energy exchange mechanisms grows by a factor of  $n^2$ . In many cases, the exchange mechanisms are poorly understood, leading to simplified theoretical models which may inadequately capture the physics of the process. The alternative is to construct empirical models, though it can often be difficult to accurately tune the parameters of the model, given the difficulty in measuring the desired phenomena.

For this work, a two-temperature thermal model [41, 77] is used, where the characteristic time scales for vibrational and electronic excitation and relaxation are sufficiently similar to be in equilibrium with one another, yet out of equilibrium with the translational and rotational modes. Furthermore, it is assumed that the vibrational and electronic states of all polyatomic constituents of the gas mixture are in equilibrium with one another, and the translational and rotational states of all species are in equilibrium with one another, such that the thermodynamic state of the gas may be defined entirely using two temperatures. Consequently, a conservation equation for the vibrational-electronic energy of the gas mixture is required,

Let  $\zeta_s$  be the energy contained the vibrational and electronic states of a particle of species  $s$ , such that

$$\zeta_s = m_s(\epsilon_s^{vib} + \epsilon_s^{el}) = m_s \epsilon_s^{ve} \quad \text{and} \quad (2.22)$$

$$\bar{\zeta}_s = m_s \bar{\epsilon}_s^{ve} = m_s e_s^{ve}. \quad (2.23)$$

To derive the conservation equation, Eqn. (2.22) is inserted into Enskog's equation of change. Noting that  $\epsilon^{ve}$  has no dependence on  $\vec{x}$  or  $\vec{v}_s$ ,

$$\frac{\partial n_s m_s \bar{\epsilon}_s^{ve}}{\partial t} + \left( \frac{\partial}{\partial \vec{x}} \cdot n_s m_s \bar{\epsilon}_s^{ve} \vec{v}_s \right) = \int m_s \epsilon_s^{ve} \left( \frac{\partial f_s}{\partial t} \right)^{coll} d\vec{v}_s. \quad (2.24)$$

Since the vibrational-electronic energy is not a collisional invariant, the source term on the right hand side persists. A particle may enter a particular vibrational-electronic state via an excitation or relaxation process, or as a consequence of a chemical reaction. The vibrational-electronic relaxation model is described further in Section 2.5. For vibrational-electronic energy generated via chemical reactions, it assumed that the new particle of the polyatomic species inherits the local, ensemble average vibrational-electronic state.

Eqn. (2.24) is summed over all chemical constituents to formulate the vibrational-electronic energy conservation equation for the gas mixture. As before, the definitions of the peculiar, mixture,

and diffusion velocities are inserted to separate the bulk fluid behavior and the atomic-scale processes such that,

$$\begin{aligned} \sum_s \left\{ \frac{\partial n_s m_s \bar{\epsilon}_s^{ve}}{\partial t} + \left( \frac{\partial}{\partial \vec{x}} \cdot n_s m_s \bar{\epsilon}^{ve} (\vec{u} + \vec{v}_s^D) \right) \right\} &= q^x + \sum_s \dot{w}_s \bar{\epsilon}_s^{ve} \\ \frac{\partial \rho e^{ve}}{\partial t} + \frac{\partial}{\partial \vec{x}} \cdot (\rho e^{ve} \vec{u}) - \frac{\partial}{\partial \vec{x}} \cdot \left( -q^{\vec{v}_e} - \sum_s \vec{J}_s e_s^{ve} \right) &= q^x + \sum_s \dot{w}_s e_s^{ve}, \end{aligned} \quad (2.25)$$

where  $q^x$  and  $\sum_s \dot{w}_s e_s^{ve}$  represent the relaxation and chemical production of vibrational-electronic energy discussed previously. As before with the total energy,  $\sum_s \rho_s \bar{v}_s^D \bar{\epsilon}^{ve}$  is re-expressed as the sum of the thermal conduction of vibrational-electronic energy,  $q^{\vec{v}_e}$  and the transport via diffusion,  $\sum_s (\vec{J}_s e_s^{ve})$ .

### 2.1.5 Summary of the Governing Equations

In summary, the coupled, nonlinear partial differential equation system, given by Eqns. (2.11), (2.15), (2.21), and (2.25), governs the transport of mass, momentum, and energy in the flow domain for a multi-component, viscous gas mixture in thermochemical nonequilibrium. A solution to this equation set, with the appropriate boundary conditions, provides a complete description of the gas state within the domain of interest, subject to the modeling assumptions discussed in the derivation. The various terms in the equations have been motivated using a fundamental description of the gas provided by the Boltzmann equation, and, by separating the bulk fluid motion from the atomic transport processes, the final result is an extension of the familiar Navier-Stokes equations for perfect gases. The PDE set may be concisely expressed using vector notation as

$$\mathcal{R}(U, \nabla U) = \frac{\partial U}{\partial t} + \nabla \cdot \vec{F}^c(U) - \nabla \cdot \vec{F}^v(U, \nabla U) - Q(U) = 0, \quad (2.26)$$

where the vector of conserved variables, convective fluxes, viscous fluxes, and source terms are defined as

$$U = \begin{bmatrix} \rho_1 \\ \vdots \\ \rho_N \\ \rho \vec{u} \\ \rho e \\ \rho e^{ve} \end{bmatrix}, \quad \vec{F}^c = \begin{bmatrix} \rho_1 \vec{u} \\ \vdots \\ \rho_N \vec{u} \\ \rho \vec{u} \vec{u}^\top + p \bar{I} \\ \rho \vec{u} h \\ \rho \vec{u} e^{ve} \end{bmatrix}, \quad \vec{F}^v = \begin{bmatrix} -\vec{J}_1 \\ \vdots \\ -\vec{J}_N \\ \bar{\sigma} \\ \vec{u}^\top \bar{\sigma} - \sum_k q^k - \sum_s \vec{J}_s h_s^{int} \\ -q^{\vec{v}_e} - \sum_s \vec{J}_s e_s^{ve} \end{bmatrix}, \quad Q = \begin{bmatrix} \dot{w}_1 \\ \vdots \\ \dot{w}_N \\ \vec{0} \\ 0 \\ q^x + \sum_s \dot{w}_s e_s^{ve} \end{bmatrix}, \quad (2.27)$$

and  $k \in \{tr, ve\}$ . Subsequent sections will provide additional details on the thermodynamic, transport coefficient, and chemical kinetic models required to resolve the physical phenomena in the flow domain.

## 2.2 Two-temperature Thermodynamic Model

As discussed previously, the energy contained within polyatomic molecules may be categorized into translational, rotational, vibrational, and electronic modes. Each mode has allowable energy states, determined from solutions to the Schrödinger wave equation, that, generally, are not independent of one another. Consider, for example, a diatomic molecule, spinning rapidly about its center of mass. The electrostatic force, provided by the shared valence electrons in the chemical bond, opposes the centrifugal force experienced by the atoms. As the speed of rotation increases or decreases, the internuclear separation changes, such that the balance between the electrostatic force and the centrifugal force is maintained, thus illustrating the coupled nature of the rotational and vibrational states.

Unfortunately, a complete description of the coupled nature of these energy states is extraordinarily complex, particularly for large molecules consisting of many atomic members. To cope with this complexity, the nature of the interdependency of these states is simplified by assuming ‘mode-separable’ behavior. That is, each energy mode is treated as being independent of all others, such that molecules translating quickly are not forced to rotate or vibrate quickly and vice-versa.

Using this mode-separable description, the total energy per unit volume of the gas mixture used in the conservation equations can be expressed as the sum over all the available energy storage modes,

$$\rho e = \sum_s \rho_s \left( e_s^{trans} + e_s^{rot} + e_s^{vib} + e_s^{el} + e_s^o + \frac{1}{2} (\vec{u} \cdot \vec{u}) \right). \quad (2.28)$$

Similarly, the mixture vibrational-electronic energy per unit volume of the mixture is the sum of the vibrational and electronic energies,

$$\rho e^{ve} = \sum_s \rho_s (e_s^{vib} + e_s^{el}). \quad (2.29)$$

Under the aforementioned simplifications, the thermodynamic state of the gas is determined using a two-temperature, rigid-rotator-harmonic-oscillator (RRHO) model [77, 41, 42, 150]. As the name suggests, the energy contained in the rotational and vibrational states are computed assuming rigidly-rotating dynamic structures and simple harmonic oscillators, respectively. It is assumed that the translational and rotational modes are in equilibrium and can be described by a single temperature,  $T$ , while the vibrational and electronic energies are in equilibrium with each other, yet out of equilibrium with the other modes, described by  $T^{ve}$ . This thermodynamic model, though simple, has been demonstrated [106, 125, 57] to be sufficiently accurate to capture surface pressures and heat fluxes corresponding to low-energy, sub-orbital or orbital entry conditions. For these trajectories, flow field temperatures are sufficiently elevated to excite vibrational modes, but not to the extent that more sophisticated, anharmonic oscillatory vibrational models are required.

To determine the energy of a gas mixture using the RRHO model, consider a set of chemical species,  $\mathcal{N} = \mathcal{M} \cup \mathcal{P} \cup \mathcal{E}$ , where  $\mathcal{M}$  is the set of all monatomic species,  $\mathcal{P}$  is the set of all polyatomic species, and  $\mathcal{E}$  is the set containing free electrons. The average translational energy of a particle

of species  $s$  may be derived directly from kinetic theory using the Maxwellian velocity distribution function for  $f_s$  and evaluating  $e_s^{trans} = \int(1/2)(\vec{v}_s^D \cdot \vec{v}_s^D) f_s d\vec{v}_s^D$ . The result is,

$$e_s^{trans} = \begin{cases} \frac{3}{2} \frac{R}{M_s} T, & \text{for } s \notin \mathcal{E}, \\ 0 & \text{for } s \in \mathcal{E}, \end{cases} \quad (2.30)$$

where  $R$  is the universal gas constant and  $M_s$  is the species molar mass. By invoking the equipartition of energy theorem and recognizing the rotational energy of a rigid body is  $(1/2)I_z\omega^2$  the average rotational energy may be expressed as,

$$e_s^{rot} = \begin{cases} 0 & \text{for } s \in \mathcal{M} \cup \mathcal{E}, \\ \frac{\xi_s}{2} \frac{R}{M_s} T, & \text{for } s \in \mathcal{P}, \end{cases} \quad (2.31)$$

where  $\xi_s$  represents the number of energy-storing rotational axes of species  $s$ . For general polyatomic molecules,  $\xi_s = 3$ , and for diatomic molecules, it is assumed that the energy contained in rotation along the axis aligned with the chemical bond is negligible as compared to the other axes, thus  $\xi_s = 2$  in these cases. Species vibrational energy is that of a simple harmonic oscillator,

$$e_s^{vib} = \begin{cases} 0 & \text{for } s \in \mathcal{M} \cup \mathcal{E}, \\ \frac{R}{M_s} \frac{\theta_s^{vib}}{\exp(\theta_s^{vib}/T^{ve}) - 1}, & \text{for } s \in \mathcal{P}, \end{cases} \quad (2.32)$$

where  $\theta_s^{vib}$  is the characteristic temperature of vibration for species  $s$ , analogous to the spring constant. Specific values for  $\theta_s^{vib}$  used in this work are tabulated in Section A. Species electronic energies are those contained in the equilibrium Maxwellian distribution given by,

$$e_s^{el} = \begin{cases} \frac{R}{M_s} \frac{\sum_{i=1}^{\infty} g_{i,s} \theta_{i,s}^{el} \exp(-\theta_{i,s}^{el}/T^{ve})}{\sum_{i=0}^{\infty} g_{i,s} \exp(-\theta_{i,s}^{el}/T^{ve})} & \text{for } s \notin \mathcal{E}. \\ \frac{3}{2} \frac{R}{M_s} T^{ve} & \text{for } s \in \mathcal{E}. \end{cases} \quad (2.33)$$

The electronic energy sums over the number of electronic energy states,  $i$ , where the electron degeneracies,  $g_{i,s}$ , and the characteristic temperatures  $\theta_{i,s}^{el}$ , are also tabulated in Section A.

Since the gas mixture is in a state of thermochemical nonequilibrium, it is neither thermally, nor calorically perfect. As a consequence, the specific heat at constant volume,  $C_v$ , for the mixture is dependent not only on the thermal state of the gas, but also on the chemical state, since each constituent contributes differently based on its internal atomic structure. The mixture  $C_v$  is a sum of the species specific heats for each energy mode,  $C_{v,s}^k = de_s^k/dT^k$ ,

$$C_{v,s}^{trans} = \begin{cases} \frac{3}{2} \frac{R}{M_s}, & \text{for } s \notin \mathcal{E}. \\ 0 & \text{for } s \in \mathcal{E}. \end{cases} \quad (2.34a)$$

$$C_{v,s}^{rot} = \begin{cases} 0 & \text{for } s \in \mathcal{M} \cup \mathcal{E}. \\ \frac{\xi_s}{2} \frac{R}{M_s}, & \text{for } s \in \mathcal{P}. \end{cases} \quad (2.34b)$$

$$C_{v,s}^{vib} = \begin{cases} 0 & \text{for } s \in \mathcal{M} \cup \mathcal{E}. \\ \frac{R}{M_s} \frac{(\theta_s^{vib}/T^{ve})^2 \exp(\theta_s^{vib}/T^{ve})}{[\exp(\theta_s^{vib}/T^{ve}) - 1]^2}, & \text{for } s \in \mathcal{P}. \end{cases} \quad (2.34c)$$

$$C_{v,s}^{el} = \begin{cases} \frac{\partial e_s^{el*}}{\partial T^{ve}} & \text{for } s \notin \mathcal{E}. \\ \frac{3}{2} \frac{R}{M_s} & \text{for } s \in \mathcal{E}. \end{cases} \quad (2.34d)$$

where,

$$\frac{\partial e_s^{el*}}{\partial T^{ve}} = \frac{R}{M_s} \left\{ \frac{\sum_{i=1}^{\infty} g_{i,s} (\theta_{i,s}^{el}/T^{ve})^2 \exp(-\theta_{i,s}^{el}/T^{ve})}{\sum_{i=0}^{\infty} g_{i,s} \exp(-\theta_{i,s}^{el}/T^{ve})} - \frac{[\sum_{i=1}^{\infty} g_{i,s} \theta_{i,s}^{el} \exp(-\theta_{i,s}^{el}/T^{ve})][\sum_{i=0}^{\infty} g_{i,s} (\theta_{i,s}^{el}/(T^{ve})^2) \exp(-\theta_{i,s}^{el}/T^{ve})]}{[\sum_{i=0}^{\infty} g_{i,s} \exp(-\theta_{i,s}^{el}/T^{ve})]^2} \right\}. \quad (2.35)$$

For convenience, a translational-rotational and vibrational-electronic specific heat is defined as the sum of the appropriate energy modes,

$$C_{v,s}^{tr} = C_{v,s}^{trans} + C_{v,s}^{rot}, \quad (2.36a)$$

$$C_{v,s}^{ve} = C_{v,s}^{vib} + C_{v,s}^{el}. \quad (2.36b)$$

These grouped specific heats have utility in thermodynamic and Jacobian calculations.

A host of additional primitive variables may now be defined using the definitions of  $e_s$  and, conversely,  $T$  and  $T^{ve}$ . Using statistical mechanics and kinetic theory [144], the species partial pressure is expressed as

$$p_s = n_s k_B T, \quad (2.37)$$

with  $k_B$  being the Boltzmann constant. Using Dalton's law of partial pressures, the mixture pressure is then the sum of the species partial pressures,

$$p = \sum_{s \neq el} \rho_s \frac{R}{M_s} T + \rho_{el} \frac{R}{M_{el}} T^{ve}. \quad (2.38)$$

Mixture total and static enthalpy are used in the definition of the total energy conservation equation.

The appropriate relations for these quantities follow their definitions from thermodynamics,

$$h = \frac{1}{\rho}(\rho e + p) \quad (2.39)$$

$$h_s^{int} = \begin{cases} R_s T + e_s^{int} & \text{for } s \notin \mathcal{E}, \\ R_s T^{ve} + e_s^{int} & \text{for } s \in \mathcal{E}, \end{cases} \quad (2.40)$$

where  $R_s = R/M_s$  is the species gas constant and  $e_s^{int}$  is defined in Eqn. (2.18).

## 2.3 Viscous Phenomena

In the derivation of the conservation equations, there exist terms from Enskog's equation of change that express the transport of mass, momentum, and energy within the gas mixture due to molecular processes, such as  $\rho_s \bar{v}_s^D e^{int}$ ,  $\sum_s (\rho_s \bar{v}_s^D \bar{v}_s^D)$ , and  $n_s m_s \vec{u}_s^D$ . These terms are observed macroscopically as diffusion, viscosity, and thermal conduction, and they are collectively grouped together into the viscous phenomena,  $\vec{F}^v$ , of the gas mixture.

In principle, it is possible to rigorously derive the functional form of the viscous fluxes and transport coefficients from kinetic theory [133, 53, 20] using approximate solutions to the Boltzmann equation. The procedure of Chapman and Cowling [15] accomplishes this task using a perturbation technique to expand the exact solution to the Boltzmann equation into an infinite series about the equilibrium solution,

$$f_s = f_s^{[0]} + \epsilon f_s^{[1]} + \epsilon^2 f_s^{[2]} + \dots, \quad (2.41)$$

where  $1/\epsilon$  is proportional to the frequency of molecular collisions and  $f_s^{[0]}$  is the Maxwellian velocity distribution function. Therefore, as the frequency of collisions increases, the solution converges to the local equilibrium. For continuum gases, there are generally enough collisions such that the series converges rapidly, and the perturbation technique is a good approximation to the true solution to the Boltzmann equation, since only a few terms from Eqn. (2.41) are required. In fact, the zeroth order solution yields the Euler equations, the first order solution yields the Navier-Stokes equations, the second order yields the Burnett equations, and so on. The mathematical formulations of the viscous phenomena that arise from this methodology are the theoretical supersets to the Fick, Newton, and Fourier models that are used in this work to represent the diffusion, viscous momentum transport, and thermal conduction processes in the gas mixture. The derivation is omitted here, as it is lengthy and widely available in the literature [53, 133], but it is important to remember that the viscous models discussed hereafter are simplifications of this general perturbation theory. For the models to be valid, they are subject to the foundational assumptions of perturbation approach, namely the equilibrium behavior of the molecular system is Maxwellian and any regions of local nonequilibria are well represented as small deviations from Maxwellian.

### 2.3.1 Viscous Terms

The species diffusion fluxes,  $\vec{J}_s$ , are modeled using Fick's law,

$$\vec{J}_s = -\rho D_s \nabla Y_s + Y_s \sum_k \rho D_k \nabla Y_k, \quad (2.42)$$

where  $Y_s = (\rho_s / \rho)$  and  $D_s$  are the mass fraction and diffusion coefficient of species  $s$  in the gas mixture. Fick's model can be derived from the rigorous multi-component diffusion equations that are an output of the perturbation solution to the Boltzmann equation discussed in Section 2.3 as a limiting case for dilute gas mixtures under the assumption of negligible diffusion from thermal or pressure gradients. Under these conditions, the diffusion process is modeled as binary diffusion between the species and the gas mixture driven by gradients in the species mass fractions,  $\nabla Y_s$ . The second term of Eqn. (2.42) ensures the sum of the diffusion fluxes is zero, which is not guaranteed under the species-mixture binary diffusion simplification. With this closure term, Fick's diffusion model has been shown [134] to be a good approximation to the more complex multi-component diffusion equations in most relevant hypersonic flow environments.

The hypersonic gas mixture is modeled as a Newtonian fluid, where the viscous stress is linearly related to the rate of strain and Stokes' hypothesis has been applied for the bulk viscosity, such that

$$\bar{\sigma} = \mu \left[ \nabla \vec{u} + (\nabla \vec{u})^\top - \frac{2}{3} \bar{I} (\nabla \cdot \vec{u}) \right], \quad (2.43)$$

where  $\mu$  is the coefficient of dynamic viscosity. Thermal conduction is modeled using Fourier's law,

$$\vec{q}^k = -\kappa^k \nabla T^k, \quad (2.44)$$

where the conduction of translational-rotational and vibrational-electric energy are handled separately such that the total thermal conduction  $\vec{q} = \vec{q}^{tr} + \vec{q}^{ve}$ . In Eqn. (2.44),  $\kappa$  is the mixture thermal conductivity corresponding to  $k \in \{tr, ve\}$ .

### 2.3.2 Transport Coefficients

The transport coefficients,  $D_s$ ,  $\mu$ , and  $\kappa^k$  are computed using a combination of well-known models in the hypersonic community. The diffusion coefficient,  $D_s$ , represents an effective diffusion coefficient of species  $s$  with the remaining constituents of the gas mixture. It is computed using a weighted sum of the binary diffusion coefficients,  $D_{ij}$ , between all components of the gas mixture, which may be derived from kinetic theory [53, 6] as

$$\rho D_{ij} = 7.1613 \times 10^{-25} \frac{M \sqrt{T \left( \frac{1}{M_i} + \frac{1}{M_j} \right)}}{\Omega_{ij}^{(1,1)}}, \quad (2.45)$$

where  $M_{ij}$  is the molar mass of species  $i$  or  $j$  and  $\Omega_{ij}^{(1,1)}$  is the collision integral for mass diffusion. The parameter  $M$  in Eqn. (2.45) is the mixture molar mass, which may be computed using the species mole fractions,  $X_s = n_s/n$ , by

$$M = \sum_s X_s M_s. \quad (2.46)$$

The collision integral for mass diffusion is computed using a curve fit [125] of the form,

$$\pi\Omega_{ij}^{(m,n)} = D^\Omega T^{[A^\Omega(\ln T)^2 + B^\Omega \ln T + C^\Omega]}. \quad (2.47)$$

with  $A$ ,  $B$ ,  $C$ , and  $D$  tabulated in Tab. (A.11) of Appendix A. The effective species-mixture diffusion coefficient [134] is computed as a weighted sum of the binary diffusion coefficients from Eqn. (2.45) as

$$\frac{(1 - X_i)}{D_i} = \sum_{j \neq i} \frac{X_j}{D_{ij}}. \quad (2.48)$$

To compute the mixture dynamic viscosities and thermal conductivities, Wilke's semi-empirical mixing rule [147] is used in conjunction with Blottner's correlations [7] for species viscosities at high temperature. Specifically, the mixture quantities are computed as the following weighted sum of species transport coefficients,

$$\mu = \sum_s \frac{X_s \mu_s}{\phi_s}, \quad (2.49a)$$

$$\kappa = \sum_s \frac{X_s \kappa_s}{\phi_s}, \quad (2.49b)$$

where  $X_s$ ,  $\mu_s$ , and  $\kappa_s$  are the species mole fractions, viscosities, and thermal conductivities respectively. The remaining term,  $\phi_s$ , is defined as,

$$\phi_s = \sum_r X_r \left[ 1 + \sqrt{\frac{\mu_s}{\mu_r}} \left( \frac{M_r}{M_s} \right)^{1/4} \right]^2 \left[ \sqrt{8 \left( 1 + \frac{M_s}{M_r} \right)} \right]^{-1}. \quad (2.50)$$

Blottner's species viscosity model employs a three-parameter curve fit to experimental data for high temperature air,

$$\mu_s = 0.1 \exp [(A_s \ln T + B_s) \ln T + C_s]. \quad (2.51)$$

This model provides good accuracy for temperatures up to 10,000 K, and for most practical cold-wall simulations of entry vehicles, this is sufficient within the boundary layer where viscous effects are most important. The parameters,  $A_s$ ,  $B_s$ , and  $C_s$ , are provided in Tab. (A.10) in Appendix A. Species thermal conductivities for the translational-rotational and vibrational-electronic modes are

calculated using Eucken's [31] formula,

$$\kappa_s^{tr} = \mu_s \left( \frac{5}{2} C_{v_s}^{trans} + C_{v_s}^{rot} \right), \quad (2.52a)$$

$$\kappa_s^{ve} = \mu_s C_{v_s}^{ve}, \quad (2.52b)$$

with the appropriate formulas for the specific heats of the various energy modes provided by Eqn. (2.34).

## 2.4 Chemical Model

The finite-rate chemical model accommodates reactive gas mixtures at hypersonic velocities. The rate of production and destruction of each chemical constituent is governed by the forward and backward reaction rate coefficients,  $k_r^f$  and  $k_r^b$ , for each chemical reaction,  $r$ , and the molar concentration of the participating chemical species. Consider a general elementary reaction,

$$\sum_s \alpha_{s,r}[S] \rightleftharpoons \sum_s \beta_{s,r}[S], \quad (2.53)$$

where  $\alpha_{s,r}$  and  $\beta_{s,r}$  are the reactant and product stoichiometric coefficients of species  $s$  in reaction  $r$  for the chemical reaction, and  $[S]$  is the molar concentration of  $s$ . As a general convention, reactions proceeding left to right are exothermic in this work. To acquire the species volumetric mass production term,  $\dot{w}_s$ , used in the species conservation law, Eqn. (2.11), it is necessary to sum over all reactions where species  $s$  is a participant. The reaction stoichiometric coefficients are multiplied by the rate of production,  $R_r^f$ , and destruction,  $R_r^b$ , to acquire the molar rate of change of species  $s$ , which is then multiplied by the molar mass to convert to a mass rate of change per volume,

$$\dot{w}_s = M_s \sum_r (\beta_{s,r} - \alpha_{s,r}) (R_r^f - R_r^b). \quad (2.54)$$

The reaction rates,  $R$ , are dependent on the rate coefficients,  $k^{f/b}$ , and the molar concentrations of the participating constituents,

$$R_r^f = k_r^f \prod_s \left( \frac{\rho_s}{M_s} \right)^{\alpha_{s,r}}, \quad (2.55a)$$

$$R_r^b = k_r^b \prod_s \left( \frac{\rho_s}{M_s} \right)^{\beta_{s,r}}. \quad (2.55b)$$

In the rate equations above, the exponents of the species molar concentrations are known as the reaction orders. Generally, these reaction orders can be integers or fractions and are not necessarily related to the stoichiometric coefficients of the reaction. However, for simple, single-step reaction mechanisms, these reaction orders *are* equal to the stoichiometric coefficients of the reaction,  $\alpha_{s,r}$  and  $\beta_{s,r}$ . For the gas models used in this work, this simplification is appropriate, and is applied

throughout.

The forward and backward reaction rate coefficients are modeled using an Arrhenius equation,

$$k_r^f = C_r (T_r^{c_f})^{\eta_r} e^{-E_r^A / (k_B T_r^{c_f})}, \quad (2.56)$$

with parameters that are fit from experimental data consolidated in Scalabrin's thesis [125]. The prefactor,  $C_r$ , activation energy per molecule,  $E_r^A$ , and exponent,  $\eta_r$  are provided in Tab. (A.7) of Appendix A. The backwards rate coefficient is related to  $k_r^f$  by the equilibrium constant,  $K_r^e$ , [58] as,

$$k_r^b = \frac{k_r^f}{K_r^e}. \quad (2.57)$$

The forward and backward reaction rate coefficients are dependent on the local thermal state of the gas, represented by rate-controlling temperatures,  $T^{c_f}$  and  $T^{c_b}$ , respectively. In a molecular ensemble, vibrationally excited molecules are more likely to undergo chemical reaction. This is accommodated in the chemical model by representing the forward rate controlling temperatures as a geometric average of the translational-rotational and vibrational-electronic temperatures [113] of the form,

$$T_r^{c_f} = (T)^{a_r^f} (T^{ve})^{b_r^f}, \quad (2.58)$$

where  $a_r^f = b_r^f = 0.5$ , or  $a_r^f = 0.7$  and  $b_r^f = 0.3$ , depending on the desired level of preferential treatment of vibrational excitation. The backward rate controlling temperature is always taken as the translational-rotational temperature,  $T$ . The reaction equilibrium constant,  $K_r^e$ , is evaluated using a curve fit of the following form [113],

$$K_r^e = \exp \left[ A_r^0 \left( \frac{T^c}{10000} \right) + A_r^1 + A_r^2 \ln \left( \frac{10000}{T^c} \right) + A_r^3 \left( \frac{10000}{T^c} \right) + A_r^4 \left( \frac{10000}{T^c} \right)^2 \right]. \quad (2.59)$$

Curve fit parameters,  $A_r^k$  for  $k = 0, \dots, 4$ , are dependent on the local mixture number density and are included in Tab. (A.9) of Appendix A. For number densities within the tabulated range, a linear interpolation scheme is used to determine the appropriate  $A_r^k$  for the local conditions. Any local conditions that fall outside the tabulated range, the values for the maximum and minimum number densities are used. To determine the backward reaction rate coefficient, both the equilibrium constant,  $K_r^e$ , and the forward reaction rate coefficient  $k_r^f$  are evaluated at the backwards rate controlling temperature  $T^{c_r}$ .

## 2.5 Vibrational Excitation and Relaxation Model

Molecular vibrational excitation is a byproduct of inelastic molecular collisions within the flow domain. Collisional events with sufficient energy can promote molecules from their ground vibrational energy state to higher states by transferring energy from other storage mechanisms during the collision. Equilibration between the vibrational energy and the translational or rotational energy may

require several hundred of these molecular interactions. Contrast this with the exchange between translational and rotational modes, which typically requires on the order of 10 interactions for equilibration to occur. This is the primary justification for tracking the vibrational (and electronic) energy modes separately and coupling the vibrational-electronic conservation equation to the total energy via the finite-rate vibrational relaxation source term,  $q^x$ .

Since the thermochemical model assumes equilibrium between the various species translational-rotational temperatures, and, separately, the species vibrational-electronic temperatures, only a single transferral mechanism between the states is required. For a system of simple harmonic oscillators in a thermal bath of uniform temperature,  $T$ , it can be shown [144] that any deviation from thermal equilibrium leads to a reversion to equilibrium at the rate given by,

$$\frac{de_s^{ve}}{dt} = \frac{(e_s^{ve})^* - e_s^{ve}}{\tau_s}, \quad (2.60)$$

where  $(e_s^{ve})^*$  is the vibrational energy evaluated at  $T$ , and  $\tau_s$  is the characteristic relaxation time. This relation holds, regardless of the difference between  $(e_s^{ve})^*$  and  $e_s^{ve}$ , representing large departures from equilibrium, provided the simple harmonic oscillator assumption holds. In principle, this is only true for the lowest vibrational energy states, and, as vibrational excitation becomes more energetic, more sophisticated anharmonic models are necessary to accurately model the atomic-scale behavior. To form  $q^x$ , which represents a mass-averaged energy transfer per unit volume, it is necessary to compute the density-weighted sum of the species vibrational relaxation times,

$$q^x = \sum_s \rho_s \frac{de_s^{ve}}{dt} = \sum_s \rho_s \frac{(e_s^{ve})^* - e_s^{ve}}{\tau_s}. \quad (2.61)$$

Evaluating Eqn. (2.61) requires an expression for the relaxation time,  $\tau_s$ , which is computed using a combination of Landau-Teller theory [76] with a limiting relaxation time,  $\tau_{ps}$ , from Park [113], such that

$$\tau_s = \langle \tau_s \rangle_{L-T} + \tau_{ps}. \quad (2.62)$$

The molar-averaged Landau-Teller relaxation time,

$$\langle \tau_s \rangle_{L-T} = \frac{\sum_r X_r}{\sum_r X_r / \tau_{sr}}, \quad (2.63)$$

is a combination of the inter-species relaxation times,  $\tau_{sr}$ ,

$$\tau_{sr} = \frac{1}{P} \exp \left[ A_{sr} (T^{-1/3} - 0.015 \mu_{sr}^{1/4}) - 18.42 \right], \quad (2.64)$$

given by curve fits from Millikan and White's [99] experiments with high temperature air. The parameters for the inter-species relaxation time,  $A_{sr}$  and  $\mu_{sr}$ , depend on the molecular properties

of species  $s$  and  $r$

$$A_{sr} = 1.16 * 10^{-3} \mu_{sr}^{1/2} (\theta_s^{vib})^{4/3} \quad (2.65a)$$

$$\mu_{sr} = \frac{M_s M_r}{M_s + M_r}, \quad (2.65b)$$

where  $\theta_s^{vib}$  is the characteristic vibrational temperature of species  $s$  and  $M_{s/r}$  is the molar mass. The Millikan and White curve fits under-predict the relaxation time for high temperatures, so a correction,  $\tau_{ps}$ , is applied, where

$$\tau_{ps} = \frac{1}{\sigma_s c_s n}. \quad (2.66)$$

The components of the correction include the average molecular speed of  $s$ , given by kinetic theory and the Maxwellian velocity distribution, as

$$c_s = \sqrt{\frac{8R_u T}{\pi M_s}}, \quad (2.67)$$

and a limiting cross-section of,

$$\sigma_s = 10^{-20} \left( \frac{50000}{T} \right)^2 m^2, \quad (2.68)$$

with temperature measured in Kelvin.



## Chapter 3

# Sensitivity Analysis Via the Adjoint Method

This chapter presents the derivation of the adjoint system of equations corresponding to the mathematical modeling of the flow environment discussed in Chapter 2. The adjoint linear system, boundary conditions, and surface sensitivities derived herein constitute the primary research contribution of this thesis, enabling efficient gradient computation using high-fidelity tools in high-dimensional design spaces. The derivation is motivated by posing an optimal shape design problem, where a scalar objective function is influenced by a design surface that is parametrically defined in terms of a vector of design variables.

### 3.1 Formulation of the Optimal Shape Design Problem

Typically, an optimal shape design problem seeks the minimum of a scalar objective function,  $J$ , via manipulations of a design surface,  $S$ , subject to a set of equality constraints,  $C = 0$ , representing the governing equations of the problem. In the context of entry vehicle design, the objective function often represents a surface-integrated momentum, or energy metric to quantify the resultant force and thermal exchange between the vehicle and the surrounding flow field. These metrics may be related to aerodynamic stability, volumetric efficiency, maximum landed mass, or peak heat flux, among others. The engineering design team has the responsibility of selecting the shape that delivers the best performance under the imposed constraints. Consider the following design problem,

$$\begin{aligned} \min_S J(U, S) &= \int_S j(U) ds \\ \text{subject to } &\int_\Omega \mathcal{R}(U) = 0, \end{aligned} \tag{3.1}$$

where  $j$  is a local surface quantity on  $S$ , and  $\mathcal{R}$  is the system of PDEs in Eqn. (2.26). Simply stated, the optimal control problem of Eqn. (3.1) seeks the minimum of a yet-to-be-defined  $J$ , with

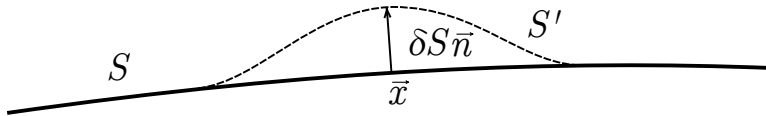


Figure 3.1: Infinitesimal surface perturbation in the local normal direction

the requirement that the physical models for the flow environment are satisfied. Specific objective functions considered in this work are defined in Section 3.3.

It is convenient to re-express Eqn. (3.1) as an unconstrained optimization problem by utilizing the method of Lagrange multipliers [9],

$$\mathcal{J} = J - \int_{\Omega} \Psi^T \mathcal{R} d\Omega. \quad (3.2)$$

Note that  $\mathcal{J} = J$ , since the constraint function is zero by definition, and we have introduced the adjoint variables,

$$\Psi^T = [\psi_{\rho_1}, \dots, \psi_{\rho_{n_s}}, \vec{\phi}, \psi_{\rho e}, \psi_{\rho e^{ve}}], \quad (3.3)$$

as the Lagrange multipliers. By seeking stationary points of the Lagrangian, given by Eqn. (3.2), we seek locations in the design space where the gradient of the objective function is aligned with the gradient of the constraint function. When the gradients are aligned, there is no direction that can be traveled along the constraint that decreases the value of the objective function, and a necessary condition for optimality is satisfied.

Calculus of variations and differential geometry provide the theoretical framework to connect arbitrary changes of  $S$  to changes in the flow state,  $U$ , and, by extension,  $\mathcal{J}$ . If  $S$  is a smooth, continuously differentiable ( $C^1$ ) surface, and  $S'$  is the shape after an arbitrary deformation,  $S'$  can be defined as,

$$S' = \{\vec{x} + \delta S(\vec{x})\vec{n}(\vec{x}) : \vec{x} \in S\}, \quad (3.4)$$

where  $\delta S$  represents an infinitesimal deformation in the local normal direction,  $\vec{n}$ , at a location,  $\vec{x}$ , on  $S$ . Changes to  $\mathcal{J}$  from an arbitrary  $\delta S$  may be quantitatively assessed by taking the first variation of the Lagrangian.

Eqn. (3.1) is an optimal control problem when framed this way. The objective function is influenced by the control surface,  $S$ , and, via multiple surface manipulations,  $\delta S$ , a locally minimal value of  $J$  is achieved. Deformations to  $S$  are imposed by the manipulation of the design variables,  $\vec{\alpha}$ , that are used to parameterize the design surface. Changes to  $J$  due to changes in  $\vec{\alpha}$  are determined by computing the gradient,  $\partial J / \partial \vec{\alpha}$ , which, in this work, is acquired using the adjoint method. The remaining sections of this chapter discuss how this gradient is acquired.

## 3.2 The Adjoint Method for Design

The optimal control problem of Eqn. (3.1) seeks the surface topology,  $S$ , that minimizes the objective function,  $J$ , subject to the PDE constraints of the flow governing equations. To accomplish this task, small, locally normal perturbations,  $\delta S$ , are strategically applied to an initial surface,  $S$ , to arrive at the optimal surface,  $S^*$ . To determine the effect of a  $\delta S$  on  $J$ , the first variation is applied to the Lagrangian of Eqn. (3.2),

$$\delta \mathcal{J} = \int_{\delta S} j ds + \int_S \delta j ds - \int_{\Omega} \Psi^T \delta \mathcal{R} d\Omega, \quad (3.5)$$

where  $\int_{\delta S} (\cdot) ds = \int_{S'} (\cdot) ds - \int_S (\cdot) ds$ . Note that the adjoint variables are treated as independent variables in the optimization problem, and are held fixed under changes in the surface definition. Surface perturbations directly influence the Lagrangian by changing the definite integral of  $j$  over  $S$  and change the flow state,  $U$ , via the boundary conditions of the governing equations. The direct influence of changes in  $S$  on  $\mathcal{J}$  are captured in the first term of Eqn. (3.5), while the second and third terms capture the the flow state dependence.

For a given  $S$ , simply solving  $\mathcal{R}$  provides the flow state information necessary to resolve many of the terms of Eqn. (3.5). These may include surface pressures, shear stresses, and thermal gradients at the boundary, depending on the definition of  $j$ . However,  $\delta j$  and  $\delta \mathcal{R}$  contain terms that depend on variations in the flow state,  $\delta U$ , by the chain rule of differentiation. The methodology for resolving this  $\delta U$  dependence for an arbitrary  $\delta S$  is less clear. One may choose to compute  $\mathcal{R}$  again, using the perturbed geometry, and approximate  $\delta U$  based on the differences observed between the two flow solutions. Indeed, this strategy is analogous to the finite-difference method for gradient computation. While straightforward, this approach is unpalatable, since each flow solution constitutes a significant investment in computational resources, and a new flow solution is required for *every* geometric perturbation. Generally, this naive approach for acquiring  $\delta \mathcal{J}$  is computationally untenable, since most problems of practical interest require a large quantity of design parameters to adequately describe  $S$ .

Alternatively,  $\delta \mathcal{J}$  may be acquired by formulating a second set of equations, using the adjoint variables, that, when solved, cancel the dependence of  $\delta \mathcal{J}$  on  $\delta U$ . If such an equation set and boundary conditions can be found, then it is possible to acquire  $\delta \mathcal{J}$  from a solution of  $\mathcal{R}$  and a solution of this alternate equation set, *regardless of the applied surface perturbation*. This approach is known as the adjoint method for design. Contrary to the finite-difference method, which scales linearly in computational cost with the dimensionality of the design space, the adjoint method has a fixed cost to acquire a particular  $\delta \mathcal{J}$ , regardless of the surface parameterization. This property makes the adjoint method attractive for problems where  $\mathcal{R}$  is expensive, and the dimensionality of the design space is large, as is the case for most aerospace applications.

The objective is clear: derive the adjoint equations and boundary conditions to achieve the cancellation of  $\delta U$ . A substantial volume of literature has been published on the adjoint method for aerospace design [2, 38, 59, 60], establishing different methodologies for acquiring the adjoint system for perfect gas environments. When using the continuous adjoint method, a *surface formulation*

of the objective function gradient is sought. A formulation of this type precludes any dependence of volume mesh sensitivity in the objective function gradient, which follows the behavior of the physical problem. By computing the solution to the adjoint problem, the expression for the surface sensitivity at each node on the design surface is computed and projected onto the surface deformation imposed by the design variable manipulations. Generally, surface formulations of the gradient are acquired using either mapping technique [64], or by using differential geometry [14]. In the mapping technique, volumetric mesh dependence in gradient is eliminated by relating variations in the flow state due to variations in the mesh definition. By replacing terms and invoking the definitions of the adjoint equations and boundary conditions a surface formulation of the gradient is defined [63]. The differential geometry method employs identities to relate surface definition changes to the flow state through linearized boundary conditions. This technique can lead to complicated expressions for the surface sensitivities that may require extensive simplification, but does not have any inherent volumetric mesh dependence. This work closely follows the differential geometry technique of Castro *et. al.* [14], Bueno-Orovio *et. al.* [10], and Economou [28], but extends the approach to include the necessary thermochemistry for nonequilibrium gas mixtures. The procedure is as follows:

1. Define the objective function of interest,  $J$ , and apply the first variation to acquire  $\delta J$ .
2. Apply the first variation to the governing equations  $\mathcal{R}$ .
3. Where possible, use Gauss' law to group boundary integrals and volume integrals.
4. Set the integrand of the volume integral to zero to form the adjoint equations.
5. Derive a set of linearized boundary conditions that can be used to relate shape changes to  $\delta U$ .
6. Apply the linearized boundary conditions and set the adjoint boundary conditions to cancel any remaining dependencies on  $\delta U$  on the boundaries.
7. Group all remaining terms into the surface sensitivity.

The remaining sections of this chapter follow the structure presented above.

To assist the derivation, it is convenient to leverage the following identities from the field of differential geometry [118, 130, 131],

$$\int_{\delta S} \xi ds = \int_S [\partial_n \xi - 2H_m \xi] \delta S ds, \quad (3.6a)$$

$$\delta \vec{n}_s = -\nabla_S \delta S, \quad (3.6b)$$

$$\int_S \nabla_S \cdot \vec{\xi} ds = 0, \quad (3.6c)$$

$$\nabla \cdot \vec{\xi} = \partial_n (\vec{\xi} \cdot \vec{n}_s) - 2H_m (\vec{\xi} \cdot \vec{n}_s) + \nabla_S \cdot \vec{\xi}, \quad (3.6d)$$

where  $\xi$  is an arbitrary scalar value, and  $\vec{\xi}$  denotes an arbitrary vector quantity. Derivative operators  $\partial_n$ , and  $\nabla_S$  denote local normal derivatives and surface tangential gradients which are related to

the full gradient by,

$$\begin{aligned}\nabla \xi &= (\nabla \xi \cdot \vec{n})\vec{n} + [\nabla \xi - (\nabla \xi \cdot \vec{n})\vec{n}] \\ \nabla \xi &= (\partial_n \xi)\vec{n} + \nabla_S \xi.\end{aligned}\quad (3.7)$$

$H_m$  is a scalar quantity denoting the local mean curvature,  $H_m = (\kappa_1 + \kappa_2)/2$ , where  $\kappa_1$  and  $\kappa_2$  are the curvatures in two orthogonal directions. These identities are used extensively throughout this chapter to cancel and reformulate terms to arrive at expressions that are easily evaluated within the unstructured numerical solver framework.

### 3.3 Definition and Variation of the Objective Functions

For entry vehicles, the aerothermodynamic environment drives the design of the vehicle. Aerodynamic properties strongly influence the permissible entry trajectories, which, in turn, affect the intensity and duration of the thermal loading on the vehicle. These thermal conditions are critical for the design the TPS, which plays a central role in the survivability of the vehicle. As a consequence, aerodynamic and thermal performance metrics are both key considerations for entry vehicle design. Two relevant objective functions are defined here to address these considerations.

#### 3.3.1 Force-Based Functionals

Many aerodynamic performance metrics, including lift and drag, are the resultant forces from projections of the integrated surface pressures and viscous stresses. These resultant forces are critical in determining the flight characteristics and performance of the vehicle. A family of useful, projected-force objective functions is defined as,

$$J = \int_S \vec{d} \cdot (p \bar{\bar{I}} - \bar{\bar{\sigma}}) \cdot \vec{n} ds. \quad (3.8)$$

The force-projection vector,  $\vec{d}$ , can be defined a variety of ways to yield

$$\vec{d} = \begin{cases} \frac{1}{C_\infty} (\cos \alpha \cos \beta, \sin \alpha \cos \beta, \sin \beta) & C_D \quad \text{Drag} \\ \frac{1}{C_\infty} (-\sin \alpha, \cos \alpha, 0) & C_L \quad \text{Lift} \\ \frac{1}{C_\infty} (-\sin \beta \cos \alpha, -\sin \beta \sin \alpha, \cos \beta) & C_{SF} \quad \text{Side-force} \\ \frac{1}{C_\infty C_D} (-\sin \alpha - \frac{C_L}{C_D} \cos \alpha \cos \beta, -\frac{C_L}{C_D} \sin \beta, \cos \alpha - \frac{C_L}{C_D} \sin \alpha \cos \beta) & \frac{C_L}{C_D} \quad \text{L/D} \\ \frac{1}{C_\infty} (0, 0, 1) & C_{f_z} \quad \text{Z-force} \\ \frac{1}{C_\infty L_{ref}} (-(y - y_0), (x - x_0), 0) & C_{m_z} \quad \text{Z-moment.} \end{cases} \quad (3.9)$$

In Eqn. (3.9),  $C_\infty = (1/2)\rho_\infty u_\infty^2 A_{Ref}$ , where  $\rho_\infty$  is the free-stream mixture density,  $u_\infty$  is the free-stream mixture flow speed, and  $A_{ref}$  is a reference area of the user's choosing. A right-handed, aircraft-fixed coordinate system is assumed, where the X-axis points down the longitudinal axis from nose to tail, the Y-axis extends out the right wing, and the Z-axis points upward, in accordance with

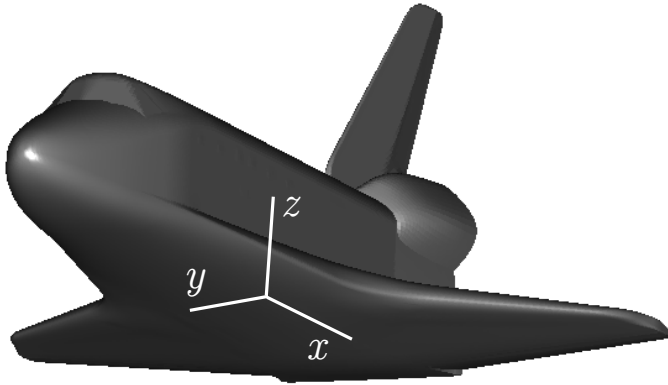


Figure 3.2: Assumed coordinate systems for the projected-force objective function.

the right hand rule. In this local coordinate system,  $\alpha$  is the angle of attack in the X-Z plane, and  $\beta$  is the sideslip angle in the X-Y plane. Moment-coefficients require an extra non-dimensionalizing length,  $L_{ref}$ , and a specified center of gravity,  $\vec{x}_{CG} = \{x_0, y_0, z_0\}$ .

With this common formulation, a single derivation may be performed to acquire sensitivities to any of the quantities listed in Eqn. (3.9). Sensitivities of these quantities can be used directly to optimize the aerodynamic performance of the vehicle, or indirectly to achieve mission requirements for cross-range capability, landed mass, aerodynamic efficiency, and longitudinal static stability.

### First Variation of the Projected-Force Functional

The influence of shape deformations on the projected-force functional is determined by the first variation of Eqn. (3.8),

$$\delta J = \int_S \delta \left[ \vec{d} \cdot (p\bar{I} - \bar{\sigma}) \cdot \vec{n} \right] ds + \int_{\delta S} \vec{d} \cdot (p\bar{I} - \bar{\sigma}) \cdot \vec{n} ds. \quad (3.10)$$

In the first integral, the variational operator is distributed to each term, in accordance with the product rule of differentiation,

$$\int_S \delta \left[ \vec{d} \cdot (p\bar{I} - \bar{\sigma}) \cdot \vec{n} \right] ds = \int_S \vec{d} \cdot (\delta p\bar{I} - \delta\bar{\sigma}) \cdot \vec{n} ds - \int_S \vec{d} \cdot (p\bar{I} - \bar{\sigma}) \cdot \nabla_S \delta S ds \quad (3.11)$$

$$= \int_S \vec{d} \cdot (\delta p\bar{I} - \delta\bar{\sigma}) \cdot \vec{n} ds + \int_S \nabla_S \cdot [\vec{d} \cdot (p\bar{I} - \bar{\sigma})] \delta S ds. \quad (3.12)$$

Note, the force projection vector,  $\vec{d}$ , is constant and therefore unaffected by the variational operator. Eqn. (3.6b) has been used on the last term of Eqn. (3.11). The final term in Eqn. (3.11) is further manipulated by applying integration by parts, such that,  $a\nabla(b) = \nabla(ab) - \nabla(a)b$ , and by using Eqn. (3.6c). To simplify the second integral of Eqn. (3.10), the differential identity from Eqn. (3.6a) is used,

$$\int_{\delta S} \vec{d} \cdot (p\bar{\bar{I}} - \bar{\sigma}) \cdot \vec{n} ds = \int_S [\partial_n(\vec{d} \cdot (p\bar{\bar{I}} - \bar{\sigma}) \cdot \vec{n}) - 2H_m(\vec{d} \cdot (p\bar{\bar{I}} - \bar{\sigma}) \cdot \vec{n})] \delta S ds. \quad (3.13)$$

Combining Eqns. (3.12) & (3.13), the objective function variation is expressed as,

$$\begin{aligned} \delta J &= \int_S \vec{d} \cdot (\delta p\bar{\bar{I}} - \delta\bar{\sigma}) \cdot \vec{n} ds \\ &\quad + \int_S [\partial_n(\vec{d} \cdot (p\bar{\bar{I}} - \bar{\sigma}) \cdot \vec{n}) - 2H_m(\vec{d} \cdot (p\bar{\bar{I}} - \bar{\sigma}) \cdot \vec{n}) + \nabla_S \cdot (\vec{d} \cdot (p\bar{\bar{I}} - \bar{\sigma}))] \delta S ds \\ &= \int_S \vec{d} \cdot (\delta p\bar{\bar{I}} - \delta\bar{\sigma}) \cdot \vec{n} ds + \int_S \vec{d} \cdot (\nabla \cdot (p\bar{\bar{I}} - \bar{\sigma})) \delta S ds, \end{aligned} \quad (3.14)$$

where Eqn. (3.6d) has been applied, and the constant vector,  $\vec{d}$ , is moved outside the divergence operator. Eqn. (3.14) can be further simplified, recognizing  $\nabla \cdot (p\bar{\bar{I}} - \bar{\sigma}) = 0$ , by writing the mixture momentum equation on  $S$  and applying the no-slip boundary condition. The variation of the force objective function can now be written simply as,

$$\delta J = \int_S \vec{d} \cdot (\delta p\bar{\bar{I}} - \delta\bar{\sigma}) \cdot \vec{n} ds. \quad (3.15)$$

### Simplifications for Inviscid Problems

For inviscid flow environments, the definition of  $J$  must be modified. No viscous stresses are present in the flow field, thus the resultant forces acting on a vehicle are from the integrated surface pressure alone,

$$J = \int_S \vec{d} \cdot (p\bar{\bar{I}}) \cdot \vec{n} ds. \quad (3.16)$$

To acquire the variation of  $J$ , we follow the procedure of Eqns. (3.10)-(3.14), applying the same expansions, manipulations and redefinitions to arrive at,

$$\delta J = \int_S \vec{d} \cdot (\delta p\bar{\bar{I}}) \cdot \vec{n} ds + \int_S (\vec{d} \cdot \nabla p) \delta S ds. \quad (3.17)$$

For inviscid flow problems, the final term of Eqn. (3.17) persists in the objective function variation. This differs from the previously derived result for viscous problems because the final term cannot be canceled in the same fashion by writing the momentum equation on the surface, due to the differences in the velocity boundary conditions at the wall.

### 3.3.2 Thermal Functionals

In many cases, mitigating the thermal loading to a hypersonic entry vehicle is the primary design consideration. For the purposes of gradient-based optimization, a continuous functional for thermal design may be defined as the  $p$ -norm of the local heat flux,

$$J = \left( \int_S \left[ -(q^{\vec{t}r} + q^{\vec{v}e}) \cdot \vec{n} \right]^p ds \right)^{1/p}. \quad (3.18)$$

In the limit of  $p \rightarrow \infty$ , the objective function is the maximum local heat flux on the vehicle's surface, whereas  $p = 1$  tracks the total thermal transfer from the flow environment to the vehicle. Often, TPS material selection is based on the peak heat flux, while the thickness of the heat shield is determined by the integrated thermal loading throughout the entry phase of the mission. Therefore, it is possible to acquire sensitivity information for both these thermal design metrics using a single objective function by simply varying the value of  $p$ . For convenience, the following additional parameters are defined,

$$\vec{q} = q^{\vec{t}r} + q^{\vec{v}e} \quad (3.19a)$$

$$q_n = \vec{q} \cdot \vec{n} \quad (3.19b)$$

$$j = (-q_n)^p \quad (3.19c)$$

$$\beta = (1/p) \left( \int_S j ds \right)^{1/p-1} \quad (3.19d)$$

#### First Variation of the Thermal Functional

The influence of shape deformations on the thermal functional may be quantitatively assessed by applying the variational operator to Eqn. (3.18),

$$\delta J = \beta \left( \int_S \delta j ds + \int_{\delta S} j ds \right). \quad (3.20)$$

For the purposes of the adjoint problem,  $\beta$  is a constant, and does not require further manipulation. Taking each term in sequence,

$$\begin{aligned} \int_S \delta j ds &= \int_S \delta \left[ - (q^{\vec{t}r} + q^{\vec{v}e}) \cdot \vec{n} \right]^p ds \\ &= \int_S p(-q_n)^{p-1} \left[ -\delta(q^{\vec{t}r} + q^{\vec{v}e}) \cdot \vec{n} - \vec{q} \cdot \delta \vec{n} \right] ds \end{aligned} \quad (3.21)$$

Applying Eqn. (3.6b), integration-by-parts, and Eqn. (3.6c) to the second term of Eqn. (3.21) yields,

$$\begin{aligned} \int_S \delta j ds &= - \int_S p(-q_n)^{p-1} (\delta q^{\vec{t}r} + \delta q^{\vec{v}e}) \cdot \vec{n} ds - \int_S \nabla_S \cdot (p(-q_n)^{p-1} \vec{q}) \delta S ds \\ &= - \int_S p(-q_n)^{p-1} (\delta q^{\vec{t}r} + \delta q^{\vec{v}e}) \cdot \vec{n} ds - \int_S \{ \nabla_S [p(-q_n)^{p-1}] \cdot \vec{q} + p(-q_n)^{p-1} \nabla_S \cdot \vec{q} \} \delta S ds. \end{aligned} \quad (3.22)$$

Proceeding with the second term of the objective function variation,

$$\begin{aligned} \int_{\delta S} j ds &= \int_S [\partial_n j - 2H_m j] \delta S ds \\ &= \int_S \{ \partial_n (-q_n)^p - 2H_m (-q_n)^p \} \delta S ds \\ &= \int_S \{ p(-q_n)^{p-1} \partial_n (-q_n) - (-q_n)^{p-1} 2H_m (-q_n) \} \delta S ds \\ &= \int_S p(-q_n)^{p-1} [\partial_n (-q_n) - 2H_m (-q_n)] \delta S ds + \int_S 2(p-1) H_m (-q_n)^p \delta S ds. \end{aligned} \quad (3.23)$$

Combining Eqn. (3.22) and (3.23) and making use of Eqn. (3.6d),

$$\begin{aligned} \int_S \delta j ds + \int_{\delta S} j ds &= - \int_S p(-q_n)^{p-1} (\delta q^{\vec{t}r} + \delta q^{\vec{v}e}) \cdot \vec{n} ds - \int_S \nabla_S [p(-q_n)^{p-1}] \cdot \vec{q} \delta S ds \\ &\quad + \int_S p(-q_n)^{p-1} \nabla \cdot (-\vec{q}) \delta S ds + \int_S 2(p-1) H_m (-q_n)^p \delta S ds. \end{aligned} \quad (3.24)$$

From Eqn. (3.24), the variation of the objective function,  $\delta J$ , is expressed as,

$$\begin{aligned} \delta J &= \frac{1}{p} \left( \int_S j ds \right)^{\frac{1}{p}-1} \left( \int_S \delta j ds + \int_{\delta S} j ds \right) \\ &= -\beta \int_S p(-q_n)^{p-1} (\delta q^{\vec{t}r} + \delta q^{\vec{v}e}) \cdot \vec{n} ds - \beta \int_S \nabla_S [p(-q_n)^{p-1}] \cdot \vec{q} \delta S ds \\ &\quad + \beta \int_S p(-q_n)^{p-1} \nabla \cdot (-\vec{q}) \delta S ds + \beta \int_S 2(p-1) H_m (-q_n)^p \delta S ds. \end{aligned} \quad (3.25)$$

For the special case,  $p = 1$ ,  $\beta = 1$  and Eqn. (3.25) simplifies to,

$$\delta J|_{p=1} = - \int_S (\delta q^{\vec{t}r} + \delta q^{\vec{v}e}) \cdot \vec{n} ds + \int_S \nabla \cdot (-\vec{q}) \delta S ds. \quad (3.26)$$

### 3.4 Variation of the Governing Equations

The boundaries of the flow domain impose a required set of conditions to solve the governing equation PDE system. Therefore, changes to the boundaries necessarily change the fluid state within the problem domain. The effect of these changes is captured in the final term of Eqn. (3.5), and requires

evaluating the variation of the flow governing equations,  $\delta\mathcal{R}$ . To aid in the derivation, the governing equations are redefined by splitting the viscous flux vector into four components,

$$\mathcal{R} = \nabla \cdot \vec{F}^c - \nabla \cdot (\mu^k \vec{F}^{vk}) - Q, \quad (3.27)$$

where we have defined each of the  $\vec{F}^{vk}$  as,

$$\vec{F}^{v1} = \begin{bmatrix} -\vec{J}_s \\ \bar{\vec{0}} \\ -\sum_s \vec{J}_s h_s^{int} \\ -\sum_s \vec{J}_s e_s^{ve} \end{bmatrix}, \quad \vec{F}^{v2} = \begin{bmatrix} 0 \\ \bar{\vec{\tau}} \\ \vec{u}^\top \bar{\vec{\tau}} \\ 0 \end{bmatrix}, \quad \vec{F}^{v3} = \begin{bmatrix} 0 \\ \bar{\vec{0}} \\ \nabla T \\ 0 \end{bmatrix}, \quad \vec{F}^{v4} = \begin{bmatrix} 0 \\ \bar{\vec{0}} \\ \nabla T^{ve} \\ \nabla T^{ve} \end{bmatrix}, \quad (3.28)$$

with corresponding transport coefficients,

$$\mu^k = \begin{cases} 1 & \text{for } k = 1 \text{ and } s = 1, \dots, n_s \\ \mu & \text{for } k = 2 \\ \kappa^{tr} & \text{for } k = 3 \\ \kappa^{ve} & \text{for } k = 4. \end{cases} \quad (3.29)$$

The matrix,  $\bar{\vec{\tau}}$ , in Eqn. (3.28) is the viscous strain-rate tensor,  $\bar{\vec{\tau}} = (1/2)(\nabla \vec{u} + \nabla \vec{u}^\top) - (2/3)\nabla \cdot \vec{u} \bar{\vec{I}}$ . Splitting the viscous fluxes and separating the transport coefficients in this manner permits a more systematic, modularized approach to deriving the adjoint system. In principle, this provides some flexibility to accommodate more complex thermochemical models with minimal re-derivation. Unfortunately, the diffusion coefficients may not be separated in the same way as the viscous and thermal transport coefficients, so they remain present in  $\vec{F}^{v1}$ .

In applying the variational operator to the terms of Eqn. (3.27), it is clear that second-derivative information is required to evaluate the variation of the viscous fluxes. Looking ahead to the numerical implementation, second-derivative information is difficult and expensive to acquire in unstructured, finite-volume solvers, and should be avoided wherever possible. To this end, the flow state,  $U$ , and the flow state gradient,  $\nabla U$ , are treated as independent variables when applying the variational operator. Under this prescription,

$$\begin{aligned} \delta\mathcal{R}(U, \nabla U) &= \delta \left[ \nabla \cdot \vec{F}^c - \nabla \cdot (\mu^k \vec{F}^{vk}) - Q \right] \\ &= \nabla \cdot \frac{\partial \vec{F}^c}{\partial U} \delta U - \nabla \cdot \left( \vec{F}^{vk} \frac{\partial \mu^k}{\partial U} \delta U \right) - \nabla \cdot \left[ \mu^k \left( \frac{\partial \vec{F}^{vk}}{\partial U} \delta U + \frac{\partial \vec{F}^{vk}}{\partial \nabla U} \cdot \delta(\nabla U) \right) \right] - \frac{\partial Q}{\partial U} \delta U \\ &= \left[ \nabla \cdot \left( \vec{A}^c - \vec{F}^{vk} \frac{\partial \mu^k}{\partial U} - \mu^k \vec{A}^{vk} \right) - \frac{\partial Q}{\partial U} \right] \delta U - \nabla \cdot \left( \mu^{vk} \bar{\vec{D}}^{vk} \cdot \delta(\nabla U) \right), \end{aligned} \quad (3.30)$$

where the following Jacobian matrices have been introduced,

$$\left. \begin{aligned} \vec{A}^c &= \{A_x^c, A_y^c, A_z^c\}, & A_i &= \frac{\partial F_i^c}{\partial U} \\ \vec{A}^{vk} &= \{A_x^{vk}, A_y^{vk}, A_z^{vk}\}, & A_i^{vk} &= \frac{\partial F_i^{vk}}{\partial U} \\ \bar{\bar{D}}^{vk} &= \begin{bmatrix} D_{xx}^{vk} & D_{xy}^{vk} & D_{xz}^{vk} \\ D_{yx}^{vk} & D_{yy}^{vk} & D_{yz}^{vk} \\ D_{zx}^{vk} & D_{zy}^{vk} & D_{zz}^{vk} \end{bmatrix}, & D_{ij}^{vk} &= \frac{\partial F_i^{vk}}{\partial \partial_j U} \end{aligned} \right\} \quad \begin{array}{l} \text{for } i, j \in \{x, y, z\} \\ \text{and } k \in \{1, 2, 3, 4\}. \end{array} \quad (3.31)$$

The Jacobian matrices of Eqn. (3.31) are included in Appendix B.

To acquire the final term in the Lagrangian variation of Eqn. (3.5), an inner product of the adjoint variables and Eqn. (3.30) is performed and integrated over the domain,  $\Omega$ , such that,

$$\begin{aligned} \int_{\Omega} \Psi^T \delta \mathcal{R} d\Omega &= \int_{\Omega} \Psi^T \left[ \nabla \cdot \left( \vec{A}^c - \vec{F}^{vk} \frac{\partial \mu^k}{\partial U} - \mu^k \vec{A}^{vk} \right) - \frac{\partial Q}{\partial U} \right] \delta U d\Omega \\ &\quad - \int_{\Omega} \Psi^T \nabla \cdot \left( \mu^{vk} \bar{\bar{D}}^{vk} \cdot \delta(\nabla U) \right) d\Omega. \end{aligned} \quad (3.32)$$

Recall the objective of the adjoint method: cancel any  $\delta U$  dependency in  $\delta \mathcal{J}$ . From Section 3.3, flow-variational terms are present on the boundaries of the flow domain. To cancel this dependency, boundary terms must be generated from Eqn. (3.32) using a combination of the product rule of differentiation and Gauss' theorem. This procedure is applied to the first term of Eqn. (3.32) below,

$$\begin{aligned} \int_{\Omega} \Psi^T \left[ \nabla \cdot \left( \vec{A}^c - \vec{F}^{vk} \frac{\partial \mu^k}{\partial U} - \mu^k \vec{A}^{vk} \right) - \frac{\partial Q}{\partial U} \right] \delta U d\Omega &= \int_{\Gamma} \left[ \Psi^T \left( \vec{A}^c - \vec{F}^{vk} \frac{\partial \mu^k}{\partial U} - \mu^k \vec{A}^{vk} \right) \delta U \right] \cdot \vec{n} ds \\ &\quad - \int_{\Omega} \nabla \Psi^T \cdot \left( \vec{A}^c - \vec{F}^{vk} \frac{\partial \mu^k}{\partial U} - \mu^k \vec{A}^{vk} \right) \delta U d\Omega \\ &\quad - \int_{\Omega} \Psi^T \frac{\partial Q}{\partial U} \delta U d\Omega. \end{aligned} \quad (3.33)$$

For the second integral of Eqn. (3.32), the product rule must be applied twice to isolate the variational term,  $\delta U$ . Applying the first product rule,

$$\begin{aligned} \int_{\Omega} \Psi^T \nabla \cdot \left( \mu^{vk} \bar{\bar{D}}^{vk} \cdot \delta(\nabla U) \right) d\Omega &= \int_{\Omega} \nabla \cdot \left( \Psi^T \mu^{vk} \bar{\bar{D}}^{vk} \cdot \delta(\nabla U) \right) d\Omega \\ &\quad - \int_{\Omega} \nabla \Psi^T \cdot \left( \mu^{vk} \bar{\bar{D}}^{vk} \cdot \nabla \delta U \right) d\Omega. \end{aligned} \quad (3.34)$$

For continuous systems, the order of differentiation may be exchanged,  $\delta(\nabla U) = \nabla \delta U$ . Applying this property to the final term of Eqn. (3.34) and recognizing,

$$\nabla \Psi^T \cdot \left( \mu^{vk} \bar{\bar{D}}^{vk} \cdot \nabla \delta U \right) = \nabla \cdot \left( \nabla \Psi^T \cdot (\mu^{vk} \bar{\bar{D}}^{vk} \delta U) \right) - \nabla \cdot (\nabla \Psi^T \cdot \mu^{vk} \bar{\bar{D}}^{vk}) \delta U, \quad (3.35)$$

it is then possible to apply Gauss' theorem, yielding,

$$\begin{aligned} \int_{\Omega} \Psi^T \nabla \cdot (\mu^{vk} \bar{\bar{D}}^{vk} \cdot \delta(\nabla U)) d\Omega &= \int_{\Gamma} (\Psi^T \mu^{vk} \bar{\bar{D}}^{vk} \cdot \delta(\nabla U)) \cdot \vec{n} ds \\ &\quad - \int_{\Gamma} (\nabla \Psi^T \cdot (\mu^{vk} \bar{\bar{D}}^{vk} \delta U)) \cdot \vec{n} ds \\ &\quad + \int_{\Omega} \nabla \cdot (\nabla \Psi^T \cdot \mu^{vk} \bar{\bar{D}}^{vk}) \delta U d\Omega. \end{aligned} \quad (3.36)$$

Having performed the appropriate simplifications to each term, the final conclusion is the assembly of Eqns. (3.33) and (3.36),

$$\begin{aligned} \int_{\Omega} \Psi^T \delta \mathcal{R} d\Omega &= \int_{\Gamma} (B_1 - B_2 + B_3) ds \\ &\quad - \int_{\Omega} \left[ \nabla \Psi^T \cdot \left( \vec{A}^c - \vec{F}^{vk} \frac{\partial \mu^k}{\partial U} - \mu^k \vec{A}^{vk} \right) + \nabla \cdot (\nabla \Psi^T \cdot \mu^k \bar{\bar{D}}^{vk}) + \Psi^T \frac{\partial Q}{\partial U} \right] \delta U d\Omega, \end{aligned} \quad (3.37)$$

where the following have been defined,

$$B_1 = \Psi^T (\vec{A}^c \cdot \vec{n}) \delta U \quad (3.38a)$$

$$B_2 = \Psi^T \left[ \left( \mu^k \vec{A}^{vk} + \vec{F}^{vk} \frac{\partial \mu^k}{\partial U} \right) \delta U + \mu^k \bar{\bar{D}}^{vk} \cdot \delta(\nabla U) \right] \cdot \vec{n} \quad (3.38b)$$

$$B_3 = \nabla \Psi^T \cdot \mu^k \bar{\bar{D}}^{vk} \cdot \vec{n} \delta U. \quad (3.38c)$$

Eqns. (3.37) and (3.38) are critical in the development of the adjoint method. By mathematically manipulating  $\int_{\Omega} \Psi^T \delta \mathcal{R} d\Omega$ , dependencies on  $\delta U$  in the flow domain have been isolated, and a set of *adjoint boundary integrals* has been defined on the domain boundaries,  $\Gamma$ , that will be used to eliminate the remaining  $\delta U$  dependencies from  $\delta J$ . With this foundation in place, a systematic elimination of all  $\delta U$  terms in  $\delta \mathcal{J}$  can take place.

Consider the volume integral in Eqn. (3.37). To eliminate  $\delta U$  in  $\Omega$ , the integral must be zero for arbitrary domains. For this to be true, the integrand must be set equal to zero,

$$-\nabla \Psi^T \cdot \left( \vec{A}^c - \vec{F}^{vk} \frac{\partial \mu^k}{\partial U} - \mu^k \vec{A}^{vk} \right) - \nabla \cdot (\nabla \Psi^T \cdot \mu^k \bar{\bar{D}}^{vk}) - \Psi^T \frac{\partial Q}{\partial U} = 0. \quad (3.39)$$

The coupled, non-conservative, linear PDEs of Eqn. (3.39) are known as the *adjoint equations*. In this equation system, the independent variables are the adjoint variables,  $\Psi$ , and the various Jacobian matrices are populated with the local solution to the flow governing equations. When these equations are satisfied, all  $\delta U$  dependence within the volume is eliminated from  $\delta \mathcal{J}$ . The boundary conditions for the adjoint equations are determined from the adjoint boundary integrals and the objective function.

## 3.5 The Adjoint Boundary Integrals

The adjoint boundary integrals are introduced into the Lagrangian variation by the application of Gauss' law. These boundary integrals are necessary to eliminate  $\delta U$  dependence on the boundaries of the flow domain introduced by the variation of the objective function  $\delta J$ . The process of canceling  $\delta U$  is unique for each objective function and direct problem boundary condition set. Before canceling, it is useful to simplify the adjoint boundary integrals using the definitions of the Jacobian matrices in Appendix B.

### 3.5.1 Simplification of the First Adjoint Boundary Integral

The first adjoint boundary integral consists of the adjoint variables, the convective flux Jacobian, and the perturbed flow state,  $\delta U$ , on the boundary. Here, it is more convenient to work with the primitive variables,

$$V = \{\rho_1, \dots, \rho_{n_s}, u, v, w, p, T^{ve}\}^\top, \quad (3.40)$$

as compared to the conserved quantities. The adjoint boundary integral,  $B_1$ , is re-stated as,

$$B_1 = \Psi^\top (\vec{A}^c \cdot \vec{n}) \delta U = \Psi^\top (\vec{A}^c \cdot \vec{n}) \frac{\partial U}{\partial V} \delta V. \quad (3.41)$$

To simplify, it is necessary to insert the definition of  $\partial U / \partial V$  and  $(\vec{A}^c \cdot \vec{n})$  from Eqns. (B.9) and Eqn. (B.11) respectively. After carrying out the matrix-matrix multiplication and evaluating  $(\vec{A}^c \cdot \vec{n})(\partial U / \partial V)$  under the no-slip,  $\vec{u} = \vec{0}$ , condition, the adjoint boundary integral is expressed as,

$$\begin{aligned} B_1 &= \begin{bmatrix} \psi_{\rho_1} \\ \vdots \\ \psi_{\rho_{n_s}} \\ \psi_{\rho u} \\ \psi_{\rho v} \\ \psi_{\rho w} \\ \psi_{\rho e} \\ \psi_{\rho e^{ve}} \end{bmatrix}^\top \begin{bmatrix} 0 & \cdots & 0 & \rho_1 \hat{n}_x & \rho_1 \hat{n}_y & \rho_1 \hat{n}_z & 0 & 0 \\ \vdots & \ddots & \vdots & \vdots & \vdots & \vdots & \vdots & \vdots \\ 0 & \cdots & 0 & \rho_{n_s} \hat{n}_x & \rho_{n_s} \hat{n}_y & \rho_{n_s} \hat{n}_z & 0 & 0 \\ 0 & \cdots & 0 & 0 & 0 & 0 & \hat{n}_x & 0 \\ 0 & \cdots & 0 & 0 & 0 & 0 & \hat{n}_y & 0 \\ 0 & \cdots & 0 & 0 & 0 & 0 & \hat{n}_z & 0 \\ 0 & \cdots & 0 & \rho h \hat{n}_x & \rho h \hat{n}_y & \rho h \hat{n}_z & 0 & 0 \\ 0 & \cdots & 0 & \rho e^{ve} \hat{n}_x & \rho e^{ve} \hat{n}_y & \rho e^{ve} \hat{n}_z & 0 & 0 \end{bmatrix} \begin{bmatrix} \delta \rho_1 \\ \vdots \\ \delta \rho_{n_s} \\ \delta u \\ \delta v \\ \delta w \\ \delta p \\ \delta T^{ve} \end{bmatrix} \\ &= \vartheta \delta \vec{u} \cdot \vec{n} + (\vec{\phi} \cdot \vec{n}) \delta p, \end{aligned} \quad (3.42)$$

where we have defined,

$$\vartheta = \sum_s \rho_s \psi_{\rho_s} + \rho h \psi_{\rho e} + \rho e^{ve} \psi_{\rho e^{ve}}. \quad (3.43)$$

The simplification of  $B_1$  may be repeated for inviscid problems. In this case,  $V$  and  $\partial U / \partial V$  are unchanged, but  $(\vec{A}^c \cdot \vec{n})$  is evaluated under the flow-tangency,  $\vec{u} \cdot \vec{n} = 0$ , boundary condition. Nevertheless, after performing the appropriate matrix-matrix multiplications, it can be shown that Eqn. (3.42) holds for inviscid problems.

### 3.5.2 Simplification of the Second Adjoint Boundary Integral

The second boundary integral consists of terms arising from the application of the variational operator to the viscous flux vector,

$$\begin{aligned} B_2 &= \Psi^\top \left[ \left( \mu^k \vec{A}^{vk} + \vec{F}^{vk} \frac{\partial \mu^k}{\partial U} \right) \delta U + \mu^k \bar{\vec{D}}^{vk} \cdot \delta(\nabla U) \right] \cdot \vec{n} \\ &= \Psi^\top \delta \left( \mu^k \vec{F}^{vk} \right) \cdot \vec{n}. \end{aligned} \quad (3.44)$$

For clarity, the viscous flux vectors,  $\vec{F}^{vk}$  are manipulated in-turn and assigned to a corresponding  $B_2^k$  such that the second boundary integral is determined by,  $B_2 = \sum_k B_2^k$ . For the diffusion phenomena,

$$\begin{aligned} B_2^1 &= \Psi^\top \delta(\mu^1 \vec{F}^{v1}) \cdot \vec{n} \\ &= - \sum_s \psi_{\rho_s} \delta \vec{J}_s \cdot \vec{n} - \psi_{\rho e} \sum_s \delta \left( \vec{J}_s h_s^{int} \right) \cdot \vec{n} - \psi_{\rho e^{ve}} \sum_s \delta \left( \vec{J}_s e_s^{ve} \right) \cdot \vec{n} \\ &= - \sum_s \psi_{\rho_s} \left( \delta \vec{J}_s \cdot \vec{n} \right) - \psi_{\rho e} \sum_s \left( \delta \vec{J}_s \cdot \vec{n} \right) h_s^{int} - \psi_{\rho e} \sum_s \left( \vec{J}_s \cdot \vec{n} \right) [(C_{v,s}^{tr} + R_s) \delta T + C_{v,s}^{ve} \delta T^{ve}] \\ &\quad - \psi_{\rho e^{ve}} \sum_s \left( \delta \vec{J}_s \cdot \vec{n} \right) e_s^{ve} - \psi_{\rho e^{ve}} \sum_s \left( \vec{J}_s \cdot \vec{n} \right) C_{v,s}^{ve} \delta T^{ve}, \end{aligned} \quad (3.45)$$

where  $R_s = R_u/M_s$  is the species gas constant. Similarly, for  $k = 2$ ,

$$\begin{aligned} B_2^2 &= \Psi^\top \delta(\mu^2 \vec{F}^{v2}) \cdot \vec{n} \\ &= \vec{\phi} \cdot \delta \bar{\vec{\sigma}} \cdot \vec{n} + \psi_{\rho e} \delta(\vec{u}^\top \cdot \bar{\vec{\sigma}}) \cdot \vec{n} \\ &= \vec{\phi} \cdot \delta \bar{\vec{\sigma}} \cdot \vec{n} + \psi_{\rho e} \delta \vec{u}^\top \cdot \bar{\vec{\sigma}} \cdot \vec{n}. \end{aligned} \quad (3.46)$$

From the second to third lines of Eqn. (3.46), the variational operator is applied to  $\bar{\vec{\sigma}}$  and  $\vec{u}$  in accordance with the product rule of differentiation. All remaining terms with  $\vec{u}$  are eliminated by applying the no-slip boundary condition. For translational-rotational thermal conduction,

$$\begin{aligned} B_2^3 &= \Psi^\top \delta(\mu^3 \vec{F}^{v3}) \cdot \vec{n} \\ &= \psi_{\rho e} \delta(\kappa^{tr} \nabla T) \cdot \vec{n}. \end{aligned} \quad (3.47)$$

Lastly, for vibrational-electronic thermal conduction,

$$\begin{aligned} B_2^4 &= \Psi^\top \delta(\mu^4 \vec{F}^{v4}) \cdot \vec{n} \\ &= (\psi_{\rho e} + \psi_{\rho e^{ve}}) \delta(\kappa^{ve} \nabla T^{ve}) \cdot \vec{n}. \end{aligned} \quad (3.48)$$

Assembling Eqns. (3.45) - (3.48), the second adjoint boundary integral is written as,

$$\begin{aligned}
B_2 &= B_2^1 + B_2^2 + B_2^3 + B_2^4 \\
&= - \sum_s \psi_{\rho_s} (\delta \vec{J}_s \cdot \vec{n}) - \psi_{\rho e} \sum_s (\delta \vec{J}_s \cdot \vec{n}) h_s^{int} - \psi_{\rho e} \sum_s (\vec{J}_s \cdot \vec{n}) (C_v^{tr} \delta T + C_v^{ve} \delta T^{ve}) \\
&\quad - \psi_{\rho e^{ve}} \sum_s (\delta \vec{J}_s \cdot \vec{n}) e_s^{ve} - \psi_{\rho e^{ve}} \sum_s (\vec{J}_s \cdot \vec{n}) C_v^{ve} \delta T^{ve} + \vec{\phi} \cdot \delta \bar{\sigma} \cdot \vec{n} \\
&\quad + \psi_{\rho e} \bar{\sigma} \cdot \delta \vec{u} \cdot \vec{n} + \psi_{\rho e} \delta(\kappa^{tr} \nabla T) \cdot \vec{n} + (\psi_{\rho e} + \psi_{\rho e^{ve}}) \delta(\kappa^{ve} \nabla T^{ve}) \cdot \vec{n}
\end{aligned} \tag{3.49}$$

Terms in  $B_2$ , such as  $\delta \vec{J}$  and  $\delta \bar{\sigma}$ , may be simplified further by applying certain boundary conditions, and this will be addressed appropriately during the assignment of the adjoint boundary integrals and simplification of the surface sensitivities.

### 3.5.3 Simplification of the Third Adjoint Boundary Integral

The third adjoint boundary integral is approached in the same fashion as  $B_2$ , where each contribution to the integrand is simplified individually for  $k = 1, 2, 3, 4$ , such that  $B_3 = \sum_k B_3^k$ . For clarity,  $B_3^k$  is expanded and evaluated as

$$\begin{aligned}
B_3^k &= \nabla \Psi^\top \cdot \mu^k \bar{D}^{vk} \cdot \vec{n} \delta U \\
&= \begin{bmatrix} \partial_x \Psi^\top \\ \partial_y \Psi^\top \\ \partial_z \Psi^\top \end{bmatrix} \cdot \mu^k \begin{bmatrix} D_{xx}^{vk} & D_{xy}^{vk} & D_{xz}^{vk} \\ D_{yx}^{vk} & D_{yy}^{vk} & D_{yz}^{vk} \\ D_{zx}^{vk} & D_{zy}^{vk} & D_{zz}^{vk} \end{bmatrix} \cdot \begin{bmatrix} \hat{n}_x & \hat{n}_y & \hat{n}_z \end{bmatrix} \delta U \\
&= \begin{bmatrix} \partial_x \Psi^\top \\ \partial_y \Psi^\top \\ \partial_z \Psi^\top \end{bmatrix} \cdot \mu^k \begin{bmatrix} D_{xx}^{vk} \hat{n}_x + D_{xy}^{vk} \hat{n}_y + D_{xz}^{vk} \hat{n}_z \\ D_{yx}^{vk} \hat{n}_x + D_{yy}^{vk} \hat{n}_y + D_{yz}^{vk} \hat{n}_z \\ D_{zx}^{vk} \hat{n}_x + D_{zy}^{vk} \hat{n}_y + D_{zz}^{vk} \hat{n}_z \end{bmatrix} \delta U
\end{aligned} \tag{3.50}$$

By inserting the definitions for the  $D_{ij}^{vk}$  from Appendix B, simplified forms of  $B_3^k$  are derived.

For  $k = 1$ , corresponding to the diffusion phenomena, Eqns. (B.19) and (B.20) are inserted into Eqn. (3.50). The row vector,  $\nabla \Psi^\top \cdot \mu^1 \bar{D}^{v1} \cdot \vec{n}$ , consists of nonzero elements in the first  $n_s$  indices, where the  $r^{th}$  entry is

$$\begin{aligned}
\nabla \Psi^\top \cdot \mu^1 \bar{D}^{v1} \cdot \vec{n} \Big|_r &= \sum_s \left[ (\nabla \psi_{\rho_s} \cdot \vec{n}) \left( \rho D_s \frac{\partial Y_s}{\partial \rho_r} - Y_s \sum_k \rho D_k \frac{\partial Y_k}{\partial \rho_r} \right) \right] \\
&\quad + (\nabla \psi_{\rho e} \cdot \vec{n}) \sum_s \left[ \rho D_s \frac{\partial Y_s}{\partial \rho_r} - Y_s \sum_k \rho D_k \frac{\partial Y_k}{\partial \rho_r} \right] h_s^{int} \\
&\quad + (\nabla \psi_{\rho e^{ve}} \cdot \vec{n}) \sum_s \left[ \rho D_s \frac{\partial Y_s}{\partial \rho_r} - Y_s \sum_k \rho D_k \frac{\partial Y_k}{\partial \rho_r} \right] e_s^{ve}.
\end{aligned} \tag{3.51}$$

Multiplying  $\nabla\Psi^\top \cdot \mu^1 \bar{D}^{v1} \cdot \vec{n}$  by the flow variation,  $\delta U$  yields,

$$\begin{aligned}
B_3^1 &= \nabla\Psi^\top \cdot \mu^1 \bar{D}^{v1} \cdot \vec{n} \delta U \\
&= \begin{bmatrix} \nabla\psi^\top \cdot \mu^1 \bar{D}^{v1} \cdot \vec{n} \\ \vdots \\ \nabla\psi^\top \cdot \mu^1 \bar{D}^{v1} \cdot \vec{n} \\ \vec{0} \\ 0 \\ 0 \end{bmatrix}_N^\top \begin{bmatrix} \delta\rho_1 \\ \vdots \\ \delta\rho_N \\ \delta(\rho\vec{u}) \\ \delta(\rho e) \\ \delta(\rho e^{ve}) \end{bmatrix} \\
&= \sum_s \left[ (\nabla\psi_{\rho_s} \cdot \vec{n})(\rho D_s \delta Y_s - Y_s \sum_k \rho D_k \delta Y_k) \right. \\
&\quad + (\nabla\psi_{\rho e} \cdot \vec{n}) \sum_s \left[ \rho D_s \delta Y_s - Y_s \sum_k \rho D_k \delta Y_k \right] h_s^{int} \\
&\quad \left. + (\nabla\psi_{\rho e^{ve}} \cdot \vec{n}) \sum_s \left[ \rho D_s \delta Y_s - Y_s \sum_k \rho D_k \delta Y_k \right] e_s^{ve} \right]. \tag{3.52}
\end{aligned}$$

The variation in the mass fractions,  $\delta Y_s$  are used in Eqn. (3.52) in favor of the  $\sum_r (\partial Y_s / \partial \rho_r) \delta \rho_r$  terms by using the definition of the chain rule of differentiation,  $\delta Y_s = (\partial Y_s / \partial U) \delta U$ . This mass fraction variation aligns with the linearized boundary conditions corresponding to catalytic and non-catalytic boundary conditions.

To determine the  $k = 2$  contribution to  $B_3$ , the definitions of  $D_{ij}^{v2}$  from Eqns. (B.26) and (B.27) are inserted into Eqn. (3.50). An underlying structure exists to write  $\nabla\Psi^\top \cdot \mu^2 \bar{D}^{v2} \cdot \vec{n}$  in a compact way by defining the following matrices,

$$\bar{\Sigma}^\phi = \nabla\vec{\phi} + (\nabla\vec{\phi})^\top - \frac{2}{3}\bar{I}\nabla \cdot \vec{\phi} \tag{3.53a}$$

$$\bar{\Sigma}^{\psi_{\rho e}} = \nabla\psi_{\rho e}\vec{u} + (\nabla\psi_{\rho e}\vec{u})^\top - \frac{2}{3}\bar{I}\nabla\psi_{\rho e} \cdot \vec{u}, \tag{3.53b}$$

where  $\vec{\phi}$  is the vector of adjoint velocities. Using Eqn. (3.53), Eqn. (3.50) is expressed as,

$$\begin{aligned}
B_3^2 &= \nabla \Psi^\top \cdot \mu^2 \bar{D}^{v2} \cdot \vec{n} \delta U \\
&= \frac{\mu}{\rho} \begin{bmatrix} -\vec{u}^\top (\bar{\Sigma}^\phi + \bar{\Sigma}^{\psi_{pe}}) \cdot \vec{n} \\ \vdots \\ -\vec{u}^\top (\bar{\Sigma}^\phi + \bar{\Sigma}^{\psi_{pe}}) \cdot \vec{n} \\ (\bar{\Sigma}^\phi + \bar{\Sigma}^{\psi_{pe}}) \cdot \vec{n} \\ 0 \\ 0 \end{bmatrix}^\top \begin{bmatrix} \delta\rho_1 \\ \vdots \\ \delta\rho_N \\ (\delta\rho)\vec{u} + \rho(\delta\vec{u}) \\ \delta(\rho e) \\ \delta(\rho e^{ve}) \end{bmatrix} \\
&= \frac{\mu}{\rho} \left\{ \left[ -\vec{u}^\top (\bar{\Sigma}^\phi + \bar{\Sigma}^{\psi_{pe}}) \cdot \vec{n} \right] \sum_s \delta\rho_s + [(\bar{\Sigma}^\phi + \bar{\Sigma}^{\psi_{pe}}) \cdot \vec{n}] (\vec{u}\delta\rho + \rho\delta\vec{u}) \right\} \\
&= \mu(\bar{\Sigma}^\phi \cdot \vec{n})\delta\vec{u}.
\end{aligned} \tag{3.54}$$

In Eqn. (3.54), the momentum variation in  $\delta U$  is expressed as  $\delta(\rho\vec{u}) = (\delta\rho)\vec{u} + \rho(\delta\vec{u})$ . This is to leverage the linearized boundary conditions applied to the primitive,  $\vec{u}$ , on the boundary. Also, by separating the momentum contribution in this way, it permits elimination of all terms that include  $\vec{u}$  by enforcing the no-slip boundary condition on  $S$ . Note,  $\bar{\Sigma}^{\psi_{pe}} = \bar{0}$  by the application of  $\vec{u} = \vec{0}$  on  $S$ .

The contributions to  $B_3$  from  $k = 3$  and  $k = 4$  follow identically from the procedure described previously. Fortunately,  $D_{ij}^{v3}$  and  $D_{ij}^{v4}$  have simple forms that lead to an easy determination of  $B_3^3$  and  $B_3^4$ . First consider  $k = 3$ ,

$$\begin{aligned}
B_3^3 &= \nabla \Psi^\top \cdot \mu^3 \bar{D}^{v3} \cdot \vec{n} \delta U \\
&= \kappa^{tr} \begin{bmatrix} \frac{\partial T}{\partial \rho_1} (\nabla \psi_{pe} \cdot \vec{n}) \\ \vdots \\ \frac{\partial T}{\partial \rho_N} (\nabla \psi_{pe} \cdot \vec{n}) \\ \frac{\partial T}{\partial \rho \vec{u}} (\nabla \psi_{pe} \cdot \vec{n}) \\ \frac{\partial T}{\partial \rho e} (\nabla \psi_{pe} \cdot \vec{n}) \\ \frac{\partial T}{\partial \rho e^{ve}} (\nabla \psi_{pe} \cdot \vec{n}) \end{bmatrix}^\top \begin{bmatrix} \delta\rho_1 \\ \vdots \\ \delta\rho_N \\ \delta(\rho\vec{u}) \\ \delta(\rho e) \\ \delta(\rho e^{ve}) \end{bmatrix} \\
&= \kappa^{tr} (\nabla \psi_{pe} \cdot \vec{n}) \delta T,
\end{aligned} \tag{3.55}$$

where  $\delta T$  has been substituted in favor of  $(\partial T / \partial U) \delta U$  to correspond to the boundary conditions applied to the temperature on  $S$ . The procedure for the vibrational-electronic thermal conduction

contribution to  $B_3$  is identical, and follows,

$$\begin{aligned}
 B_3^4 &= \nabla \Psi^\top \cdot \mu^4 \bar{D}^{v4} \cdot \vec{n} \delta U \\
 &= \kappa^{ve} \begin{bmatrix} \frac{\partial T^{ve}}{\partial \rho_1} [(\nabla \psi_{\rho e} + \nabla \psi_{\rho e^{ve}}) \cdot \vec{n}] \\ \vdots \\ \frac{\partial T^{ve}}{\partial \rho_N} [(\nabla \psi_{\rho e} + \nabla \psi_{\rho e^{ve}}) \cdot \vec{n}] \\ \frac{\partial T^{ve}}{\partial \rho \vec{u}} [(\nabla \psi_{\rho e} + \nabla \psi_{\rho e^{ve}}) \cdot \vec{n}] \\ \frac{\partial T^{ve}}{\partial \rho e} [(\nabla \psi_{\rho e} + \nabla \psi_{\rho e^{ve}}) \cdot \vec{n}] \\ \frac{\partial T^{ve}}{\partial \rho e^{ve}} [(\nabla \psi_{\rho e} + \nabla \psi_{\rho e^{ve}}) \cdot \vec{n}] \end{bmatrix}^\top \begin{bmatrix} \delta \rho_1 \\ \vdots \\ \delta \rho_N \\ \delta (\rho \vec{u}) \\ \delta (\rho e) \\ \delta (\rho e^{ve}) \end{bmatrix} \\
 &= \kappa^{ve} [(\nabla \psi_{\rho e} + \nabla \psi_{\rho e^{ve}}) \cdot \vec{n}] \delta T^{ve}.
 \end{aligned} \tag{3.56}$$

Again,  $\delta T^{ve}$  is preferred over  $(\partial T^{ve}/\partial U)\delta U$  to align with the thermal boundary conditions applied to  $T^{ve}$ .

Collecting the simplified results from each  $B_3^k$ ,

$$\begin{aligned}
 B_3 &= B_3^1 + B_3^2 + B_3^3 + B_3^4 \\
 &= \sum_s [(\nabla \psi_{\rho s} \cdot \vec{n}) + (\nabla \psi_{\rho e} \cdot \vec{n}) h_s^{int} + (\nabla \psi_{\rho e^{ve}} \cdot \vec{n}) e_s^{ve}] \left( \rho D_s \delta Y_s - Y_s \sum_k \rho D_k \delta Y_k \right) \\
 &\quad + \mu (\bar{\Sigma}^\phi \cdot \vec{n}) \delta \vec{u} + \kappa^{tr} (\nabla \psi_{\rho e} \cdot \vec{n}) \delta T + \kappa^{ve} [(\nabla \psi_{\rho e} + \nabla \psi_{\rho e^{ve}}) \cdot \vec{n}] \delta T^{ve}.
 \end{aligned} \tag{3.57}$$

### 3.5.4 Summary of the Adjoint Boundary Integrals

For convenience, the simplified adjoint boundary conditions are gathered here,

$$B_1 = \vartheta \delta \vec{u} \cdot \vec{n} + (\vec{\phi} \cdot \vec{n}) \delta p \tag{3.58a}$$

$$\begin{aligned}
 B_2^1 &= - \sum_s \psi_{\rho s} (\delta \vec{J}_s \cdot \vec{n}) - \psi_{\rho e} \sum_s (\delta \vec{J}_s \cdot \vec{n}) h_s^{int} - \psi_{\rho e^{ve}} \sum_s (\delta \vec{J}_s \cdot \vec{n}) e_s^{ve} \\
 &\quad - \psi_{\rho e} \sum_s (\vec{J}_s \cdot \vec{n}) [(C_{v,s}^{tr} + R_s) \delta T + C_{v,s}^{ve} \delta T^{ve}] - \psi_{\rho e^{ve}} \sum_s (\vec{J}_s \cdot \vec{n}) C_{v,s}^{ve} \delta T^{ve}
 \end{aligned} \tag{3.58b}$$

$$B_2^2 = \vec{\phi} \cdot \delta \bar{\sigma} \cdot \vec{n} + \psi_{\rho e} \bar{\sigma} \cdot \delta \vec{u} \cdot \vec{n} \tag{3.58c}$$

$$B_2^3 = \psi_{\rho e} \delta (\kappa^{tr} \nabla T) \cdot \vec{n} \tag{3.58d}$$

$$B_2^4 = (\psi_{\rho e} + \psi_{\rho e^{ve}}) \delta (\kappa^{ve} \nabla T^{ve}) \cdot \vec{n} \tag{3.58e}$$

$$B_3^1 = \sum_s [(\nabla \psi_{\rho s} \cdot \vec{n}) + (\nabla \psi_{\rho e} \cdot \vec{n}) h_s^{int} + (\nabla \psi_{\rho e^{ve}} \cdot \vec{n}) e_s^{ve}] \left( \rho D_s \delta Y_s - Y_s \sum_k \rho D_k \delta Y_k \right) \tag{3.58f}$$

$$B_3^2 = \mu (\bar{\Sigma}^\phi \cdot \vec{n}) \delta \vec{u} \tag{3.58g}$$

$$B_3^3 = \kappa^{tr} (\nabla \psi_{\rho e} \cdot \vec{n}) \delta T \tag{3.58h}$$

$$B_3^4 = \kappa^{ve} [(\nabla \psi_{\rho e} + \nabla \psi_{\rho e^{ve}}) \cdot \vec{n}] \delta T^{ve}. \tag{3.58i}$$

For the adjoint method, the appropriate values for  $\Psi$  must be selected on the boundary such that there are no remaining variational flow quantities in  $\delta\mathcal{J}$  from either  $\delta J$ , or from the adjoint boundary integrals themselves. A balance exists between the flow variational terms in the objective function and those from the adjoint boundary integrals, and, as a consequence, not all objective functions are guaranteed to have a set of well-defined adjoint boundary conditions [3, 59, 36]. In some cases, auxiliary boundary equations may be defined in the Lagrangian to generate the necessary terms for cancellation [5], leading to admissible adjoint boundary conditions for a larger class of problems. This is a limitation of the adjoint method when applied directly to the continuous PDE system. Nevertheless, a large number of design problems with relevant objective functions may be addressed using the continuous adjoint method, and great freedom is available for discretizing the continuous adjoint PDE system.

## 3.6 Linearized Boundary Conditions

It is possible to relate shape deformations on  $S$  to local changes in the flow state near the domain boundaries by using the flow boundary conditions. These linearized boundary conditions are essential for eliminating  $\delta U$  dependence on  $S$  by reducing the number of terms containing variational flow quantities from the adjoint boundary integrals. Using the linearized boundary conditions is a necessary component to establishing a set of well-defined adjoint boundary conditions and to arrive at a set of surface sensitivities that can be evaluated to provide gradient information for  $J$ .

Linearized boundary conditions are derived for Dirichlet- and Neumann-type boundaries, corresponding to flow-tangency, no-slip, adiabatic, isothermal, non-catalytic, and catalytic walls. The linearized boundary conditions are derived generally, using a dummy variable. By assigning the dummy variable to velocity, mass-fraction, or temperature, the appropriate linearized boundary conditions for the chemical, momentum, and thermal states are derived.

### 3.6.1 Dirichlet Boundary Conditions

A dummy variable,  $\xi$ , is defined, representing a physical quantity on  $S$ . For Dirichlet-type boundaries, the value of  $\xi$  is specified explicitly,

$$\xi = \xi^*, \quad \text{on } S. \quad (3.59)$$

Consider a perturbed value for the dummy variable,  $\xi'$ , induced by a deformation in  $S$ . The perturbed variable can be evaluated using a local linearization,

$$\xi' = \xi + \delta\xi + \partial_n \xi \delta S, \quad (3.60)$$

where the second term on the right side of the equation represents the change in  $\xi$  induced by the shape deformation, and the third term is the change in  $\xi$  solely from the geometry of the deformation.

Since both  $\xi'$  and  $\xi$  must satisfy the initial boundary condition,  $\xi^*$ ,

$$\delta\xi = -\partial_n \xi \delta S. \quad (3.61)$$

Therefore, no-slip, catalytic, and isothermal boundaries may relate variations in their respective primitive variables to changes in the surface definition,  $\delta S$ , using Eqn. (3.61). Explicitly, these primitive variables are,

$$\xi = \begin{cases} \vec{u} & \text{for no-slip boundaries.} \\ Y_s & \text{for catalytic boundaries.} \\ T^k & \text{where } k = \{\text{tr, ve}\} \text{ for isothermal boundaries.} \end{cases} \quad (3.62)$$

### 3.6.2 Neumann Boundary Conditions

For Neumann boundary conditions, a value of the surface normal derivative is prescribed on  $S$ ,

$$\vec{\xi} \cdot \vec{n} = \xi_n^*, \quad (3.63)$$

where  $\vec{\xi}$  is a dummy vector quantity. The Neumann condition is linearized by considering perturbed values of  $\vec{\xi}$  and the local normal vector,  $\vec{n}$ ,

$$\vec{\xi}' = \vec{\xi} + \delta\vec{\xi} + \partial_n \vec{\xi} \delta S \quad (3.64)$$

$$\vec{n}' = \vec{n} + \delta\vec{n}. \quad (3.65)$$

The linearized boundary condition is then derived by considering a projection of the perturbed dummy variable onto the perturbed surface normal vector,

$$\begin{aligned} \vec{\xi}' \cdot \vec{n}' &= (\vec{\xi} + \delta\vec{\xi} + \partial_n \vec{\xi} \delta S) \cdot (\vec{n} + \delta\vec{n}) \\ &= \vec{\xi} \cdot \vec{n} + \delta\vec{\xi} \cdot \vec{n} + \partial_n \vec{\xi} \cdot \vec{n} \delta S + \vec{\xi} \cdot \delta\vec{n}, \end{aligned} \quad (3.66)$$

where products of two or more  $\delta(\cdot)$  terms are neglected. By enforcing the boundary condition,  $\vec{\xi} \cdot \vec{n} = \vec{\xi}' \cdot \vec{n}' = \xi_n^*$ ,

$$\delta\vec{\xi} \cdot \vec{n} = -\partial_n \vec{\xi} \cdot \vec{n} \delta S + \vec{\xi} \cdot \nabla_S \delta S. \quad (3.67)$$

Using Eqn. (3.67), variational flow parameters may be related to shape deformations for flow-tangency, adiabatic, and non-catalytic boundaries for the following definitions of the dummy variable,

$$\vec{\xi} = \begin{cases} \vec{u} & \text{for flow-tangency boundaries.} \\ \vec{J}_s & \text{for non-catalytic boundaries.} \\ q^k & \text{where } k = \{\text{tr, ve}\} \text{ for adiabatic boundaries.} \end{cases} \quad (3.68)$$

### 3.7 Adjoint Boundary Condition Assignment

The assignment of a set of admissible boundary conditions is the final stage in the derivation of the adjoint problem. Doing so requires the definition of the objective function,  $J$ , its variation,  $\delta J$ , and the simplified forms of the adjoint boundary integrals, summarized in Eqn. (3.58). It is useful to return to the general expression for the Lagrangian variation,

$$\begin{aligned}
\delta \mathcal{J} = & \delta J - \int_{\Gamma} (B_1 - B_2 + B_3) ds \\
& - \int_{\Omega} \left[ -\nabla \Psi^T \cdot \left( \vec{A}^c - \vec{F}^{vk} \frac{\partial \mu^k}{\partial U} - \mu^k \vec{A}^{vk} \right) - \nabla \cdot \left( \nabla \Psi^T \cdot \mu^k \bar{D}^{vk} \right) - \Psi^T \frac{\partial Q}{\partial U} \right] \delta U d\Omega \\
= & \delta J - \int_{\Gamma} (\vartheta \delta \vec{u} \cdot \vec{n} + (\vec{\phi} \cdot \vec{n}) \delta p) ds \\
& + \int_{\Gamma} \left[ - \sum_s \psi_{\rho_s} (\delta \vec{J}_s \cdot \vec{n}) - \psi_{\rho e} \sum_s (\delta \vec{J}_s \cdot \vec{n}) h_s^{int} - \psi_{\rho e^{ve}} \sum_s (\delta \vec{J}_s \cdot \vec{n}) e_s^{ve} \right. \\
& \quad \left. - \psi_{\rho e} \sum_s (\vec{J}_s \cdot \vec{n}) [(C_{v,s}^{tr} + R_s) \delta T + C_{v,s}^{ve} \delta T^{ve}] - \psi_{\rho e^{ve}} \sum_s (\vec{J}_s \cdot \vec{n}) C_{v,s}^{ve} \delta T^{ve} \right] ds \\
& + \int_{\Gamma} (\vec{\phi} \cdot \delta \bar{\sigma} \cdot \vec{n} + \psi_{\rho e} \bar{\sigma} \cdot \delta \vec{u} \cdot \vec{n}) ds + \int_{\Gamma} (\psi_{\rho e} \delta (\kappa^{tr} \nabla T) \cdot \vec{n}) ds \\
& + \int_{\Gamma} ((\psi_{\rho e} + \psi_{\rho e^{ve}}) \delta (\kappa^{ve} \nabla T^{ve}) \cdot \vec{n}) ds \\
& - \int_{\Gamma} \left\{ \sum_s [(\nabla \psi_{\rho_s} \cdot \vec{n}) + (\nabla \psi_{\rho e} \cdot \vec{n}) h_s^{int} + (\nabla \psi_{\rho e^{ve}} \cdot \vec{n}) e_s^{ve}] \left( \rho D_s \delta Y_s - Y_s \sum_k \rho D_k \delta Y_k \right) \right\} ds \\
& - \int_{\Gamma} (\mu (\bar{\Sigma}^{\phi} \cdot \vec{n}) \delta \vec{u}) ds - \int_{\Gamma} (\kappa^{tr} (\nabla \psi_{\rho e} \cdot \vec{n}) \delta T) ds - \int_{\Gamma} (\kappa^{ve} [(\nabla \psi_{\rho e} + \nabla \psi_{\rho e^{ve}}) \cdot \vec{n}] \delta T^{ve}) ds \\
& - \int_{\Omega} \left[ -\nabla \Psi^T \cdot \left( \vec{A}^c - \vec{F}^{vk} \frac{\partial \mu^k}{\partial U} - \mu^k \vec{A}^{vk} \right) - \nabla \cdot \left( \nabla \Psi^T \cdot \mu^k \bar{D}^{vk} \right) - \Psi^T \frac{\partial Q}{\partial U} \right] \delta U d\Omega. \quad (3.69)
\end{aligned}$$

Eqn. (3.69) is the most general representation of the Lagrangian variation using the conclusions from this Chapter. Since the adjoint boundary conditions are unique for each objective function and flow state boundary condition pairing, Eqn. (3.69) is the common foundation for addressing each case individually. Admissible adjoint boundary conditions are prescribed by first applying the appropriate linearized boundary conditions, then by examining the remaining terms containing variational flow quantities.

An additional set of terms with  $\delta S$  dependence is present in the Lagrangian variation. These terms may originate from  $\delta J$  or from the application of the linearized boundary conditions, and represent the influence of locally-normal surface deformations of  $S$  to the value of  $\delta \mathcal{J}$ . These terms are denoted the ‘surface sensitivity’ and are the mechanism by which the objective function gradient,  $\partial \mathcal{J} / \partial \vec{\alpha}$ , is calculated. These terms may not have any  $\delta U$  dependency, but are typically functions of the flow and adjoint variables. The procedure for projecting the surface sensitivities onto the surface deformation for computing  $\partial \mathcal{J} / \partial \vec{\alpha}$  is described in Section 4.10.1.

### 3.7.1 Boundary Conditions for the Projected Force Objective Function

Recall the projected force objective function and its variation, defined by Eqns. (3.8) and (3.15),

$$J = \int_S \vec{d} \cdot (p\bar{I} - \bar{\sigma}) \cdot \vec{n} ds \quad \delta J = \int_S \vec{d} \cdot (\delta p\bar{I} - \delta\bar{\sigma}) \cdot \vec{n} ds.$$

Five cases are considered, corresponding to the different velocity, thermal, and chemical states enforceable on  $S$ . For each case, the definition of  $\delta J$  is inserted into Eqn. (3.69), and an assignment to the adjoint variables on  $S$  is made, such that all dependence on variational flow terms are eliminated. The terms of the surface sensitivity are then collected and simplified, where appropriate, to facilitate implementation into the solver architecture described in Chapter 4.

#### No-slip, Adiabatic, Non-catalytic Walls

For adiabatic, non-catalytic walls, Neumann boundary conditions are necessary for the thermal and chemical state near the wall. Before proceeding, the following linearized boundary conditions are applied to the general expression for the Lagrangian given by Eqn. (3.69),

$$\begin{aligned} \delta\vec{u} &= -\partial_n \vec{u} \delta S \\ \delta(\kappa \nabla T) \cdot \vec{n} &= -\partial_n (\kappa \nabla T) \cdot \vec{n} \delta S + (\kappa \nabla T) \cdot \nabla_S \delta S \\ \delta(\kappa^{ve} \nabla T^{ve}) \cdot \vec{n} &= -\partial_n (\kappa^{ve} \nabla T^{ve}) \cdot \vec{n} \delta S + (\kappa^{ve} \nabla T^{ve}) \cdot \nabla_S \delta S \\ \delta(\vec{J}_s) \cdot \vec{n} &= -(\partial_n \vec{J}_s) \cdot \vec{n} \delta S + \vec{J}_s \cdot \nabla_S \delta S. \end{aligned}$$

After applying the linearized boundary conditions, the Lagrangian takes the form,

$$\begin{aligned} \delta\mathcal{J} = & \int_S \vec{d} \cdot (\delta p\bar{I} - \delta\bar{\sigma}) \cdot \vec{n} ds - \int_{\Gamma} ((\vec{\phi} \cdot \vec{n}) \delta p) ds + \int_{\Gamma} (\vec{\phi} \cdot \delta\bar{\sigma} \cdot \vec{n}) ds \\ & - \int_{\Gamma} \left\{ \sum_s [(\nabla \psi_{\rho_s} \cdot \vec{n}) + (\nabla \psi_{\rho_e} \cdot \vec{n}) h_s^{int} + (\nabla \psi_{\rho e^{ve}} \cdot \vec{n}) e_s^{int}] \left( \rho D_s \delta Y_s - Y_s \sum_k \rho D_k \delta Y_k \right) \right\} ds \\ & - \int_{\Gamma} (\kappa^{tr} (\nabla \psi_{\rho_e} \cdot \vec{n}) \delta T) ds - \int_{\Gamma} (\kappa^{ve} [(\nabla \psi_{\rho_e} + \nabla \psi_{\rho e^{ve}}) \cdot \vec{n}] \delta T^{ve}) ds \\ & + \int_{\Gamma} \left\{ \frac{\partial \mathcal{J}}{\partial S} \right\} \delta S ds + \int_{\Omega} \left\{ \Psi^T \frac{\partial \mathcal{R}}{\partial U} \right\} \delta U d\Omega, \end{aligned} \quad (3.70)$$

where  $(\partial \mathcal{J} / \partial S)$  is a collection of the surface sensitivities, consisting of all terms multiplied by the surface perturbation,  $\delta S$ , and  $(\Psi^T \partial \mathcal{R} / \partial U)$  is a shorthand representation of the adjoint equations. Note, the Lagrangian of Eqn. (3.70) is shown after the application of the no slip, adiabatic, and non-catalytic boundary conditions. Therefore terms that explicitly contain  $\vec{u}$ ,  $(\vec{J} \cdot \vec{n})$ , and  $(\nabla T^k \cdot \vec{n})$  are zero.

An examination of the remaining terms in Eqn. (3.70) reveals the required prescription to the adjoint variables to cancel the dependence on variational flow quantities. If the following conditions

are applied to the adjoint system,

$$\nabla \psi_{\rho_s} \cdot \vec{n} = 0 \quad (3.71a)$$

$$\vec{\phi} = \vec{d} \quad (3.71b)$$

$$\nabla \psi_{\rho_e} \cdot \vec{n} = 0 \quad (3.71c)$$

$$\nabla \psi_{\rho_e^{ve}} \cdot \vec{n} = 0, \quad (3.71d)$$

the necessary cancellation occurs, and  $\delta\mathcal{J}$  may be determined by evaluating the surface sensitivities, from a single flow and a single adjoint solution, regardless of the surface deformation.

**Surface Sensitivity** The surface sensitivities for adiabatic, non-catalytic walls corresponding to the projected force objective function are the terms from the Lagrangian with  $\delta S$  dependency,

$$\begin{aligned} \frac{\partial \mathcal{J}}{\partial S} \delta S = & -\vartheta \delta \vec{u} \cdot \vec{n} - \sum_s \psi_{\rho_s} (\delta \vec{J}_s \cdot \vec{n}) - \psi_{\rho_e} \sum_s (\delta \vec{J}_s \cdot \vec{n}) h_s^{int} - \psi_{\rho_e^{ve}} \sum_s (\delta \vec{J}_s \cdot \vec{n}) e_s^{ve} \\ & + \psi_{\rho_e} \bar{\sigma} \cdot \delta \vec{u} \cdot \vec{n} + \psi_{\rho_e} \delta(\kappa^{tr} \nabla T) \cdot \vec{n} + ((\psi_{\rho_e} + \psi_{\rho_e^{ve}}) \delta(\kappa^{ve} \nabla T^{ve}) \cdot \vec{n}) - (\mu(\bar{\Sigma}^\phi \cdot \vec{n}) \delta \vec{u}). \end{aligned} \quad (3.72)$$

Applying the linearized boundary conditions and the simplified forms of  $\delta J_s$  and  $\delta(\kappa^k \nabla T^k)$  from Sections C.1 - C.3 in Appendix C,

$$\begin{aligned} \frac{\partial \mathcal{J}}{\partial S} = & \sum_s \nabla_S \psi_{\rho_s} \cdot \vec{J}_s + \sum_s \nabla_S (\psi_{\rho_e} h_s^{int}) \cdot \vec{J}_s + \sum_s \nabla_S (\psi_{\rho_e^{ve}} e_s^{ve}) \cdot \vec{J}_s \\ & - (\nabla_S \psi_{\rho_e}) \cdot (\kappa^{tr} \nabla T) - \psi_{\rho_e} \sum_s \vec{J} \cdot \nabla h_s^{int} - \nabla_S (\psi_{\rho_e} + \psi_{\rho_e^{ve}}) \cdot (\kappa^{ve} \nabla T^{ve}) \\ & - (\psi_{\rho_e^{ve}}) \sum_s \vec{J}_s \cdot \nabla e_s^{ve} + (\psi_{\rho_e^{ve}}) q^x + \mu(\bar{\Sigma}^\phi \cdot \vec{n}) \partial_n \vec{u} + \sum_s [\psi_{\rho_s} + \psi_{\rho_e^{ve}} e_s^{ve}] \dot{w}_s. \end{aligned} \quad (3.73)$$

Eqn. (3.73) can be further simplified by recognizing,

$$\begin{aligned} \psi_{\rho_e} \sum_s \vec{J}_s \cdot \nabla h_s^{int} &= \sum_s \nabla (\psi_{\rho_e} h_s^{int}) \cdot \vec{J}_s - \sum_s (\nabla \psi_{\rho_e} \cdot \vec{J}_s) h_s^{int} \\ &= \sum_s \nabla_S (\psi_{\rho_e} h_s^{int}) \cdot \vec{J}_s - \sum_s \nabla_S \psi_{\rho_e} \cdot \vec{J}_s h_s^{int}, \end{aligned} \quad (3.74)$$

since  $\partial_n \psi_{\rho_e} = 0$  and  $\partial_n h_s^{int}(T, T^{ve}) = (\partial h_s^{int}/\partial T) \partial_n T + (\partial h_s^{int}/\partial T^{ve}) \partial_n T^{ve} = 0$  from the direct, and adjoint boundary conditions. Similarly,

$$\psi_{\rho_e^{ve}} \sum_s \vec{J}_s \cdot \nabla e_s^{ve} \delta S = \sum_s \nabla_S (\psi_{\rho_e^{ve}} e_s^{ve}) \cdot \vec{J}_s \delta S - \sum_s \nabla_S \psi_{\rho_e^{ve}} \cdot \vec{J}_s e_s^{ve} \delta S. \quad (3.75)$$

Inserting Eqns. (3.74) and (3.75) into (3.73),

$$\begin{aligned} \frac{\partial \mathcal{J}}{\partial S} = & \sum_s [\nabla_S \psi_{\rho_s} + (\nabla_S \psi_{\rho_e}) h_s^{int} + (\nabla_S \psi_{\rho_e^{ve}}) e_s^{ve}] \cdot \vec{J}_s \\ & - \nabla_S \psi_{\rho_e} \cdot (\kappa^{tr} \nabla T) - \nabla_S (\psi_{\rho_e} + \psi_{\rho_e^{ve}}) \cdot (\kappa^{ve} \nabla T^{ve}) \\ & + \psi_{\rho_e^{ve}} q^x + \sum_s [\psi_{\rho_s} + \psi_{\rho_e^{ve}} e_s^{ve}] \dot{w}_s + \mu (\bar{\Sigma}^\phi \cdot \vec{n}) \partial_n \vec{u}. \end{aligned} \quad (3.76)$$

### Isothermal, Non-catalytic Walls

For isothermal, non-catalytic walls, a Dirichlet condition is enforced for the temperatures, while a Neumann conditions applied to the species mass fraction gradients at the wall. The following linearized boundary conditions are applied to the general expression for  $\delta \mathcal{J}$ , given by Eqn. (3.69),

$$\begin{aligned} \delta \vec{u} &= -\partial_n \vec{u} \delta S \\ \delta T &= -\partial_n T \delta S \\ \delta T^{ve} &= -\partial_n T^{ve} \delta S \\ \delta (\vec{J}_s) \cdot \vec{n} &= -(\partial_n \vec{J}_s) \cdot \vec{n} \delta S + \vec{J}_s \cdot \nabla_S \delta S. \end{aligned}$$

After applying the linearized boundary conditions, the Lagrangian variation takes the form,

$$\begin{aligned} \delta \mathcal{J} = & \int_S \vec{d} \cdot (\delta p \bar{I} - \delta \bar{\sigma}) \cdot \vec{n} ds - \int_\Gamma ((\vec{\phi} \cdot \vec{n}) \delta p) ds + \int_\Gamma (\vec{\phi} \cdot \delta \bar{\sigma} \cdot \vec{n}) ds \\ & + \int_\Gamma (\psi_{\rho_e} \delta (\kappa^{tr} \nabla T) \cdot \vec{n}) ds + \int_\Gamma ((\psi_{\rho_e} + \psi_{\rho_e^{ve}}) \delta (\kappa^{ve} \nabla T^{ve}) \cdot \vec{n}) ds \\ & - \int_\Gamma \left\{ \sum_s [(\nabla \psi_{\rho_s} \cdot \vec{n}) + (\nabla \psi_{\rho_e} \cdot \vec{n}) h_s^{int} + (\nabla \psi_{\rho_e^{ve}} \cdot \vec{n}) e_s^{ve}] \left( \rho D_s \delta Y_s - Y_s \sum_k \rho D_k \delta Y_k \right) \right\} ds \\ & + \int_\Gamma \left\{ \frac{\partial \mathcal{J}}{\partial S} \right\} \delta S ds + \int_\Omega \left\{ \Psi^\tau \frac{\partial \mathcal{R}}{\partial U} \right\} \delta U d\Omega. \end{aligned} \quad (3.77)$$

Note, the Lagrangian of Eqn.(3.77) is shown after the application of the no-slip, isothermal, and non-catalytic boundary conditions. Therefore, terms that explicitly contain  $\vec{u}$ ,  $\nabla_S T^k$ , and  $\vec{J} \cdot \vec{n}$  are zero.

An examination of the remaining terms in Eqn. (3.77) reveals the required prescription to the adjoint variables to cancel the dependence on variational flow quantities. If the following conditions are applied to the adjoint system,

$$\nabla \psi_{\rho_s} \cdot \vec{n} = -(\nabla \psi_{\rho_e} \cdot \vec{n}) h_s^{int} - (\nabla \psi_{\rho_e^{ve}} \cdot \vec{n}) e_s^{ve} \quad (3.78a)$$

$$\vec{\phi} = \vec{d} \quad (3.78b)$$

$$\psi_{\rho_e} = 0 \quad (3.78c)$$

$$\psi_{\rho_e^{ve}} = 0, \quad (3.78d)$$

the necessary cancellation occurs, and the variation of the Lagrangian,  $\delta\mathcal{J}$ , may be determined by evaluating the surface sensitivities from a single flow and single adjoint solution, regardless of the surface deformation.

**Surface Sensitivity** The surface sensitivities for isothermal, non-catalytic walls corresponding to the projected force objective function are the terms from the Lagrangian with  $\delta S$  dependency,

$$\begin{aligned} \frac{\partial\mathcal{J}}{\partial S}\delta S = & -\vartheta\delta\vec{u}\cdot\vec{n} - \sum_s \psi_{\rho_s} \left( \delta\vec{J}_s \cdot \vec{n} \right) - \psi_{\rho e} \sum_s \left( \delta\vec{J}_s \cdot \vec{n} \right) h_s^{int} - \psi_{\rho e^{ve}} \sum_s \left( \delta\vec{J}_s \cdot \vec{n} \right) e_s^{ve} \\ & + \psi_{\rho e}\bar{\sigma}\cdot\delta\vec{u}\cdot\vec{n} - \mu(\bar{\Sigma}^\phi\cdot\vec{n})\delta\vec{u} - \kappa^{tr}(\nabla\psi_{\rho e}\cdot\vec{n})\delta T - \kappa^{ve}[(\nabla\psi_{\rho e} + \nabla\psi_{\rho e^{ve}})\cdot\vec{n}]\delta T^{ve} \end{aligned} \quad (3.79)$$

Applying the linearized boundary conditions and the simplified form of  $\delta\vec{J}_s\cdot\vec{n}$  from Eqn. (C.11),

$$\begin{aligned} \frac{\partial\mathcal{J}}{\partial S} = & \sum_s \nabla_S \psi_{\rho_s} \cdot \vec{J}_s + \sum_s \nabla_S (\psi_{\rho e} h_s^{int}) \cdot \vec{J}_s + \sum_s \nabla_S (\psi_{\rho e^{ve}} e_s^{ve}) \cdot \vec{J}_s + \mu(\bar{\Sigma}^\phi\cdot\vec{n})\partial_n\vec{u} \\ & + (\nabla\psi_{\rho e}\cdot\vec{n})\kappa^{tr}\partial_n T + [(\nabla\psi_{\rho e} + \nabla\psi_{\rho e^{ve}})\cdot\vec{n}]\kappa^{ve}\partial_n T^{ve} + \sum_s \psi_{\rho_s} \dot{w}_s. \end{aligned} \quad (3.80)$$

More terms can be eliminated by distributing the tangential gradient operator in the second and third terms of Eqn.(3.80) and recognizing

$$\nabla_S h_s^{int} = (\partial h_s^{int}/\partial T)\nabla_S T + (\partial h_s^{int}/\partial T^{ve})\nabla_S T^{ve} = 0, \quad (3.81)$$

$$\nabla_S e_s^{ve} = (\partial e_s^{ve}/\partial T^{ve})\nabla_S T^{ve} = 0, \quad (3.82)$$

$$\nabla_S \psi_{\rho e} = 0, \quad (3.83)$$

$$\nabla_S \psi_{\rho e^{ve}} = 0, \quad (3.84)$$

due to the isothermal and adjoint boundary conditions enforced on  $S$ . Consequently,

$$\begin{aligned} \frac{\partial\mathcal{J}}{\partial S} = & \sum_s \nabla_S \psi_{\rho_s} \cdot \vec{J}_s \delta S + \mu(\bar{\Sigma}^\phi\cdot\vec{n})\partial_n\vec{u}\delta S + (\nabla\psi_{\rho e}\cdot\vec{n})\kappa^{tr}\partial_n T\delta S \\ & + [(\nabla\psi_{\rho e} + \nabla\psi_{\rho e^{ve}})\cdot\vec{n}]\kappa^{ve}\partial_n T^{ve}\delta S + \sum_s \psi_{\rho_s} \dot{w}_s. \end{aligned} \quad (3.85)$$

### Adiabatic, Catalytic Walls

For adiabatic, catalytic walls, Neumann conditions are enforced on the temperatures, while Dirichlet conditions are applied to the species mass fractions at the wall. Before proceeding, the following linearized boundary conditions are applied to the general expression for the Lagrangian variation

given by Eqn. (3.69),

$$\begin{aligned}\delta \vec{u} &= -\partial_n \vec{u} \delta S \\ \delta(\kappa \nabla T) \cdot \vec{n} &= -\partial_n (\kappa \nabla T) \cdot \vec{n} \delta S + (\kappa \nabla T) \cdot \nabla_S \delta S \\ \delta(\kappa^{ve} \nabla T^{ve}) \cdot \vec{n} &= -\partial_n (\kappa^{ve} \nabla T^{ve}) \cdot \vec{n} \delta S + (\kappa^{ve} \nabla T^{ve}) \cdot \nabla_S \delta S \\ \delta Y_s &= -\partial_n Y_s \delta S.\end{aligned}$$

After applying the linearized boundary conditions,  $\delta \mathcal{J}$  takes the form,

$$\begin{aligned}\delta \mathcal{J} &= \int_S \vec{d} \cdot (\delta p \bar{I} - \delta \bar{\sigma}) \cdot \vec{n} - \int_{\Gamma} \left( (\vec{\phi} \cdot \vec{n}) \delta p \right) ds \\ &\quad + \int_{\Gamma} \left[ -\sum_s \psi_{\rho_s} (\delta \vec{J}_s \cdot \vec{n}) - \psi_{\rho e} \sum_s (\delta \vec{J}_s \cdot \vec{n}) h_s^{int} - \psi_{\rho e^{ve}} \sum_s (\delta \vec{J}_s \cdot \vec{n}) e_s^{ve} \right. \\ &\quad \left. - \psi_{\rho e} \sum_s (\vec{J}_s \cdot \vec{n}) [(C_{v,s}^{tr} + R_s) \delta T + C_{v,s}^{ve} \delta T^{ve}] - \psi_{\rho e^{ve}} \sum_s (\vec{J}_s \cdot \vec{n}) C_{v,s}^{ve} \delta T^{ve} \right] ds \\ &\quad + \int_{\Gamma} (\vec{\phi} \cdot \delta \bar{\sigma} \cdot \vec{n}) ds - \int_{\Gamma} (\kappa^{tr} (\nabla \psi_{\rho e} \cdot \vec{n}) \delta T) ds - \int_{\Gamma} (\kappa^{ve} [(\nabla \psi_{\rho e} + \nabla \psi_{\rho e^{ve}}) \cdot \vec{n}] \delta T^{ve}) ds \\ &\quad + \int_{\Gamma} \left\{ \frac{\partial \mathcal{J}}{\partial S} \right\} \delta S ds + \int_{\Omega} \left\{ \Psi^T \frac{\partial \mathcal{R}}{\partial U} \right\} \delta U d\Omega.\end{aligned}\tag{3.86}$$

Note, the Lagrangian of Eqn. (3.86) is shown after the application of the no-slip, adiabatic, catalytic boundary conditions, therefore any terms containing  $\vec{u}$ ,  $\nabla T^k \cdot \vec{n}$ , or  $\nabla_S Y_s$  are zero.

An examination of the remaining terms in Eqn. (3.86) reveals the required prescription to the adjoint variables to cancel the dependence on variational flow quantities. If the following conditions are applied to the adjoint system,

$$\psi_{\rho_s} = -\psi_{\rho e} h_s^{int} - \psi_{\rho e^{ve}} e_s^{ve}\tag{3.87a}$$

$$\vec{\phi} = \vec{d}\tag{3.87b}$$

$$\nabla \psi_{\rho e} \cdot \vec{n} = -\frac{\psi_{\rho e}}{\kappa^{tr}} \sum_s (\vec{J}_s \cdot \vec{n}) (C_{v,s}^{tr} + R_s)\tag{3.87c}$$

$$\begin{aligned}\nabla \psi_{\rho e^{ve}} \cdot \vec{n} &= -\frac{\psi_{\rho e} + \psi_{\rho e^{ve}}}{\kappa^{ve}} \sum_s (\vec{J}_s \cdot \vec{n}) C_{v,s}^{ve} \\ &\quad + \frac{\psi_{\rho e}}{\kappa^{tr}} \sum_s (\vec{J}_s \cdot \vec{n}) (C_{v,s}^{tr} + R_s),\end{aligned}\tag{3.87d}$$

the necessary cancellation occurs, and the variation of the Lagrangian,  $\delta \mathcal{J}$ , may be determined by evaluating the surface sensitivities from a single flow and a single adjoint solution, regardless of the surface deformation.

**Surface Sensitivity** The surface sensitivities for adiabatic, catalytic walls, corresponding to the projected force objective function, are the terms from the Lagrangian with  $\delta S$  dependency,

$$\begin{aligned} \frac{\partial \mathcal{J}}{\partial S} \delta S = & -\vartheta \delta \vec{u} \cdot \vec{n} + \psi_{\rho e} \bar{\sigma} \cdot \delta \vec{u} \cdot \vec{n} + \psi_{\rho e} \delta(\kappa^{tr} \nabla T) \cdot \vec{n} + (\psi_{\rho e} + \psi_{\rho e^{ve}}) \delta(\kappa^{ve} \nabla T^{ve}) \cdot \vec{n} \\ & - \sum_s [(\nabla \psi_{\rho s} \cdot \vec{n}) + (\nabla \psi_{\rho e} \cdot \vec{n}) h_s^{int} + (\nabla \psi_{\rho e^{ve}} \cdot \vec{n}) e_s^{ve}] \left( \rho D_s \delta Y_s - Y_s \sum_k \rho D_k \delta Y_k \right) \\ & - \mu (\bar{\Sigma}^\phi \cdot \vec{n}) \delta \vec{u}. \end{aligned} \quad (3.88)$$

Applying the adjoint boundary conditions, linearized boundary conditions, and the simplified forms of  $\delta(\kappa^k \nabla T^k)$  from Eqns. (C.22) and (C.31),

$$\begin{aligned} \frac{\partial \mathcal{J}}{\partial S} = & \vartheta \partial_n \vec{u} \cdot \vec{n} - \sum_s [(\nabla \psi_{\rho s} \cdot \vec{n}) + (\nabla \psi_{\rho e} \cdot \vec{n}) h_s^{int} + (\nabla \psi_{\rho e^{ve}} \cdot \vec{n}) e_s^{ve}] (\vec{J}_s \cdot \vec{n}) \\ & + \mu (\bar{\Sigma}^\phi \cdot \vec{n}) \partial_n \vec{u} - \nabla_S \psi_{\rho e} \cdot (\kappa^{tr} \nabla T) - \psi_{\rho e} \sum_s h_s^{int} \dot{w}_s - \psi_{\rho e} \sum_s \vec{J}_s \cdot \nabla h_s^{int} \\ & - \nabla_S (\psi_{\rho e} + \psi_{\rho e^{ve}}) \cdot (\kappa^{ve} \nabla T^{ve}) - \psi_{\rho e^{ve}} \sum_s \vec{J}_s \cdot \nabla e_s^{ve} + \psi_{\rho e^{ve}} \left( \sum_s \dot{w}_s e_s^{ve} + q^x \right). \end{aligned} \quad (3.89)$$

### Isothermal, Catalytic Walls

For isothermal, catalytic walls, Dirichlet conditions are applied to the temperatures and the mass fractions on  $S$ . Before proceeding, the following linearized boundary conditions are applied to the general expression for the Lagrangian variation given by Eqn. (3.69),

$$\begin{aligned} \delta \vec{u} &= -\partial_n \vec{u} \delta S \\ \delta T &= -\partial_n T \delta S \\ \delta T^{ve} &= -\partial_n T^{ve} \delta S \\ \delta Y_s &= -\partial_n Y_s \delta S. \end{aligned}$$

After applying the linearized boundary conditions,  $\delta \mathcal{J}$  takes the form,

$$\begin{aligned} \delta \mathcal{J} = & \int_S \vec{d} \cdot (\delta p \bar{I} - \delta \bar{\sigma}) \cdot \vec{n} ds - \int_\Gamma ((\vec{\phi} \cdot \vec{n}) \delta p) ds \\ & - \int_\Gamma \sum_s [\psi_{\rho s} + \psi_{\rho e} h_s^{int} + \psi_{\rho e^{ve}} e_s^{ve}] (\delta \vec{J}_s \cdot \vec{n}) ds + \int_\Gamma (\vec{\phi} \cdot \delta \bar{\sigma} \cdot \vec{n}) ds \\ & + \int_\Gamma (\psi_{\rho e} \delta(\kappa^{tr} \nabla T) \cdot \vec{n}) ds + \int_\Gamma ((\psi_{\rho e} + \psi_{\rho e^{ve}}) \delta(\kappa^{ve} \nabla T^{ve}) \cdot \vec{n}) ds \\ & + \int_\Gamma \left\{ \frac{\partial \mathcal{J}}{\partial S} \right\} \delta S ds + \int_\Omega \left\{ \Psi^\top \frac{\partial \mathcal{J}}{\partial U} \right\} \delta U d\Omega. \end{aligned} \quad (3.90)$$

Note, the Lagrangian of Eqn. (3.90) is shown after the application of the no-slip, isothermal, and catalytic boundary conditions. Therefore, any terms that include  $\vec{u}$ ,  $\nabla_S T^k$ , or  $\nabla_S Y_s$  are omitted.

An examination of the remaining terms in Eqn. (3.90) reveals the required prescription of the adjoint variables to cancel the dependence on variational flow quantities. If the following conditions are applied to the adjoint system,

$$\psi_{\rho_s} = 0 \quad (3.91a)$$

$$\vec{\phi} = \vec{d} \quad (3.91b)$$

$$\psi_{\rho_e} = 0 \quad (3.91c)$$

$$\psi_{\rho_e^{ve}} = 0, \quad (3.91d)$$

the necessary cancellation occurs, and the variation of the Lagrangian,  $\delta\mathcal{J}$ , may be determined by evaluating the surface sensitivities from a single flow and a single adjoint solution, regardless of the deformation.

**Surface Sensitivity** The surface sensitivities for isothermal, catalytic walls, corresponding to the projected force objective function are the terms from the Lagrangian with  $\delta S$  dependency,

$$\begin{aligned} \frac{\partial \mathcal{J}}{\partial S} \delta S = & -\vartheta \delta \vec{u} \cdot \vec{n} - \psi_{\rho_e} \sum_s (\vec{J}_s \cdot \vec{n}) [(C_{v,s}^{tr} + R_s) \delta T + C_{v,s}^{ve} \delta T^{ve}] - \psi_{\rho_e^{ve}} \sum_s (\vec{J}_s \cdot \vec{n}) C_{v,s}^{ve} \delta T^{ve} \\ & - \sum_s [(\nabla \psi_{\rho_s} \cdot \vec{n}) + (\nabla \psi_{\rho_e} \cdot \vec{n}) h_s^{int} + (\nabla \psi_{\rho_e^{ve}} \cdot \vec{n}) e_s^{ve}] \left( \rho D_s \delta Y_s - Y_s \sum_k \rho D_k \delta Y_k \right) \\ & + \psi_{\rho_e} \bar{\sigma} \cdot \delta \vec{u} \cdot \vec{n} - \mu (\bar{\Sigma}^\phi \cdot \vec{n}) \delta \vec{u} - \kappa^{tr} (\nabla \psi_{\rho_e} \cdot \vec{n}) \delta T - \kappa^{ve} [(\nabla \psi_{\rho_e} + \nabla \psi_{\rho_e^{ve}}) \cdot \vec{n}] \delta T^{ve}. \end{aligned} \quad (3.92)$$

Applying the linearized boundary conditions and the adjoint boundary conditions,

$$\begin{aligned} \frac{\partial \mathcal{J}}{\partial S} = & - \sum_s [(\nabla \psi_{\rho_s} \cdot \vec{n}) + (\nabla \psi_{\rho_e} \cdot \vec{n}) h_s^{int} + (\nabla \psi_{\rho_e^{ve}} \cdot \vec{n}) e_s^{ve}] (\vec{J}_s \cdot \vec{n}) \\ & + \mu (\bar{\Sigma}^\phi \cdot \vec{n}) \partial_n \vec{u} + (\nabla \psi_{\rho_e} \cdot \vec{n}) \kappa^{tr} \nabla T \cdot \vec{n} + [(\nabla \psi_{\rho_e} + \nabla \psi_{\rho_e^{ve}}) \cdot \vec{n}] \kappa^{tr} \nabla T^{ve} \cdot \vec{n}. \end{aligned} \quad (3.93)$$

### Inviscid Flow

For inviscid problems, the effects of viscosity are neglected in the objective function, the governing equations, and the adjoint equations. The appropriate force-based functional under these conditions is given by Eqn. (3.16), with the corresponding variation given by, Eqn. (3.17) of Section 3.3.1,

$$\begin{aligned} J &= \int_S \vec{d} \cdot (p \bar{\bar{I}}) \cdot \vec{n} ds \\ \delta J &= \int_S \vec{d} \cdot (\delta p \bar{\bar{I}}) \cdot \vec{n} ds + \int_S (\vec{d} \cdot \nabla p) \delta S ds. \end{aligned}$$

The Lagrangian variation, neglecting adjoint boundary integrals  $B_2$  and  $B_3$ , simplifies to

$$\begin{aligned}\delta\mathcal{J} = & \int_S \vec{d} \cdot (\delta p \bar{I}) \cdot \vec{n} ds + \int_S (\vec{d} \cdot \nabla p) \delta S ds - \int_{\Gamma} (\vartheta \delta \vec{u} \cdot \vec{n} + (\vec{\phi} \cdot \vec{n}) \delta p) ds \\ & - \int_{\Omega} \left[ \nabla \Psi^T \cdot (\vec{A}^c) + \Psi^T \frac{\partial Q}{\partial U} \right] \delta U d\Omega,\end{aligned}\quad (3.94)$$

which is subject to the linearized boundary condition,

$$\delta \vec{u} \cdot \vec{n} = -\partial_n \vec{u} \cdot \vec{n} \delta S + \vec{u} \cdot \nabla_S \delta S. \quad (3.95)$$

A further examination of Eqn. (3.94) reveals the prescription on the adjoint variables to eliminate variational flow dependency. If the following condition is applied,

$$\vec{\phi} \cdot \vec{n} = \vec{d} \cdot \vec{n}, \quad (3.96)$$

the necessary cancellation occurs, and the variation of the Lagrangian,  $\delta\mathcal{J}$  may be evaluated by resolving the surface sensitivity ( $\partial\mathcal{J}/\partial S$ ) with a single flow and a single adjoint solution, independent of the surface parameterization.

**Surface Sensitivity** The surface sensitivity for the inviscid problem consists of all terms in Eqn. (3.94) with dependence on the surface deformation,  $\delta S$ ,

$$\frac{\partial \mathcal{J}}{\partial S} \delta S = (\vec{d} \cdot \nabla p) \delta S + \vartheta \partial_n \vec{u} \cdot \vec{n} \delta S - \vartheta \vec{u} \cdot \nabla_S \delta S, \quad (3.97)$$

where the linearized boundary condition of Eqn. (3.95) has been applied. The final term is manipulated using integration by parts,

$$\vartheta \vec{u} \cdot \nabla_S \delta S = \nabla_S \cdot (\vartheta \vec{u} \delta S) - \nabla_S \cdot (\vartheta \vec{u}) \delta S. \quad (3.98)$$

Note, the the first term of Eqn. (3.98) is zero when integrated over the surface and is neglected from the subsequent analysis. Inserting Eqn. (3.98) into Eqn. (3.97),

$$\frac{\partial \mathcal{J}}{\partial S} \delta S = (\vec{d} \cdot \nabla p) \delta S + \vartheta \partial_n \vec{u} \cdot \vec{n} \delta S + \nabla_S \cdot (\vartheta \vec{u}) \delta S \quad (3.99)$$

The final term in Eqn. (3.98) is further manipulated using the differential geometry identity from Eqn. (3.6d),  $\nabla \cdot \vec{\xi} = \partial_n \vec{\xi} \cdot \vec{n} + \nabla_S \cdot \vec{\xi} - 2H_m \vec{\xi} \cdot \vec{n}$ , and noting that  $\vec{u} \cdot \vec{n} = 0$  on  $S$ , in accordance with the flow-tangency boundary condition,

$$\begin{aligned}\frac{\partial \mathcal{J}}{\partial S} = & (\vec{d} \cdot \nabla p) + \vartheta \partial_n \vec{u} \cdot \vec{n} + (\nabla \cdot (\vartheta \vec{u}) - \partial_n (\vartheta \vec{u} \cdot \vec{n})) \\ = & (\vec{d} \cdot \nabla p) + \nabla \cdot (\vartheta \vec{u}).\end{aligned}\quad (3.100)$$

### 3.7.2 Boundary Conditions for the Thermal Objective Function

Recall the thermal objective function and its variation, defined by Eqns. (3.18) and (3.25),

$$\begin{aligned} J &= \left( \int_S [-(q^{\vec{t}r} + q^{\vec{v}e}) \cdot \vec{n}]^p ds \right)^{1/p} \\ \delta J &= -\beta \int_S p(-q_n)^{p-1} (\delta q^{\vec{t}r} + \delta q^{\vec{v}e}) \cdot \vec{n} ds - \beta \int_S \nabla_S [p(-q_n)^{p-1}] \cdot \vec{q} \delta S ds \\ &\quad + \beta \int_S p(-q_n)^{p-1} \nabla \cdot (-\vec{q}) \delta S ds + \beta \int_S 2(p-1) H_m(-q_n)^p \delta S ds, \end{aligned}$$

where  $\beta$ ,  $\vec{q}$ , and  $q_n$  are defined in Eqn. (3.19). To derive the adjoint boundary conditions corresponding to the thermal objective function, the definition of  $\delta J$  is inserted into the Lagrangian variation of Eqn. (3.69). Boundary conditions for catalytic and non-catalytic, no-slip, isothermal walls are presented.

#### Isothermal, Non-catalytic Walls

Following the procedure used for the projected-force objective function, the adjoint boundary conditions for the thermal objective function under isothermal, non-catalytic wall boundary conditions are determined by first applying the following linearized boundary conditions to Eqn. (3.69),

$$\begin{aligned} \delta \vec{u} &= -\partial_n \vec{u} \delta S \\ \delta T &= -\partial_n T \delta S \\ \delta T^{ve} &= -\partial_n T^{ve} \delta S \\ \delta(\vec{J}_s) \cdot \vec{n} &= -(\partial_n \vec{J}_s) \cdot \vec{n} \delta S + \vec{J}_s \cdot \nabla_S \delta S. \end{aligned}$$

After applying the linearized boundary conditions and inserting the definition of the thermal objective function variation,  $\delta \mathcal{J}$  takes the form,

$$\begin{aligned} \delta \mathcal{J} &= \beta \int_S p(-q_n)^{p-1} (-\delta q^{\vec{t}r} - \delta q^{\vec{v}e}) \cdot \vec{n} ds - \int_{\Gamma} ((\vec{\phi} \cdot \vec{n}) \delta p) ds + \int_{\Gamma} (\vec{\phi} \cdot \delta \bar{\sigma} \cdot \vec{n}) ds \\ &\quad + \int_{\Gamma} (\psi_{pe} \delta(-q^{\vec{t}r}) \cdot \vec{n}) ds + \int_{\Gamma} ((\psi_{pe} + \psi_{pe^{ve}}) \delta(-q^{\vec{v}e}) \cdot \vec{n}) ds \\ &\quad - \int_{\Gamma} \left\{ \sum_s [(\nabla \psi_{\rho_s} \cdot \vec{n}) + (\nabla \psi_{pe} \cdot \vec{n}) h_s^{int} + (\nabla \psi_{pe^{ve}} \cdot \vec{n}) e_s^{ve}] \left( \rho D_s \delta Y_s - Y_s \sum_k \rho D_k \delta Y_k \right) \right\} ds \\ &\quad + \int_{\Gamma} \left\{ \frac{\partial \mathcal{J}}{\partial S} \right\} \delta S ds + \int_{\Omega} \left\{ \Psi^T \frac{\partial \mathcal{R}}{\partial U} \right\} \delta U ds. \end{aligned} \tag{3.101}$$

An examination of the remaining terms in Eqn. (3.101) reveals the necessary prescription of the adjoint variables to cancel variational flow dependence. If the following conditions are applied on  $S$ ,

$$\nabla \psi_{\rho_s} \cdot \vec{n} = -(\nabla \psi_{\rho e} \cdot \vec{n}) h_s^{int} - (\nabla \psi_{\rho e^{ve}} \cdot \vec{n}) e_s^{ve} \quad (3.102a)$$

$$\vec{\phi} = \vec{0} \quad (3.102b)$$

$$\psi_{\rho e} = -\beta p(-q_n)^{p-1} \quad (3.102c)$$

$$\psi_{\rho e^{ve}} = 0, \quad (3.102d)$$

the necessary cancellation occurs, and the variation of the Lagrangian may be determined by evaluating the surface sensitivities from a single flow and a single adjoint solution, regardless of the surface deformation.

**Surface Sensitivity** The adjoint surface sensitivities for isothermal, non-catalytic boundaries, corresponding to the thermal objective functions, are the terms from the Lagrangian variation with  $\delta S$  dependency,

$$\begin{aligned} \frac{\partial \mathcal{J}}{\partial S} \delta S = & -\beta \nabla_S [p(-q_n)^{p-1}] \cdot \vec{q} \delta S + \beta p(-q_n)^{p-1} \nabla \cdot (-\vec{q}) \delta S + \beta 2(p-1) H_m(-q_n)^p \delta S - \vartheta \delta \vec{u} \cdot \vec{n} \\ & + \psi_{\rho e} \bar{\sigma} \cdot \delta \vec{u} \cdot \vec{n} - \sum_s \psi_{\rho_s} (\delta \vec{J}_s \cdot \vec{n}) - \psi_{\rho e} \sum_s (\delta \vec{J}_s \cdot \vec{n}) h_s^{int} - \psi_{\rho e^{ve}} \sum_s (\delta \vec{J}_s \cdot \vec{n}) e_s^{ve} \\ & - \mu (\bar{\Sigma}^\phi \cdot \vec{n}) \delta \vec{u} - (\kappa^{tr} (\nabla \psi_{\rho e} \cdot \vec{n}) \delta T) - (\kappa^{ve} [(\nabla \psi_{\rho e} + \nabla \psi_{\rho e^{ve}}) \cdot \vec{n}] \delta T^{ve}). \end{aligned} \quad (3.103)$$

Applying the adjoint boundary conditions, the linearized boundary conditions, and the simplified forms of  $\delta \vec{J}_s$ ,  $\nabla \cdot (-q \vec{t}^r)$ , and  $\nabla \cdot (-q \vec{t}^r)$  from Eqns. (C.11), (C.20), and (C.30) respectively,

$$\begin{aligned} \frac{\partial \mathcal{J}}{\partial S} = & -\beta \nabla_S [p(-q_n)^{p-1}] \cdot \vec{q} + \beta p(-q_n)^{p-1} \left[ \sum_s h_s^{int} \dot{w}_s + \sum_s \vec{J}_s \cdot \nabla h_s^{int} \right] \\ & + \beta 2(p-1) H_m(-q_n)^p + \sum_s \nabla_S \psi_{\rho_s} \cdot \vec{J}_s + \sum_s (\nabla_S \psi_{\rho e}) h_s^{int} \cdot \vec{J}_s \\ & + \sum_s \psi_{\rho e} (\nabla_S h_s^{int}) \cdot \vec{J}_s + \sum_s (\nabla_S \psi_{\rho e^{ve}}) e_s^{ve} \cdot \vec{J}_s + \sum_s \psi_{\rho e^{ve}} (\nabla_S e_s^{ve}) \cdot \vec{J}_s \\ & + \sum_s (\psi_{\rho_s} + \psi_{\rho e} h_s^{int} + \psi_{\rho e^{ve}} e_s^{ve}) \dot{w}_s + \mu (\bar{\Sigma}^\phi \cdot \vec{n}) \partial_n \vec{u} \\ & + (\nabla \psi_{\rho e} \cdot \vec{n}) \kappa^{tr} \partial_n T + [(\nabla \psi_{\rho e} + \nabla \psi_{\rho e^{ve}}) \cdot \vec{n}] \kappa^{ve} \partial_n T^{ve}. \end{aligned} \quad (3.104)$$

By applying the isothermal and adjoint boundary conditions, surface gradient terms can be eliminated such that,

$$\begin{aligned} \frac{\partial \mathcal{J}}{\partial S} = & -\beta \nabla_S [p(-q_n)^{p-1}] \cdot \vec{q} + \beta p(-q_n)^{p-1} \left[ \sum_s \vec{J}_s \cdot \nabla h_s^{int} \right] + \beta 2(p-1) H_m(-q_n)^p \\ & + \sum_s \nabla_S \psi_{\rho_s} \cdot \vec{J}_s + \sum_s (\nabla_S \psi_{\rho_e}) h_s^{int} \cdot \vec{J}_s + \sum_s \psi_{\rho_s} \dot{w}_s + \mu(\bar{\Sigma}^\phi \cdot \vec{n}) \partial_n \vec{u} \\ & + (\nabla \psi_{\rho_e} \cdot \vec{n}) \kappa^{tr} \partial_n T + [(\nabla \psi_{\rho_e} + \nabla \psi_{\rho_e^{ve}}) \cdot \vec{n}] \kappa^{ve} \partial_n T^{ve}. \end{aligned} \quad (3.105)$$

For the special case,  $p = 1$ , the surface sensitivity may be simplified further,

$$\begin{aligned} \frac{\partial \mathcal{J}}{\partial S} \Big|_{p=1} = & \sum_s \vec{J}_s \cdot \nabla h_s^{int} + \sum_s \nabla_S \psi_{\rho_s} \cdot \vec{J}_s + \sum_s \psi_{\rho_s} \dot{w}_s + \mu(\bar{\Sigma}^\phi \cdot \vec{n}) \partial_n \vec{u} \\ & + (\nabla \psi_{\rho_e} \cdot \vec{n}) \kappa^{tr} \partial_n T + [(\nabla \psi_{\rho_e} + \nabla \psi_{\rho_e^{ve}}) \cdot \vec{n}] \kappa^{ve} \partial_n T^{ve}. \end{aligned} \quad (3.106)$$

### Isothermal, Catalytic Walls

Adjoint boundary conditions for isothermal, catalytic wall boundaries with the thermal objective function are determined by applying the following linearized boundary conditions to Eqn. (3.69),

$$\begin{aligned} \delta \vec{u} &= -\partial_n \vec{u} \delta S \\ \delta T &= -\partial_n T \delta S \\ \delta T^{ve} &= -\partial_n T^{ve} \delta S \\ \delta Y_s &= -\partial_n Y_s \delta S, \end{aligned}$$

such that,

$$\begin{aligned} \delta \mathcal{J} = & -\beta \int_S p(-q_n)^{p-1} (\delta q^{\vec{t}r} + \delta q^{\vec{v}e}) \cdot \vec{n} ds - \int_\Gamma ((\vec{\phi} \cdot \vec{n}) \delta p) ds \\ & + \int_\Gamma \left[ -\sum_s \psi_{\rho_s} (\delta \vec{J}_s \cdot \vec{n}) - \psi_{\rho_e} \sum_s (\delta \vec{J}_s \cdot \vec{n}) h_s^{int} - \psi_{\rho_e^{ve}} \sum_s (\delta \vec{J}_s \cdot \vec{n}) e_s^{ve} \right] \\ & + \int_\Gamma (\vec{\phi} \cdot \delta \bar{\sigma} \cdot \vec{n}) ds + \int_\Gamma (\psi_{\rho_e} \delta(\kappa^{tr} \nabla T) \cdot \vec{n}) ds + \int_\Gamma ((\psi_{\rho_e} + \psi_{\rho_e^{ve}}) \delta(\kappa^{ve} \nabla T^{ve}) \cdot \vec{n}) ds \\ & + \int_\Gamma \left\{ \frac{\partial \mathcal{J}}{\partial S} \right\} \delta S ds + \int_\Omega \left\{ \Psi^\top \frac{\partial \mathcal{R}}{\partial U} \right\} \delta U ds. \end{aligned} \quad (3.107)$$

An examination of the remaining terms in Eqn. (3.107) reveals the necessary prescription of the adjoint variables to cancel variational flow dependence. If the following conditions are applied on  $S$ ,

$$\psi_{\rho_s} = -\psi_{\rho_e} h_s^{int} \quad (3.108a)$$

$$\vec{\phi} = \vec{0} \quad (3.108b)$$

$$\psi_{\rho_e} = -\beta p(-q_n)^{p-1} \quad (3.108c)$$

$$\psi_{\rho_e^{ve}} = 0, \quad (3.108d)$$

the necessary cancellation occurs, and the variation of the Lagrangian,  $\delta\mathcal{J}$ , may be determined by evaluating the surface sensitivities from a single flow and a single adjoint solution, regardless of the surface deformation.

**Surface Sensitivity** The adjoint surface sensitivities for isothermal, catalytic boundaries, corresponding to the thermal objective functions, are the terms from the Lagrangian variation with  $\delta S$  dependency after the application of the linearized boundary conditions,

$$\begin{aligned} \frac{\partial\mathcal{J}}{\partial S} = & -\beta\nabla_S [p(-q_n)^{p-1}] \cdot \vec{q} + \beta p(-q_n)^{p-1} \nabla \cdot (-\vec{q}) + \beta 2(p-1)H_m(-q_n)^p + \vartheta \partial_n \vec{u} \cdot \vec{n} \\ & + \psi_{\rho_e} \sum_s (\vec{J}_s \cdot \vec{n}) [(C_{v,s}^{tr} + R_s) \partial_n T + C_{v,s}^{ve} \partial_n T^{ve}] + \psi_{\rho_e^{ve}} \sum_s (\vec{J}_s \cdot \vec{n}) C_{v,s}^{ve} \partial_n T^{ve} \\ & - \psi_{\rho_e} \bar{\sigma} \cdot \partial_n \vec{u} \cdot \vec{n} + \sum_s [(\nabla \psi_{\rho_s} \cdot \vec{n}) + (\nabla \psi_{\rho_e} \cdot \vec{n}) h_s^{int} + (\nabla \psi_{\rho_e^{ve}} \cdot \vec{n}) e_s^{ve}] (\vec{J}_s \cdot \vec{n}) \\ & + \mu (\bar{\Sigma}^\phi \cdot \vec{n}) \partial_n \vec{u} + (\nabla \psi_{\rho_e} \cdot \vec{n}) \kappa^{tr} \partial_n T + [(\nabla \psi_{\rho_e} + \nabla \psi_{\rho_e^{ve}}) \cdot \vec{n}] \kappa^{ve} \partial_n T^{ve}. \end{aligned} \quad (3.109)$$

Applying the isothermal, catalytic, and adjoint boundary conditions, as well as the simplified forms of  $\nabla \cdot (-q^{tr})$ , and  $\nabla \cdot (-q^{tr})$  from Eqns. (C.20), and (C.30) respectively, the surface sensitivity may be expressed as,

$$\begin{aligned} \frac{\partial\mathcal{J}}{\partial S} = & -\beta\nabla_S [p(-q_n)^{p-1}] \cdot \vec{q} + \beta 2(p-1)H_m(-q_n)^p + \vartheta \partial_n \vec{u} \cdot \vec{n} \\ & + \beta p(-q_n)^{p-1} \left[ \sum_s h_s^{int} w_s + \sum_s \vec{J}_s \cdot \nabla h_s^{int} \right] \\ & + \psi_{\rho_e} \sum_s (\vec{J}_s \cdot \vec{n}) [(C_{v,s}^{tr} + R_s) \partial_n T + C_{v,s}^{ve} \partial_n T^{ve}] \\ & + \sum_s [(\nabla \psi_{\rho_s} \cdot \vec{n}) + (\nabla \psi_{\rho_e} \cdot \vec{n}) h_s^{int} + (\nabla \psi_{\rho_e^{ve}} \cdot \vec{n}) e_s^{ve}] (\vec{J}_s \cdot \vec{n}) \\ & + \mu (\bar{\Sigma}^\phi \cdot \vec{n}) \partial_n \vec{u} + (\nabla \psi_{\rho_e} \cdot \vec{n}) \kappa^{tr} \partial_n T + [(\nabla \psi_{\rho_e} + \nabla \psi_{\rho_e^{ve}}) \cdot \vec{n}] \kappa^{ve} \partial_n T^{ve}. \end{aligned} \quad (3.110)$$

Recognizing  $\vartheta = 0$  by the application of the adjoint boundary conditions, and  $\sum_s \vec{J}_s \cdot \nabla h_s^{int} = \sum_s (\vec{J}_s \cdot \vec{n}) [(C_{v,s}^{tr} + R_s) \partial_n T + C_{v,s}^{ve} \partial_n T^{ve}]$  by the application of the isothermal boundary condition,

the surface sensitivity may be simplified to

$$\begin{aligned} \frac{\partial \mathcal{J}}{\partial S} = & -\beta \nabla_S [p(-q_n)^{p-1}] \cdot \vec{q} + \beta 2(p-1) H_m(-q_n)^p + \beta p(-q_n)^{p-1} \sum h_s^{int} \dot{w}_s \\ & + \sum_s [(\nabla \psi_{\rho_s} \cdot \vec{n}) + (\nabla \psi_{\rho_e} \cdot \vec{n}) h_s^{int} + (\nabla \psi_{\rho_e^{ve}} \cdot \vec{n}) e_s^{ve}] (\vec{J}_s \cdot \vec{n}) \\ & + \mu (\bar{\Sigma}^\phi \cdot \vec{n}) \partial_n \vec{u} + (\nabla \psi_{\rho_e} \cdot \vec{n}) \kappa^{tr} \partial_n T + [(\nabla \psi_{\rho_e} + \nabla \psi_{\rho_e^{ve}}) \cdot \vec{n}] \kappa^{ve} \partial_n T^{ve}. \end{aligned} \quad (3.111)$$

For the special case,  $p = 1$ , the surface sensitivity may be simplified further,

$$\begin{aligned} \left. \frac{\partial \mathcal{J}}{\partial S} \right|_{p=1} = & \sum h_s^{int} \dot{w}_s + \sum_s [(\nabla \psi_{\rho_s} \cdot \vec{n}) + (\nabla \psi_{\rho_e} \cdot \vec{n}) h_s^{int} + (\nabla \psi_{\rho_e^{ve}} \cdot \vec{n}) e_s^{ve}] (\vec{J}_s \cdot \vec{n}) \\ & + \mu (\bar{\Sigma}^\phi \cdot \vec{n}) \partial_n \vec{u} + (\nabla \psi_{\rho_e} \cdot \vec{n}) \kappa^{tr} \partial_n T + [(\nabla \psi_{\rho_e} + \nabla \psi_{\rho_e^{ve}}) \cdot \vec{n}] \kappa^{ve} \partial_n T^{ve}. \end{aligned} \quad (3.112)$$

## Chapter 4

# Numerical Implementation

A capability to acquire solutions to the flow and adjoint partial differential equation systems is necessary to evaluate the objective functions and adjoint sensitivities. This chapter discusses the methodology by which the solutions to the equation systems of Chapters 2 and 3 are numerically obtained. Additionally, this chapter provides a description of the design variables used to perturb the surface topologies and the mesh deformation algorithms necessary for evaluating the flow and adjoint states for deformed geometries.

The discretized PDE systems governing the direct and adjoint problems, as well as the mesh deformation algorithms are implemented within the SU2 computational analysis suite [107]. This software package is architected specifically for the solution of PDE systems and PDE-constrained optimization problems on unstructured computational mesh topologies. The package is unique in the sense that it is built from the ground up to provide gradient information, via the adjoint method, for complex, multi-physics problems. For this reason, SU2 is particularly well suited for the multidisciplinary analysis and design of aerospace systems. The software package is composed of C++ analysis modules for solution to the flow and adjoint PDE systems, mesh deformation, and others. These modules are linked together using python scripting to enable powerful simulation-based analysis and design.

The governing equations are discretized and solved on an unstructured computational mesh. This discretization of the domain utilizes triangular, quadrilateral, tetrahedral, pyramidal, and hexahedral cells to populate the volumetric mesh surrounding a body of interest. With this approach, it is significantly easier to generate computational meshes for complex geometries as compared to structure-based approaches that restrict cell topologies to quadrilaterals and hexahedra. The discretization procedure discussed in this chapter follows the method of lines [153, 65, 143], where the spatial derivatives are discretized first, leaving the time derivatives continuous. This approach leads to a system of coupled ordinary differential equations in time that can be marched forward using an approximate temporal integration scheme to arrive at the steady-state flow solution.

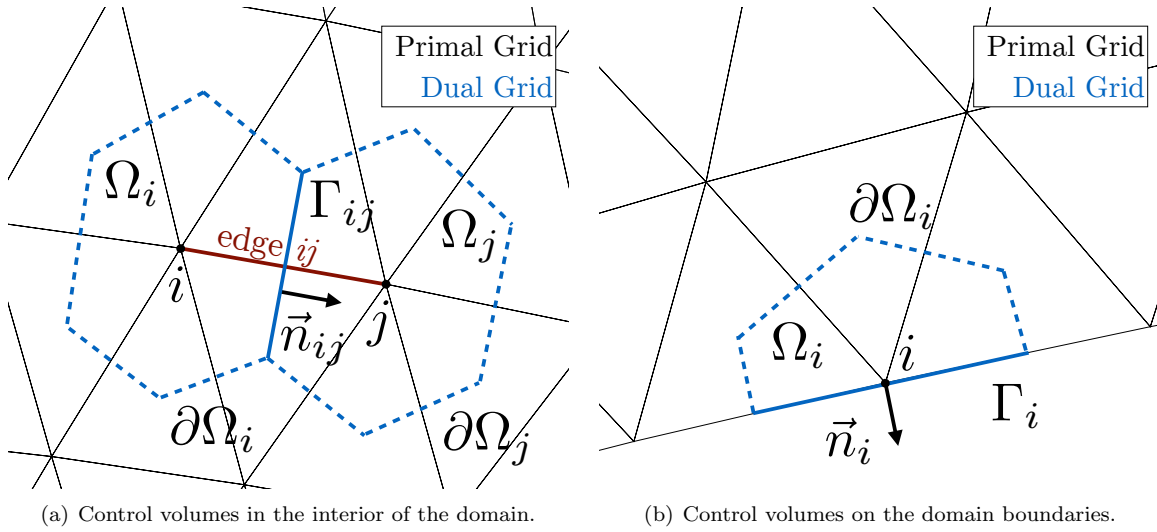


Figure 4.1: Computational grid topologies

## 4.1 Discretization of the Flow Equations

To simulate the hypersonic, nonequilibrium flow environment, the mathematical model presented in Chapter 2 must be evaluated. Generally, Eqn. (2.26) does not have a closed-form analytic solution, except in simple, canonical cases, so a numerical procedure is used to acquire approximate solutions. This is accomplished by evaluating Eqn. (2.26) at many discrete points in the flow domain, using local approximations of the nonlinear PDE system. An initial flow state is defined everywhere in the domain, and the discretized equation system is evaluated, subject to boundary conditions that are consistent with the physical system. The final flow state is determined by marching forward in time until convergence is achieved.

To integrate the governing equations, the Finite Volume Method (FVM) [85, 115, 86, 11] is applied. In the FVM, the governing equations are integrated over the dual grid control volumes surrounding the nodes of the primal computational mesh. Use of the Divergence theorem on the convective and viscous flux vectors converts volumetric integration of these quantities to surface integration, which may be performed by evaluating the fluxes at the faces of the control volumes. Because the formulation of the governing equations, given by Eqn. (2.26), is conservative, the flux of any quantity out of one control volume is acquired by the adjacent volumes, resulting in a simple, efficient spatial integration scheme.

The computational mesh is constructed from a tessellation of the flow domain, consisting of triangular and quadrilateral cells in two-dimensions, or tetrahedral, pyramidal, and hexahedral cells in three dimensions. Vertices of the geometric shapes within the mesh form the nodes of the primal grid, which are connected along edges of the cell faces. The state of the gas,  $U$ , is stored at each of these primal grid nodes. Control volumes surrounding each primal grid node are constructed by connecting the cell centroids, face centroids, and edge midpoints that surround a particular node, as

shown in Fig. (4.1), into the median dual-grid. The dual-grid control volumes provide the framework to apply the FVM within the computational domain.

The discretized form of the governing equations is derived by integrating Eqn. (2.26) over each dual-grid control volume,  $\Omega_i$ ,

$$\int_{\Omega_i} \left[ \frac{\partial U}{\partial t} + \nabla \cdot (\vec{F}^c - \vec{F}^v) - Q \right] d\Omega_i = 0. \quad (4.1)$$

The divergence theorem is applied to the flux terms, transforming the volume integrals to surface integrals over  $\partial\Omega_i$  such that,

$$\int_{\Omega_i} \frac{\partial U}{\partial t} d\Omega_i + \int_{\partial\Omega_i} (\vec{F}^c - \vec{F}^v) \cdot \vec{n} ds - \int_{\Omega_i} Q d\Omega_i = 0. \quad (4.2)$$

To resolve these surface integrals, the continuous fluxes are replaced with numerical representations of the fluxes at the faces of the dual grid,  $\hat{F}_{ij}$ . Surface integration is performed by summing  $\hat{F}_{ij}$  from all the faces of the control volume, multiplied by the face area,  $\Gamma_{ij}$ . By assuming piecewise-constant source terms,  $Q$ , within each  $\Omega_i$ , the semi-discrete form of the governing equations is expressed as,

$$\frac{dU}{dt} |\Omega_i| + \sum_{j \in \mathcal{N}_i} (\hat{F}_{ij}^c - \hat{F}_{ij}^v) \Gamma_{ij} - Q_i |\Omega_i| = 0, \quad (4.3)$$

where  $|\Omega_i|$  is the volume of the control volume and  $\mathcal{N}_i$  is the set of all neighboring nodes of  $i$ . The spatial terms are often grouped together,

$$\frac{dU}{dt} |\Omega_i| + \mathcal{R}_i(U) = 0, \quad (4.4)$$

into a ‘residual’,  $\mathcal{R}_i(U)$ , at each node. By inserting the numerical flux functions, which depend on locally on the flow state,  $U$ , at a particular time step, the governing equations have been transformed into a set of coupled *ordinary* differential equations in time, that may be marched forward to convergence using an approximate time integration scheme.

The vertex-centered, median dual-grid FVM described above is stored in memory as an edge-based data structure. Each edge has member nodes where the solution state is stored, so a single pass over all edges within the domain can be used to evaluate the fluxes across all dual-grid cell faces. In this manner, the governing equations are solved efficiently and with minimal data storage requirements. Recalling Eqn. (4.3) is a first-order ordinary differential equation, it can be solved as an initial value problem by specifying an initial flow state, which then evolves forward in time to the steady-state solution. At each time step, the procedure is as follows:

1. Loop over primal grid edges to resolve convective,  $\hat{F}_{ij}^c$ , and viscous,  $\hat{F}_{ij}^v$ , fluxes.
2. Loop over primal grid nodes to calculate source terms,  $Q$ .
3. Loop over boundary nodes to apply the appropriate spatial boundary conditions.

Using this approach,  $\mathcal{R}_i$  is determined at each node within the grid, the solution state is updated, and the process is repeated until  $\mathcal{R}_i$  is sufficiently small everywhere in the domain, indicating the governing equations are solved to a satisfactory level of convergence.

## 4.2 Flow Spatial Integration

In the FVM, spatial integration of the convective and viscous fluxes is performed by surface integrals over the control volumes that represent the discretized flow domain. Numerical flux functions are utilized to resolve the flux calculations between neighboring control volumes. Accurate, low-dissipation numerical flux functions are more capable of faithfully representing the true flow phenomena of the continuous governing equation system. The properties of the convective and viscous flux discretizations are discussed in this section.

### 4.2.1 Convective Fluxes

Low-dissipation, non-oscillatory numerical flux functions are desirable for evaluating convective fluxes in hyperbolic PDE systems. Oscillatory behavior from the discretization of the continuous fluxes affects the simulated flow state in regions near shockwaves and near walls. These regions are critically important for assessing the vehicle's predicted performance. Numerical diffusion that is introduced by the discretization scheme is necessary for algorithmic stability, but has deleterious effects on the accuracy of the solution, since the dissipation is solely an artifact of the numerical method, and not due to a physical convection or diffusion process. The 'correct' numerical representation of the continuous fluxes in gasdynamics continues to be the subject of active research.

This work utilizes two numerical schemes that are based on the hyperbolic nature of the governing PDEs. It is shown that convective information is propagated within the domain at finite wave speeds, determined by the eigenvalues of the convective flux Jacobian. The numerical techniques in this work are constructed to mimic this propagation of information by taking the 'upwind' scalar quantities that are transported across control volume boundaries.

#### Modified Steger-Warming

The Steger-Warming flux vector splitting method [132] is an effective numerical technique for resolving the convective fluxes in strongly-shocked, nonequilibrium hypersonic flows. The method has been employed extensively on structured finite-difference [13, 88, 90, 91, 87], structured finite-volume [148, 22, 119], and unstructured finite-volume [125, 106] formulations of the viscous nonequilibrium equations. The Steger-Warming scheme is more dissipative than other upwinding methods, which negatively impacts the solution quality, but exhibits good stability in hypersonic environments.

The scheme leverages first-degree homogeneity of the convective fluxes,

$$\vec{F}^c \cdot \vec{n} = \frac{\partial(\vec{F}^c \cdot \vec{n})}{\partial U} U = (\vec{A}^c \cdot \vec{n})U. \quad (4.5)$$

An eigenvalue-eigenvector decomposition of the projected flux Jacobian,  $\vec{A}^c \cdot \vec{n}$ , reveals the characteristic wave propagation speeds within the flow field,

$$\vec{A}^c \cdot \vec{n} = P \Lambda P^{-1} = P \begin{bmatrix} (\vec{u} \cdot \vec{n})_s & & & & & & \\ & \cdot & \cdot & \cdot & \cdot & \cdot & \cdot \\ & (\vec{u} \cdot \vec{n}) & \cdot & \cdot & \cdot & \cdot & \cdot \\ & \cdot & \cdot & (\vec{u} \cdot \vec{n}) & \cdot & \cdot & \cdot \\ & \cdot & \cdot & \cdot & (\vec{u} \cdot \vec{n}) + c & \cdot & \cdot \\ & \cdot & \cdot & \cdot & \cdot & (\vec{u} \cdot \vec{n}) - c & \cdot \\ & \cdot & \cdot & \cdot & \cdot & \cdot & (\vec{u} \cdot \vec{n}) \end{bmatrix} P^{-1}, \quad (4.6)$$

where  $c$  is the local speed of sound. An eigenvalue's sign determines the direction of information propagation along  $\vec{n}$ . The Steger-Warming method splits the flux from node  $i$  to node  $j$  into upwind and downwind components by separating the flux vector in accordance with the sign of the eigenvalues,

$$\hat{F}_{ij}^{SW} = (\vec{A}^c \cdot \vec{n})_i^+ U_i + (\vec{A}^c \cdot \vec{n})_j^- U_j, \quad (4.7)$$

where

$$(\vec{A}^c \cdot \vec{n})^\pm = P \Lambda^\pm P^{-1}, \quad (4.8)$$

and the elements of  $\Lambda^\pm$  are  $(\Lambda^\pm)_k = (\Lambda)_k \pm |(\Lambda)_k|$ . The left and right eigenvector matrices,  $P$  and  $P^{-1}$  are included in Section B.4. With this ‘split-flux’ formulation, flow quantities are transported across cell boundaries in accordance with the physical propagation as dictated by the hyperbolic nature of the governing equations.

Compared to other classical upwinding schemes, such as the Roe [120], AUSM [83], CUSP [129], and HLLE [29] methods, the classical Steger-Warming flux vector splitting method described above is more numerically dissipative. The differencing method smooths sharp flow features within the domain, degrading the quality of the solution in regions with large gradients, such as in boundary and shock layers. This negatively impacts the accuracy of the solution in these regions.

It is possible to reduce the numerical dissipation in the Steger-Warming scheme by evaluating the projected flux Jacobian at the cell boundary using an average of the flow solutions at  $i$  and  $j$ . This approach is effective in regions with weak gradients, but lacks sufficient dissipation to be robust in the presence of strong shock waves and steep pressure gradients. A pressure switch may be used to detect the presence of steep gradients and modulate the numerical scheme [93, 106, 125], to blend the traditional and modified Steger-Warming methods such that dissipation is added when needed for stability, and removed when not. This ‘modified’ Steger-Warming method is formulated as,

$$\hat{F}_{ij}^{MSW} = (\vec{A}^c \cdot \vec{n})_{ij}^+ U_i + (\vec{A}^c \cdot \vec{n})_{ji}^- U_j, \quad (4.9)$$

where the face states  $ij$  and  $ji$  are calculated as,

$$U_{ij} = (1 - w)U_i + wU_j \quad \text{and} \quad U_{ji} = wU_i + (1 - w)U_j. \quad (4.10)$$

The parameter,  $w$ , acts as a weighting term and is based on the local pressure gradient,

$$w = \frac{1}{2} \frac{1}{(\epsilon \nabla p)^2 + 1}, \quad (4.11)$$

with  $\epsilon$  included as a tunable parameter for the scheme. A value of  $\epsilon = 5$  is used in this work. When  $\nabla p$  is large,  $w$  approaches zero and the numerical scheme asymptotically approaches the traditional Steger-Warming flux method. Conversely, when  $\nabla p$  is small,  $w$  approaches unity and the scheme asymptotically approaches the face-averaged Steger-Warming method. Using this adaptive scheme, the dissipation within the computational domain is dynamically tailored for stability and accuracy.

### Advection Upstream Splitting Method (AUSM)

The Advection Upstream Splitting Method (AUSM) by Liou and Steffen [83] is another successful scheme for accurately simulating hypersonic flow environments. The method is constructed to retain the advantages of the two primary families of upwind numerical schemes, while mitigating their disadvantages. Flux Vector Splitting (FVS) methods, like the previously described Steger-Warming scheme, tend to be more computationally efficient, but more numerically dissipative, particularly at low Mach numbers. Flux Difference Splitting (FDS) methods, like Roe's scheme, are known to be more accurate, but carry greater computational expense as compared to FVS methods. AUSM is unique in the sense that it breaks the flux vector into two components which may be separately discretized and propagated. In this way, a family of new flux schemes [82, 69, 68] have been constructed that are tailored for different applications.

AUSM is constructed by recognizing the projected flux vector,  $\vec{F}^c \cdot \vec{n}$ , is composed of two distinct parts: (1) the convective terms and (2) the pressure terms,

$$\vec{F}^c \cdot \vec{n} = \begin{bmatrix} \rho_s \\ \rho \vec{u} \\ \rho h \\ \rho e^{ve} \end{bmatrix} (\vec{u} \cdot \vec{n}) + \begin{bmatrix} 0 \\ p \bar{\vec{I}} \cdot \vec{n} \\ 0 \\ 0 \end{bmatrix}. \quad (4.12)$$

The convected terms are transported through the domain at the local flow velocity,  $\vec{u}$ , while the pressure term is propagated at the local acoustic speed,  $c$ . In the AUSM, these two processes are discretized separately. For the convected terms, a suitable cell-interface velocity is required to convect the conserved scalar variables. The method proposed by Liou and Steffen determines this interface velocity by considering a combination of the wave speeds that travel toward the interface,  $ij$ ,

$$M_{ij} = M_i^+ + M_j^- . \quad (4.13)$$

The split Mach numbers,  $M^\pm$ , are defined using Van Leer splitting [141],

$$M^\pm = \begin{cases} \pm \frac{1}{4}(M \pm 1)^2 & \text{for } |M| \leq 1, \\ \frac{1}{2}(M \pm |M|) & \text{otherwise,} \end{cases} \quad (4.14)$$

with the local Mach number,  $M_i = u_i/c_i$ . The pressure term can be discretized similarly as wave propagation to the interface,

$$P_{ij} = P_i^+ + P_j^- . \quad (4.15)$$

The pressure splitting is weighted based on polynomial expansions of the characteristic acoustic wave propagation speeds,  $M \pm 1$ ,

$$P^\pm = \begin{cases} \frac{p}{4}(M \pm 1)^2(2 \mp M) & \text{for } |M| \leq 1, \\ \frac{p}{2}(M \pm |M|)/M & \text{otherwise.} \end{cases} \quad (4.16)$$

Assembling the components, the numerical flux function for AUSM is,

$$\hat{F}_{ij}^{AUSM} = \frac{(M_{ij} + |M_{ij}|)}{2} \begin{bmatrix} \rho_s c \\ \rho \vec{u} c \\ \rho h c \\ \rho e^{ve} c \end{bmatrix}_i + \frac{(M_{ij} - |M_{ij}|)}{2} \begin{bmatrix} \rho_s c \\ \rho \vec{u} c \\ \rho h c \\ \rho e^{ve} c \end{bmatrix}_j + P_{ij} \begin{bmatrix} 0 \\ \bar{I} \cdot \vec{n} \\ 0 \\ 0 \end{bmatrix} . \quad (4.17)$$

The AUSM scheme described here is accurate and robust for simulating hypersonic flow environments. Because the interface advection Mach number is chosen carefully based on wave propagation, the method is accurate enough to resolve shear layers in viscous flow fields. In this respect, AUSM is superior to the Modified Steger-Warming method of Section 4.2.1 because it injects less numerical dissipation. Also, because AUSM does not require a matrix-vector product to resolve the flux function, it is more computationally efficient than the Modified Steger-Warming method as well.

### 4.2.2 Viscous Fluxes

The mathematical character of the viscous terms results in no preferential direction of information propagation. Therefore, the numerical representation of the viscous flux vectors does not require the same level of sophistication required for the convective fluxes, and the viscous terms do not have a direct influence on the numerical solution algorithm. For this reason, there is more flexibility to select different numerical methods to resolve the mass, momentum, and energy transport from these processes. Both the flow state and the gradients are necessary to resolve the viscous fluxes, defined in Eqn. (2.26) as,

$$\vec{F}^v = \begin{bmatrix} -\vec{J}_1 \\ \vdots \\ -\vec{J}_N \\ \bar{\sigma} \\ \bar{\sigma} \vec{u} - \sum_k \vec{q}^k - \sum_s \vec{J}_s h_s^{int} \\ -q^{ve} - \sum_s \vec{J}_s e_s^{ve} \end{bmatrix}, \quad \begin{aligned} \vec{J}_s &= -\rho D_s \nabla Y_s + Y_s \sum_k \rho D_k \nabla Y_k, \\ \bar{\sigma} &= \mu \left[ \nabla \vec{u} + (\nabla \vec{u})^\top - \frac{2}{3} \bar{I} (\nabla \cdot \vec{u}) \right], \\ \vec{q}^k &= -\kappa^k \nabla T^k. \end{aligned}$$

The viscous fluxes are numerically represented using a centered discretization scheme [146, 106,

[14] where the fluxes are evaluated directly at the median dual-grid interface,  $ij$ , using the mean state of the primitive variables,  $V_{ij} = (1/2)(V_i + V_j)$  and transport coefficients,  $\mu_{ij} = \frac{1}{2}(\mu_i + \mu_j)$ .

Flow state gradients at each primal grid node are computed using the Green-Gauss or Weighted least squares methodologies described in Section 4.8. Both techniques can be prone to numerical errors in regions with highly skewed or high aspect ratio cells [97]. These skewed and stretched mesh topologies are common in boundary layer grids, as sufficient wall-normal resolution is required to accurately capture the large velocity and thermal gradients near the body. To combat this, a correction [70, 106] is applied to the cell gradient when it is used for viscous flux calculations at the median dual grid faces.

Consider a scalar quantity,  $\xi$ , and its gradient,  $\nabla\xi$ , at a node of the primal grid. Between nodes  $i$  and  $j$ , it is reasonable to approximate the gradient at the cell interface,  $ij$ , as the average of the gradients at the cell centers,  $\nabla\xi_i$  and  $\nabla\xi_j$ ,

$$\overline{\nabla\xi_{ij}} = \frac{\nabla\xi_i + \nabla\xi_j}{2}. \quad (4.18)$$

It is also reasonable to assume along the unit vector connecting  $i$  and  $j$ , denoted here as  $\vec{e}$ , the most accurate approximation of the gradient that only uses information from  $i$  and  $j$  is simply,

$$\nabla\xi_{ij} \cdot \vec{e} \approx \frac{\xi_j - \xi_i}{d_{ij}}, \quad (4.19)$$

where  $d_{ij}$  is the distance between nodes  $i$  and  $j$ . To obtain the corrected gradient, subtract the component of the gradient along the line of centers and replace it with the more accurate finite-difference approximation,

$$\nabla\xi_{ij} = (\nabla\xi_{ij} \cdot \vec{e})\vec{e} + [\overline{\nabla\xi_{ij}} - (\overline{\nabla\xi_{ij}} \cdot \vec{e})\vec{e}], \quad (4.20)$$

such that,

$$\nabla\xi_{ij} = \left( \frac{\xi_j - \xi_i}{d_{ij}} \right) \vec{e} + \left( \bar{I} - \vec{e} \otimes \vec{e} \right) \frac{(\nabla\xi_i + \nabla\xi_j)}{2}. \quad (4.21)$$

The corrected ‘face-gradients’ for velocity, temperature, and species mass fraction are calculated in this fashion and used directly to evaluate the viscous fluxes.

### 4.2.3 Viscous Jacobians using the TSL Approximation

For implicit time-stepping, or adjoint calculations, a Jacobian of the viscous fluxes is required. Analytically, the viscous Jacobian depends on second derivative information within the flow domain, which is difficult and expensive to acquire on general, mixed-element unstructured meshes, as it necessitates the use of information at non-local, “neighbor-of-neighbor” nodes. This can be avoided by applying the Thin Shear Layer (TSL) [95, 96, 51, 25] approximation, where dual-grid face tangential gradient information is neglected. Under the TSL approximation, scalar gradients are the

finite difference gradients between nodes  $i$  and  $j$ , projected into the cartesian directions,

$$\frac{\partial \xi}{\partial x_k} = \left( \frac{\xi_j - \xi_i}{d_{ij}} \right) n_k, \quad \text{where } k = 1, 2, 3. \quad (4.22)$$

The TSL approximation is similar to the Thin Layer Navier-Stokes Equations (TLNS) [105] that was popular in the 1980s, where only wall-normal terms in the viscous shear stress tensor are retained. The influence of the TSL simplification on the solution quality is minimal, even in cases that are sensitive to viscous effects [110]. Under the TSL approximation, only local quantities on opposing sides of the dual-grid interface are required, which makes the approximation well-suited to edge-based, unstructured solvers, like SU2. Applying the TSL approximation, the terms of the projected viscous flux vector can be rewritten as,

$$\begin{aligned} F_{ij}^{TSL}|_{\rho_s} &= -\rho_{s,ij} \frac{D_{s,ij}}{d_{ij}} (n_x^2 + n_y^2 + n_z^2) (Y_{s,j} - Y_{s,i}) + \\ &\quad Y_{s,ij} \sum_k \rho_{k,ij} \frac{D_{k,ij}}{d_{ij}} (n_x^2 + n_y^2 + n_z^2) (Y_{k,j} - Y_{k,i}) \quad \text{for } s = 1, \dots, n_s. \end{aligned} \quad (4.23a)$$

$$F_{ij}^{TSL}|_{\rho u} = \frac{\mu_{ij}}{d_{ij}} \left[ \left( \frac{4}{3} n_x^2 + n_y^2 + n_z^2 \right) (u_j - u_i) + \frac{n_x n_y}{3} (v_j - v_i) + \frac{n_x n_z}{3} (w_j - w_i) \right] \quad (4.23b)$$

$$F_{ij}^{TSL}|_{\rho v} = \frac{\mu_{ij}}{d_{ij}} \left[ \frac{n_x n_y}{3} (u_j - u_i) + \left( n_x^2 + \frac{4}{3} n_y^2 + n_z^2 \right) (v_j - v_i) + \frac{n_y n_z}{3} (w_j - w_i) \right] \quad (4.23c)$$

$$F_{ij}^{TSL}|_{\rho w} = \frac{\mu_{ij}}{d_{ij}} \left[ \frac{n_x n_z}{3} (u_j - u_i) + \frac{n_y n_z}{3} (v_j - v_i) + \left( n_x^2 + n_y^2 + \frac{4}{3} n_z^2 \right) (w_j - w_i) \right] \quad (4.23d)$$

$$\begin{aligned} F_{ij}^{TSL}|_{\rho e} &= \vec{F}^v \cdot \vec{n}|_{n_s+1} u_{ij} + \vec{F}^v \cdot \vec{n}|_{n_s+2} v_{ij} + \vec{F}^v \cdot \vec{n}|_{n_s+3} w_{ij} + \frac{\kappa_{ij}^{tr}}{d_{ij}} (n_x^2 + n_y^2 + n_z^2) (T_j - T_i) + \\ &\quad \frac{\kappa_{ij}^{ve}}{d_{ij}} (n_x^2 + n_y^2 + n_z^2) (T_j^{ve} - T_i^{ve}) + \sum_k \vec{F}^v \cdot \vec{n}|_k h_{k,ij} \end{aligned} \quad (4.23e)$$

$$F_{ij}^{TSL}|_{\rho e^{ve}} = \frac{\kappa_{ij}^{ve}}{d_{ij}} (n_x^2 + n_y^2 + n_z^2) (T_j^{ve} - T_i^{ve}) + \sum_s \vec{F}^v \cdot \vec{n}|_k e_{k,ij}^{ve}. \quad (4.23f)$$

All face quantities and gradients,  $(\cdot)_{ij}$ , are averaged from the adjacent nodes,  $i$  and  $j$  in accordance with the procedure described in Section 4.2.2.

If the transport coefficients are held fixed under differentiation, and if Eqn. (4.23) is differentiated with respect to the primitive variables,

$$V = \{\rho_s, u, v, w, T, T^{ve}\}^\top, \quad (4.24)$$

the TSL Jacobian takes a particularly simple form,

$$\frac{\partial F_{ij}^{TSL}}{\partial V_{j/i}} = \begin{bmatrix} \beta_{s,r}^{j/i} & 0 & 0 & 0 & 0 & 0 \\ 0 & \pm \frac{\mu_{ij}\theta_x}{d_{ij}} & \pm \frac{\mu_{ij}\eta_z}{d_{ij}} & \pm \frac{\mu_{ij}\eta_y}{d_{ij}} & 0 & 0 \\ 0 & \pm \frac{\mu_{ij}\eta_z}{d_{ij}} & \pm \frac{\mu_{ij}\theta_y}{d_{ij}} & \pm \frac{\mu_{ij}\eta_x}{d_{ij}} & 0 & 0 \\ 0 & \pm \frac{\mu_{ij}\eta_y}{d_{ij}} & \pm \frac{\mu_{ij}\eta_x}{d_{ij}} & \pm \frac{\mu_{ij}\theta_z}{d_{ij}} & 0 & 0 \\ \sum_k \beta_{k,r}^{j/i} h_k & \pm \pi_x + \frac{F_{ij}^v|_{\rho_u}}{2} & \pm \pi_y + \frac{F_{ij}^v|_{\rho_v}}{2} & \pm \pi_z + \frac{F_{ij}^v|_{\rho_w}}{2} & \pm \frac{\kappa^{tr}\theta}{d_{ij}} + \alpha^h & \pm \frac{\kappa^{ve}\theta}{d_{ij}} + \alpha^{ve} \end{bmatrix} \quad (4.25)$$

where the subscript  $j/i$  indicates differentiation with respect to the primitive variables at node  $j$  or  $i$  and the following parameters are defined,

$$\begin{aligned} \beta_{s,r}^{j/i} &= \frac{\partial F_{ij}^{TSL}|_{\rho_s}}{\partial \rho_{r,j/i}} \\ &= \frac{D_{s,ij}\theta}{2d_{ij}} \left( \frac{1}{\rho_i} \delta_{i,j/i} + \frac{1}{\rho_j} \delta_{j,j/i} \right) [\mp(\rho_i + \rho_j)\delta_{s,r} \pm (Y_{s,j}\rho_i + Y_{s,i}\rho_j)] + \\ &\quad \frac{1}{4} \left( \frac{1}{\rho_i} \delta_{i,j/i} + \frac{1}{\rho_j} \delta_{j,j/i} \right) [(\rho_i + \rho_j)\delta_{s,r} \pm \rho_j Y_{s,i} \mp \rho_i Y_{s,j}] \sum_k \frac{D_{k,ij}\theta}{d_{ij}} (Y_{k,j} - Y_{k,i}) \pm \\ &\quad Y_{s,ij}\rho_{ij} \frac{D_{r,ij}\theta}{d_{ij}} \left( \frac{1}{\rho_i} \delta_{i,j/i} + \frac{1}{\rho_j} \delta_{j,j/i} \right) \mp Y_{s,ij}\rho_{ij} \sum_k \frac{D_{k,ij}\theta}{d_{ij}} \left( \frac{Y_{k,j}}{\rho_j} \delta_{j,j/i} + \frac{Y_{k,i}}{\rho_i} \delta_{i,j/i} \right) \end{aligned} \quad (4.26)$$

$$\begin{aligned} \theta &= n_x^2 + n_y^2 + n_z^2 & \alpha^h &= \sum_k \frac{J_{k,ij}}{2} \frac{\partial h_{s,ij}}{\partial T_{j/i}} & \alpha^{ve} &= \sum_k \frac{J_{k,ij}}{2} C_{v,k,ij} \\ \theta_x &= \frac{4}{3}n_x^2 + n_y^2 + n_z^2 & \eta_x &= \frac{n_x n_z}{3} & \pi_x &= \frac{\mu_{ij}}{d_{ij}} (\theta_x u_{ij} + \eta_z v_{ij} + \eta_y w_{ij}) \\ \theta_y &= n_x^2 + \frac{4}{3}n_y^2 + n_z^2 & \eta_y &= \frac{n_x n_z}{3} & \pi_y &= \frac{\mu_{ij}}{d_{ij}} (\eta_y u_{ij} + \theta_y v_{ij} + \eta_x w_{ij}) \\ \theta_z &= n_x^2 + n_y^2 + \frac{4}{3}n_z^2 & \eta_z &= \frac{n_x n_y}{3} & \pi_z &= \frac{\mu_{ij}}{d_{ij}} (\eta_y u_{ij} + \eta_x v_{ij} + \theta_z w_{ij}) \end{aligned} \quad (4.27)$$

To recover the viscous Jacobian with respect to the conserved quantities, the transformation matrix  $\frac{\partial V}{\partial U}$  must be applied to Eqn. (4.25) such that,

$$\frac{\partial F_{ij}^{TSL}}{\partial U_{j/i}} = \frac{\partial F_{ij}^{TSL}}{\partial V_{j/i}} \frac{\partial V_{j/i}}{\partial U_{j/i}} \quad (4.28)$$

The transformation matrix,  $\frac{\partial V}{\partial U}$ , is provided in Appendix B.

### 4.3 Flow Boundary Conditions

A set of boundary conditions are necessary to solve the governing equations of Chapter 2 at each time step. These conditions must enforce the observed physical behavior without over- or under-specifying the state vector at the wall to create a mathematically well-posed problem.

For node-centric, FVM solvers, the solution is stored directly on the computational boundary. This allows boundary conditions to be enforced either weakly or strongly. In weak enforcement, the governing equations are written on the boundary and a flux is computed such that when the solution

achieves convergence, the boundary condition is satisfied. In strong enforcement, Dirichlet conditions are set for one or more scalar variables on the boundary and any contribution to the solution residual or Jacobian from flux calculations is eliminated to preserve the specified boundary condition during the solution update at the end of the current time step. The number of boundary conditions required for a well-posed problem is the subject of the mathematical theory of hyperbolic-elliptic PDE systems, and many excellent resources are available for supplemental reading [46, 52, 35]. The required boundary conditions and their numerical implementation for the current work are described in this section.

### 4.3.1 No-Slip Wall

A no-slip boundary condition is used to simulate the presence of physical walls in viscous flows. For continuum fluids, no relative velocity between the wall and the fluid is allowed on the boundary,

$$\vec{u}|_{\Gamma} = \vec{0}. \quad (4.29)$$

The no-slip condition is strongly enforced on the boundary by setting the momentum terms of the solution state,  $U_i$ , to zero and by setting the corresponding Jacobian elements to unity. This procedure forces the flow velocity to be zero on the boundary and does not change the state of the momentum equations at  $i$  for the next time-step.

Under the no-slip condition, the governing equations are locally elliptic near the wall and require specification of the thermal and chemical state at the boundary. For the energy equations, adiabatic or isothermal boundaries may be selected. Adiabatic boundaries prevent heat transfer to or from the domain through the boundary, and under these conditions,

$$\begin{aligned} \nabla T \cdot \vec{n} &= 0, & \text{on } \Gamma_{\text{adiabatic}}. \\ \nabla T^{ve} \cdot \vec{n} &= 0, \end{aligned} \quad (4.30)$$

A boundary of this type may be used when an object is in a state of thermal equilibrium with the surrounding flow environment. However, most entry vehicles never achieve thermal equilibrium with the flow environment since the aerodynamic heating is intense, but short in duration. For these cases, it is more appropriate to use a cold-wall, isothermal condition where

$$\begin{aligned} T &= T_{\text{wall}} & \text{on } \Gamma_{\text{isothermal}}, \\ T^{ve} &= T_{\text{wall}}^{ve} \end{aligned} \quad (4.31)$$

The species continuity equations require specification of the chemical system on the boundary. For hypersonic systems in chemically reactive flow environments, the vehicle surface can act as a catalyst, promoting chemical recombination. These recombination reactions are exothermal and can contribute significantly to the overall energy transfer to the vehicle. In this work, catalytic boundary

conditions are enforced by specifying the species mass-fractions,  $Y_s$ , on the boundary,

$$Y_s = Y_{s,wall} \quad \text{on } \Gamma_{catalytic} \text{ for } s = 1, \dots, N. \quad (4.32)$$

By setting wall mass fractions to the free-stream composition,  $Y_{s,wall} = Y_{s,\infty}$ , a ‘super-catalytic’ wall is simulated. Under these conditions, all free radicals in the boundary layer recombine at the surface, constituting the highest possible thermal transfer from chemical reactions to the TPS. This is often performed to acquire a conservative estimate vehicle heat transfer for TPS design. Conversely, a non-catalytic wall may be prescribed by enforcing,

$$\nabla Y_s \cdot \vec{n} = 0 \quad \text{on } \Gamma_{non-catalytic}, \text{ for } s = 1, \dots, n_s. \quad (4.33)$$

Under non-catalytic conditions, no surface chemical reactions take place. This corresponds to a lower-bound of expected heating from the flow environment.

The thermal and chemical boundary conditions are enforced weakly. The numerical fluxes out of the computational domain at the domain control volume are determined by writing the flux vectors on the no-slip wall,

$$\left( \hat{F}_i^c - \hat{F}_i^v \right) \Gamma_i = \left( \begin{bmatrix} \cdot \\ \cdot \\ \cdot \\ \cdot \end{bmatrix} - \begin{bmatrix} \vec{J}_s \\ \cdot \\ q^{\vec{r}} + q^{\vec{v}e} \sum_s \vec{J}_s h_s \\ q^{\vec{v}e} + \sum_s \vec{J}_s e_s^{ve} \end{bmatrix} \right) \cdot \vec{n}_i \Gamma_i. \quad (4.34)$$

Momentum terms in the numerical fluxes are omitted due to the strong enforcement of the no-slip wall. The thermal and mass fluxes from  $\vec{q}^k \cdot \vec{n}_i$  and  $\vec{J}_s \cdot \vec{n}_i$  are evaluated after applying the corresponding thermal and chemical boundary conditions. For isothermal and catalytic boundaries, the gradients at the wall are recalculated after the application of the Dirichlet condition on  $T$ ,  $T^{ve}$ , and  $Y_s$ . For adiabatic and non-catalytic boundaries, the corresponding  $\vec{q}^k \cdot \vec{n}_i$  and  $\vec{J}_s \cdot \vec{n}_i$  are zero by definition.

### 4.3.2 Flow Tangency

A flow tangency boundary condition requires the local velocity field to align with the boundary and is used to represent physical objects in inviscid flow environments, or to represent planes of symmetry in the domain. Explicitly, the boundary condition is stated as,

$$\vec{u} \cdot \vec{n} = 0, \quad (4.35)$$

$$\nabla(\cdot) \cdot \vec{n} = 0. \quad (4.36)$$

Under these conditions, the convective and viscous fluxes on the boundary are,

$$\left( \hat{F}_i^c - \hat{F}_i^v \right) \Gamma_i = \left( \begin{bmatrix} \cdot \\ p_i \bar{\mathbf{I}} \cdot \vec{n}_i \\ \cdot \\ \cdot \end{bmatrix} - \begin{bmatrix} \cdot \\ \cdot \\ \cdot \\ \cdot \end{bmatrix} \right) \Gamma_i. \quad (4.37)$$

The flow tangency boundary condition is weakly enforced by imposing the numerical flux,

$$\hat{F}_i^c = \begin{bmatrix} \cdot \\ p_i \bar{\mathbf{I}} \cdot \vec{n}_i \\ \cdot \\ \cdot \end{bmatrix} \Gamma_i, \quad (4.38)$$

from the flow domain to the boundary at each boundary node for each time step.

### 4.3.3 Characteristic-Based Far Field

A far field, characteristic-based boundary condition is typically imposed on the outer boundaries to represent the connectivity of the simulation domain to the distant, ‘infinite’ atmospheric conditions. This far field boundary condition is imposed by performing an upwind flux computation between the boundary node,  $i$ , and the specified free-stream conditions,  $\infty$ . This upwind flux computation appropriately propagates information from the boundary to the  $\infty$  state and vice-versa in accordance with the sign of the eigenvalues of the convective flux Jacobian discussed in Section 4.2.1. The flux computation is performed directly using the Modified Steger-Warming scheme,

$$(\hat{F}_i^c - \hat{F}_i^v) \Gamma_i = (\hat{F}_{i\infty}^{MSW}) \Gamma_i. \quad (4.39)$$

It is assumed that the domain boundaries are sufficiently far from the body that flow field gradients are small. Under these conditions, the viscous flux is omitted. In most hypersonic simulations, inflow and outflow boundary Mach numbers are greater than unity. For these cases, the inward and outward fluxes are specified entirely by the upstream state.

## 4.4 Discretization of the Adjoint Equations

The adjoint method provides a mechanism to efficiently calculate objective function gradients in high dimensional spaces, using high-fidelity analysis tools. This gradient information is acquired by evaluating the adjoint surface sensitivities, projected onto the surface deformation incurred from the manipulation of the design variables. The adjoint linear system, given by Eqn. (3.39) and repeated here as

$$\nabla \Psi^\tau \cdot \left( \vec{A}^c - \vec{F}^{vk} \frac{\partial \mu^k}{\partial U} - \mu^k \vec{A}^{vk} \right) + \nabla \cdot \left( \nabla \Psi^\tau \cdot \mu^k \bar{D}^{vk} \right) + \Psi^\tau \frac{\partial Q}{\partial U} = 0,$$

must be solved within the flow domain to resolve the adjoint surface sensitivities. It is important to remember that the adjoint and flow variables are independent of one another, and that the flow state within the domain is held fixed for the adjoint problem. Therefore, the adjoint equations are a set of coupled, *linear*, PDEs. Because the system is linear, it is possible to perform a direct matrix inversion to acquire the solution to the adjoint problem, but often this approach is too computationally expensive for most mesh sizes of practical interest [102]. Alternatively, the matrix system may be solved iteratively using the FVM in an analogous fashion to the direct problem. This iterative approach is used in this work.

To facilitate the comparison to the direct problem, the adjoint equations are reorganized into convective, viscous and source terms. A time-derivative is also added such that the method of lines may be applied to the adjoint problem in the same fashion as for the flow governing equations. Lastly, the adjoint equations are integrated over a local control volume,  $\Omega_i$ , in accordance with the FVM. The result is,

$$\begin{aligned} & \int_{\Omega_i} \frac{\partial \Psi}{\partial t} d\Omega_i + \int_{\Omega_i} \nabla \Psi^\top \cdot \vec{A}^c d\Omega_i + \int_{\Omega_i} \nabla \cdot (\nabla \Psi^\top \cdot \mu^k \bar{D}^{vk}) d\Omega_i \\ & + \int_{\Omega_i} \left( -\nabla \Psi^\top \cdot \vec{F}^{vk} \frac{\partial \mu^k}{\partial U} - \nabla \Psi^\top \cdot \mu^k \vec{A}^{vk} + \Psi^\top \frac{\partial Q}{\partial U} \right) d\Omega_i = 0. \end{aligned} \quad (4.40)$$

To solve Eqn. (4.40), numerical flux functions are applied to the convective, viscous, and source terms (to be discussed in greater detail in Section 4.5), and the adjoint state is marched forward in time to convergence.

The adjoint equations, as written in Eqn. (4.40), are a nonconservative PDE system. It is possible to refactor the adjoint system into conservation-law form by using the product rule and treating the additional terms as sources in the scheme. Instead, the nonconservative form is discretized directly by moving the constant Jacobian matrix,  $\vec{A}^c$ , outside the volume integral and applying the Divergence law to the convective and viscous terms,

$$\begin{aligned} & \int_{\Omega_i} \frac{\partial \Psi}{\partial t} d\Omega_i + \int_{\partial \Omega_i} \Psi^\top \vec{n} ds \cdot \vec{A}^c + \int_{\partial \Omega_i} \nabla \Psi^\top \cdot \mu^k \bar{D}^{vk} \cdot \vec{n} ds \\ & + \int_{\Omega_i} \left( -\nabla \Psi^\top \cdot \vec{F}^{vk} \frac{\partial \mu^k}{\partial U} - \nabla \Psi^\top \cdot \mu^k \vec{A}^{vk} + \Psi^\top \frac{\partial Q}{\partial U} \right) d\Omega_i = 0. \end{aligned} \quad (4.41)$$

If the source terms are treated as piecewise constant within a control volume,  $\Omega_i$ , and a set of convective and viscous adjoint numerical flux functions are defined, Eqn. (4.41) may be expressed in semi-discrete form as

$$\int_{\Omega_i} \frac{\partial \Psi}{\partial t} d\Omega_i + \sum_{j \in \mathcal{N}_i} \left( \hat{\Phi}_{ij}^c + \hat{\Phi}_{ij}^v \right) \Gamma_{ij} + |\Omega_i| \left( -\nabla \Psi_i^\top \cdot \vec{F}_i^{vk} \frac{\partial \mu_i^k}{\partial U_i} - \nabla \Psi_i^\top \cdot \mu_i^k \vec{A}_i^{vk} + \Psi_i^\top \frac{\partial Q_i}{\partial U_i} \right) = 0, \quad (4.42)$$

where the adjoint numerical fluxes are defined as,

$$\hat{\Phi}_{ij}^c \approx \vec{\Phi}^c \cdot \vec{n} = \Psi^\top (\vec{A}^c \cdot \vec{n}) \quad (4.43a)$$

$$\hat{\Phi}_{ij}^v \approx \vec{\Phi}^v \cdot \vec{n} = \nabla \Psi^\top \cdot \mu^k \bar{\bar{D}}^{vk} \cdot \vec{n}. \quad (4.43b)$$

Because the adjoint system is nonconservative,  $\hat{\Phi}_{ij}^k \neq \hat{\Phi}_{ji}^k$ , for  $k = c, v$ . As with the direct problem, Eqn. (4.41) is a first-order ordinary differential equation in time after the numerical flux functions have been applied.

With this procedure, the adjoint equations may be solved using the same algorithmic framework as the flow problem. The adjoint state is stored at the nodes of the computational mesh, and a pass over the edge-based data structure is performed to evaluate the adjoint fluxes. After the flux computation, another pass over all computational nodes is performed to compute the source terms. An initial condition of  $\Psi = 0$  is used to initialize the adjoint system, and the solution is integrated forward in time until a desired level of convergence is achieved.

## 4.5 Adjoint Spatial Integration

To solve the adjoint linear system using the FVM, the convective, viscous, and source terms must be integrated over each control volume within the computational domain. Numerically, this is achieved by prescribing numerical flux functions to approximate the adjoint fluxes, and computing the integral over the control volume by summing the contribution from each face in a similar manner to the direct problem. Naturally, the accuracy of the adjoint surface sensitivities are dependent on the properties of the numerical scheme employed. This section discusses the convective and viscous spatial integration schemes used for the adjoint problem.

### 4.5.1 Adjoint Convective Fluxes

The semi-discrete form of the adjoint equations, shown in Eqn. (4.42), organizes the terms of the adjoint linear system in accordance with their inherited physical significance from the flow governing equations. In the Euler equations, conserved flow quantities are convected through the domain as prescribed by the local convective flux Jacobian  $\vec{A}^c$ . The adjoint convective flux,  $\vec{\Phi}^c$ ,

$$\vec{\Phi}^c \cdot \vec{n} = \Psi^\top (\vec{A}^c \cdot \vec{n}),$$

behaves in the same fashion, transporting information through the domain along characteristics of  $\vec{A}^c$ , though in the opposite direction of the direct problem due to the negative sign introduced by the formulation of the Lagrangian. Nevertheless, an extensive body of literature has been published on numerical methods for the Euler equations, and much of the theoretical framework established may be brought to bear on the discretization of the adjoint convective fluxes.

The adjoint convective flux may be written analytically by introducing the definition of the

projected convective flux Jacobian, given by Eqn. (B.11),

$$\vec{\Phi}_{ij}^c \cdot \vec{n} = \begin{bmatrix} \left( \psi_{\rho_s} - \sum_k Y_k \psi_{\rho_k} + (\vec{\phi} \cdot \vec{u}) + \psi_{\rho e} \left( \frac{\partial p}{\partial \rho_s} - h \right) - \psi_{\rho e^{ve}} \frac{\rho e^{ve}}{\rho} \right) (\vec{u} \cdot \vec{n}) + (\vec{\phi} \cdot \vec{n}) \frac{\partial p}{\partial \rho_s} \\ \left( \sum_k Y_k \psi_{\rho_k} + (\vec{\phi} \cdot \vec{u}) + \psi_{\rho e} h \right) n_x + \left( \phi_x + \psi_{\rho e} \frac{\partial p}{\partial \rho u} + \psi_{\rho e^{ve}} \frac{\rho e^{ve}}{\rho} \right) (\vec{u} \cdot \vec{n}) + (\vec{\phi} \cdot \vec{n}) \frac{\partial p}{\partial \rho u} \\ \left( \sum_k Y_k \psi_{\rho_k} + (\vec{\phi} \cdot \vec{u}) + \psi_{\rho e} h \right) n_y + \left( \phi_y + \psi_{\rho e} \frac{\partial p}{\partial \rho v} + \psi_{\rho e^{ve}} \frac{\rho e^{ve}}{\rho} \right) (\vec{u} \cdot \vec{n}) + (\vec{\phi} \cdot \vec{n}) \frac{\partial p}{\partial \rho v} \\ \left( \sum_k Y_k \psi_{\rho_k} + (\vec{\phi} \cdot \vec{u}) + \psi_{\rho e} h \right) n_z + \left( \phi_z + \psi_{\rho e} \frac{\partial p}{\partial \rho w} + \psi_{\rho e^{ve}} \frac{\rho e^{ve}}{\rho} \right) (\vec{u} \cdot \vec{n}) + (\vec{\phi} \cdot \vec{n}) \frac{\partial p}{\partial \rho w} \\ \frac{\partial p}{\partial \rho e} (\vec{\phi} \cdot \vec{n}) + \psi_{\rho e} \left( 1 + \frac{\partial p}{\partial \rho e} \right) (\vec{u} \cdot \vec{n}) \\ \frac{\partial p}{\partial \rho e^{ve}} (\vec{\phi} \cdot \vec{n}) + \left( \psi_{\rho e} \frac{\partial p}{\partial \rho e^{ve}} + \psi_{\rho e^{ve}} \right) (\vec{u} \cdot \vec{n}) \end{bmatrix}. \quad (4.44)$$

A centered and an upwind spatial discretization scheme are available to numerically resolve the adjoint fluxes across dual grid cell faces.

### Upwind-biased Scheme

An upwind-biased spatial discretization scheme is used to integrate the adjoint convective fluxes. The numerical fluxes are computed by propagating the interface adjoint state using the local convective flux Jacobian, where the interface state is the average of the adjoint state vectors at  $i$  and  $j$ . Scalar diffusion, based on the local spectral radius,  $\lambda_i$ , is applied for numerical stability to prevent odd-even decoupling of the solution within the domain. This scheme is known as the Rusanov [121], or the local Lax-Friedrich method, and may be written as,

$$\hat{\Phi}_{ij}^c = \hat{\Phi}_{ij}^{LF} = \frac{(\Psi_i^\top + \Psi_j^\top)}{2} \left( \vec{A}_i^c \cdot \vec{n} \right) - \epsilon_0 s_0 \lambda_{ij} (\Psi_j - \Psi_i). \quad (4.45)$$

The dissipation coefficient is computed using three parameters: the mean spectral radius,  $\lambda_{ij}$ , the stretching factor,  $s_0$ , and a user-specified parameter,  $\epsilon_0$ . The spectral radius is the maximum eigenvalue of the convective flux Jacobian, which may be taken directly from Eqn. (B.37). Explicitly, the local spectral radius is

$$\lambda_i = |(\vec{u}_i \cdot \vec{n}_i + c_i)| \quad (4.46a)$$

$$\lambda_{ij} = \frac{\lambda_i + \lambda_j}{2}. \quad (4.46b)$$

The stretching factor,  $s_0$ , is computed using the spectral radii of the adjacent control volumes, such that

$$\phi_i = \left( \frac{\lambda_i}{4\lambda_{ij} + \epsilon} \right)^{0.3}, \quad (4.47a)$$

$$s_0 = \left( \frac{4\phi_i \phi_j}{\phi_i + \phi_j + \epsilon} \right). \quad (4.47b)$$

The final term in the dissipation coefficient is given by,

$$\epsilon_0 = k_0 N_{dim} \frac{(N_i + N_j)}{N_i N_j}, \quad (4.48)$$

where  $N_i$  and  $N_j$  are the number of nodes adjacent to  $i$  and  $j$  and  $N_{dim}$  is the number of spatial dimensions to the problem. Parameter  $k_0$  is specified at runtime by the user and may be increased or decreased to adjust the amount of artificial dissipation in the numerical scheme. Typical values span the range,  $k_0 \in [0.05, 0.2]$ , and a value of 0.15 is the default in this work unless otherwise specified.

### Upwind Scheme

An upwind, flux vector splitting method, based on the Steger-Warming method [132] is also available for computing the adjoint convective fluxes. As in the direct problem, the flux from  $i$  to  $j$  consists of quantities convected across the interface, as determined by the sign of the eigenvalues of the projected convective flux Jacobian. Explicitly,

$$\hat{\Phi}_{ij}^c = \hat{\Phi}_{ij}^{SW} = \frac{(\Psi_i^\top + \Psi_j^\top)}{2} \left( \vec{A}_i^c \cdot \vec{n} \right) - \frac{1}{2} P_i |\Lambda_i| P_i^{-1} (\Psi_j - \Psi_i), \quad (4.49)$$

where the eigenvalue-eigenvector decomposition of the convective flux Jacobian is discussed in Section 4.2.1 and the left and right eigenvector matrices,  $P$  and  $P^{-1}$  respectively, are presented in Appendix B. Note, to compute the flux from node  $i$  to node  $j$ , the flow state vector,  $U$ , at  $i$  is used to calculate the projected convective Jacobian, and the eigenvalue-eigenvector decomposition. For the flux from  $j$  to  $i$ , these matrices are computed using  $U$  from node  $j$ .

#### 4.5.2 Adjoint Viscous Fluxes

Dissipative terms in the adjoint equations are grouped into the adjoint viscous flux vector,  $\vec{\Phi}_{ij}^v$ . The numerical flux from node  $i$  to node  $j$ ,  $\hat{\Phi}_{ij}^v$ , is computed using the mean gradient of the adjoint variables,  $\nabla \Psi_{ij} = (1/2)(\nabla \Psi_i + \nabla \Psi_j)$ , and the local flow state,  $U_i$ , such that

$$\hat{\Phi}_{ij}^v = \sum_k \hat{\Phi}_{ij}^{vk} = \sum_k \nabla \Psi_{ij}^\top \cdot (\mu^k \bar{D}^{vk} \cdot \vec{n})_i, \quad (4.50)$$

where  $k$  corresponds to the separated viscous flux vectors, defined by Eqn. (3.28). By inserting the definition of  $\bar{D}^{vk}$  into Eqn. (4.50) and simplifying in a similar manner as the adjoint boundary integrals of Section 3.5.3, the  $\Phi^{vk}$  are

$$\begin{aligned}
\hat{\Phi}_{ij}^{v1} &= \begin{bmatrix} \sum_s \nu_{ij}^s \left( \rho D_s \frac{\partial Y_s}{\partial \rho_1} - Y_s \sum_k \rho D_k \frac{\partial Y_k}{\partial \rho_1} \right)_i \\ \vdots \\ \sum_s \nu_{ij}^s \left( \rho D_s \frac{\partial Y_s}{\partial \rho_N} - Y_s \sum_k \rho D_k \frac{\partial Y_k}{\partial \rho_N} \right)_i \\ \vec{0} \\ 0 \\ 0 \end{bmatrix} \quad \hat{\Phi}_{ij}^{v2} = \begin{pmatrix} \mu \\ \rho \end{pmatrix}_i \begin{bmatrix} -\vec{u}_i^\top \left( \bar{\Sigma}_{ij}^\phi + \bar{\Sigma}_i^{\psi_{\rho e}} \right) \cdot \vec{n}_{ij} \\ \vdots \\ -\vec{u}_i^\top \left( \bar{\Sigma}_{ij}^\phi + \bar{\Sigma}_i^{\psi_{\rho e}} \right) \cdot \vec{n}_{ij} \\ (\bar{\Sigma}_{ij}^\phi + \bar{\Sigma}_i^{\psi_{\rho e}}) \cdot \vec{n}_{ij} \\ 0 \\ 0 \end{bmatrix} \\
\hat{\Phi}_{ij}^{v3} &= \kappa_i^{tr} \begin{bmatrix} \left( \frac{\partial T}{\partial \rho_1} \right)_i (\nabla \psi_{\rho e} \cdot \vec{n})_{ij} \\ \vdots \\ \left( \frac{\partial T}{\partial \rho_N} \right)_i (\nabla \psi_{\rho e} \cdot \vec{n})_{ij} \\ \left( \frac{\partial T}{\partial \rho \vec{u}} \right)_i (\nabla \psi_{\rho e} \cdot \vec{n})_{ij} \\ \left( \frac{\partial T}{\partial \rho e} \right)_i (\nabla \psi_{\rho e} \cdot \vec{n})_{ij} \\ \left( \frac{\partial T}{\partial \rho e^{ve}} \right)_i (\nabla \psi_{\rho e} \cdot \vec{n})_{ij} \end{bmatrix} \quad \hat{\Phi}_{ij}^{v4} = \kappa_i^{ve} \begin{bmatrix} \left( \frac{\partial T^{ve}}{\partial \rho_1} \right)_i [(\nabla \psi_{\rho e} + \nabla \psi_{\rho e^{ve}}) \cdot \vec{n}]_{ij} \\ \vdots \\ \left( \frac{\partial T^{ve}}{\partial \rho_N} \right)_i [(\nabla \psi_{\rho e} + \nabla \psi_{\rho e^{ve}}) \cdot \vec{n}]_{ij} \\ \left( \frac{\partial T^{ve}}{\partial \rho \vec{u}} \right)_i [(\nabla \psi_{\rho e} + \nabla \psi_{\rho e^{ve}}) \cdot \vec{n}]_{ij} \\ \left( \frac{\partial T^{ve}}{\partial \rho e} \right)_i [(\nabla \psi_{\rho e} + \nabla \psi_{\rho e^{ve}}) \cdot \vec{n}]_{ij} \\ \left( \frac{\partial T^{ve}}{\partial \rho e^{ve}} \right)_i [(\nabla \psi_{\rho e} + \nabla \psi_{\rho e^{ve}}) \cdot \vec{n}]_{ij} \end{bmatrix}, 
\end{aligned} \tag{4.51}$$

where the parameter  $\nu_{ij}^s$  has been defined as

$$\nu_{ij}^s = (\nabla \psi_{\rho_s} \cdot \vec{n})_{ij} + (\nabla \psi_{\rho e} \cdot \vec{n})_{ij} (h_s^{int})_i + (\nabla \psi_{\rho e^{ve}} \cdot \vec{n})_{ij} (e_s^{ve})_i, \tag{4.52}$$

and the  $k = 2$  matrices,  $\bar{\Sigma}^\phi$  and  $\bar{\Sigma}^{\psi_{\rho e}}$ , follow the definitions of Eqns. (3.53a) and (3.53b). Wherever the subscript  $ij$  is applied, the quantity should be computed using the mean adjoint or flow state. Note that  $\bar{\Sigma}^{\psi_{\rho e}}$ , depends on the local flow velocity,  $\vec{u}$ , hence the subscript  $i$  instead of  $ij$ . Since the adjoint equations are nonconservative, it is necessary to compute the viscous adjoint flux from  $j$  to  $i$  separately and apply it to the residual appropriately. To do so, simply reverse the direction of the normal and treat node  $j$  as node  $i$ , repeating the computation.

Adjoint state gradients are calculated at the primal grid nodes using either the Green-Gauss or Weighted Least-Squares Method described in Section 4.8. The gradients for the adjoint problem are prone to the same numerical errors as in the direct flow problem in regions with steep gradients and highly skewed, or high aspect-ratio cells. The corrected gradient method discussed in Section 4.2.2 is applied to  $\nabla \Psi$  appropriately in the viscous flux computations.

### 4.5.3 Adjoint Viscous Jacobians Using the TSL Method

An implicit time-marching scheme for the adjoint problem requires Jacobians of the adjoint viscous fluxes. As in the direct problem, the analytic form of these Jacobians contains second derivative terms in the adjoint variables that are difficult and expensive to acquire on general, unstructured mesh topologies, since such a computation requires neighbor-of-neighbor information. The problem is addressed in the same manner as before, using the TSL approximation, given by Eqn. (4.22), for

the gradient of the adjoint variables.

Consider the  $k = 1$  viscous adjoint flux from node  $i$  to node  $j$ , given in Eqn. (4.51), after the application of the TSL approximation,

$$\hat{\Phi}_{ij}^{v1,TSL} \Big|_r = \sum_s \left[ \frac{(\psi_{\rho_s,j} - \psi_{\rho_s,i})\theta}{d_{ij}} + \frac{(\psi_{\rho_e,j} - \psi_{\rho_e,i})\theta h_{s,i}^{int}}{d_{ij}} + \frac{(\psi_{\rho_e^{ve},j} - \psi_{\rho_e^{ve},i})\theta e_{s,i}^{ve}}{d_{ij}} \right] \xi_i^{s,r}, \quad (4.53)$$

where

$$\xi_{j/i}^{s,r} = \left( \rho D_s \frac{\partial Y_s}{\partial \rho_r} - Y_s \sum_k \rho D_k \frac{\partial Y_k}{\partial \rho_r} \right)_{j/i}. \quad (4.54)$$

In the adjoint problem,  $\xi_{j/i}$ , is constant, and the only dependence on the adjoint variables is contained in the leading coefficient. Therefore, differentiation with respect to the adjoint variables to obtain the TSL Jacobian yields

$$\frac{\partial \hat{\Phi}_{ij}^{v1}}{\partial \Psi_{j/i}} = \pm \frac{\theta}{d_{ij}} \begin{bmatrix} \xi_i^{s,r} & 0 & 0 & 0 & \sum_k \xi_i^{k,r} h_{k,i}^{int} & \sum_k \xi_i^{k,r} e_{k,i}^{ve} \\ 0 & 0 & 0 & 0 & 0 & 0 \\ 0 & 0 & 0 & 0 & 0 & 0 \\ 0 & 0 & 0 & 0 & 0 & 0 \\ 0 & 0 & 0 & 0 & 0 & 0 \\ 0 & 0 & 0 & 0 & 0 & 0 \end{bmatrix}, \quad (4.55)$$

where  $r$  is the row index, and  $s$  is the column index. Note that differentiation of the  $ij$  flux with respect to the adjoint state at  $i$  and  $j$  only changes the sign of the TSL Jacobian. For the  $ji$  flux, the  $\xi_i^{s,r}$  are replaced with  $\xi_j^{s,r}$ . For the  $k = 2$  adjoint viscous flux Jacobian, the TSL approximation must be applied to the component matrices,  $\bar{\Sigma}^\phi$  and  $\bar{\Sigma}^{\psi_{\rho_e}}$ . Since the form of  $\bar{\Sigma}^\phi$  is identical to  $\bar{\tau}$ , the TSL approximation from Section 4.2.3 is valid. Borrowing the definitions of  $\theta_k$  and  $\eta_k$  from Eqn. (4.27) and redefining  $\pi_k$  in the nonconservative framework as,

$$\pi_{x,(j/i)} = \theta_x u_{j/i} + \eta_z v_{j/i} + \eta_y w_{j/i} \quad (4.56)$$

$$\pi_{y,(j/i)} = \eta_z u_{j/i} + \theta_y v_{j/i} + \eta_x w_{j/i} \quad (4.57)$$

$$\pi_{z,(j/i)} = \eta_y u_{j/i} + \eta_x v_{j/i} + \theta_z w_{j/i} \quad (4.58)$$

the  $k = 2$  adjoint viscous flux Jacobian may be written as,

$$\frac{\partial \hat{\Phi}_{ij}^{v2}}{\partial \Psi_{j/i}} = \pm \frac{\mu_i}{\rho_i d_{ij}} \begin{bmatrix} 0 & \pi_{x,i} & \pi_{y,i} & \pi_{z,i} & (\pi_{x,i} u_i + \pi_{y,i} v_i + \pi_{z,i} w_i) & 0 \\ 0 & \theta_x & \eta_z & \eta_y & \pi_{x,i} & 0 \\ 0 & \eta_z & \theta_y & \eta_x & \pi_{y,i} & 0 \\ 0 & \eta_y & \eta_x & \theta_z & \pi_{z,i} & 0 \\ 0 & 0 & 0 & 0 & 0 & 0 \\ 0 & 0 & 0 & 0 & 0 & 0 \end{bmatrix}. \quad (4.59)$$

Similarly, the definitions of the Jacobians for  $k = 3$  and  $k = 4$  are

$$\frac{\partial \hat{\Phi}_{ij}^{v3}}{\partial \Psi_{j/i}} = \pm \frac{\kappa_i^{tr}\theta}{d_{ij}} \begin{bmatrix} 0 & 0 & 0 & 0 & 0 & 0 \\ 0 & 0 & 0 & 0 & 0 & 0 \\ 0 & 0 & 0 & 0 & 0 & 0 \\ 0 & 0 & 0 & 0 & 0 & 0 \\ \left(\frac{\partial T}{\partial \rho_r}\right)_i & \left(\frac{\partial T}{\partial \rho u}\right)_i & \left(\frac{\partial T}{\partial \rho v}\right)_i & \left(\frac{\partial T}{\partial \rho w}\right)_i & \left(\frac{\partial T}{\partial \rho e}\right)_i & \left(\frac{\partial T}{\partial \rho e^{ve}}\right)_i \\ 0 & 0 & 0 & 0 & 0 & 0 \end{bmatrix}, \quad (4.60)$$

and

$$\frac{\partial \hat{\Phi}_{ij}^{v4}}{\partial \Psi_{j/i}} = \pm \frac{\kappa_i^{ve}\theta}{d_{ij}} \begin{bmatrix} 0 & 0 & 0 & 0 & 0 & 0 \\ 0 & 0 & 0 & 0 & 0 & 0 \\ 0 & 0 & 0 & 0 & 0 & 0 \\ 0 & 0 & 0 & 0 & 0 & 0 \\ \left(\frac{\partial T^{ve}}{\partial \rho_r}\right)_i & \left(\frac{\partial T^{ve}}{\partial \rho u}\right)_i & \left(\frac{\partial T^{ve}}{\partial \rho v}\right)_i & \left(\frac{\partial T^{ve}}{\partial \rho w}\right)_i & \left(\frac{\partial T^{ve}}{\partial \rho e}\right)_i & \left(\frac{\partial T^{ve}}{\partial \rho e^{ve}}\right)_i \\ \left(\frac{\partial T^{ve}}{\partial \rho_r}\right)_i & \left(\frac{\partial T^{ve}}{\partial \rho u}\right)_i & \left(\frac{\partial T^{ve}}{\partial \rho v}\right)_i & \left(\frac{\partial T^{ve}}{\partial \rho w}\right)_i & \left(\frac{\partial T^{ve}}{\partial \rho e}\right)_i & \left(\frac{\partial T^{ve}}{\partial \rho e^{ve}}\right)_i \end{bmatrix}. \quad (4.61)$$

As in the direct problem, the TSL approximation is a linearization of the gradient information along the control volume face-normal directions. Because the method ignores face-tangential gradient information, the approximation suffers the same limitations in accuracy when the mesh topology is not aligned with the strongest gradients in the domain. However, the TSL approximation has been shown to be accurate for a wide variety of viscous flow problems and it is reasonable to assume that its performance translates to the adjoint problem, since the dominant features of the adjoint problem are based on local flow states.

## 4.6 Adjoint Boundary Conditions

The nonconservative, linear, PDE system of equations governing the adjoint problem are solved using the same framework as the direct problem. The discretized equations are generated from the continuous equations by first applying numerical flux functions to the spatial integration to create a first-order ODE in time, which is marched forward to convergence using a temporal integration scheme. The IBVP requires the application of well-posed boundary conditions at each time step for the solver to converge to the correct solution. Analytically, the boundary conditions for the adjoint problem were derived in Sections 3.7.1 and 3.7.2, corresponding to the force and thermal objective functions, under different thermal and chemical states at the wall.

A symmetry exists between the direct and adjoint problems in regards to the required boundary conditions. For example, a no-slip wall boundary condition prescribes a Dirichlet for both the flow and adjoint velocities. This symmetry holds for the energy and mass variables and is dictated by the nature of the chemical and thermal conditions at the wall. Generally speaking, Dirichlet conditions

are strongly enforced in both problems by setting the appropriate wall values and replacing the appropriate entries in the Jacobian with unity to prevent any change to the variable during the update of the solution state at the subsequent time step. Conversely, Neumann boundary conditions are generally enforced weakly by writing the adjoint fluxes at the wall subject to the imposed boundary conditions, such that the boundary condition is satisfied at convergence. The following sections discuss the application of these boundary conditions in additional detail, as needed.

#### 4.6.1 Boundary Condition Enforcement: Projected Force Functional No-slip, Adiabatic, Non-catalytic Walls

The adjoint boundary conditions for no-slip, adiabatic, non-catalytic walls are analytically derived in Section 3.7.1. These boundary conditions,

$$\begin{aligned}\nabla \psi_{\rho_s} \cdot \vec{n} &= 0 \\ \vec{\phi} &= \vec{d} \\ \nabla \psi_{\rho_e} \cdot \vec{n} &= 0 \\ \nabla \psi_{\rho^{eve}} \cdot \vec{n} &= 0,\end{aligned}$$

are imposed by strongly enforcing the Dirichlet conditions in the adjoint momentum equations, and weakly enforcing the boundary conditions on the remaining variables. This is achieved by setting the adjoint momentum variables,  $\vec{\phi} = \vec{d}$ , on  $S$  and setting the momentum entries at  $i$  in the sparse Jacobian of Eqn. (4.86) to unity, zeroing all other entries to the row, to prevent updates to these variables at the next time step. For the remaining adjoint variables, the adjoint convective and viscous fluxes are written on  $S$ , replacing the appropriate terms in the fluxes with the boundary condition values such that

$$\hat{\Phi}_{\Gamma_i}^c \cdot \vec{n} = \left[ \begin{array}{c} \frac{\partial p}{\partial \rho_s} (\vec{\phi} \cdot \vec{n}) \\ \vec{0} \\ \frac{\partial p}{\partial \rho_e} (\vec{\phi} \cdot \vec{n}) \\ \frac{\partial p}{\partial \rho^{eve}} (\vec{\phi} \cdot \vec{n}) \end{array} \right]_i, \quad (4.62)$$

and

$$\hat{\Phi}_{\Gamma_i}^{vk} = \vec{0} \quad \text{for } k = 1, \dots, 4. \quad (4.63)$$

Nonzero entries for the momentum equations in the convective and viscous fluxes are neglected, since the boundary condition on these variables is strongly enforced.

### No-slip, Isothermal, Non-catalytic Walls

The adjoint boundary conditions for no-slip, isothermal, non-catalytic walls are derived analytically in Section 3.7.1. These boundary conditions,

$$\begin{aligned}\nabla \psi_{\rho_s} \cdot \vec{n} &= -(\nabla \psi_{\rho e} \cdot \vec{n}) h_s^{int} - (\nabla \psi_{\rho e^{ve}} \cdot \vec{n}) e_s^{ve} \\ \vec{\phi} &= \vec{d} \\ \psi_{\rho e} &= 0 \\ \psi_{\rho e^{ve}} &= 0,\end{aligned}$$

are imposed by strongly enforcing the Dirichlet conditions on the adjoint momentum and energy equations, and weakly enforcing the boundary conditions on the adjoint mass variables. This is achieved by setting the momentum variables,  $\vec{\phi} = \vec{d}$  and energy variables,  $\psi_{\rho e} = \psi_{\rho e^{ve}} = 0$ , on  $S$ , and replacing the appropriate entries of node  $i$  in the sparse Jacobian of Eqn. (4.86) with unity, zeroing all other row entries, to prevent a change in the adjoint variables on the following time step. The adjoint mass boundary conditions are enforced by computing the convective and viscous fluxes on  $S$ ,

$$\vec{\Phi}_{\Gamma_i}^c \cdot \vec{n} = \begin{bmatrix} \frac{\partial p}{\partial \rho_s} (\vec{\phi} \cdot \vec{n}) \\ \vec{0} \\ 0 \\ 0 \end{bmatrix}_i, \quad (4.64)$$

and

$$\begin{aligned}\hat{\Phi}_{\Gamma_i}^{v1} &= \vec{0} & \hat{\Phi}_{\Gamma_i}^{v2} &= \vec{0} \\ \hat{\Phi}_{\Gamma_i}^{v3} &= \kappa_i^{tr} \begin{bmatrix} \left( \frac{\partial T}{\partial \rho_s} \right) (\nabla \psi_{\rho e} \cdot \vec{n}) \\ \vec{0} \\ 0 \\ 0 \end{bmatrix}_i & \hat{\Phi}_{\Gamma_i}^{v4} &= \kappa_i^{ve} \begin{bmatrix} \left( \frac{\partial T^{ve}}{\partial \rho_s} \right) [(\nabla \psi_{\rho e} + \nabla \psi_{\rho e^{ve}}) \cdot \vec{n}] \\ \vec{0} \\ 0 \\ 0 \end{bmatrix}_i.\end{aligned} \quad (4.65)$$

As before, contributions to strongly enforced adjoint variables are omitted from the boundary fluxes.

### No-slip, Adiabatic, Catalytic Walls

The adjoint boundary conditions for no-slip, adiabatic, catalytic walls are derived analytically in Section 3.7.1. These boundary conditions,

$$\begin{aligned}\psi_{\rho_s} &= -\psi_{\rho e} h_s^{int} - \psi_{\rho e^{ve}} e_s^{ve} \\ \vec{\phi} &= \vec{d} \\ \nabla \psi_{\rho e} \cdot \vec{n} &= -\frac{\psi_{\rho e}}{\kappa^{tr}} \sum_s (\vec{J}_s \cdot \vec{n}) (C_{v,s}^{tr} + R_s) \\ \nabla \psi_{\rho e^{ve}} \cdot \vec{n} &= -\frac{\psi_{\rho e} + \psi_{\rho e^{ve}}}{\kappa^{ve}} \sum_s (\vec{J}_s \cdot \vec{n}) C_{v,s}^{ve} \\ &\quad + \frac{\psi_{\rho e}}{\kappa^{tr}} \sum_s (\vec{J}_s \cdot \vec{n}) (C_{v,s}^{tr} + R_s),\end{aligned}$$

are imposed by strongly enforcing the Dirichlet conditions on the adjoint momentum equations, and weakly enforcing the boundary conditions on the remaining adjoint variables. This is performed, as always, by setting the value of  $\vec{\phi} = \vec{d}$  on  $S$  and setting the appropriate Jacobian entries in Eqn. (4.86) to unity for node  $i$ . The remaining mass and energy boundary conditions are enforced by writing the adjoint fluxes on the surface using the adjoint boundary conditions appropriately, such that

$$\vec{\Phi}_{\Gamma_i}^c \cdot \vec{n} = \begin{bmatrix} \frac{\partial p}{\partial \rho_s} (\vec{\phi} \cdot \vec{n}) \\ \vec{0} \\ \frac{\partial p}{\partial \rho e} (\vec{\phi} \cdot \vec{n}) \\ \frac{\partial p}{\partial \rho e^{ve}} (\vec{\phi} \cdot \vec{n}) \end{bmatrix}_i, \quad (4.66)$$

and

$$\begin{aligned}\hat{\Phi}_{\Gamma_i}^{v1} &= \begin{bmatrix} \sum_r \nu^r \left( \rho D_r \frac{\partial Y_r}{\partial \rho_s} - Y_r \sum_k \rho D_k \frac{\partial Y_k}{\partial \rho_s} \right) \\ \vec{0} \\ 0 \\ 0 \end{bmatrix} \quad \hat{\Phi}_{\Gamma_i}^{v2} = \vec{0} \\ \hat{\Phi}_{\Gamma_i}^{v3} &= \kappa_i^{tr} \begin{bmatrix} \left( \frac{\partial T}{\partial \rho_s} \right) (\nabla \psi_{\rho e} \cdot \vec{n}) \\ \vec{0} \\ \left( \frac{\partial T}{\partial \rho e} \right)_i (\nabla \psi_{\rho e} \cdot \vec{n})_{ij} \\ \left( \frac{\partial T}{\partial \rho e^{ve}} \right)_i (\nabla \psi_{\rho e} \cdot \vec{n})_{ij} \end{bmatrix}_i \quad \hat{\Phi}_{\Gamma_i}^{v4} = \kappa_i^{ve} \begin{bmatrix} \left( \frac{\partial T^{ve}}{\partial \rho_s} \right) [(\nabla \psi_{\rho e} + \nabla \psi_{\rho e^{ve}}) \cdot \vec{n}] \\ \vec{0} \\ \left( \frac{\partial T^{ve}}{\partial \rho e} \right) [(\nabla \psi_{\rho e} + \nabla \psi_{\rho e^{ve}}) \cdot \vec{n}] \\ \left( \frac{\partial T^{ve}}{\partial \rho e^{ve}} \right) [(\nabla \psi_{\rho e} + \nabla \psi_{\rho e^{ve}}) \cdot \vec{n}] \end{bmatrix}_i.\end{aligned} \quad (4.67)$$

### No-slip, Isothermal, Catalytic Walls

Adjoint boundary conditions for no-slip, isothermal, catalytic walls are derived analytically in Section 3.7.1. These boundary conditions,

$$\begin{aligned}\psi_{\rho_s} &= 0 \\ \vec{\phi} &= \vec{d} \\ \psi_{\rho e} &= 0 \\ \psi_{\rho e^{ve}} &= 0,\end{aligned}$$

are imposed by strongly enforcing the Dirichlet condition on the adjoint mass, momentum, and energy variables. By explicitly setting the adjoint state vector at  $i$  and replacing all entries in the sparse Jacobian of Eqn. (4.86) corresponding to node  $i$  with the identity matrix, the adjoint state is held fixed for future time steps. Since the adjoint state is fixed, there is no need to propagate adjoint fluxes through the boundaries, therefore

$$\vec{\Phi}_{\Gamma_i}^c \cdot \vec{n} = \vec{0} \quad (4.68)$$

and

$$\hat{\Phi}_{\Gamma_i}^{vk} = \vec{0} \quad \text{for } k = 1, \dots, 4. \quad (4.69)$$

### Flow-tangency & Symmetry Boundaries

The flow-tangency adjoint boundary condition is also derived analytically in Section 3.7.1 and is

$$\vec{\phi} \cdot \vec{n} = \vec{d} \cdot \vec{n}.$$

The boundary condition is enforced weakly by computing the adjoint convective flux at the boundary, inserting the  $\vec{\phi} \cdot \vec{n}$  appropriately, such that

$$\begin{aligned}\vec{\Phi}_{\Gamma_i}^c \cdot \vec{n} &= \Psi_i^T \vec{A}_i^c \cdot \vec{n} \\ &= \left[ \begin{array}{l} \left( \psi_{\rho_s} - \sum_k Y_k \psi_{\rho_k} + (\vec{\phi} \cdot \vec{u}) + \psi_{\rho e} \left( \frac{\partial p}{\partial \rho_s} - h \right) - \psi_{\rho e^{ve}} \frac{\rho e^{ve}}{\rho} \right) (\vec{u} \cdot \vec{n}) + (\vec{\phi} \cdot \vec{n}) \frac{\partial p}{\partial \rho_s} \\ \left( \sum_k Y_k \psi_{\rho_k} + (\vec{\phi} \cdot \vec{u}) + \psi_{\rho e} h \right) n_x + \left( \phi_x + \psi_{\rho e} \frac{\partial p}{\partial \rho u} + \psi_{\rho e^{ve}} \frac{\rho e^{ve}}{\rho} \right) (\vec{u} \cdot \vec{n}) + (\vec{\phi} \cdot \vec{n}) \frac{\partial p}{\partial \rho u} \\ \left( \sum_k Y_k \psi_{\rho_k} + (\vec{\phi} \cdot \vec{u}) + \psi_{\rho e} h \right) n_y + \left( \phi_y + \psi_{\rho e} \frac{\partial p}{\partial \rho v} + \psi_{\rho e^{ve}} \frac{\rho e^{ve}}{\rho} \right) (\vec{u} \cdot \vec{n}) + (\vec{\phi} \cdot \vec{n}) \frac{\partial p}{\partial \rho v} \\ \left( \sum_k Y_k \psi_{\rho_k} + (\vec{\phi} \cdot \vec{u}) + \psi_{\rho e} h \right) n_z + \left( \phi_z + \psi_{\rho e} \frac{\partial p}{\partial \rho w} + \psi_{\rho e^{ve}} \frac{\rho e^{ve}}{\rho} \right) (\vec{u} \cdot \vec{n}) + (\vec{\phi} \cdot \vec{n}) \frac{\partial p}{\partial \rho w} \\ \frac{\partial p}{\partial \rho e} (\vec{\phi} \cdot \vec{n}) + \psi_{\rho e} \left( 1 + \frac{\partial p}{\partial \rho e} \right) (\vec{u} \cdot \vec{n}) \\ \frac{\partial p}{\partial \rho e^{ve}} (\vec{\phi} \cdot \vec{n}) + \left( \psi_{\rho e} \frac{\partial p}{\partial \rho e^{ve}} + \psi_{\rho e^{ve}} \right) (\vec{u} \cdot \vec{n}) \end{array} \right]_i.\end{aligned} \quad (4.70)$$

To enforce symmetry boundary conditions for computational domain boundaries that are not part of the design surface, it is necessary to re-examine the variation of the Lagrangian for  $\Gamma \neq S$ . For these cases, setting

$$\vec{\phi} \cdot \vec{n} = 0 \quad (4.71)$$

achieves the desired cancellation on the domain boundary. This boundary condition is enforced identically to the flow-tangency wall condition described above, by inserting the boundary condition into the definition of the adjoint convective flux and computing the flux through the boundary.

#### 4.6.2 Boundary Condition Enforcement: Thermal Functional

##### No-slip, Isothermal, Non-catalytic Walls

Adjoint boundary conditions for no-slip, isothermal, non-catalytic walls are analytically derived for the thermal objective function in Section 3.7.2. These boundary conditions,

$$\begin{aligned} \nabla \psi_{\rho_s} \cdot \vec{n} &= -(\nabla \psi_{\rho e} \cdot \vec{n}) h_s^{int} - (\nabla \psi_{\rho e^{ve}} \cdot \vec{n}) e_s^{ve} \\ \vec{\phi} &= \vec{0} \\ \psi_{\rho e} &= -\beta p(-q_n)^{p-1} \\ \psi_{\rho e^{ve}} &= 0, \end{aligned}$$

are imposed by strongly enforcing the Dirichlet conditions on the momentum and energy variables, and weakly enforcing the remaining adjoint boundary conditions. Adjoint momentum and energy values are set to the specified values, and the corresponding entries in the sparse Jacobian of Eqn. (4.86) are set to unity to prevent any change to the variables as the solver updates with the next time step. The adjoint mass variables are set by performing a flux computation on the boundary, neglecting the contributions to the momentum and energy equations. These fluxes are,

$$\hat{\Phi}_{\Gamma_i}^c \cdot \vec{n} = \begin{bmatrix} (\vec{\phi} \cdot \vec{n}) \frac{\partial p}{\partial \rho_s} \\ \vec{0} \\ 0 \\ 0 \end{bmatrix}. \quad (4.72)$$

and

$$\hat{\Phi}_{ij}^{v1} = \vec{0} \quad \hat{\Phi}_{ij}^{v2} = \vec{0}$$

$$\hat{\Phi}_{ij}^{v3} = \kappa_i^{tr} \begin{bmatrix} \left( \frac{\partial T}{\partial \rho_s} \right)_i (\nabla \psi_{\rho e} \cdot \vec{n})_{ij} \\ \vec{0} \\ 0 \\ 0 \end{bmatrix} \quad \hat{\Phi}_{ij}^{v4} = \kappa_i^{ve} \begin{bmatrix} \left( \frac{\partial T^{ve}}{\partial \rho_s} \right)_i [(\nabla \psi_{\rho e} + \nabla \psi_{\rho e^{ve}}) \cdot \vec{n}]_{ij} \\ \vec{0} \\ 0 \\ 0 \end{bmatrix}. \quad (4.73)$$

### No-slip, Isothermal, Catalytic Walls

The adjoint boundary conditions for no-slip, isothermal, catalytic walls are analytically derived in Section 3.7.2. These boundary conditions,

$$\psi_{\rho_s} = -\psi_{\rho e} h_s^{int} \quad (4.74)$$

$$\vec{\phi} = \vec{0} \quad (4.75)$$

$$\psi_{\rho e} = -\beta p(-q_n)^{p-1} \quad (4.76)$$

$$\psi_{\rho e^{ve}} = 0, \quad (4.77)$$

are imposed by strongly enforcing the Dirichlet conditions for the adjoint mass, momentum, and energy variables on  $S$ . By explicitly setting the adjoint state vector at  $i$  and replacing the appropriate entries of the sparse Jacobian in Eqn. (4.86) to unity, the adjoint state at  $i$  is held fixed as the solution advances forward in time. Since all adjoint variables are fixed on the boundary, there is no need to propagate adjoint fluxes out of the domain, therefore

$$\hat{\Phi}_{\Gamma_i}^c \cdot \vec{n} = \vec{0}, \quad (4.78)$$

and

$$\hat{\Phi}_{\Gamma_i}^{vk} = \vec{0} \quad \text{for } k = 1, \dots, 4. \quad (4.79)$$

### 4.6.3 Boundary Condition Enforcement: Far Field Boundaries

To eliminate the adjoint boundary integrals in the far field, the adjoint state vector must be zero,

$$\Psi = \vec{0}. \quad (4.80)$$

For the discrete representation of the adjoint equations, the finite computational boundary must communicate with the theoretical far field adjoint state, given by Eqn. (4.80). This communication is handled by performing an upwind computation between the discrete boundary state and the far field adjoint state, using the upwind convective scheme discussed in Section 4.5.1. Viscous fluxes are neglected on the boundary, since it is assumed the gradients of the adjoint variables are small.

## 4.7 Temporal Integration

Sections 4.1 and 4.4 contain derivations of the semi-discrete forms of the flow and adjoint equations equations, that, by the insertion of the numerical flux functions, transforms the continuous PDE systems into coupled ordinary differential equations in time. These semi-discrete equations can then be discretized temporally using a variety of well-established explicit or implicit schemes. The resulting initial value boundary problem (IVBP) is then solved by initializing the flow domain and marching forward in time.

To proceed, a complete discretization of Eqn. (4.3) is constructed by replacing the continuous time derivative with a forward difference approximation,

$$\begin{aligned} \int_{\Omega_i} \frac{\partial U}{\partial t} d\Omega_i + \mathcal{R}_i(U) &= 0, \\ \frac{|\Omega_i|}{\Delta t} (U_i^{n+1} - U_i^n) + \mathcal{R}_i(U) &= 0. \end{aligned} \quad (4.81)$$

The selection of the time integration scheme places restrictions on the allowable time-step to advance the solution. This time step restriction is based on the numerical and physical information propagation speeds within the domain and will be discussed in more detail alongside the description of the two time integration schemes implemented in this work. For this work, steady-state solutions to the flow and adjoint equations are desired, therefore it is not necessary that the time integration scheme have high-order accuracy, simply that it is efficient and stable. To accelerate convergence, a local time-stepping method is applied, where each control volume computes the allowable time step based on the local flow and adjoint state.

#### 4.7.1 Explicit Forward Euler Scheme

If the flow residuals are evaluated using the flow state at the  $n^{th}$  time step, Eqn. (4.81) may be manipulated to solve for the new solution state explicitly,

$$U_i^{n+1} = U_i^n - \frac{\Delta t}{|\Omega_i|} \mathcal{R}_i(U^n). \quad (4.82)$$

The explicit forward Euler scheme of Eqn. (4.82) is simple to execute, is easily parallelizable, and is computationally efficient. These characteristics make it attractive for large-scale numerical simulations on distributed memory computing architectures that are common in the scientific computing community. However, the stability requirements of the algorithm place restrictions on size of the time step that is allowable. Stability is loosely defined here as the notion that perturbations and oscillations in the solution do not grow unbounded within the computational domain. The CFL condition [18, 19] articulates this more specifically by requiring the ‘numerical domain of dependence’ fully encloses the ‘physical domain of dependence’. To illustrate this, consider the one-dimensional problem shown in Fig. (4.2). It is shown in Section 4.2.1 that the hyperbolic nature of the convective fluxes leads to information propagation along ‘characteristic lines’, and the fastest of these is  $\lambda_i = |u + c|$ , where  $u$  is the flow velocity and  $c$  is the local sonic speed. Therefore in a time step of size  $\Delta t$ , the fastest wave propagates a distance of  $\lambda_i \Delta t$ . If  $\lambda_i \Delta t$  is less than the width of the adjacent cell,  $\Delta x$ , then the numerical flux between  $i$  and  $j$  is resolved without difficulty using information from nodes  $i$  and  $j$ . However, if  $\lambda_i \Delta t > \Delta x$ , then the flux at the  $ij$  interface requires information from node  $k$ , which is not part of the nearest-neighbor stencil that is used to compute the numerical flux function. As a consequence, the integration is not numerically stable for the larger time step.

In calculations with thermochemical nonequilibrium, there are additional constraints placed on the allowable time step from the thermodynamic and chemical models. Vibrational relaxation and

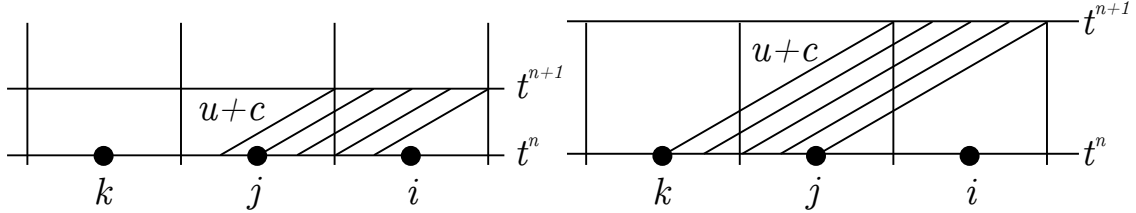


Figure 4.2: Numerical and physical domains of dependence.

finite-rate chemical processes frequently occur on smaller time scales than the convective wave propagation characteristic time[112], and to resolve these phenomena, the time step must be restricted to smaller values than those dictated by the hydrodynamics alone. Many semi-implicit techniques [151, 75, 11] have been developed in an attempt to retain the advantageous characteristics of explicit methods while mitigating the time-step restriction, but none have retained lasting popularity. These methods have been superseded by fully-implicit time integration schemes that exhibit more favorable stability characteristics as compared to the semi-implicit, or explicit methods. This issue is largely bypassed in this work as a consequence of the piecewise-constant treatment of the source terms in the FVM. Nevertheless, the time step restriction can be prohibitive in hypersonic flow environments with high convective speeds.

#### 4.7.2 Implicit Backward Euler Scheme

The explicit forward Euler method of Section 4.7.1 has advantageous qualities for large-scale scientific computing. However, the CFL condition places significant restrictions on the allowable time-step for advancing the solution within the domain based on the nearest-neighbor spatial discretization method. Two solutions are available: (1) expand the stencil for calculating fluxes to include ‘neighbor-of-neighbor’ cells, or (2) expand the numerical domain of dependence by evaluating the residuals at the  $n + 1$  time step. Generally, expanding the stencil is not efficient for arbitrary unstructured mesh topologies, which makes this first option undesirable. Instead, consider Eqn. (4.81) with the residual evaluated at the  $n + 1$  time step,

$$\frac{|\Omega_i|}{\Delta t} (U_i^{n+1} - U_i^n) + \mathcal{R}_i(U^{n+1}) = 0. \quad (4.83)$$

This backward Euler time integration scheme requires an update of the residual with the unknown solution state,  $U^{n+1}$ . By applying a Taylor series expansion, a first-order approximation of this term is acquired,

$$\begin{aligned} \mathcal{R}_i(U^{n+1}) &= \mathcal{R}_i(U^n) + \frac{\Delta t}{1!} \frac{\partial \mathcal{R}_i}{\partial t}(U^n) + \mathcal{O}(\Delta t^2), \\ \mathcal{R}_i(U^{n+1}) &= \mathcal{R}_i(U^n) + \sum_{j \in \mathcal{N}_i} \frac{\partial \mathcal{R}_i}{\partial U_j} \Delta U_j^n + \mathcal{O}(\Delta t^2). \end{aligned} \quad (4.84)$$

Above,  $\Delta U_i^n = U_i^{n+1} - U_i^n$  is defined and the chain rule of differentiation is applied to  $\partial \mathcal{R}_i / \partial t$ , such that differentiation of  $\mathcal{R}_i$  is expressed with respect to the solution state at the set of points,  $\mathcal{N}_i$ , that includes  $i$  and its neighbors. By inserting Eqn. (4.84) into Eqn. (4.83), the implicit discretization is written as

$$\frac{|\Omega_i|}{\Delta t_i} (\Delta U_i^n) + \mathcal{R}_i(U^n) + \sum_{j \in \mathcal{N}_i} \frac{\partial \mathcal{R}_i}{\partial U_j} \Delta U_j^n = 0. \quad (4.85)$$

Or alternatively,

$$\left( \bar{I} \frac{|\Omega|}{\Delta t} + \frac{\partial \mathcal{R}}{\partial U} \right) \Delta U^n = -\mathcal{R}(U^n), \quad (4.86)$$

where the global time, update, and residual vectors are defined as

$$\frac{|\Omega|}{\Delta t} = \begin{bmatrix} |\Omega_0|/\Delta t_0 \\ |\Omega_1|/\Delta t_1 \\ \vdots \\ |\Omega_{n_p}|/\Delta t_{n_p} \end{bmatrix}, \quad \Delta U^n = \begin{bmatrix} \Delta U_0^n \\ \Delta U_1^n \\ \vdots \\ \Delta U_{n_p}^n \end{bmatrix}, \quad \mathcal{R}(U^n) = \begin{bmatrix} \mathcal{R}_0(U^n) \\ \mathcal{R}_1(U^n) \\ \vdots \\ \mathcal{R}_{n_p}(U^n) \end{bmatrix}. \quad (4.87)$$

By updating the solution using the entire solution state,  $U^{n+1}$ , the numerical domain of dependence is expanded to include all points within the computational domain. The admissible time step, as dictated by the CFL condition, is much less restrictive under these conditions than the explicit scheme of Section 4.7.1 and depends on the implicit update procedure. Gradient accuracy and approximations in the numerical flux functions can also have an effect on the stability of the algorithm at large time steps. Nevertheless, fully implicit time integration schemes, like the backward Euler method described here, relax the numerical stiffness of the governing equations and exhibit good numerical stability qualities.

Implicit time-stepping leads to the formation of a large, sparse linear system consisting of the Jacobian,  $\partial \mathcal{R} / \partial U$ , the solution update vector,  $\Delta U^n$ , and the flow residual,  $\mathcal{R}$ . Entries in the Jacobian are populated based on the nodal connectivity within the grid and the spatial discretization scheme. As an example, a small computational mesh and its corresponding linear system is presented in Fig. (4.3) and Eqn. (4.88) respectively. To acquire the solution update vector, a linear solver is required to invert  $\partial \mathcal{R} / \partial U$ . This inversion is performed using the Generalized Minimum Residual Method (GMRES) [122], preconditioned using the Lower-Upper Symmetric-Gauss-Seidel (LU-SGS) [66, 152] method to improve the convergence of the linear solver.

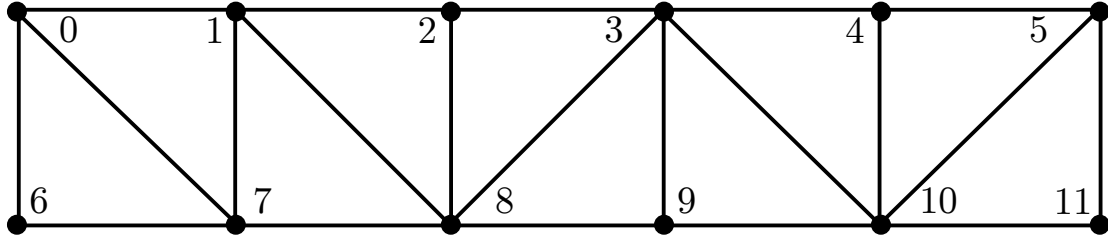


Figure 4.3: Sample computational mesh

$$\left[ \begin{array}{ccccccccc} A_0 & \frac{\partial \mathcal{R}_0}{\partial U_1} & 0 & 0 & 0 & \frac{\partial \mathcal{R}_0}{\partial U_6} & \frac{\partial \mathcal{R}_0}{\partial U_7} & 0 & 0 \\ \frac{\partial \mathcal{R}_1}{\partial U_0} & A_1 & \frac{\partial \mathcal{R}_1}{\partial U_2} & 0 & 0 & 0 & \frac{\partial \mathcal{R}_1}{\partial U_7} & \frac{\partial \mathcal{R}_1}{\partial U_8} & 0 \\ 0 & \frac{\partial \mathcal{R}_2}{\partial U_1} & A_2 & \frac{\partial \mathcal{R}_2}{\partial U_3} & 0 & 0 & 0 & \frac{\partial \mathcal{R}_2}{\partial U_8} & 0 \\ 0 & 0 & \frac{\partial \mathcal{R}_3}{\partial U_2} & A_3 & \frac{\partial \mathcal{R}_3}{\partial U_4} & 0 & 0 & \frac{\partial \mathcal{R}_3}{\partial U_8} & \frac{\partial \mathcal{R}_3}{\partial U_9} \\ 0 & 0 & 0 & \frac{\partial \mathcal{R}_4}{\partial U_3} & A_4 & \frac{\partial \mathcal{R}_4}{\partial U_5} & 0 & 0 & \frac{\partial \mathcal{R}_4}{\partial U_{10}} \\ 0 & 0 & 0 & 0 & \frac{\partial \mathcal{R}_5}{\partial U_4} & A_5 & 0 & 0 & \frac{\partial \mathcal{R}_5}{\partial U_{10}} \\ \frac{\partial \mathcal{R}_6}{\partial U_0} & 0 & 0 & 0 & 0 & A_6 & \frac{\partial \mathcal{R}_6}{\partial U_7} & 0 & 0 \\ \frac{\partial \mathcal{R}_7}{\partial U_1} & 0 & 0 & 0 & 0 & \frac{\partial \mathcal{R}_7}{\partial U_6} & A_7 & \frac{\partial \mathcal{R}_7}{\partial U_8} & 0 \\ 0 & \frac{\partial \mathcal{R}_8}{\partial U_1} & \frac{\partial \mathcal{R}_8}{\partial U_2} & \frac{\partial \mathcal{R}_8}{\partial U_3} & 0 & 0 & \frac{\partial \mathcal{R}_8}{\partial U_7} & A_8 & \frac{\partial \mathcal{R}_8}{\partial U_9} \\ 0 & 0 & 0 & \frac{\partial \mathcal{R}_9}{\partial U_3} & 0 & 0 & 0 & \frac{\partial \mathcal{R}_9}{\partial U_8} & A_9 & \frac{\partial \mathcal{R}_9}{\partial U_{10}} \\ 0 & 0 & 0 & \frac{\partial \mathcal{R}_{10}}{\partial U_3} & \frac{\partial \mathcal{R}_{10}}{\partial U_4} & \frac{\partial \mathcal{R}_{10}}{\partial U_5} & 0 & 0 & \frac{\partial \mathcal{R}_{10}}{\partial U_9} \\ 0 & 0 & 0 & 0 & 0 & \frac{\partial \mathcal{R}_{11}}{\partial U_5} & 0 & 0 & \frac{\partial \mathcal{R}_{11}}{\partial U_{10}} \end{array} \right] \left[ \begin{array}{c} \Delta U_0^n \\ \Delta U_1^n \\ \Delta U_2^n \\ \Delta U_3^n \\ \Delta U_4^n \\ \Delta U_5^n \\ \Delta U_6^n \\ \Delta U_7^n \\ \Delta U_8^n \\ \Delta U_9^n \\ \Delta U_{10}^n \\ \Delta U_{11}^n \end{array} \right] = \left[ \begin{array}{c} \mathcal{R}_0 \\ \mathcal{R}_1 \\ \mathcal{R}_2 \\ \mathcal{R}_3 \\ \mathcal{R}_4 \\ \mathcal{R}_5 \\ \mathcal{R}_6 \\ \mathcal{R}_7 \\ \mathcal{R}_8 \\ \mathcal{R}_9 \\ \mathcal{R}_{10} \\ \mathcal{R}_{11} \end{array} \right] \quad (4.88)$$

Where  $A_i$  is defined as

$$A_i = \frac{|\Omega_i|}{\Delta t_i} + \frac{\partial \mathcal{R}_i}{\partial U_i}. \quad (4.89)$$

## 4.8 Gradient Computation

To acquire second-order spatial accuracy on the computational domain, conserved and primitive variable gradients are required [52]. In the FVM, two families of gradient reconstruction techniques are common: (1) element-based and (2) element-free methods. Element-based approaches use the mesh topology to inform gradient calculations, while element-free approaches determine the gradient based solely on the information from the neighboring computational nodes. In this work, both methods are available via an implementation of the Green-Gauss (GG) and Weighted Least-Squares (WLS) algorithms.

### 4.8.1 Green-Gauss

The Green-Gauss theorem can be directly applied to determine the gradient of a scalar field,  $\xi$ , in the computational domain. This element-based gradient reconstruction method uses the definition of the divergence theorem to infer the value of the gradient,  $\nabla \xi_i$ , in a control volume,  $\Omega_i$ , by the

flux of  $\xi$  through the control volume surface,  $\partial\Omega_i$ . Explicitly,

$$\int_{\Omega_i} \nabla \xi d\Omega = \int_{\partial\Omega_i} \xi \vec{n} ds. \quad (4.90)$$

If a piecewise-linear representation of  $\xi$  is used on the computational domain,  $\nabla\xi_i$  is constant within each  $\Omega_i$ . Under these conditions, a semi-discrete formulation of the gradient can be written as,

$$|\Omega_i| \nabla \xi_i \approx \int_{\partial\Omega_i} \xi \vec{n} ds. \quad (4.91)$$

To evaluate Eqn. (4.91), an approximation of  $\xi$  on the control volume boundary,  $\partial\Omega_i$  is necessary. For this work, the value of  $\xi$  on the interface connecting nodes  $i$  and  $j$  is taken as the mean value between the nodes. The surface integral is then evaluated by summing over all the faces of  $\Omega_i$ ,

$$\nabla \xi_i \approx \frac{1}{|\Omega_i|} \sum_{j \in \mathcal{N}_i} \left( \frac{\xi_i + \xi_j}{2} \right) \vec{n}_{ij} \Gamma_{ij}, \quad (4.92)$$

where  $\Gamma_{ij}$  is the face area. In the edge-based data structure of SU2, the gradient field is computed by looping over all edges in the computational domain. A compound assignment modifies the stored value of the gradient in the nodes  $i$  and  $j$  associated with the current edge. By looping over all edges, the full contribution to  $\nabla\xi_i$  is accounted for at each node without unnecessary calls to the nodal connectivity data structure.

#### 4.8.2 Weighted Least Squares

An alternative method for calculating flow variable gradients in the discretized domain is the weighted least-squares method. In this element-free approach, the gradient at node  $i$  represents the minimum-error comparison between the true value of  $\xi_j$  at neighboring nodes,  $j \in \mathcal{N}_i$ , and a predicted value of  $\xi$  at  $j$ , denoted by,  $f_{ij}$ . The error,  $\mathcal{F}_i$ , is defined as the squared difference between  $\xi_j$  and  $f_{ij}$ , weighted by the square of the inter-nodal distance,  $d_{ij}^2$ ,

$$\begin{aligned} d_{ij}^2 &= \Delta \vec{x}_{ij} \cdot \Delta \vec{x}_{ij} \\ &= (\vec{x}_j - \vec{x}_i) \cdot (\vec{x}_j - \vec{x}_i) \end{aligned} \quad (4.93)$$

$$\mathcal{F}_i = \sum_{j \in \mathcal{N}_i} \left[ \frac{\xi_j - f_{ij}(\Delta \vec{x}_{ij}, \nabla \xi_i)}{d_{ij}} \right]^2. \quad (4.94)$$

The prediction function,  $f_{ij}$ , is a linear extrapolation of  $\xi$  from  $i$  to  $j$  using the to-be-determined gradient,  $\nabla\xi_i$ ,

$$f_{ij}(\Delta \vec{x}_{ij}, \nabla \xi_i) = \xi_i + (\Delta \vec{x}_{ij} \cdot \nabla \xi_i). \quad (4.95)$$

To find the  $\nabla \xi_i$  that minimizes the error, differentiate  $\mathcal{F}_i$  and find the stationary point,

$$\frac{\partial \mathcal{F}_i}{\partial \nabla \xi_i} = 2 \sum_{j \in \mathcal{N}_i} \frac{1}{d_{ij}^2} (\xi_j - f_{ij}) \left( -\frac{\partial f_{ij}}{\partial \nabla \xi_i} \right) = \vec{0}. \quad (4.96)$$

By definition, the least-squares fitting error,  $\mathcal{F}_i$ , is quadratic in  $\nabla \xi_i$ . Therefore a single minimum is guaranteed, and no additional specifications are required on the stationary points of  $\mathcal{F}_i$ . Inserting the definition of  $f_{ij}$  from Eqn. (4.95) into Eqn. (4.96), noting  $\partial f_{ij}/\partial \nabla \xi_i = \Delta \vec{x}_{ij}$ , and rearranging yields,

$$\begin{aligned} \sum_{j \in \mathcal{N}_i} \frac{1}{d_{ij}^2} (\Delta \vec{x}_{ij} \cdot \nabla \xi_i) \Delta \vec{x}_{ij} &= \sum_{j \in \mathcal{N}_i} \frac{1}{d_{ij}^2} (\xi_j - \xi_i) \Delta \vec{x}_{ij} \\ X^\top W X (\nabla \xi_i) &= X^\top W \Xi, \end{aligned} \quad (4.97)$$

where  $X$ ,  $W$ , and  $\Xi$  are defined as,

$$X = \begin{bmatrix} \Delta \vec{x}_{i,j_1} \\ \vdots \\ \Delta \vec{x}_{i,j_n} \end{bmatrix}, \quad W = \begin{bmatrix} 1/d_{ij_1}^2 & & \\ & \ddots & \\ & & 1/d_{ij_n}^2 \end{bmatrix}, \quad \Xi = \begin{bmatrix} (\xi_{j_1} - \xi_i) \\ \vdots \\ (\xi_{j_n} - \xi_i) \end{bmatrix}, \quad \forall j_k \in \mathcal{N}_i. \quad (4.98)$$

To acquire the weighted least-squares gradient, Eqn. (4.97) is rearranged to solve for  $\nabla \xi_i$ ,

$$\nabla \xi_i = (X^\top W X)^{-1} X^\top W \Xi. \quad (4.99)$$

The implementation of the WLS algorithm in SU2 follows the method described above. A loop over all nodes in the domain is performed, and the matrices  $X$ ,  $W$ , and  $\Xi$  are created by gathering the information from the neighboring nodes. After performing the necessary linear algebra operations,  $\nabla \xi_i$  is stored, and the loop proceeds to the next node in the domain. Because a matrix inversion is necessary to solve for  $\nabla \xi_i$ , the algorithm cannot be performed using partial sums in the same fashion as the GG method described in Section 4.8.1. Comparing the two methods, the WLS method requires more arithmetic operations and memory access calls to the mesh connectivity, constituting a greater computational expense than GG. However, this expense can be justified by the higher quality in the gradient information, particularly in meshes with high aspect ratio cells [21].

## 4.9 Flux Reconstruction and Limiters

Fundamentally, the discretization of the governing equations is an approximation of the true, continuous PDE system. Numerical error is introduced from the spatial and temporal integration schemes that is dependent on the step size in the time or space dimensions. For steady-state solutions, such as those sought in this work, the error in the temporal integration is not a concern, since any time-dependent terms are zero, by definition, in the converged solution. However, the spatial accuracy

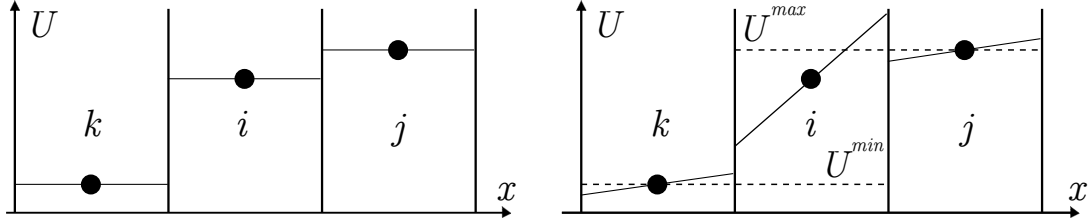


Figure 4.4: Hypothetical first- and second-order accurate spatial schemes with flux limiting.

is quite important, as the presence of numerical error corrupts the quality of the solution, affecting the predicted performance metrics.

The spatial order of accuracy of a numerical schemes is based on the discrete representation of the solution on the computational domain. To this point, it has been assumed that the solution within any computational node of the mesh is the mean value of the solution within the node at that spatial location. This piecewise-constant representation leads to first-order,  $\mathcal{O}(\Delta x)$ , spatial accuracy. Higher order accuracy can be achieved using more sophisticated representations of the solution within the control volumes that constitute the computational domain. For second order accuracy,  $\mathcal{O}(\Delta x^2)$ , a piecewise linear reconstruction of the solution is required using the solution gradient as determined by the GG or WLS methods of Sections 4.8.1, and 4.8.2. The scalar variables are projected out to the cell interfaces and the numerical flux functions are resolved using the reconstructed solution on the ‘left’ and ‘right’ sides of the cell interface,

$$\hat{F}_{ij}^c = \hat{F}_{ij}^c(U_L, U_R), \quad (4.100)$$

Using the reconstructed solutions directly in the numerical flux functions can reduce the stability of the algorithm. The presence of steep gradients or discontinuities in the solution variables may introduce numerical oscillations that grow unbounded in time [78]. To prevent this, a *flux limiter* [137, 138, 139, 140] is applied to the projected gradient to preserve the monotonicity and Total Variation Diminishing (TVD) properties of a flux scheme. This limiter,  $\phi_i \in [0, 1]$ , permits the full use of the reconstruction where possible, and reverts to first-order accuracy when necessary for stability, such that,

$$\begin{aligned} U_L &= U_i + \frac{\phi_i}{2} (\nabla U_i \cdot \Delta \vec{x}_{ij}) \\ U_R &= U_j + \frac{\phi_j}{2} (\nabla U_j \cdot \Delta \vec{x}_{ji}). \end{aligned} \quad (4.101)$$

In this work, Venkatakrishnan’s limiter [142] for unstructured meshes is used,

$$\phi_i = \frac{\Delta_+^2 + 2\Delta_- \Delta_+ + \epsilon^2}{\Delta_+^2 + 2\Delta_-^2 + \Delta_- \Delta_+ + \epsilon^2}, \quad (4.102)$$

where the left and right interface gradients are defined as,

$$\begin{aligned}\Delta_- &= U_L - U_i \\ \Delta_+ &= \begin{cases} U_i^{\max} - U_i & \text{for } \Delta_- > 0 \\ U_i^{\min} - U_i & \text{for } \Delta_- \leq 0. \end{cases}\end{aligned}\quad (4.103)$$

The  $U_i^{\max}$  and  $U_i^{\min}$  terms are the largest and smallest values of the scalar conserved variables in the adjacent nodes of  $i$ . The limiter is computed for each variable in the solution vector and the minimum of all  $\phi$  is taken as  $\phi_i$  for the flux reconstruction. This is a more aggressive limiting strategy as compared to the traditional approach, where the limiter is calculated and applied uniquely for each variable, but necessary to prevent non-physical gas states in the reconstruction.

## 4.10 Shape Parametrization, Deformation, and Surface Sensitivity

The adjoint method provides a framework for acquiring gradient information via the surface sensitivities that remain from the adjoint boundary integrals. By parameterizing a vehicle's shape, a design engineer can manipulate the definition of the outer surface by changing the value of the design variables. Using the adjoint method, the effect of these surface changes on the objective function are determined by projecting the surface sensitivities onto the deformed surface geometry. By perturbing each design variable in-turn, the objective function gradient is determined.

The process described above requires a definition of the vehicle shape and a parameterization of that shape. Simple geometries may be defined analytically, but more sophisticated tools may be necessary to define more complex air vehicle shapes. Computer-aided Drafting (CAD) packages are powerful tools for just such a purpose. These packages can be used directly to drive the geometric changes, via user-specified parameterizations within the CAD environment. This CAD-driven approach allows great specificity in the definition of the design variables, often resulting in configurations that are easier to manufacture, but it can also limit the design space to a parameterization that does not include the optimal configuration. Moreover, CAD ‘in the loop’ optimization requires exposure of the CAD package’s API to the optimization driver script, which is not always possible with commercial software packages.

An alternative to CAD-based shape manipulation is to operate directly on the discretized surface geometry. Given the adjoint method is insensitive to the dimensionality of the design space, it is possible to treat each discrete point on the surface as a unique design variable. In principle, this approach delivers infinite geometric flexibility, but requires gradient smoothing [64] for robustness. For this work, a technique from the computer graphics industry is used to deform the surface topology, guaranteeing smooth deformations. This methodology is described in Section 4.10.2.

Once the surface deformation is prescribed, a new volumetric mesh is needed for the simulation. There are two common methodologies: (1) procedurally re-generate the mesh from scratch for the

new surface topology, or (2) deform the existing computational mesh to remain conformal to the new surface shape. Cartesian grid methods [98] are a popular technique for automatic meshing, where an initial cartesian grid is automatically refined to discretize the volume and capture the surface topology. This technique has been proven to be effective for subsonic and supersonic inviscid simulations [1, 30, 101], but are less reliable in viscous, hypersonic environments. The near-body cartesian mesh is generally not aligned with the body normal direction, corrupting the propagation of the viscous fluxes in the boundary layer, and the misaligned cells at shock waves introduce numerical artifacts along the shock front. Alternatively, hyperbolic or algebraic extrusion methods can be used to automatically generate meshes from a discretized surface mesh using an advancing front of nodes. These techniques generally provide high-quality meshes, but are often not robust enough to accommodate complex geometries.

In situations where automatic meshing is not possible, or yields undesirable results, a baseline mesh can be deformed to accommodate new surface geometry. This technique is especially favorable for purpose-built meshes that are designed to resolve specific flow features *a priori*. To perform the deformation, the computational grid is modeled as a deformable structure. This technique is adopted in the current work and is described in detail in Section 4.10.3.

#### 4.10.1 Projecting the Adjoint Surface Sensitivities onto the Design Space

The adjoint surface sensitivities provide a mechanism for acquiring the gradient of a specified objective function,  $J$ , to a set of design variables,  $\alpha_k$ . Recall from the derivation of the adjoint system, the surface sensitivities are composed of the remaining terms on  $S$  after the adjoint boundary conditions are applied,

$$\delta\mathcal{J} = - \int_S \left\{ \frac{\partial\mathcal{J}}{\partial S} \right\} \delta S ds. \quad (4.104)$$

These surface sensitivities determine the effect of localized normal geometric changes on  $J$ . Numerically, the sensitivities are evaluated by projecting  $\partial\mathcal{J}/\partial S$  onto the deformation imposed by the manipulation of the design variables,

$$\frac{\delta\mathcal{J}}{\delta\alpha_k} = - \int_S \left\{ \frac{\partial\mathcal{J}}{\partial S} \right\} \frac{\delta S}{\delta\alpha_k} ds \approx - \sum_{i \in \mathcal{N}_S} \left\{ \frac{\partial\mathcal{J}}{\partial S} \right\}_i \frac{\vec{n}_i \cdot \Delta\vec{x}_i}{\Delta\alpha_k} \Gamma_i. \quad (4.105)$$

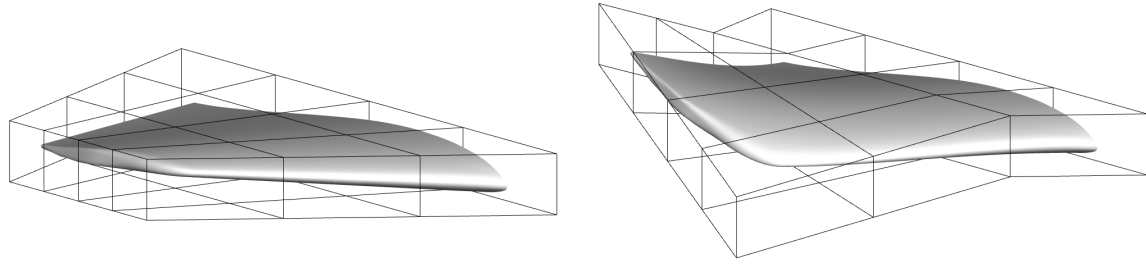
In Eqn. (4.105),  $\mathcal{N}_S$  is the set of all nodes on  $S$ ,  $\Delta\vec{x}_i$  is the change in the cartesian coordinates of node  $i$  induced by the deformation,  $\Delta\alpha_k$  is the change in the design variable value, and  $\Gamma_i$  is the face area on  $S$  from the control volume that surrounds  $i$ . For a given geometry, the solution of the governing and adjoint equations provides  $\partial\mathcal{J}/\partial S$ , while the remaining terms required to evaluate  $\partial\mathcal{J}/\partial\alpha_k$  are determined from the change in geometry alone. As a consequence, evaluating the  $k$  terms of the objective function gradient are of trivial expense once the direct and adjoint solutions have been acquired, provided there is an efficient mechanism for perturbing the surface geometry.

### 4.10.2 Surface Deformation

For this work, surface deformation is achieved using a Free-Form Deformation (FFD) strategy [127, 124], wherein a box is constructed that fully encloses the design surface. This box is parameterized as a Bézier solid, and the surface coordinates are mapped from the cartesian grid to a new coordinate system in  $\mathbb{R}^3$ , using a trivariate tensor product Bernstein polynomial,

$$X(u, v, w) = \sum_{i=0}^l \sum_{j=0}^m \sum_{k=0}^n P_{i,j,k} B_i^l(u) B_j^m(v) B_k^n(w), \quad (4.106)$$

where  $l, m, n$  are the orders of the Bernstein polynomials,  $B_i^l(u)$ ,  $B_j^m(v)$  and  $B_k^n(w)$ , and  $u, v, w \in [0, 1]$  are the parametric coordinates. The shape of the box can be changed by manipulating the Cartesian locations of the control points,  $P_{i,j,k}$ , which, in turn, deform the contents of the FFD box. The new, deformed surface can be transformed back into the Cartesian grid by performing the inverse mapping. Using FFD, engineering variables, like sweep, twist, and thickness can be constructed by the coordinated movement of one or more control points, or general, free-body deformation can be performed using the same framework. Also, once the initial mapping between the surface points and the FFD box has been created, evaluating any sequence of deformations thereafter is computationally cheap, since it only requires evaluating the existing mapping between  $\{u, v, w\}$  and  $\{x, y, z\}$  coordinates.



(a) Original surface definition and FFD box.      (b) Deformed surface from FFD control point movement.

Figure 4.5: Wing twist using FFD-based deformation.

### 4.10.3 Volumetric Deformation

Once the surface geometry has been perturbed, a new volumetric mesh is required that conforms to the new surface shape. This mesh is acquired by treating the computational domain as an elastic solid and applying deformations,  $\vec{u} = (u_x, u_y, u_z)^\top$ , that are consistent with the motion of the design surface [104, 26]. The motion of the domain and constituent cells is resolved using the linear elasticity equations,

$$\nabla \cdot \bar{\sigma} = f, \quad (4.107)$$

where  $\bar{\sigma}$  is the stress tensor and  $f$  is a body force. Stress,  $\bar{\sigma}$ , and strain,  $\bar{\epsilon}$ , are related by the constitutive relation,

$$\bar{\sigma} = \lambda \text{Tr}(\bar{\epsilon}) \bar{I} + 2\mu \bar{\epsilon}, \quad (4.108)$$

while the strain-displacement relation completes the chain of dependency to the surface deformations,

$$\bar{\epsilon} = \frac{1}{2}(\nabla \vec{u} + \nabla \vec{u}^T), \quad (4.109)$$

The Lamé constants in Eqn. (4.108) are given by,

$$\lambda = \frac{\nu E}{(1+\nu)(1-2\nu)}, \quad \text{and} \quad \mu = \frac{E}{2(1+\nu)}, \quad (4.110)$$

where  $E$  and  $\nu$  are Young's modulus and Poisson's ratio, respectively. Poisson's ratio determines the amount of lateral shrinkage relative to axial extension of the material, while Young's modulus represents the rigidity, or stiffness of the material. To preserve the shape of the mesh in the viscous, near-body grid, a variable Young's modulus is used in the algorithm. By setting an inverse relationship between  $E$  and the cell volume, the quality of the boundary-layer mesh is preserved under deformation, while larger cells accommodate the boundary motion. Consequently, the algorithm is robust, even under sizable deformations.

The linear elasticity equations are discretized using a Finite Element Method (FEM), using a standard Galerkin approximation. Boundary conditions are the displacement of the surface points as determined by the output of the surface deformation method of Section 4.10.2, and are applied as Dirichlet boundary conditions. The resulting linear system is solved iteratively using the same preconditioned, GMRES solver as the flow and adjoint problems.



# Chapter 5

## Adjoint Gradient Verification

This chapter presents a verification of the adjoint equations, boundary conditions, and surface sensitivities, derived in Chapter 3. The verification is performed by posing a variety of shape design problems for geometries of practical interest to the hypersonic community. For each problem, a surface parameterization is prescribed to enable changes in the surface definition by manipulating the design variables. Gradients of the objective function with respect to the design variables are calculated using both the continuous adjoint and finite-difference methods. By comparing the outputs for a variety of boundary conditions and objective functions, the validity of the derivation presented in Chapter 3 is established.

### 5.1 RAM C-II Flight Test Article (Inviscid)

This verification case addresses the derivation and formulation of the adjoint equations for inviscid, nonequilibrium flow environments. The projected-force objective function gradient is evaluated over the forebody of a ballistic entry vehicle at hypersonic, high-altitude free stream conditions.

**Background and Problem Setup** During the late 1960s and early 1970s, the Radio Attenuation Measurements (RAM) project was conducted by NASA's Langley Research Center. The objective of the program was to characterize the plasma sheath surrounding hypersonic vehicles during the entry phase and to quantify the effect of free electrons in the shock layer on radio communications. The radio "black-out" from the attenuation of electromagnetic signals between ground stations and flight vehicles impacted mission planning, navigation, control, data storage requirements, and other mission critical activities. The tests were conducted by boosting a probe into a sub-orbital trajectory using a Scout rocket, then accelerating the probe back toward the earth using the upper stages of the rocket system to acquire the desired entry velocity. Microwave reflectometers and an electrostatic rake were used to acquire data on the number density of the free electron gas surrounding the vehicle during its re-entry to the Earth's atmosphere. A detailed report by Jones and Cross [67] summarizes the project, the experimental conditions, and the conclusions from the tests.

The data acquired by the RAM C-II flight test experiment is of sufficient quality to be used for the verification and validation of numerical simulation tools, and it has been used extensively to test new thermochemical models and simulation methodologies [12, 125, 89]. This well-known experiment is the first verification test case of this work, and is representative of conditions in the shock layer for ballistic entry vehicles returning from Low Earth Orbit (LEO).

Parameter	Value
Altitude	61km
$T_\infty$	254.0K
$Re$	19500
$M_\infty$	23.9
$P_\infty$	19.76 Pa
$\alpha$	0°
$\beta$	0°
$Y_{N_2}$	0.766
$Y_{O_2}$	0.231
$Y_{NO}$	0.001
$Y_N$	0.001
$Y_O$	0.001

Table 5.1: RAM C-II simulation free stream conditions.

The simulation free-stream conditions are those from ‘Case 5’ of the second flight (C-II), shown in Tab. (5.1). For the simulation, a five-species air chemical model is used. This model lacks a free electron species, so direct comparison with the flight data from Jones and Cross is not possible. However, the purpose of this case is not to validate the accuracy of the flow solver, such a test case is provided in Appendix D, but rather to verify the accuracy of the *gradient* of  $C_D$  on a known geometry. The simplified air chemical model permits such a verification activity because it keeps the computational cost down to accommodate the many solutions required to compute the gradient using finite-difference methods.

**Geometry** The probe from the RAM C-II flight test is a ballistic entry vehicle with a spherical nose cap connected to a conical frustum at the tangent point of the sphere. The axisymmetric body of revolution is shown schematically in Fig. (5.1) with the design parameters summarized in Tab. (5.2).

**Computational Grid** A body-conformal mesh consisting of 50,424 points and 43,776 hexahedral cells is used to discretize the flow domain surrounding the flight vehicle. To reduce computational cost, a 90° sector of the body and flow domain is used to represent the full environment, since an axis of symmetry exists along the centerline of the vehicle. Hexahedral cells are exclusively used to preserve the quality of the solution in the shock layer and to accurately propagate fluxes along the vehicle surface.

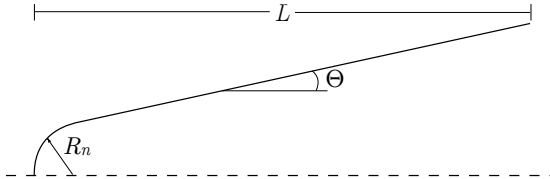


Figure 5.1: RAM-C II vehicle definition

Parameter	Symbol	Value
Nose Radius	$R_n$	0.1524m
Cone Angle	$\theta$	9°
Length	$L$	1.295m

Table 5.2: RAM-C II geometry values

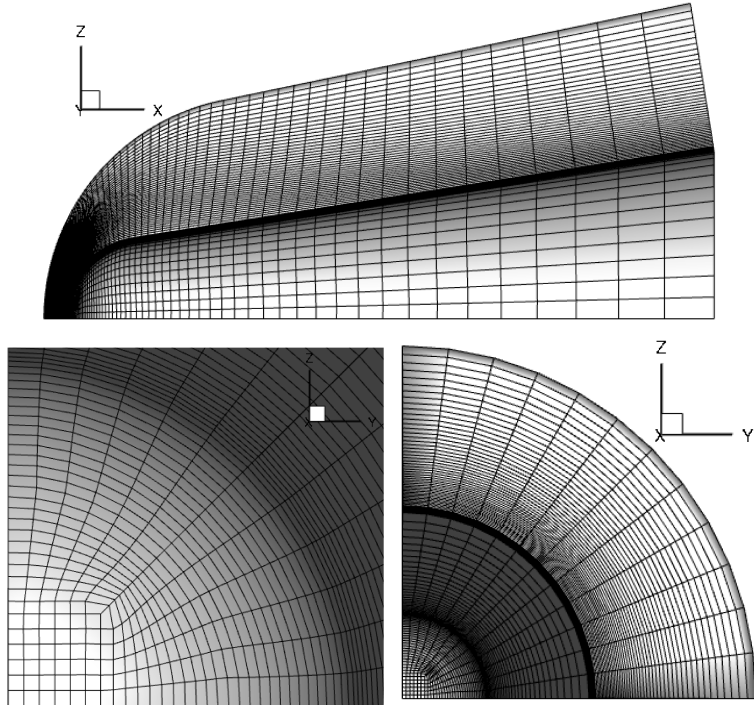


Figure 5.2: Computational mesh for the RAM C-II test case.

A technique from the structured, multi-block solver community is employed to prevent a polar singularity at the axis of symmetry for the vehicle. The surface mesh is created by defining a  $7 \times 7$  quadrilateral domain at the nose, connected to a second domain along the remaining surface area of the geometry. This surface mesh is then extruded normally to generate the volume mesh, with 65 nodes in the wall-normal direction. Geometric stretching biases the mesh density near the surface of the vehicle to sufficiently resolve the phenomena in the shock layer. A validation test of this geometry by Scalabrin [125] includes a mesh refinement study, which indicates little effect on the predicted heat transfer rates for meshes varying from 64-128 nodes in the wall-normal direction. Candler's validation of this test case [13] showed good agreement with experimental data using as few as 50 wall-normal nodes. Fig. (5.2) shows projections of the mesh in the X-Z and Y-Z planes,

and includes a close-up of the interface between the two surface mesh domains at the nose of the vehicle.

**Design Variables** A surface parameterization of the RAM C-II vehicle is achieved using the Free-Form Deformation (FFD) box technique described in Section 4.10.2. The FFD box is constructed using 4<sup>th</sup>, 2<sup>nd</sup>, and 2<sup>nd</sup> order Bernstein polynomials in the  $(i, j, k)$  directions of the box, leading to a total of 60 total control points available to manipulate the surface of the RAM C-II vehicle. The corners of this box are shown in Tab. (5.4) and all control points are equally spaced in the  $(i, j, k)$  directions respectively. Therefore, by defining the corners of the box and the number of control points in each direction, the cartesian location of all the control points are determined. The design space is constructed by selecting 12 of the control points and prescribing their motion in cartesian space. By moving the control points along scalar multiples of the displacement vectors,  $\Delta\vec{x}$ , the surface is perturbed and the design space is established. The FFD box and surface geometry are shown in Fig. (5.3), while the definition of the design variables is shown in Tab. (5.3).

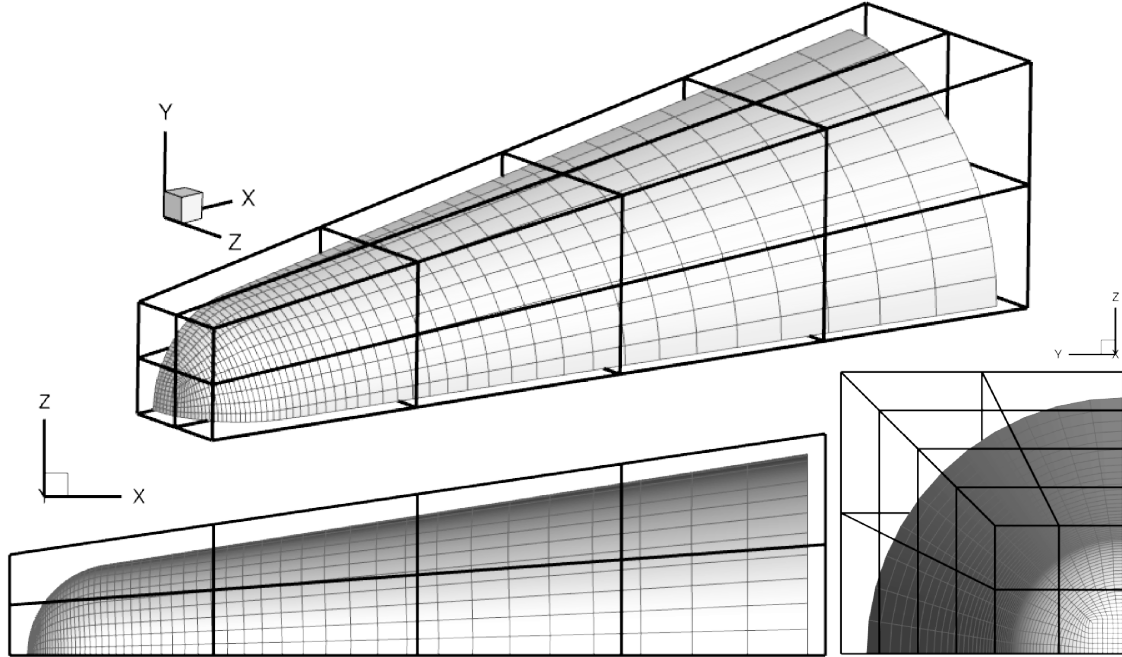


Figure 5.3: Definition of the FFD box for the RAM-C II geometry.

**Results** To reproduce the flight environment of the RAM C-II vehicle, with the free stream conditions prescribed by Tab. (5.1), characteristic far-field boundaries are imposed on the inflow and outflow domains of the computational mesh. Symmetry conditions on the X-Z and X-Y are enforced

DV #	FFD Index	$\Delta \vec{x}$
1	(1,1,1)	{ -1.0, 1.0, 1.0 }
2	(1,2,2)	{ 0.0, 1.0, 1.0 }
3	(2,1,1)	{ 0.0, 1.0, 1.0 }
4	(3,1,1)	{ 0.0, 1.0, 1.0 }
5	(0,2,1)	{ 0.0, 1.0, 0.0 }
6	(1,2,1)	{ 0.0, 1.0, 0.0 }
7	(2,2,1)	{ 0.0, 1.0, 0.0 }
8	(3,2,1)	{ 0.0, 1.0, 0.0 }
9	(0,1,2)	{ 0.0, 0.0, 1.0 }
10	(1,1,2)	{ 0.0, 0.0, 1.0 }
11	(2,1,2)	{ 0.0, 0.0, 1.0 }
12	(3,1,2)	{ 0.0, 0.0, 1.0 }

Table 5.3: RAM-C II design variable definitions.

Node	$\vec{x}$
(0,0,0)	{ -2.95E-2, -1.00E-4, -1.00E-4 }
(4,0,0)	{ 1.32E0, -1.00E-4, -1.00E-4 }
(4,2,0)	{ 1.32E0, 3.69E-1, 0.0 }
(0,2,0)	{ -2.95E-2, 1.68E-1, 0.0 }
(0,0,2)	{ -2.95E-2, 0.0, 1.68E-1 }
(4,0,2)	{ 1.32E0, 0.0, 3.69E-1 }
(4,2,2)	{ 1.32E0, 3.69E-1, 3.69E-1 }
(0,2,2)	{ -2.95E-2, 1.68E-1, 1.68E-1 }

Table 5.4: Corners of the FFD box surrounding the RAM C-II geometry.

as a consequence of the zero angle-of-attack and angle-of-sideslip flight condition, and the vehicle surface is also prescribed as a flow-tangency boundary condition. The flow is initialized to the free-stream values everywhere and marched forward in time, achieving eight orders of magnitude convergence in the  $N_2$  density residual, using the AUSM spatial integration scheme and implicit time-stepping.

Solving the adjoint equations, using the converged flow solution, follows a similar procedure. Boundary conditions on the computational domain are applied in accordance with the requirements placed on the adjoint system from the boundary conditions of the direct problem, as described in Section 3.7. The adjoint system is initialized to the free-stream,  $\Psi_\infty = 0$ , everywhere in the domain and marched forward in time, achieving six-orders of magnitude convergence in the  $\psi_{\rho N_2}$  residual, using Local Lax-Friedrich spatial integration and Backward Euler implicit time stepping.

Scalar field variables from the flow and adjoint solutions are shown in Fig. (5.4). The variables are extracted from the three dimensional domain along a plane normal to  $\vec{n} = \{0, -1, 1\}$ . The y-axis variable,  $\vartheta$ , represents the wall-normal distance on the extracted plane, and is determined by the

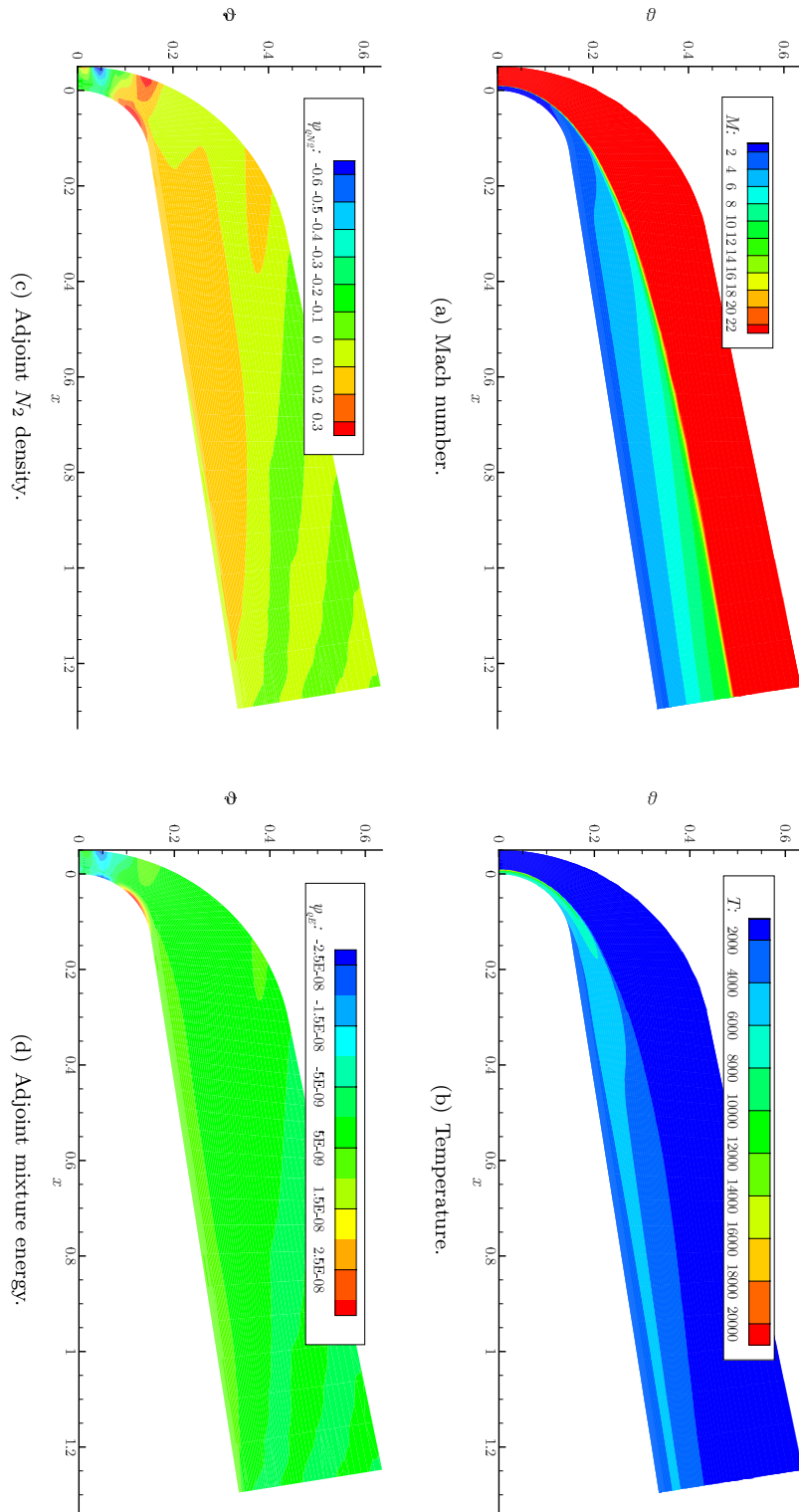


Figure 5.4: Flow and adjoint field variables for the RAM C-II simulation

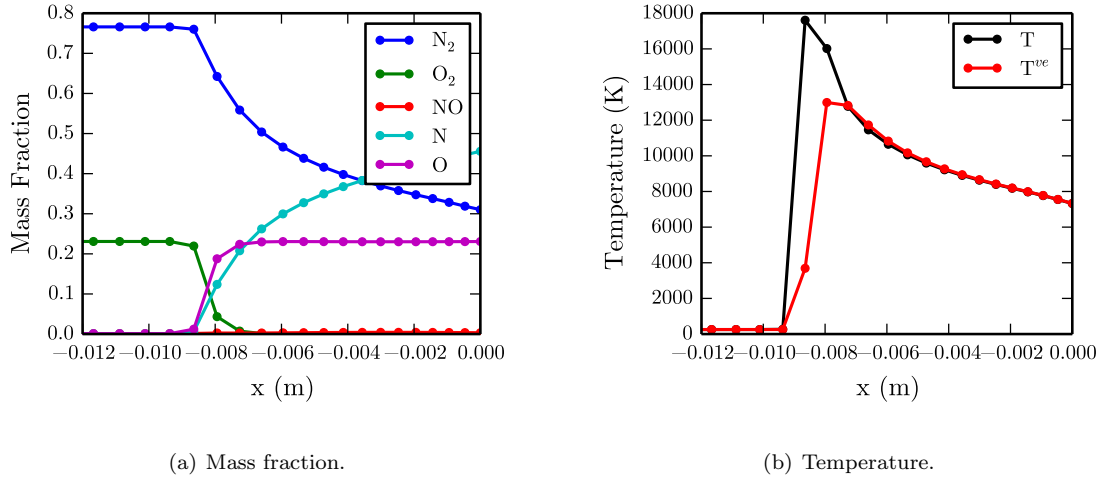


Figure 5.5: Flow quantities on the stagnation line.

relation,  $\vartheta = \sqrt{y^2 + z^2}$ . The visualizations of the flow domain show a strong, detached bow shock that sits roughly 9mm from the surface of the vehicle along the stagnation line. The compressed flow in the shock layer is then rapidly expanded around the shoulder of the probe and continues to the exit of the flow domain. The field plots of temperature show a thin layer of high temperature immediately behind the shock, reaching nearly 18,000K. The flow cools as it expands around the probe shoulder, with additional energy transfer to the vibrational modes further downstream. Mass fractions and temperatures on the stagnation streamline, plotted in Fig. (5.5), indicate modest thermal nonequilibrium immediately behind the shock and more significant chemical nonequilibrium that persists to the vehicle surface.

Recall from the adjoint derivation that the adjoint variables are the Lagrange multipliers of the objective function Lagrangian. Therefore, a derivative of the Lagrangian with respect to the adjoint variables returns the equality constraint enforced locally by the flow governing equations. It is possible, then, to interpret the adjoint variables as indicators of how infinitesimal violations of the constraint affect the objective function. Examining the adjoint  $N_2$  density and adjoint energy variables in the domain indicates that there are regions near the stagnation line and the shoulder of the probe where the flow governing equations have a large effect on the objective function (either positively or negatively). The ‘ripples’ in the domain near the top and exit boundaries are numerical artifacts from the centered spatial integration scheme.

Local surface sensitivity values,  $\partial\mathcal{J}/\partial S$ , are shown in Fig. (5.6), indicating the effect of locally normal surface perturbations on the objective function. Note that in the formulation of the Lagrangian, a negative sign is introduced, therefore negative values in  $\partial\mathcal{J}/\partial S$  indicate an *increase* in the value of the objective function with respect to a normal vector pointing from the body into the computational domain. An examination of the sensitivity map indicates that normal perturbations to the geometry at the shoulder lead to an increase in the predicted  $C_D$ , while perturbations nearer

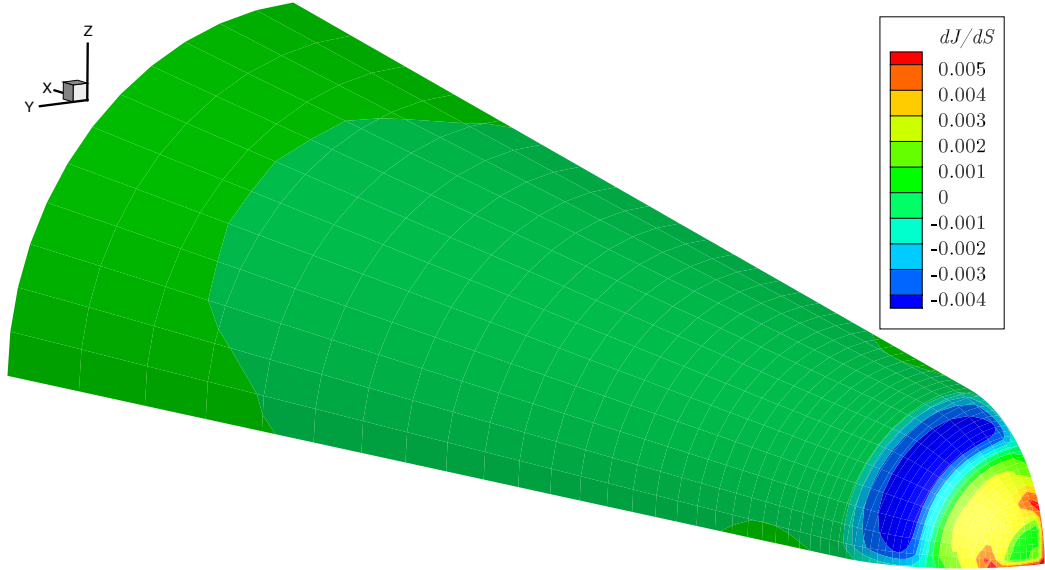


Figure 5.6: Surface sensitivity map for the RAM C-II.

the stagnation point lead to a decrease in  $C_D$ . This behavior agrees with the observed phenomena of the adjoint solution in the volume discussed previously, as well as with the fundamental theory of blunt body aerodynamics at hypersonic speeds. For more complex geometries, surface sensitivity maps are useful in identifying critical areas on the design surface and can be used, strategically, to identify the most critical design variables in the surface parameterization. The sensitivity map, shown in Fig. (5.6), includes the local dual-grid face area in the computation of  $\partial\mathcal{J}/\partial S$ , which is responsible for some of the non axisymmetric behavior along the X-Z and X-Y boundaries. However, the boundaries have a non-negligible effect on the surface sensitivities, breaking the axisymmetry in the adjoint surface solution. This behavior is not observed in the subsequent test case, discussed in Section 5.2, and is likely due to mesh dependent inaccuracies near the stagnation point. The issue is avoided by the selection of the design variables.

Gradients in the drag coefficient of the probe are calculated using the finite-difference and adjoint methods by perturbing the surface geometry via the manipulation of the control points specified in Tab. (5.3). Each control point is moved a distance of  $(0.005) \times \Delta\vec{x}$  and the deformations to the surface and volume meshes are performed in accordance with the procedures described in Sections 4.10.2 and 4.10.3. Perturbed  $C_D$  values are subtracted by the baseline value of  $C_D = 0.01953$  and divided by the design variable perturbation, 0.005, to compute the finite-difference gradient entries. The results from the finite-difference and adjoint-based gradient computations are co-plotted in Fig. (5.7), and explicitly tabulated in Tab. (5.5). An examination of the gradients shows good agreement between the two methods. Minor discrepancies are expected, due to the truncation error inherent in the finite-difference scheme, as well as from the numerical error from the spatial integration schemes of the flow and adjoint problems. These differences are more significant for design variables 4, 8, and

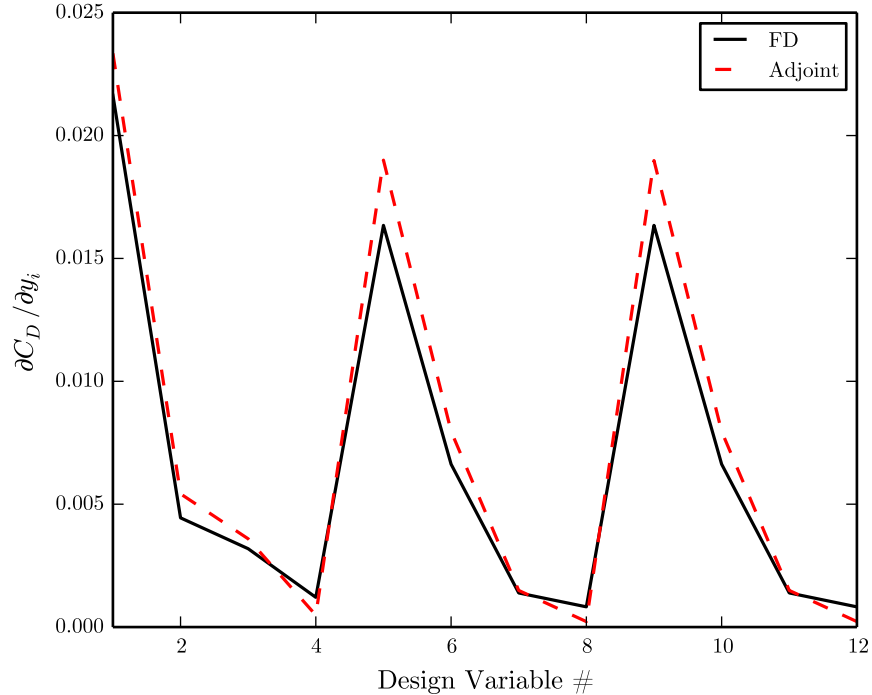


Figure 5.7: A comparison of the drag coefficient gradient from the finite-difference and adjoint methods.

12, since the magnitude of the gradient is particularly small for these variables. The accuracy of the finite-difference gradients are step-size dependent and trials with greater control point movement lead to poorer agreement in regions where the  $\nabla C_D$  signal was large. With decreasing step size at fixed solution convergence levels, agreement between the methods again deteriorated, but in regions where the  $\nabla C_D$  signal was small, indicating greater levels of solution convergence were required to resolve the gradient. The results shown in Fig. (5.7) represent the best agreement at the prescribed eight orders of magnitude convergence. Design variables 5-8 and 9-12 are positioned symmetrically about the centerline of the vehicle, therefore manipulation of these variables should lead to the same influence on  $C_D$ . This behavior is observed in the gradient plot for both the finite-difference and adjoint methods, indicating good convergence of the flow and adjoint problems. Two important conclusion may be drawn from the close agreement of the two methods: (1) that the inviscid adjoint equations, boundary conditions , and surface sensitivities are formulated correctly; (2) the discretized representations of the adjoint convective fluxes and source terms accurately capture the behavior of the continuous adjoint system for blunt-body entry vehicles.

DV #	$\nabla J$ (Adjoint)	$\nabla J$ (FD)	$ \nabla J^A - \nabla J^{FD} $
1	2.334E-2	2.164E-2	1.704E-3
2	5.422E-3	4.444E-3	9.779E-4
3	3.591E-3	3.188E-3	4.034E-4
4	4.852E-4	1.210E-3	7.243E-4
5	1.900E-2	1.635E-2	2.654E-3
6	7.967E-3	6.627E-3	1.339E-3
7	1.491E-3	1.388E-3	1.024E-4
8	2.222E-4	8.239E-4	6.017E-4
9	1.898E-2	1.635E-2	2.637E-3
10	7.962E-3	6.628E-3	1.334E-3
11	1.490E-3	1.389E-3	1.012E-4
12	2.225E-4	8.224E-4	5.999E-4

Table 5.5:  $\nabla C_D$  values for the finite-difference and adjoint gradient methods.

## 5.2 Space Shuttle Wing Cross-Section (Viscous)

The inviscid test case of Section 5.1 verified the formulation and implementation of the adjoint problem for inviscid, nonequilibrium environments. To assess the accuracy of the viscous adjoint, a second problem is posed, using airfoil geometry taken from the Space Shuttle’s outer mold line. This numerical experiment verifies the adjoint-based gradient against a finite-difference gradient for the projected-force objective function for adiabatic/noncatalytic and isothermal/super-catalytic wall boundary conditions.

**Background and Problem Setup** This numerical experiment is constructed using the Shuttle’s wing geometry and entry trajectory to be representative of the configuration and free stream conditions of high L/D, trans-atmospheric vehicles. The verification exercise is performed for adiabatic/noncatalytic and isothermal/catalytic wall boundary conditions, denoted ‘Case 1’ and ‘Case 2’ respectively, for the purpose of demonstrating the adjoint method under both Neumann- and Dirichlet-type boundary conditions for the chemical and thermal wall states. Physically, Case 1 represents a state of thermal and chemical equilibration between the boundary and flow environment, which is representative of the conditions imposed on long-duration hypersonic vehicle concepts for space access and prompt global access. Case 2, on the other hand, is mimics short duration entry processes, where a long period of cold-soak is followed by rapid thermal loading from the convective heat transfer between the flow environment and the vehicle surface.

Free stream conditions for the test case are shown in Tab. (5.6), and are collected from the STS-2 flight conditions from Kleb & Weilmuenster [74], originally sourced from Hartung [48, 49, 50]. The angle of attack for both cases is reduced from original  $\alpha = 40^\circ$  to  $\alpha = 3^\circ$  to prevent massive separation in the wake of the wing. In doing so, a more accurate prediction of the drag coefficient is possible, thus making a better verification exercise. A two-species Nitrogen gas model is used to keep

computational cost down, yet maintain the relevant problem physics, while demonstrating the flexibility of the adjoint methodology in accommodating different gas mixtures. For Case 2, chemical and thermal conditions at the surface are listed in Tab. (5.6), corresponding to a cold-wall, super-catalytic boundary.

Parameter	Value
$H$	69.2 km
$M_\infty$	24.3
$\alpha$	3°
$\beta$	0°
$Y_{N_2}$	0.999
$Y_N$	0.001
$p_\infty$	3.33 Pa
$T_\infty$	202 K
$T_{wall}$	1500 K
$Y_{N_2}^{wall}$	0.999
$Y_N^{wall}$	0.001

Table 5.6: Shuttle wing section free stream conditions.

**Geometry** The test case geometry is acquired by taking a cross section of the Space Shuttle's wing at a spanwise location of  $y = 9$  m, and extruding the airfoil 1 m in the positive  $y$ -direction to create a simple, rectangular wing. The spanwise location and airfoil profile are shown in Fig. (5.8).

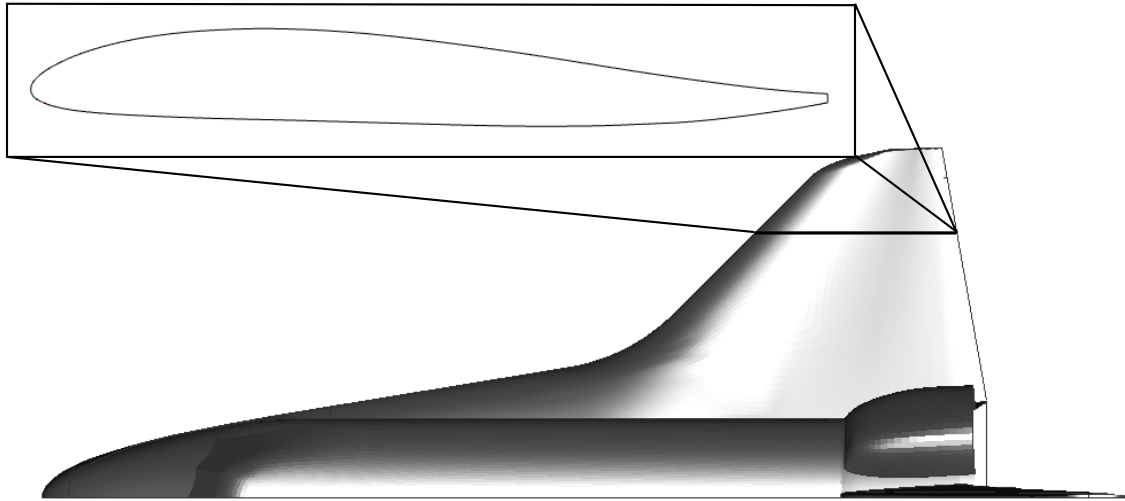


Figure 5.8: Shuttle wing cross-section.

**Computational Mesh** The discretized domain for the Shuttle airfoil is generated using a multi-block strategy consisting of hexahedral cells. A total of three logical blocks are used to represent the flow domain. First, a near-field O-mesh is extruded normally from the airfoil surface to capture the boundary layer. A second block extends from the trailing edge to the outflow boundary. The third block is a C-mesh enclosing the near-field O-mesh and airfoil wake region. This mesh topology is used to preserve alignment of the nodal connectivity with the leading bow shock wave in the wake of the wing. A total of 325 nodes are used to resolve the airfoil profile, extruded a distance of 1m in the positive y direction for a total of seven spanwise nodes in the computational domain. A total of 91 nodes in the wall-normal direction are used to resolve the shock and boundary layers for a total of 277,095 nodes and 231,888 unstructured, hexahedral cells. Fig. (5.9) shows a projection of the mesh in the X-Z plane and includes a zoomed perspective of the near field leading and trailing edge meshes.

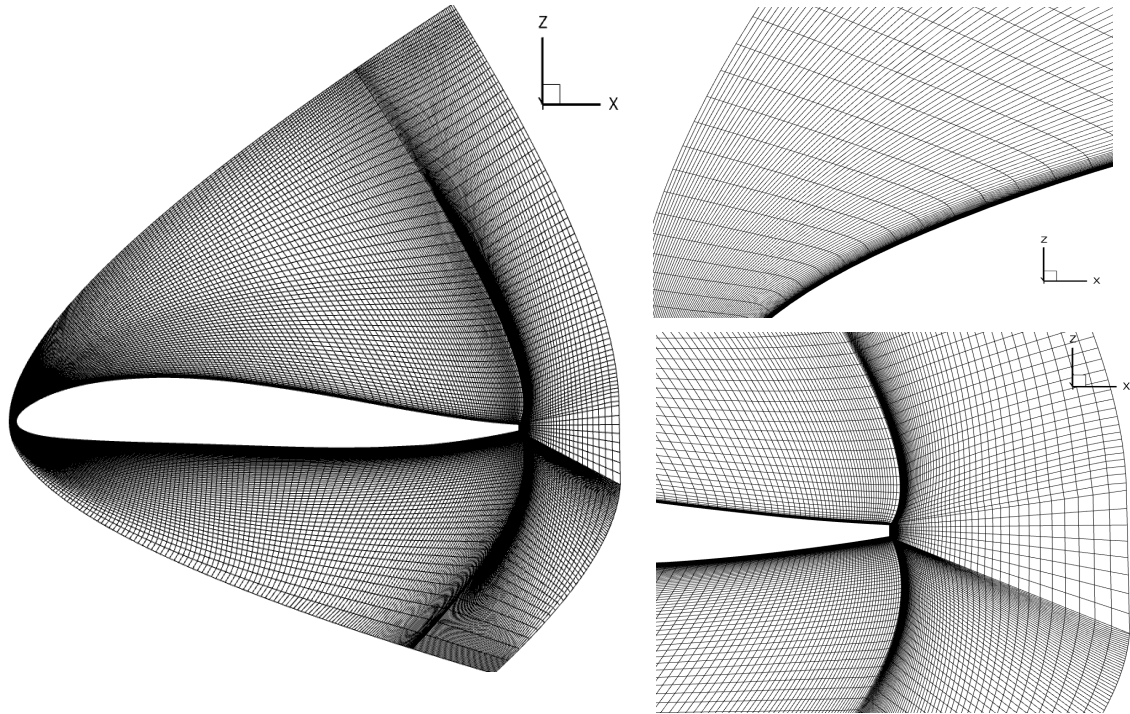


Figure 5.9: Computational mesh for the Shuttle airfoil test case.

**Design Variables** The rectangular wing is parameterized using a FFD box of order (4,2,1) in the  $(i, j, k)$  directions. A total of 30 control points are available to manipulate the surface, from which 10 were selected to represent the design space. FFD box corners and the design variable definitions are shown in Tabs. (5.7) and (5.8). Perturbations in the design variables increase the wing thickness along the centerline, but not at the tips, breaking the two-dimensionality of the domain.

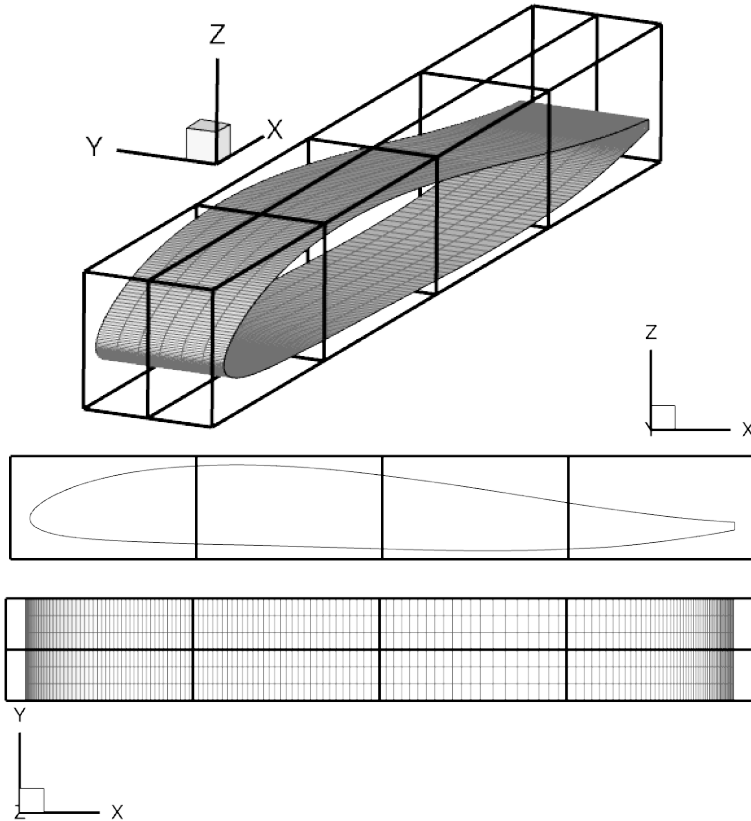


Figure 5.10: Definition of the FFD box for the shuttle airfoil verification test case.

Node	$\vec{x}$
(0,0,0)	{ -1.921E-1, -1.000E-3, -3.866E-1 }
(4,0,0)	{ 7.100E0, -1.000E-3, -3.866E-1 }
(4,2,0)	{ 7.100E0, 1.001E0, -3.866E-1 }
(0,2,0)	{ -1.921E-1, 1.001E0, -3.866E-1 }
(0,0,1)	{ -1.921E-1, -1.000E-3, 6.243E-1 }
(4,0,1)	{ 7.100E0, -1.000E-3, 6.243E-1 }
(4,2,1)	{ 7.100E0, 1.001E0, 6.243E-1 }
(0,2,1)	{ -1.921E-1, 1.001E0, 6.243E-1 }

Table 5.7: Corners of the FFD box surrounding the Shuttle wing section.

**Results** Flow field solutions are computed after specifying far field boundaries on the inflow and outflow faces of the computational domain, symmetry boundaries on the faces aligned with the  $y$ -axis, and appropriate wall boundary conditions corresponding to Case 1 and Case 2 on the wing surface. The spatial integration for the flow problem uses the AUSM and corrected average gradient

DV #	FFD Index	$\Delta \vec{x}$
1	(0,1,0)	{ 0.0, 0.0, -1.0 }
2	(1,1,0)	{ 0.0, 0.0, -1.0 }
3	(2,1,0)	{ 0.0, 0.0, -1.0 }
4	(3,1,0)	{ 0.0, 0.0, -1.0 }
5	(4,1,0)	{ 0.0, 0.0, -1.0 }
6	(0,1,1)	{ 0.0, 0.0, 1.0 }
7	(1,1,1)	{ 0.0, 0.0, 1.0 }
8	(2,1,1)	{ 0.0, 0.0, 1.0 }
9	(3,1,1)	{ 0.0, 0.0, 1.0 }
10	(4,1,1)	{ 0.0, 0.0, 1.0 }

Table 5.8: Shuttle airfoil design variable definitions.

methods for the convective and viscous fluxes. Backward Euler implicit time integration, with local time-stepping, is used to converge the  $N_2$  density residual six orders of magnitude in Case 1, and four orders of magnitude in Case 2.

Flow field solutions, showing Mach number,  $N_2$  mass fraction, and  $T^{ve}$  for both cases are shown in Fig. (5.11). Despite identical free stream conditions, the near field flow environment is strongly influenced by the boundary conditions enforced on the wing surface. An examination of the Mach fields indicates thinner boundary layer profiles in Case 2, as compared to Case 1, which is a byproduct of the influence of the cold-wall on the dynamic viscosity near the surface of the wing. Quantitatively, this is substantiated by the converged values for  $C_D = 0.62118$  and  $C_D = 0.54683$  for Cases 1 and 2 respectively. Boundary layer thickness affects the leading bow shock by increasing the apparent thickness of the wing, which, in turn, affects the boundary layer; this phenomena is known as ‘viscous interaction’ in the hypersonic community. An examination of the mass fraction and vibrational-electronic temperature plots provides insight on the near field thermochemical state of the gas. In Case 1, high temperatures and lower flow velocities in the boundary layer leads to a substantial amount of  $N_2$  dissociation that persists in to the wake of the wing, while the cold-wall, forced recombination in Case 2 dramatically reduces the chemical reactivity in the boundary layer. As a consequence, particularly large thermal and mass fraction gradients are present in the wall normal direction of Case 2.

The adjoint equations are solved after applying the appropriate boundary conditions, described in Section 3.7. Spatial integration of the adjoint fluxes is performed using the Steger-Warming and corrected average gradient methods for the convective and viscous fluxes, respectively. After initializing the adjoint state to the free stream,  $\Psi_\infty = \vec{0}$ , everywhere in the domain, the adjoint state is marched forward in time using an implicit time integration scheme, with local time-stepping, to four orders of magnitude convergence in the adjoint  $N_2$  density variables for both Case 1 and 2.

Solutions to the adjoint problem in the volume are shown for Case 1 and 2 in Fig. (5.12). The plots indicate critical regions of dependence near the leading edge of the wing around the stagnation point. Structures in the adjoint solution can be seen extending from the wing trailing edge toward

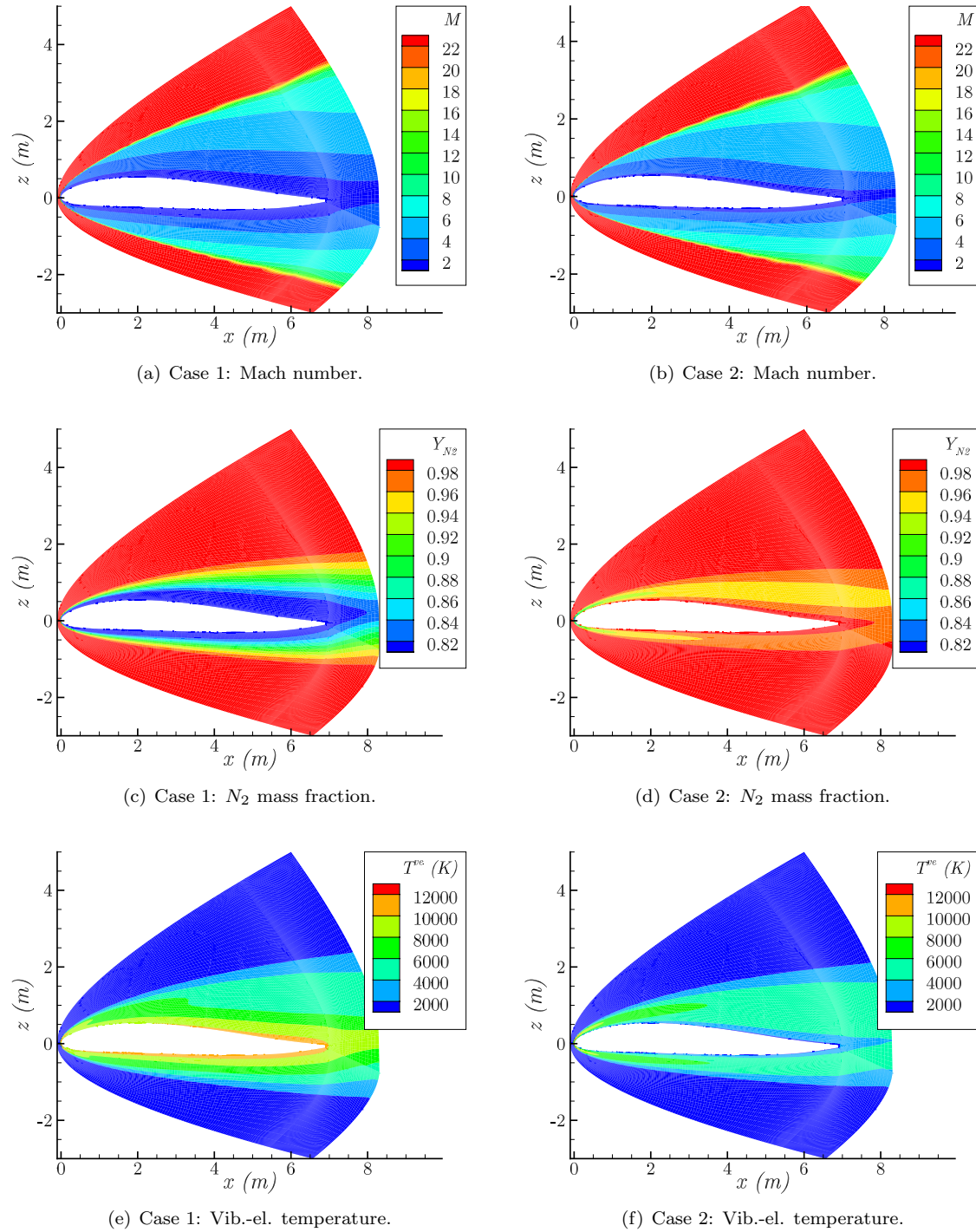


Figure 5.11: Flow field solutions for Case 1 and Case 2 of the Shuttle airfoil.

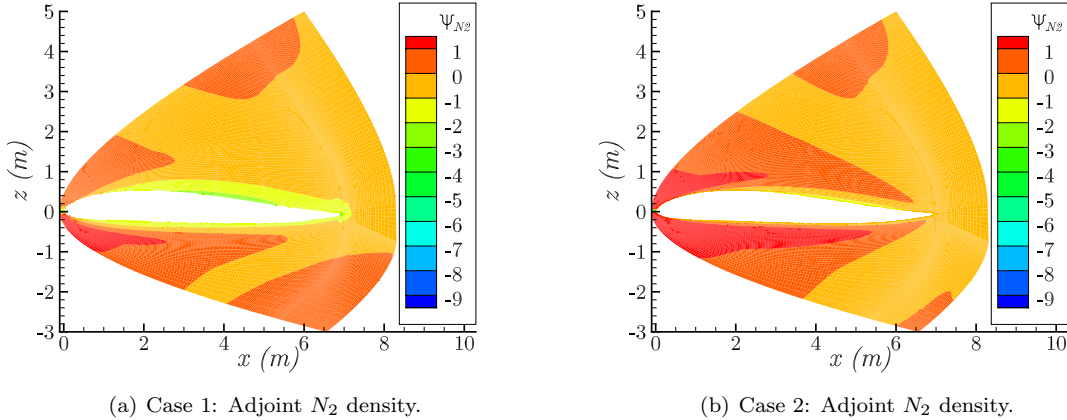


Figure 5.12: Adjoint field solutions for Case 1 and Case 2 of the Shuttle airfoil.

the inflow boundary. This shows a reversal in the characteristic wave propagation of the adjoint problem as compared to the flow problem, which is a byproduct of the negative sign introduced by the formation of the Lagrangian. Surface sensitivity plots for the wing are shown in Fig. (5.13) for Case 1 and 2. In these sensitivity maps, the leading edge is at the left of each subfigure, and the trailing edge is on the right. In both cases, the geometric sensitivity of the wing is highest near the nose, extending back toward the quarter-chord, where the flow is strongly compressed and rapidly expanded around the airfoil profile. As before, the sensitivity maps include the local dual-grid face area in the computation of  $\partial\mathcal{J}/\partial S$ , which accounts for the spanwise variation of the sensitivity. When the local area is not included, no spanwise variation in  $\partial\mathcal{J}/\partial S$  is present. Recalling that negative values of the surface sensitivity lead to increases in  $C_D$ , and vice versa, the trends in geometric sensitivity follow those expected from hypersonic aerodynamics. As the nose radius is decreased, through locally normal deformations near the stagnation point, drag is reduced via a reduction in the shock strength. Conversely, as the total airfoil thickness is increased further aft of the stagnation point, shock strength increases and  $C_D$  increases.

Finite-difference and adjoint gradients are computed by imposing a  $0.005 \times \Delta\vec{x}$  motion of the FFD control point design variables in Tab. (5.8), and the results are shown in Figs. (5.14) and (5.15) for Case 1 and 2 respectively. Qualitatively, good agreement exists between the finite-difference and adjoint gradients, though not to the extent exhibited in the inviscid test case, shown in Fig. (5.7). This is likely due to several reasons linked to the complexities of the viscous environment. Section 3.7 derives the adjoint surface sensitivities, which depend on many contributing terms from the various convective and viscous phenomena at the surface. These terms depend on gradient information in the flow and adjoint solutions, primarily in wall-normal and wall-tangential directions. Often these terms are large in magnitude, but opposite in sign, which makes  $\partial\mathcal{J}/\partial S$  particularly susceptible to numerical error. In the spatial integration of the adjoint convective fluxes, a Steger-Warming method is used, which is known to be very stable, but also quite numerically dissipative. In the

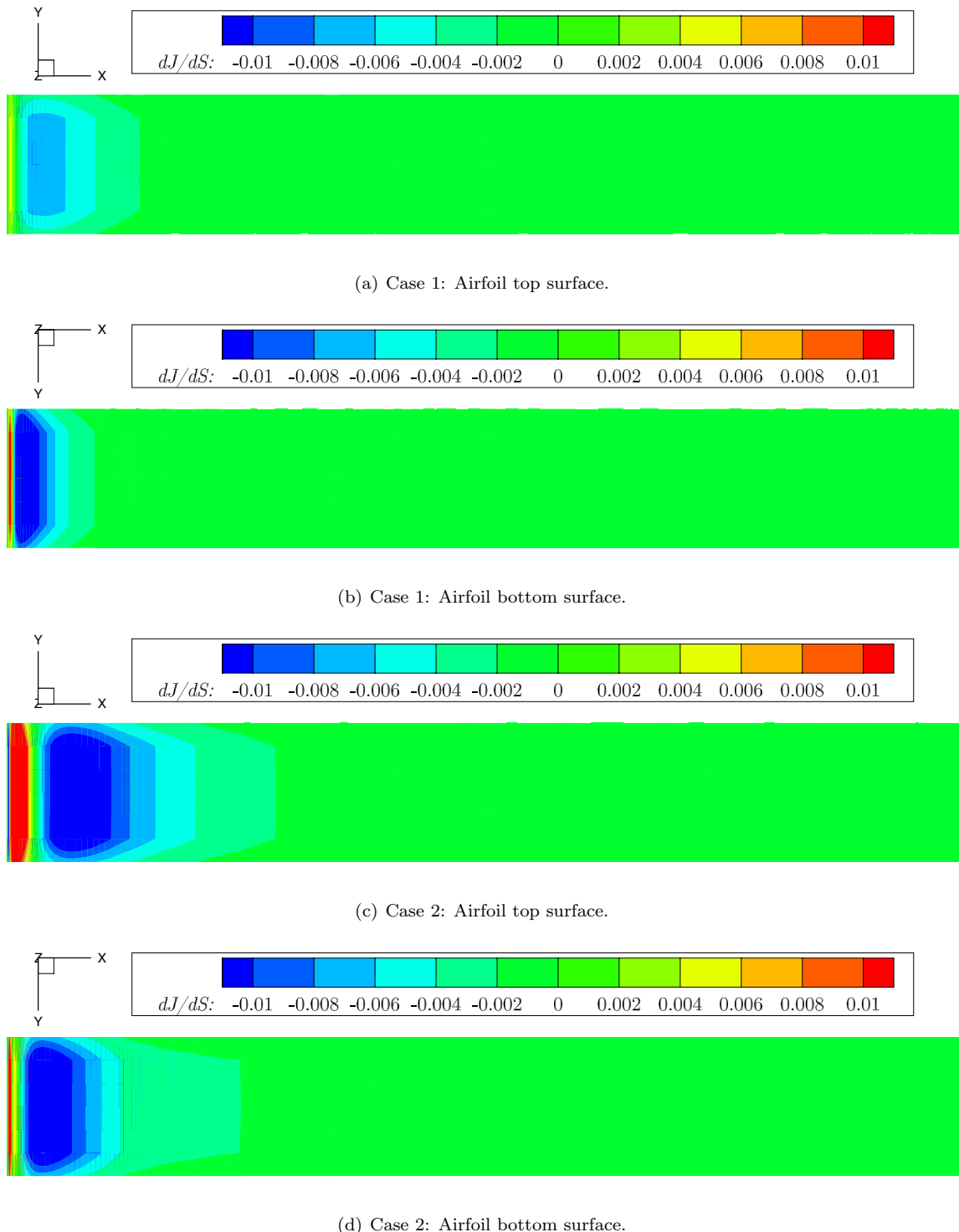


Figure 5.13: Adjoint surface sensitivity maps for Case 1 and Case 2 of the Shuttle airfoil.

flow problem, Steger-Warming is unsuitable for resolving boundary layer flows because the artificial dissipation can significantly corrupt the accuracy of the solution, and it is likely that the same issue is affecting the accuracy of the adjoint state in the boundary layer. A comparison of the performance of the adjoint methods in Case 1 and Case 2, relative to the finite-difference results, corroborates this claim. The adjoint-based gradient for Case 2 is computed primarily using wall-normal derivative information, which is much larger in magnitude than the wall-tangential gradient information, and, consequently, more affected by the artificial dissipation of the numerical method. Case 1, conversely, is computed primary from wall-tangential gradient information, which is captured more accurately, leading to better agreement.

A simplifying assumption is applied to the adjoint problem which may also be contributing to the discrepancies between the adjoint and finite-difference gradients. For this case, the source term,  $(\nabla \Psi^T \cdot \vec{F}^{vk})(\partial \mu^k / \partial U)$ , is omitted from the adjoint equations. This ‘frozen viscosity’ technique is a common simplifying assumption applied in the solution of the adjoint equations, but may not be appropriate in the hypersonic regime because of the larger thermal gradients in the boundary layer. The transport coefficients are a function of temperature, and, since the temperature varies strongly in the boundary layers of hypersonic vehicles, that dependence is not being captured and it may be significant, particularly in Case 2 where the thermal gradients are largest.

The gradient comparison for both Case 1 and Case 2 are favorable, and speak to the power of the adjoint method. These numerical experiments prove the adjoint equations of Chapter 3 may be solved in viscous environments to provide accurate gradient information from high-fidelity simulation tools. It is also clear that the numerical implementation of the adjoint system strongly affects the accuracy of the gradient information. This is not unlike solving the nonequilibrium flow problem, where the numerical methods strongly impact the accuracy of the simulation. For the flow problem, a body of literature exists to combat these challenges, but no such body of literature is present for adjoint methods in hypersonic environments. Additional research is necessary, but fortunately, the continuous formulation of the adjoint problem permits great flexibility in the numerical treatment of the adjoint equations.

At this point, it is difficult to draw general conclusions about the use of adjoint methods in the hypersonic nonequilibrium environment. At times, excellent agreement exists between the finite-difference and adjoint gradients, such as design variables 1-5 of Case 1. However, those same design variables under different boundary conditions in Case 2 are substantially less accurate. Several possible explanations for the observed discrepancies are posed in this section, and, clearly, additional research is necessary to isolate the effects of the mesh, the numerical methods, and the underlying assumptions in the formulation of the adjoint on the gradient accuracy. Additional tests, under carefully controlled conditions, will provide the clues necessary to improve the accuracy and reliability of adjoints in the hypersonic environment.

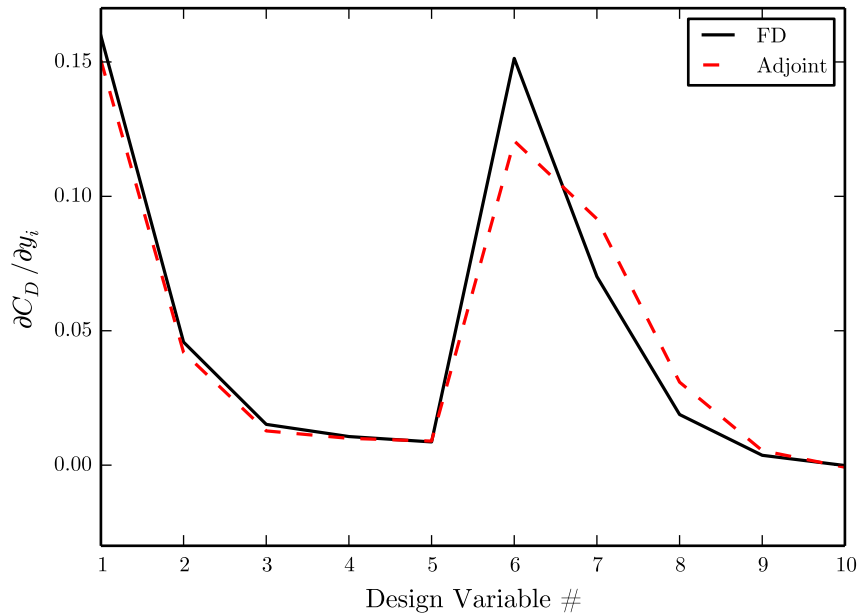


Figure 5.14: Case 1: Shuttle airfoil gradient verification.

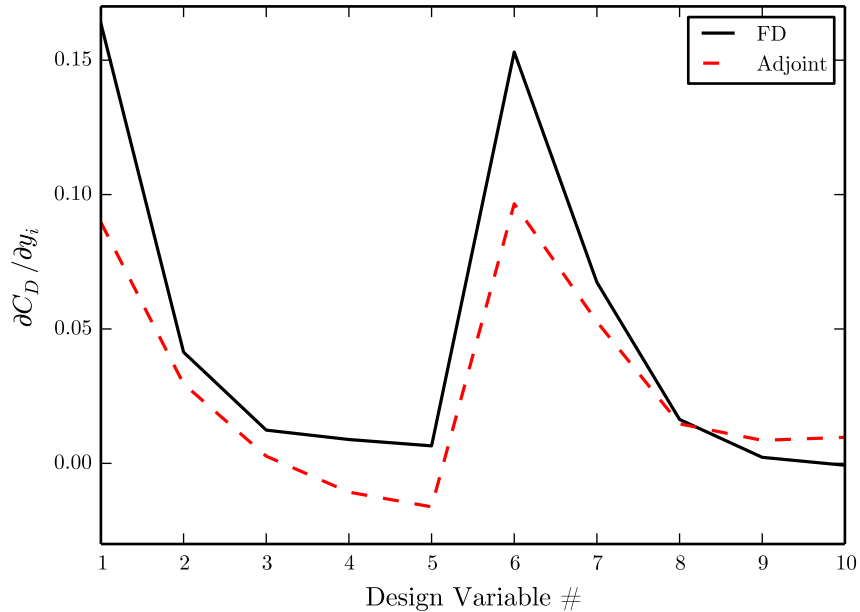


Figure 5.15: Case 2: Shuttle airfoil gradient verification.



## Chapter 6

# Conclusions & Future Work

This thesis pursues the formulation of the adjoint problem for high-enthalpy gas mixtures in thermochemical nonequilibrium for the purpose of delivering an efficient mechanism for computing gradient information from high-fidelity, hypersonic simulation tools. Such a capability enables the use of powerful analysis and design techniques, including optimal shape design, uncertainty quantification, error estimation early in the design phase of hypersonic systems. These methodologies can be used to quantitatively determine optimal vehicle configurations and assess the reliability and robustness of those systems. It is the author's opinion that these methodologies will be necessary to design entry systems capable of meeting the near-term objectives of government space agencies and the commercial space industry. The following three objectives guide the development of this work:

1. Derive, for the first time, the continuous adjoint equations, boundary conditions, and surface sensitivities for high-enthalpy gas mixtures in thermochemical nonequilibrium.
2. Implement the adjoint problem in an unstructured FVM solver and prove the equations can be solved, providing accurate gradient information.
3. Allow, to the greatest extent possible, flexibility and extensibility in the adjoint formulation to accommodate a variety of thermochemical models.

These objectives address the theoretical foundation of the procedure, its practical application in modern analysis frameworks, and the extensibility of the method, so that others in the community may build upon it for their own, specific applications.

Chapter 3 presents the formulation of the adjoint problem for viscous, nonequilibrium environments using differential geometry and a linearization procedure for the viscous fluxes. Projected-force and thermal objective functions are treated for a variety of boundary conditions on the chemical, momentum, and thermal states at the wall to accommodate aerothermodynamic shape design of hypersonic systems under a variety of conditions. Special care is applied in the formulation of the adjoint surface sensitivities to avoid second derivative information that is challenging to acquire in unstructured FVM solvers. However, by formulating the adjoint problem from the continuous

governing equations, any consistent numerical representation of the adjoint equations, boundary conditions, and surface sensitivities may be used, opening a rich area of further research.

Chapters 4 and 5 describe the numerical implementation of the adjoint problem and test its accuracy via a series of numerical verification tests. A procedure is developed, using the method of lines, to solve the adjoint linear system of equations. In doing so, the same solver infrastructure may be used to solve both the flow and adjoint problems, streamlining the development of the analysis software. To integrate the non-conservative adjoint fluxes, both upwind and centered spatial integration schemes were developed and employed. The verification tests prove the adjoint system of Chapter 3 may be solved, and that the output sensitivities are of good quality for both inviscid and viscous flow problems. Some discrepancies between the adjoint and finite-difference gradients exist, particularly in the viscous cases, which are likely due to a combination of factors related to the numerical techniques employed to solve the adjoint problem.

While the work contained in this thesis addresses the aforementioned research objectives, it is clear that additional research is necessary to improve the quality of the gradient information acquired from the solution of the hypersonic adjoint problem. An assessment of the viscous verification results, discussed more thoroughly in Section 5.2 points toward the susceptibility of the adjoint problem to errors in the accuracy of the gradients in the flow and adjoint states within the computational domain. Numerically dissipative spatial integration schemes, such as the Steger-Warming and Lax-Friedrich methods employed in adjoint problem for this work, provide stability but are not likely not accurate enough to sufficiently resolve the steep gradients near the wall. The observed discrepancies in the adjoint and finite-difference gradients may also be affected by a variety of other simplifications to the adjoint problem that have been applied out of convenience for the numerical representation of the adjoint system. Specifically, the simplifications applied in the derivation corresponding to the linearization of the viscous fluxes to arrive at the  $\bar{D}^{vk}$  terms, the omission of the transport coefficient term,  $(\nabla \Psi^\top \cdot \vec{F}^{vk})(\partial \mu^k / \partial U)$ , by applying the ‘frozen viscosity’ assumption, and the refactoring of the surface sensitivities to eliminate second derivatives, may all be affecting the gradient accuracy, and isolating the effect of these simplifying assumptions is an item of key importance moving forward.

All signs point toward the need for additional investment in developing numerical methods for the hypersonic adjoint problem. Fortunately, numerical methods for the hypersonic flow problem have advanced tremendously in the last two decades, and there are opportunities to apply these methods to the adjoint system. Accurately representing the nonequilibrium flow environment using an unstructured FVM architecture is a well documented challenge, and there is value in recognizing the advantages of structured mesh topologies and finite-element techniques. The convenience of high-order accuracy spatial integration schemes with these solver architectures make them very attractive for the adjoint problem and warrant investigation.

The work contained in this thesis represents a first step toward adjoint-based design for the hypersonic community. From the foundation established here, it is important to expand the capabilities of the adjoint problem to address additional physical processes that are present in the hypersonic environment. For CFD, sophisticated boundary conditions are necessary to accurately model surface catalycity, mass injection from TPS pyrolysis gases, and surface energy balance via

re-radiation. Derivations of the corresponding adjoint boundary conditions and surface sensitivities would enable vehicle design under these, more realistic, boundary conditions. Turbulence modeling continues to be a tremendous challenge for the numerical simulation of aerospace environments, and it is particularly true in the hypersonic regime. Sensitivity data from the adjoint method may be used to identify critical turbulence model parameters and lead to more accurate models. Doing so requires the formulation of the adjoint problem that includes, not just the nonequilibrium thermochemistry, but also the conservation equations for the turbulence model. For many entry systems, energy transfer via radiation from the shock layer can be a significant fraction of the overall thermal transport to the vehicle. Certainly, accommodating radiative processes in the adjoint problem is critically important in accurately predicting the thermal performance of a hypersonic vehicle. Accommodating these physical models in an adjoint-based framework requires formulation and coupling of the various adjoint systems, which has been proven for aeroelastic problems in commercial aviation, but not for aerothermodynamic problems.

Looking further into the future, the real power of adjoint-based design lies in the integrated aerodynamic and thermal design of entry systems. If the flow physics, which may include turbulence and radiation, are accommodated in the flow and adjoint problems, then aerodynamic sensitivities are well-captured using the projected-force objective function derived in this work. The thermal objective, of Section 3.3.2, may be used for the thermal design of entry systems, but misses the true objective, which is to arrive at the minimum safe TPS thickness. By formulating the adjoint problem for the mathematical model that governs the material response of ablative TPS systems, it may be possible to specify a not-to-exceed bond line temperature at the back of the heat shield, and perform an integrated aerodynamic and thermal design that targets the true thermal objective. In this way, truly ‘aerothermodynamically’ optimal vehicle designs are possible.



# Appendix A

## Thermochemical Parameters

Chapter 2 describes, in detail, the thermochemical models used in this work for simulating high-enthalpy, nonequilibrium gas mixtures. This appendix contains the relevant information pertaining to the parameters required for the thermodynamic, chemical, and transport coefficient models.

### A.1 Species Properties

The RRHO thermodynamic model requires basic properties regarding the structure of the chemical constituents in the gas mixture. Total mixture energy is determined by summing the contributions from the translational, rotational, vibrational, and electronic energy modes of each species, provided by Eqns. (2.30), (2.31), (2.32), (2.33) respectively. Tab. (A.1) contains the molar masses, formation enthalpies, rotational modes, and characteristic vibrational temperatures of the chemical species used in the two gas models of this work,

Species	Mass (kg/kmol)	$h^\circ$ (J/kg)	$\xi_s$	$\theta^{vib}$ (K)
$N_2$	28.013	0.0	2	3395.0
$O_2$	31.999	0.0	2	2239.0
$NO$	30.006	3.00E+6	2	2817.0
$N$	14.007	3.36E+7	0	N/A
$O$	15.999	1.54E+7	0	N/A

Table A.1: Species chemical properties.

### A.2 Electronic Energy Parameters

The species electronic energy is determined by evaluating the energy contained in the equilibrium Maxwellian distribution function at the vibrational-electronic temperature, given by Eqn. (2.33) and

restated below,

$$e_s^{el} = \begin{cases} \frac{R}{M_s} \frac{\sum_{i=1}^{\infty} g_{i,s} \theta_{i,s}^{el} \exp(-\theta_{i,s}^{el}/T^{ve})}{\sum_{i=0}^{\infty} g_{i,s} \exp(-\theta_{i,s}^{el}/T^{ve})} & \text{for } s \notin \mathcal{E}, \\ \frac{3}{2} \frac{R}{M_s} T^{ve} & \text{for } s \in \mathcal{E}. \end{cases}$$

The electron energy is summed over the energy levels,  $i$ , and requires data on the species energy level degeneracy,  $g_{i,s}$ , and the characteristic electronic temperature,  $\theta_{i,s}^{el}$  provided in Tabs. (A.2)-(A.6).

Level	$\theta_{i,N_2}^{el}$ (K)	g
0	0.000000000000000E+00	1
1	7.223156514095200E+04	3
2	8.577862640384000E+04	6
3	8.605026716160000E+04	6
4	9.535118627874400E+04	3
5	9.805635702203200E+04	1
6	9.968267656935200E+04	2
7	1.048976467715200E+05	2
8	1.116489555200000E+05	5
9	1.225836470400000E+05	1
10	1.248856873600000E+05	6
11	1.282476158188320E+05	6
12	1.338060936000000E+05	10
13	1.404296391107200E+05	6
14	1.504958859200000E+05	6

Table A.2:  $N_2$  electron energy data.

Level	$\theta_{i,O_2}^{el}$ (K)	g
0	0.000000000000000E+00	3
1	1.139156019700800E+04	2
2	1.898473947826400E+04	1
3	4.755973576639200E+04	1
4	4.991242097343200E+04	6
5	5.092268575561600E+04	3
6	7.189863255967200E+04	3

Table A.3:  $O_2$  electron energy data.

Level	$\theta_{i,NO}^{el}$ (K)	g
0	0.000000000000000E+00	4
1	5.467345760000000E+04	8
2	6.317139627802400E+04	2
3	6.599450342445600E+04	4
4	6.906120960000000E+04	4
5	7.049998480000000E+04	4
6	7.491055017560000E+04	4
7	7.628875293968000E+04	2
8	8.676188537552000E+04	4
9	8.714431182368000E+04	2
10	8.886077063728000E+04	4
11	8.981755614528000E+04	4
12	8.988445919208000E+04	2
13	9.042702132000000E+04	2
14	9.064283760000000E+04	2
15	9.111763341600000E+04	4

Table A.4: NO electron energy data.

Species	Level	$\theta_{i,N}^{el}$ (K)	g
$N$	0	0.000000000000000E+00	4
$N$	1	2.766469645581980E+04	10
$N$	2	4.149309313560210E+04	6

Table A.5: N electron energy data.

Level	$\theta_{i,O}^{el}$ (K)	g
0	0.000000000000000E+00	5
1	2.277077570280000E+02	3
2	3.265688785704000E+02	1
3	2.283028632262240E+04	5
4	4.861993036434160E+04	1

Table A.6: O electron energy data.

Reaction	$C_r$ ( $cm^3/(mol \cdot s)$ )	$\eta_r$	$E_r^A$ (K)
$N_2 + N_2 \rightleftharpoons 2N + N_2$	7.0E+21	-1.60	113200
$N_2 + O_2 \rightleftharpoons 2N + O_2$	7.0E+21	-1.60	113200
$N_2 + NO \rightleftharpoons 2N + NO$	7.0E+21	-1.60	113200
$N_2 + N \rightleftharpoons 2N + NO$	3.0E+22	-1.60	113200
$N_2 + O \rightleftharpoons 2N + NO$	3.0E+22	-1.60	113200
$O_2 + N_2 \rightleftharpoons 2O + N_2$	2.0E+21	-1.50	59500
$O_2 + O_2 \rightleftharpoons 2O + O_2$	2.0E+21	-1.50	59500
$O_2 + NO \rightleftharpoons 2O + NO$	2.0E+21	-1.50	59500
$O_2 + N \rightleftharpoons 2O + N$	1.0E+22	-1.50	59500
$O_2 + O \rightleftharpoons 2O + O$	1.0E+22	-1.50	59500
$NO + N_2 \rightleftharpoons N + O + N_2$	5.0E+15	0.00	75500
$NO + O_2 \rightleftharpoons N + O + O_2$	5.0E+15	0.00	75500
$NO + NO \rightleftharpoons N + O + NO$	5.0E+15	0.00	75500
$NO + N \rightleftharpoons N + O + N$	1.1E+17	0.00	75500
$NO + O \rightleftharpoons N + O + O$	1.1E+17	0.00	75500
$N_2 + O \rightleftharpoons NO + N$	6.4E+17	-1.00	38400
$NO + O \rightleftharpoons O_2 + N$	8.4E+12	0.00	19450

Table A.7: Arrhenius parameters for the forward reaction rate coefficient.

### A.3 Reaction Rate Parameters

The finite-rate chemical model is discussed in detail in Section 2.4. The model uses the Law of Mass Action in conjunction with empirically determined reaction rate coefficients to establish the production and destruction rate of each chemical constituent in the mixture at the local thermodynamic state. The forward reaction rate coefficient is modeled using an Arrhenius-type equation, given in Eqn. 2.56 and restated here, as

$$k_r^f = C_r(T_r^{cf})^{\eta_r} e^{-E_r^A/(k_B T_r^{cf})}.$$

Evaluating the expression for the forward rate coefficient requires a definition of the exponential pre-factor,  $C_r$ , the exponent on the rate-controlling temperature,  $\eta_r$ , and the reaction activation energy,  $E_r^A$  for each reaction in the gas model. Tab. (A.7) defines the parameters used in this work, which were drawn from Scalabrin [125]. The backwards reaction rate coefficient is determined by evaluating the forward rate-coefficient Arrhenius equation at the backwards rate-controlling temperature, and dividing by the reaction equilibrium constant,

$$k_r^b = \frac{k_r^f}{K_r^e}.$$

Forward and backwards rate controlling temperatures,  $T_r^{cf}$  and  $T_r^{cb}$  respectively, are constructed to account for the preferential dissociation of vibrationally excited chemical species. The controlling

Reaction	$a_r^f$	$b_r^f$	$a_r^b$	$b_r^b$
$N_2 + M \rightleftharpoons 2N + M$	0.5	0.5	1.0	0.0
$O_2 + M \rightleftharpoons 2O + M$	0.5	0.5	1.0	0.0
$NO + M \rightleftharpoons N + O + M$	0.5	0.5	1.0	0.0
$N_2 + O \rightleftharpoons NO + N$	1.0	0.0	1.0	0.0
$NO + O \rightleftharpoons O_2 + N$	1.0	0.0	1.0	0.0

Table A.8: Forward and backward reaction rate coefficient controlling temperature factors.

temperature is a weighted geometric mean of the local translational-rotational and vibrational-electronic temperatures,

$$T_r^{c,f/b} = (T)^{a_r^{f/b}} (T^{ve})^{b_r^{f/b}}, \quad (\text{A.1})$$

where  $a$  and  $b$  are the weights corresponding to the forward and backward direction of each reaction. These weights may be adjusted to “tune” the model to more faithfully represent the observed behavior of a chosen gas model. This work uses the standard weighting from the Park 1990 air chemical model [113]. Dissociation reactions equally weight  $T$  and  $T^{ve}$  in the forward direction, while using only  $T$  for the backward rate controlling temperature. Exchange reactions also rely solely on the translational-rotational temperature,  $T$ , in the forward and backward directions. Explicitly, the weights for each reaction are shown in Tab. (A.8). The equilibrium reaction constant,  $K_r^e$ , is empirically fit to experimental data using five parameters,  $A_r^k$ , such that,

$$K_r^e = \exp \left[ A_r^0 \left( \frac{T^c}{10000} \right) + A_r^1 + A_r^2 \ln \left( \frac{10000}{T^c} \right) + A_r^3 \left( \frac{10000}{T^c} \right) + A_r^4 \left( \frac{10000}{T^c} \right)^2 \right],$$

where  $T^c$  is the rate-controlling temperature in (K). These parameters, also from the Park chemical model, are dependent on the local mixture number density, and are shown in Tab. (A.9). A linear interpolation is performed for each  $A_r^k$  that lies inside the tabulated number density range. When  $N$  falls outside this range, the appropriate minimum or maximum tabulated value is used. The rate coefficients and equilibrium constant are evaluated at the appropriate forward and backward rate-controlling temperature,  $T_r^c$ . This rate-controlling temperature is constructed to account for the preferential dissociation of vibrationally excited molecules, such that,

## A.4 Transport Coefficient Parameters

The transport coefficients are determined using a combination of empirically-derived models for high-temperature air, and they are discussed in detail in Section 2.3.2. The mixture viscosity and thermal conductivity is determined using Wilke’s semi-empirical mixing rule [147] in conjunction with Blottner’s three-parameter curve fits [7] for high temperature air species given by Eqns. (2.49)

and (2.51), restated here,

$$\mu = \sum_s \frac{X_s \mu_s}{\phi_s},$$

$$\kappa = \sum_s \frac{X_s \kappa_s}{\phi_s}.$$

The species viscosities are given by,

$$\mu_s = 0.1 \exp [(A_s \ln T + B_s) \ln T + C_s],$$

where  $T$  is the translational-rotational temperature in (K) and the parameters,  $A$ ,  $B$ , and  $C$  are provided in Tab. (A.10).

The species-mixture diffusion coefficients are calculated using an aggregate of the species-species binary diffusion coefficients, given by Eqn. (2.45) and restated here,

$$\rho D_{ij} = 7.1613 \times 10^{-25} \frac{M \sqrt{T \left( \frac{1}{M_i} + \frac{1}{M_j} \right)}}{\Omega_{ij}^{(1,1)}}.$$

Inter-species (1,1) collision integral,  $\Omega_{ij}^{(1,1)}$ , is evaluated using a four-parameter empirical curve fit given by,

$$\pi \Omega_{ij}^{(m,n)} = D^\Omega T^{[A^\Omega (\ln T)^2 + B^\Omega \ln T + C^\Omega]}.$$

Reaction	$N(1/cm^3)$	$A_0$	$A_1$	$A_2$	$A_3$	$A_4$
$N_2 + M \rightleftharpoons 2N + M$	1E+14	3.4907	0.83133	4.0978	-12.728	0.07487
	1E+15	2.0723	1.38970	2.0617	-11.828	0.015105
	1E+16	1.6060	1.57320	1.3923	-11.533	-0.004543
	1E+17	1.5351	1.60610	1.2993	-11.494	-0.00698
	1E+18	1.4766	1.62910	1.2153	-11.457	-0.00944
$O_2 + M \rightleftharpoons 2O + M$	1E+14	1.8103	1.9607	3.5716	-7.3623	0.083861
	1E+15	0.91354	2.3160	2.2885	-6.7969	0.046338
	1E+16	0.64183	2.4253	1.9026	-6.6277	0.035151
	1E+17	0.55388	2.4600	1.7763	-6.5720	0.031445
	1E+18	0.52455	2.4715	1.7342	-6.55534	0.030209
$NO + M \rightleftharpoons N + O + M$	1E+14	0.50989	2.4773	1.7132	-6.5441	0.029591
	1E+15	2.1649	0.078577	2.8508	-8.5422	0.053043
	1E+16	1.0072	0.53545	1.1911	-7.8098	0.004394
	1E+17	0.63817	0.68189	0.66336	-7.5773	-0.011025
	1E+18	0.55889	0.71558	0.55396	-7.5304	-0.014089
$N_2 + O \rightleftharpoons N + O + M$	1E+14	0.5150	0.73286	0.49096	-7.5025	-0.015938
	1E+15	0.50765	0.73575	0.48042	-7.4979	-0.016247
	1E+16	1.3261	0.75268	1.2474	-4.1857	0.02184
	1E+17	1.0653	0.85417	0.87093	-4.0188	0.010721
	1E+18	0.96794	0.89131	0.7291	-3.9555	0.006488
$NO + O \rightleftharpoons N + O + M$	1E+14	0.97646	0.89043	0.74572	-3.9642	0.007123
	1E+15	0.96188	0.89617	0.72479	-3.955	0.006509
	1E+16	0.96921	0.89329	0.73531	-3.9596	0.006818
	1E+17	0.35438	-1.8821	-0.72111	-1.1797	-0.030831
	1E+18	0.093613	-1.7806	-1.0975	-1.0128	-0.041949
$NO + O \rightleftharpoons O_2 + N$	1E+15	-0.003732	-1.7434	-1.2394	-0.94952	-0.046182
	1E+16	0.004815	-1.7443	-1.2227	-0.95824	-0.045545
	1E+17	-0.009758	-1.7386	-1.2436	-0.949	-0.046159
	1E+18	-0.002428	-1.7415	-1.2331	-0.95365	-0.04585

Table A.9: Parameters for the Park 1990 equilibrium reaction constants.

Species	A	B	C
$N_2$	2.68E-2	3.18E-1	-1.13E+1
$O_2$	4.49E-2	-8.26E-2	-9.20E0
$NO$	4.36E-2	-3.36E-2	-9.58E0
$N$	1.16E-2	6.03E-1	-1.24E+1
$O$	2.03E-2	4.29E-1	-1.16E+1

Table A.10: Blottner viscosity parameters

Collision Pair	A	B	C	D
$N_2 - N_2$	-6.0614558E-03	1.2689102E-01	-1.0616948E+00	8.0955466E+02
$N_2 - O_2$	-3.7959091E-03	9.5708295E-02	-1.0070611E+00	8.9392313E+02
$N_2 - NO$	-1.9295666E-03	2.7995735E-02	-3.1588514E-01	1.2880734E+02
$N_2 - N$	-1.0796249E-02	2.2656509E-01	-1.7910602E+00	4.0455218E+03
$N_2 - O$	-2.7244269E-03	6.9587171E-02	-7.9538667E-01	4.0673730E+02
$O_2 - O_2$	-8.0682650E-04	1.6602480E-02	-3.1472774E-01	1.4116458E+02
$O_2 - NO$	-6.4433840E-04	8.5378580E-03	-2.3225102E-01	1.1371608E+02
$O_2 - N$	-1.1453028E-03	1.2654140E-02	-2.2435218E-01	7.7201588E+01
$O_2 - O$	-4.8405803E-03	1.0297688E-01	-9.6876576E-01	6.1629812E+02
$NO - NO$	-0.0000000E+00	-1.1056066E-02	-5.9216250E-02	7.2542367E+01
$NO - N$	-1.5770918E-03	1.9578381E-02	-2.7873624E-01	9.9547944E+01
$NO - O$	-1.0885815E-03	1.1883688E-02	-2.1844909E-01	7.5512560E+01
$N - N$	-9.6083779E-03	2.0938971E-01	-1.7386904E+00	3.3587983E+03
$N - O$	-7.8147689E-03	1.6792705E-01	-1.4308628E+00	1.6628859E+03
$O - O$	-6.4040535E-03	1.4629949E-01	-1.3892121E+00	2.0903441E+03

Table A.11:  $\Omega_{i,j}^{(1,1)}$  collision integral correlation parameters.

# Appendix B

## Jacobian Matrices

Chapters 2, 3, and 4 discuss the formulation and discretization of the nonequilibrium flow and adjoint problems. The mathematical modeling of the environment relies heavily on the definition of the Jacobian matrices of the convective and viscous flux vectors. This appendix contains additional details pertaining to these Jacobian matrices that are not included in the research narrative discussed in the body of this thesis.

### B.1 Derivatives of the Primitive Variables

Derivatives of the primitive variables,  $T$ ,  $T^{ve}$ , and  $p$  are referenced throughout this work in an effort to maintain generality in the formulation of the direct and adjoint problems. This is done so that the insertion of other chemical models by the research community may be performed with a minimal amount of re-derivation. This section presents the derivatives of these variables with respect to the conserved quantities for the thermochemical model discussed in Chapter 2.

An explicit relation for translational-rotational temperature may be derived from the definition of the mixture total and vibrational-electronic energies of Eqns. (2.28) and (2.29) using the RRHO model for the energy modes, given by Eqns.(2.30)-(2.33). When inverted, translational-rotational temperature may be written as

$$T = \frac{\rho e - \rho e^{ve} - \sum_k \rho_k e_k^\circ - \frac{1}{2} \frac{(\rho \vec{u} \cdot \rho \vec{u})}{\sum_k \rho_k}}{\sum_k \rho_k C_{v,k}^{tr}}. \quad (\text{B.1})$$

Differentiating with respect to the conserved variables yields

$$\frac{\partial T}{\partial \rho_r} = \frac{-e_r^\circ + \frac{1}{2}\vec{u} \cdot \vec{u}}{\sum_k \rho_k C_{v,k}^{tr}} - T \frac{C_{v,r}^{tr}}{\sum_k \rho_k C_{v,k}^{tr}} \quad (\text{B.2a})$$

$$\frac{\partial T}{\partial \rho u} = \frac{-u}{\sum_k \rho_k C_{v,k}^{tr}} \quad (\text{B.2b})$$

$$\frac{\partial T}{\partial \rho v} = \frac{-v}{\sum_k \rho_k C_{v,k}^{tr}} \quad (\text{B.2c})$$

$$\frac{\partial T}{\partial \rho w} = \frac{-w}{\sum_k \rho_k C_{v,k}^{tr}} \quad (\text{B.2d})$$

$$\frac{\partial T}{\partial \rho e} = \frac{1}{\sum_k \rho_k C_{v,k}^{tr}} \quad (\text{B.2e})$$

$$\frac{\partial T}{\partial \rho e^{ve}} = \frac{-1}{\sum_k \rho_k C_{v,k}^{tr}}. \quad (\text{B.2f})$$

Unlike the translational-rotational temperature, the vibrational-electronic temperature may not be written explicitly as a function of the conserved variables. Derivatives of  $T^{ve}$  with respect to  $U$  are determined using the definition of the vibrational-electronic energy,

$$\rho e^{ve} = \sum_k \rho_k e_k^{ve} \quad (\text{B.3})$$

and the chain rule of differentiation, recognizing that  $\partial e_k^{ve} / \partial U = C_{v,k}^{ve} \partial T^{ve} / \partial U$ , such that

$$\frac{\partial \rho e^{ve}}{\partial U} = \sum_k \left( \frac{\partial \rho_k}{\partial U} e_k^{ve} + \rho_k C_{v,k}^{ve} \frac{\partial T^{ve}}{\partial U} \right). \quad (\text{B.4})$$

Solving for  $(\partial T^{ve} / \partial U)$ ,

$$\frac{\partial T^{ve}}{\partial \rho_r} = \frac{-e_r^{ve}}{\sum_k \rho_k C_{v,k}^{ve}} \quad (\text{B.5a})$$

$$\frac{\partial T^{ve}}{\partial \rho u} = 0 \quad (\text{B.5b})$$

$$\frac{\partial T^{ve}}{\partial \rho v} = 0 \quad (\text{B.5c})$$

$$\frac{\partial T^{ve}}{\partial \rho w} = 0 \quad (\text{B.5d})$$

$$\frac{\partial T^{ve}}{\partial \rho e} = 0 \quad (\text{B.5e})$$

$$\frac{\partial T^{ve}}{\partial \rho e^{ve}} = \frac{1}{\sum_k \rho_k C_{v,k}^{ve}}. \quad (\text{B.5f})$$

From Dalton's law of partial pressure, the mixture pressure can be expressed in terms of the

species densities and temperature as

$$p = \sum_k \rho_k \frac{R}{M_k} T = \sum_k \rho_k R_k T, \quad (\text{B.6})$$

where  $R$  is the universal gas constant and  $R_k$  is the species gas constant. Using the definitions of the temperature derivatives from Eqn. (B.2), the pressure derivatives may be expressed as

$$\frac{\partial p}{\partial \rho_r} = R_r T + \sum_k \rho_k R_k \frac{\partial T}{\partial \rho_r} \quad (\text{B.7a})$$

$$\frac{\partial p}{\partial \rho_u} = \sum_k \rho_k R_k \frac{\partial T}{\partial \rho_u} \quad (\text{B.7b})$$

$$\frac{\partial p}{\partial \rho_v} = \sum_k \rho_k R_k \frac{\partial T}{\partial \rho_v} \quad (\text{B.7c})$$

$$\frac{\partial p}{\partial \rho_w} = \sum_k \rho_k R_k \frac{\partial T}{\partial \rho_w} \quad (\text{B.7d})$$

$$\frac{\partial p}{\partial \rho_e} = \sum_k \rho_k R_k \frac{\partial T}{\partial \rho_e} \quad (\text{B.7e})$$

$$\frac{\partial p}{\partial \rho e^{ve}} = \sum_k \rho_k R_k \frac{\partial T}{\partial \rho e^{ve}}. \quad (\text{B.7f})$$

At times, it is more convenient to use the primitive variables,  $V = [\rho_1, \dots, \rho_{n_s}, \vec{u}, p, T^{ve}]^\top$ , in the analysis of the flow and adjoint equations. Using the definitions of Eqn. (B.8),

$$\frac{\partial \rho e}{\partial \rho_s} = \left( C_{v,s}^{tr} - \frac{\overline{C_v^{tr}}}{R} \frac{R}{M_s} \right) T + e_s^{vib} + e_s^{el} + e_s^o - C_{v,s}^{tr} T^{ref} + \frac{1}{2} \vec{u} \cdot \vec{u} \quad (\text{B.8a})$$

$$\frac{\partial \rho e}{\partial \rho \vec{u}} = \rho \vec{u} \quad (\text{B.8b})$$

$$\frac{\partial \rho e}{\partial p} = \frac{\overline{C_v^{tr}}}{R} \quad (\text{B.8c})$$

$$\frac{\partial \rho e}{\partial T^{ve}} = - \frac{\overline{C_v^{tr}}}{R} \frac{R}{M_{el}} \rho_{el} + \overline{\rho C_v^{ve}}, \quad (\text{B.8d})$$

where,  $\overline{\rho C_v^k} = \sum_s \rho_s C_{v,s}^k$ ,  $\overline{C_v^k} = \overline{\rho C_v^k}/\rho$ , and  $\bar{R}$  is the local mixture gas constant. The transformation

matrix between the conserved and primitive variables is expressed as,

$$M = \frac{\partial U}{\partial V} = \begin{bmatrix} 1 & 0 & 0 & 0 & 0 & 0 \\ u & \rho & 0 & 0 & 0 & 0 \\ v & 0 & \rho & 0 & 0 & 0 \\ w & 0 & 0 & \rho & 0 & 0 \\ \frac{\partial \rho e}{\partial \rho_s} & \rho u & \rho v & \rho w & \frac{\partial \rho e}{\partial p} & \frac{\partial \rho e}{\partial T^{ve}} \\ e_s^{ve} & 0 & 0 & 0 & 0 & \frac{\partial C_v^{ve}}{\partial \rho e} \end{bmatrix}. \quad (\text{B.9})$$

## B.2 Convective Flux Jacobian

The convective flux Jacobian,  $\vec{A}^c$ , is introduced into the system of governing equations by leveraging the first-order homogeneity property of the convective flux vector,

$$\vec{F}^c = \frac{\partial \vec{F}^c}{\partial U} U = \vec{A}^c U. \quad (\text{B.10})$$

This provides a convenient mechanism through which the system of governing equations may be locally linearized and spatially integrated. Analytically, the projected convective flux Jacobian is,

$$\vec{A}^c \cdot \vec{n} = \begin{bmatrix} (\delta_{sr} - Y_s)u_n & Y_s \hat{n}_x & Y_s \hat{n}_y & Y_s \hat{n}_z & 0 & 0 \\ -uu_n + \frac{\partial p}{\partial \rho_r} n_x & u_n + u \hat{n}_x + \frac{\partial p}{\partial \rho_u} \hat{n}_x & u \hat{n}_y + \frac{\partial p}{\partial \rho_v} \hat{n}_x & u \hat{n}_z + \frac{\partial p}{\partial \rho_w} \hat{n}_x & \frac{\partial p}{\partial \rho_e} \hat{n}_x & \frac{\partial p}{\partial \rho e^{ve}} \hat{n}_x \\ -vu_n + \frac{\partial p}{\partial \rho_r} \hat{n}_y & v \hat{n}_x + \frac{\partial p}{\partial \rho_u} \hat{n}_y & u_n + v \hat{n}_y + \frac{\partial p}{\partial \rho_v} \hat{n}_y & v \hat{n}_z + \frac{\partial p}{\partial \rho_w} \hat{n}_y & \frac{\partial p}{\partial \rho_e} \hat{n}_y & \frac{\partial p}{\partial \rho e^{ve}} \hat{n}_y \\ -wu_n + \frac{\partial p}{\partial \rho_r} \hat{n}_z & w \hat{n}_x + \frac{\partial p}{\partial \rho_u} \hat{n}_z & w \hat{n}_y + \frac{\partial p}{\partial \rho_v} \hat{n}_z & u_n + w \hat{n}_z + \frac{\partial p}{\partial \rho_w} \hat{n}_z & \frac{\partial p}{\partial \rho_e} \hat{n}_z & \frac{\partial p}{\partial \rho e^{ve}} \hat{n}_z \\ \left(\frac{\partial p}{\partial \rho_r} - h\right)u_n & \frac{\partial p}{\partial \rho_u} u_n + h \hat{n}_x & \frac{\partial p}{\partial \rho_v} u_n + h \hat{n}_y & \frac{\partial p}{\partial \rho_w} u_n + h \hat{n}_z & \left(1 + \frac{\partial p}{\partial \rho_e}\right)u_n & \frac{\partial p}{\partial \rho e^{ve}} u_n \\ -e^{ve}u_n & e^{ve} \hat{n}_x & e^{ve} \hat{n}_y & e^{ve} \hat{n}_z & 0 & u_n \end{bmatrix} \quad (\text{B.11})$$

where  $u_n = (\vec{u} \cdot \vec{n})$  and  $\vec{n} = \{\hat{n}_x, \hat{n}_y, \hat{n}_z\}$ .

## B.3 Viscous Flux Jacobians

The linearized viscous flux Jacobians used in the formulation and derivation of the adjoint problem are contained in this section. Each subsection addresses one of the split viscous fluxes of Eqn. (3.28) and presents the corresponding  $\vec{A}^{vk}$  and  $\bar{\vec{D}}^{vk}$  Jacobian matrices.

### B.3.1 Diffusion

For the diffusion viscous flux vector given by

$$\vec{F}^{v1} = \begin{bmatrix} -\vec{J}_s & \bar{0} & -\sum_k \vec{J}_k h_k^{int} & -\sum_k \vec{J}_k e_k^{ve} \end{bmatrix}^T, \quad (\text{B.12})$$

the Jacobian matrix,  $\vec{A}^{v1} = \partial \vec{F}^{v1} / \partial U$  is given by,

$$A_i^{v1} = - \begin{bmatrix} \frac{\partial J_{i,s}}{\partial \rho_r} & 0 & 0 & 0 & 0 & 0 \\ 0 & 0 & 0 & 0 & 0 & 0 \\ 0 & 0 & 0 & 0 & 0 & 0 \\ 0 & 0 & 0 & 0 & 0 & 0 \\ \sum_k \eta_k & \sum_s J_{i,s} \frac{\partial h_s^{int}}{\partial \rho_u} & \sum_s J_{i,s} \frac{\partial h_s^{int}}{\partial \rho_v} & \sum_s J_{i,s} \frac{\partial h_s^{int}}{\partial \rho_w} & \sum_s J_{i,s} \frac{\partial h_s^{int}}{\partial \rho_e} & \sum_s J_{i,s} \frac{\partial h_s^{int}}{\partial \rho_e^{ve}} \\ \sum_k \xi_k & \sum_s J_{i,s} \frac{\partial e_s^{ve}}{\partial \rho_u} & \sum_s J_{i,s} \frac{\partial e_s^{ve}}{\partial \rho_v} & \sum_s J_{i,s} \frac{\partial e_s^{ve}}{\partial \rho_w} & \sum_s J_{i,s} \frac{\partial e_s^{ve}}{\partial \rho_e} & \sum_s J_{i,s} \frac{\partial e_s^{ve}}{\partial \rho_e^{ve}} \end{bmatrix}, \quad (\text{B.13})$$

where the subscript  $i$  on  $A_i^{v1}$  corresponds to the  $i^{th}$  cartesian direction. In Eqn. (B.13), the first  $s$  rows and  $r$  columns of the Jacobian, corresponding to the species density variables and the derivatives with respect to each of the  $\rho_r$ , are compressed into the first row and first column of the matrix. Definitions for the inserted terms are

$$\eta_k = \left( \frac{\partial J_{i,k}}{\partial \rho_r} h_k^{int} + J_{i,k} \frac{\partial h_k^{int}}{\partial \rho_r} \right) \quad (\text{B.14})$$

$$\xi_k = \left( \frac{\partial J_{i,s}}{\partial \rho_1} e_s^{ve} + J_{i,s} \frac{\partial e_s^{ve}}{\partial \rho_1} \right), \quad (\text{B.15})$$

and the derivatives of the internal enthalpy and vibrational-electronic energy may be determined from their respective definitions,

$$\frac{\partial h_s^{int}}{\partial U} = (R_s + C_{v,s}^{tr}) \frac{\partial T}{\partial U} + C_{v,s}^{ve} \frac{\partial T^{ve}}{\partial U} \quad (\text{B.16})$$

$$\frac{\partial e_s^{ve}}{\partial U} = C_{v,s}^{ve} \frac{\partial T^{ve}}{\partial U}. \quad (\text{B.17})$$

The derivative of the diffusion flux with respect to species density may be written as

$$\begin{aligned} \frac{\partial J_{i,s}}{\partial \rho_r} &= \frac{1}{\rho} \left[ \delta_{sr} \left( D_s - \sum_k D_k Y_k \right) - Y_s \left( D_s + D_r - 2 \sum_k D_k Y_k \right) \right] \partial_i \rho \\ &\quad + \frac{1}{\rho} (\delta_{sr} - Y_s) \sum_k \frac{D_k}{\rho} \partial_i \rho_k - \rho \frac{\partial D_s}{\partial \rho_r} \partial_i Y_s - Y_s \sum_k \rho \frac{\partial D_k}{\partial \rho_r} \partial_i Y_k \end{aligned} \quad (\text{B.18})$$

where derivatives with respect to the species diffusion coefficients have been neglected. The Jacobians  $\bar{D}^{vk} = \partial \vec{F}^{vk} / \partial \nabla U$  are

$$D_{ii}^{v1} = \begin{bmatrix} \rho D_s \frac{\partial Y_s}{\partial \rho_r} - Y_s \sum_k \rho D_k \frac{\partial Y_k}{\partial \rho_r} & 0 & 0 & 0 & 0 & 0 \\ 0 & 0 & 0 & 0 & 0 & 0 \\ 0 & 0 & 0 & 0 & 0 & 0 \\ 0 & 0 & 0 & 0 & 0 & 0 \\ \sum_s \left( \rho D_s \frac{\partial Y_s}{\partial \rho_r} - Y_s \sum_k \rho D_k \frac{\partial Y_k}{\partial \rho_r} \right) h_s^{int} & 0 & 0 & 0 & 0 & 0 \\ \sum_s \left( \rho D_s \frac{\partial Y_s}{\partial \rho_r} - Y_s \sum_k \rho D_k \frac{\partial Y_k}{\partial \rho_r} \right) e_s^{ve} & 0 & 0 & 0 & 0 & 0 \end{bmatrix}, \quad (\text{B.19})$$

and

$$D_{ij}^{v1} = \bar{0}, \quad (\text{B.20})$$

in accordance with the definitions of the various  $D_{ij}^{vk}$  from Eqn. (3.31).

### B.3.2 Viscosity

For the viscous flux vector given by

$$\vec{F}^{v2} = \begin{bmatrix} 0 & \bar{\tau} & \bar{u}^\top \bar{\tau} & 0 \end{bmatrix}^\top, \quad (\text{B.21})$$

the Jacobian matrix,  $\vec{A}^{v2} = \partial \vec{F}^{v2} / \partial U$  is given by,

$$A_i^{v2} = \begin{bmatrix} 0 & 0 & 0 & 0 & 0 & 0 \\ -\eta_{i1} & \partial_i \frac{1}{\rho} + \frac{1}{3} \partial_1 \frac{1}{\rho} \delta_{i1} & \partial_1 \frac{1}{\rho} \delta_{i2} - \frac{2}{3} \partial_2 \frac{1}{\rho} \delta_{i1} & \partial_1 \frac{1}{\rho} \delta_{i3} - \frac{2}{3} \partial_3 \frac{1}{\rho} \delta_{i1} & 0 & 0 \\ -\eta_{i2} & \partial_2 \frac{1}{\rho} \delta_{i1} - \frac{2}{3} \partial_1 \frac{1}{\rho} \delta_{i2} & \partial_i \frac{1}{\rho} + \frac{1}{3} \partial_2 \frac{1}{\rho} \delta_{i2} & \partial_2 \frac{1}{\rho} \delta_{i3} - \frac{2}{3} \partial_3 \frac{1}{\rho} \delta_{i2} & 0 & 0 \\ -\eta_{i3} & \partial_3 \frac{1}{\rho} \delta_{i1} - \frac{2}{3} \partial_1 \frac{1}{\rho} \delta_{i3} & \partial_3 \frac{1}{\rho} \delta_{i2} - \frac{2}{3} \partial_2 \frac{1}{\rho} \delta_{i3} & \partial_i \frac{1}{\rho} + \frac{1}{3} \partial_3 \frac{1}{\rho} \delta_{i3} & 0 & 0 \\ u_j \pi_{ij} & u_j \partial_j \frac{1}{\rho} \delta_{i1} + \zeta_{i1} + \frac{1}{\rho} \tau_{i1} & u_j \partial_j \frac{1}{\rho} \delta_{i2} + \zeta_{i2} + \frac{1}{\rho} \tau_{i2} & u_j \partial_j \frac{1}{\rho} \delta_{i3} + \zeta_{i3} + \frac{1}{\rho} \tau_{i3} & 0 & 0 \\ 0 & 0 & 0 & 0 & 0 & 0 \end{bmatrix}, \quad (\text{B.22})$$

where the subscript  $i$  corresponds to the  $i^{th}$  cartesian direction. As described in Section B.3.1, the first  $s$  rows and  $r$  columns of the Jacobian are compressed into a single row and column. In Eqn. (B.22),  $\delta_{ij}$  is the Kronecker delta function,

$$\delta_{sr} = \begin{cases} 1 & \text{for } i = j \\ 0 & \text{otherwise,} \end{cases} \quad (\text{B.23})$$

and  $\bar{\tau}$  is the viscous rate of strain tensor, given by

$$\bar{\tau} = -\nabla \vec{u} - \nabla \vec{u}^\top + \frac{2}{3} \nabla \cdot \vec{u}. \quad (\text{B.24})$$

The other auxiliary matrices are defined as

$$\bar{\eta} = -\frac{\partial \bar{\tau}}{\partial \rho_r} = \nabla \left( \frac{\vec{u}}{\rho} \right) + \nabla \left( \frac{\vec{u}}{\rho} \right)^\top - \frac{2}{3} \nabla \cdot \left( \frac{\vec{u}}{\rho} \right) \quad (\text{B.25a})$$

$$\bar{\pi} = \bar{\eta} - \frac{1}{\rho} \bar{\tau}, \quad (\text{B.25b})$$

$$\bar{\zeta} = \vec{u} \nabla \frac{1}{\rho} - \left( \vec{u} \nabla \frac{1}{\rho} \right)^\top + \frac{1}{3} \vec{u} \nabla \frac{1}{\rho}. \quad (\text{B.25c})$$

The Jacobians  $\bar{D}^{v2} = \partial \vec{F}^{v2} / \partial \nabla U$  are

$$D_{ii}^{v2} = \frac{1}{\rho} \begin{bmatrix} 0 & 0 & 0 & 0 & 0 & 0 \\ -(1 + \frac{1}{3}\delta_{i1})u_1 & (1 + \frac{1}{3}\delta_{i1}) & 0 & 0 & 0 & 0 \\ -(1 + \frac{1}{3}\delta_{i2})u_2 & 0 & (1 + \frac{1}{3}\delta_{i2}) & 0 & 0 & 0 \\ -(1 + \frac{1}{3}\delta_{i3})u_3 & 0 & 0 & (1 + \frac{1}{3}\delta_{i2}) & 0 & 0 \\ -(\vec{u} \cdot \vec{u}) - \frac{u_i^2}{3} & (1 + \frac{1}{3}\delta_{i1})u_1 & (1 + \frac{1}{3}\delta_{i2})u_2 & (1 + \frac{1}{3}\delta_{i3})u_3 & 0 & 0 \\ 0 & 0 & 0 & 0 & 0 & 0 \end{bmatrix} \quad (\text{B.26})$$

and

$$D_{ij}^{v2} = \frac{1}{\rho} \begin{bmatrix} 0 & 0 & 0 & 0 & 0 & 0 \\ \frac{2}{3}u_j\delta_{i1} - u_i\delta_{j1} & \delta_{i1}\delta_{j1} - \frac{2}{3}\delta_{i1}\delta_{j1} & \delta_{i2}\delta_{j1} - \frac{2}{3}\delta_{i1}\delta_{j2} & \delta_{i3}\delta_{j1} - \frac{2}{3}\delta_{i1}\delta_{j3} & 0 & 0 \\ \frac{2}{3}u_j\delta_{i2} - u_i\delta_{j2} & \delta_{i1}\delta_{j2} - \frac{2}{3}\delta_{i2}\delta_{j1} & \delta_{i2}\delta_{j2} - \frac{2}{3}\delta_{i2}\delta_{j2} & \delta_{i3}\delta_{j2} - \frac{2}{3}\delta_{i2}\delta_{j3} & 0 & 0 \\ \frac{2}{3}u_j\delta_{i3} - u_i\delta_{j3} & \delta_{i1}\delta_{j3} - \frac{2}{3}\delta_{i3}\delta_{j1} & \delta_{i2}\delta_{j3} - \frac{2}{3}\delta_{i3}\delta_{j2} & \delta_{i3}\delta_{j3} - \frac{2}{3}\delta_{i3}\delta_{j3} & 0 & 0 \\ -\frac{1}{3}u_iu_j & u_j\delta_{i1} - \frac{2}{3}u_i\delta_{j1} & u_j\delta_{i2} - \frac{2}{3}u_i\delta_{j2} & u_j\delta_{i3} - \frac{2}{3}u_i\delta_{j3} & 0 & 0 \\ 0 & 0 & 0 & 0 & 0 & 0 \end{bmatrix} \quad (\text{B.27})$$

in accordance with the definitions of the various  $D_{ij}^{vk}$  from Eqn. (3.31).

### B.3.3 Translational-rotational Thermal Conduction

For the viscous flux vector given by

$$\vec{F}^{v3} = \begin{bmatrix} 0 & \bar{0} & \nabla T & 0 \end{bmatrix}^\top, \quad (\text{B.28})$$

the Jacobian matrix,  $\vec{A}^{v3} = \partial \vec{F}^{v3} / \partial U$  is

$$A_i^{v3} = \begin{bmatrix} 0 & 0 & 0 & 0 & 0 & 0 \\ 0 & 0 & 0 & 0 & 0 & 0 \\ 0 & 0 & 0 & 0 & 0 & 0 \\ 0 & 0 & 0 & 0 & 0 & 0 \\ \partial_i \left( \frac{\partial T}{\partial \rho_r} \right) & \partial_i \left( \frac{\partial T}{\partial \rho u} \right) & \partial_i \left( \frac{\partial T}{\partial \rho v} \right) & \partial_i \left( \frac{\partial T}{\partial \rho w} \right) & \partial_i \left( \frac{\partial T}{\partial \rho e} \right) & \partial_i \left( \frac{\partial T}{\partial \rho e^{ve}} \right) \\ 0 & 0 & 0 & 0 & 0 & 0 \end{bmatrix}, \quad (\text{B.29})$$

where the subscript  $i$  corresponds to the  $i^{th}$  cartesian direction. As described in Section B.3.1, the first  $s$  rows and  $r$  columns of the Jacobian are compressed into a single row and column. The Jacobians  $\bar{D}^{v3} = \partial \vec{F}^{v3} / \partial \nabla U$  are given by

$$D_{ii}^{v3} = \begin{bmatrix} 0 & 0 & 0 & 0 & 0 & 0 \\ 0 & 0 & 0 & 0 & 0 & 0 \\ 0 & 0 & 0 & 0 & 0 & 0 \\ 0 & 0 & 0 & 0 & 0 & 0 \\ \frac{\partial T}{\partial \rho_r} & \frac{\partial T}{\partial \rho u} & \frac{\partial T}{\partial \rho v} & \frac{\partial T}{\partial \rho w} & \frac{\partial T}{\partial \rho e} & \frac{\partial T}{\partial \rho e^{ve}} \\ 0 & 0 & 0 & 0 & 0 & 0 \end{bmatrix} \quad (\text{B.30})$$

and

$$D_{ij}^{v3} = \bar{0} \quad (\text{B.31})$$

in accordance with the definitions of the various  $D_{ij}^{v3}$  from Eqn. (3.31).

### B.3.4 Vibrational-electronic Thermal Conduction

For the viscous flux vector given by

$$\vec{F}^{v4} = \begin{bmatrix} 0 & \bar{0} & \nabla T^{ve} & \nabla T^{ve} \end{bmatrix}^T \quad (\text{B.32})$$

The Jacobian matrix,  $\vec{A}^{v4} = \partial \vec{F}^{v4} / \partial U$  is

$$A_i^{v4} = \begin{bmatrix} 0 & 0 & 0 & 0 & 0 & 0 \\ 0 & 0 & 0 & 0 & 0 & 0 \\ 0 & 0 & 0 & 0 & 0 & 0 \\ 0 & 0 & 0 & 0 & 0 & 0 \\ \partial_i \left( \frac{\partial T^{ve}}{\partial \rho_r} \right) & \partial_i \left( \frac{\partial T^{ve}}{\partial \rho_u} \right) & \partial_i \left( \frac{\partial T^{ve}}{\partial \rho_v} \right) & \partial_i \left( \frac{\partial T^{ve}}{\partial \rho_w} \right) & \partial_i \left( \frac{\partial T^{ve}}{\partial \rho_e} \right) & \partial_i \left( \frac{\partial T^{ve}}{\partial \rho_{e^{ve}}} \right) \\ \partial_i \left( \frac{\partial T^{ve}}{\partial \rho_r} \right) & \partial_i \left( \frac{\partial T^{ve}}{\partial \rho_u} \right) & \partial_i \left( \frac{\partial T^{ve}}{\partial \rho_v} \right) & \partial_i \left( \frac{\partial T^{ve}}{\partial \rho_w} \right) & \partial_i \left( \frac{\partial T^{ve}}{\partial \rho_e} \right) & \partial_i \left( \frac{\partial T^{ve}}{\partial \rho_{e^{ve}}} \right) \end{bmatrix}, \quad (\text{B.33})$$

where the subscript  $i$  corresponds to the  $i^{th}$  cartesian direction. As described in Section B.3.1, the first  $s$  rows and  $r$  columns are compressed into a single row and column. The Jacobians  $\bar{D}^{v4} = \partial \vec{F}^{v4} / \partial \nabla U$  are given by

$$D_{ii}^{v4} = \begin{bmatrix} 0 & 0 & 0 & 0 & 0 & 0 \\ 0 & 0 & 0 & 0 & 0 & 0 \\ 0 & 0 & 0 & 0 & 0 & 0 \\ 0 & 0 & 0 & 0 & 0 & 0 \\ \frac{\partial T^{ve}}{\partial \rho_r} & \frac{\partial T^{ve}}{\partial \rho_u} & \frac{\partial T^{ve}}{\partial \rho_v} & \frac{\partial T^{ve}}{\partial \rho_w} & \frac{\partial T^{ve}}{\partial \rho_e} & \frac{\partial T^{ve}}{\partial \rho_{e^{ve}}} \\ \frac{\partial T^{ve}}{\partial \rho_r} & \frac{\partial T^{ve}}{\partial \rho_u} & \frac{\partial T^{ve}}{\partial \rho_v} & \frac{\partial T^{ve}}{\partial \rho_w} & \frac{\partial T^{ve}}{\partial \rho_e} & \frac{\partial T^{ve}}{\partial \rho_{e^{ve}}} \end{bmatrix} \quad (\text{B.34})$$

and

$$D_{ij}^{v4} = \bar{0} \quad (\text{B.35})$$

in accordance with the definitions of the various  $D_{ij}^{vk}$  from Eqn. (3.31).

## B.4 Eigenvalue-eigenvector Decomposition of the Convective Flux Jacobian

The eigenvalue-eigenvector decomposition of the projected flux Jacobian is used to identify the direction of information within the computational domain. Upwinding numerical schemes discussed in Sections 4.2.1 and 4.5.1 for the direct and adjoint problems rely on the eigenvalue-eigenvector decomposition to pose a stable numerical scheme based on the physical propagation as dictated by the nature of the partial differential equation system. If a matrix is full rank and has a full set of linearly independent eigenvectors, it is possible to diagonalize the matrix such that

$$\vec{A}^c \cdot \vec{n} = P \Lambda P^{-1}, \quad (\text{B.36})$$

where  $\Lambda$  is a diagonal matrix consisting of the eigenvalues of the projected flux Jacobian,  $\vec{A}^c \cdot \vec{n}$ , while  $P$  and  $P^{-1}$  are the left and right eigenvector matrices. It can be shown [41] that despite non-unique eigenvalues of  $\vec{A}^c \cdot \vec{n}$ ,

$$\Lambda = \begin{bmatrix} (\vec{u} \cdot \vec{n}) & 0 & 0 & 0 & 0 & 0 \\ 0 & (\vec{u} \cdot \vec{n}) & 0 & 0 & 0 & 0 \\ 0 & 0 & (\vec{u} \cdot \vec{n}) & 0 & 0 & 0 \\ 0 & 0 & 0 & (\vec{u} \cdot \vec{n}) + c & 0 & 0 \\ 0 & 0 & 0 & 0 & (\vec{u} \cdot \vec{n}) - c & 0 \\ 0 & 0 & 0 & 0 & 0 & (\vec{u} \cdot \vec{n}) \end{bmatrix}, \quad (\text{B.37})$$

a full set of linearly independent eigenvectors may be constructed

$$P = \begin{bmatrix} \frac{\delta_{sr}}{c^2} & 0 & 0 & \frac{Y_s}{2c^2} & \frac{Y_s}{2c^2} & 0 \\ \frac{u}{c^2} & l_x & m_x & \frac{u+cn_x}{2c^2} & \frac{u-cn_x}{2c^2} & 0 \\ \frac{v}{c^2} & l_y & m_y & \frac{v+cn_y}{2c^2} & \frac{v-cn_y}{2c^2} & 0 \\ \frac{w}{c^2} & l_z & m_z & \frac{w+cn_z}{2c^2} & \frac{w-cn_z}{2c^2} & 0 \\ \frac{(\frac{\partial p}{\partial \rho_e})(\vec{u} \cdot \vec{u}) - (\frac{\partial p}{\partial \rho_r})}{(\frac{\partial p}{\partial \rho_e})c^2} & (\vec{u} \cdot \vec{l}) & (\vec{u} \cdot \vec{m}) & \frac{[h+c(\vec{u} \cdot \vec{n})]}{2c^2} & \frac{[h-c(\vec{u} \cdot \vec{n})]}{2c^2} & -\frac{(\frac{\partial p}{\partial \rho_e v_e})}{(\frac{\partial p}{\partial \rho_e})c^2} \\ 0 & 0 & 0 & \frac{e^{ve}}{2c^2} & \frac{e^{ve}}{2c^2} & \frac{1}{c^2} \end{bmatrix} \quad (\text{B.38})$$

$$P^{-1} =$$

$$\begin{bmatrix} c^2 \delta_{sr} - Y_s \left( \frac{\partial p}{\partial \rho_r} \right) & -Y_s \left( \frac{\partial p}{\partial \rho u} \right) & -Y_s \left( \frac{\partial p}{\partial \rho v} \right) & -Y_s \left( \frac{\partial p}{\partial \rho w} \right) & -Y_s \left( \frac{\partial p}{\partial \rho e} \right) & -Y_s \left( \frac{\partial p}{\partial \rho e^{ve}} \right) \\ -(\vec{u} \cdot \vec{l}) & l_x & l_y & l_z & 0 & 0 \\ -(\vec{u} \cdot \vec{m}) & m_x & m_y & m_z & 0 & 0 \\ \frac{\partial p}{\partial \rho_r} - (\vec{u} \cdot \vec{n})c & \frac{\partial p}{\partial \rho u} + cn_x & \frac{\partial p}{\partial \rho v} + cn_y & \frac{\partial p}{\partial \rho w} + cn_z & \frac{\partial p}{\partial \rho e} & \frac{\partial p}{\partial \rho e^{ve}} \\ \frac{\partial p}{\partial \rho_r} + (\vec{u} \cdot \vec{n})c & \frac{\partial p}{\partial \rho u} - cn_x & \frac{\partial p}{\partial \rho v} - cn_y & \frac{\partial p}{\partial \rho w} - cn_z & \frac{\partial p}{\partial \rho e} & \frac{\partial p}{\partial \rho e^{ve}} \\ -e^{ve} \left( \frac{\partial p}{\partial \rho_r} \right) & -e^{ve} \left( \frac{\partial p}{\partial \rho u} \right) & -e^{ve} \left( \frac{\partial p}{\partial \rho v} \right) & -e^{ve} \left( \frac{\partial p}{\partial \rho w} \right) & -e^{ve} \left( \frac{\partial p}{\partial \rho e} \right) & c^2 - e^{ve} \left( \frac{\partial p}{\partial \rho e^{ve}} \right) \end{bmatrix}, \quad (\text{B.39})$$

such that diagonalization of the convective flux Jacobian is possible. The eigenvectors make use of an orthonormal set of basis vectors,  $\vec{n}$ ,  $\vec{l}$ , and  $\vec{m}$ , where  $\vec{n}$  is the direction of the projection, which is typically aligned with the normal vector of a control volume face. Vectors  $\vec{l}$  and  $\vec{m}$  are necessarily tangent to the control volume face under these circumstances, and are not unique. Any specification for  $\vec{l}$  and  $\vec{m}$  is acceptable, provided they form an orthonormal basis of  $\mathbb{R}^3$ . The speed of sound,  $c$ ,

may be determined using

$$c = \sqrt{(1 + \frac{\partial p}{\partial \rho e}) \frac{p}{\rho}}. \quad (\text{B.40})$$



## Appendix C

# Details of Adjoint Derivation

### C.1 Variation of the Species Diffusion Flux

The variation of the diffusion flux,  $\delta \vec{J}_s$ , appears throughout the derivation of the adjoint problem. Specifically, in the application of the linearized boundary conditions for non-catalytic walls, a simplified form of  $\delta \vec{J}$  is required to evaluate the surface sensitivity. Specifically the terms in question are,

$$\sum_s \psi_{\rho_s} (\delta \vec{J}_s \cdot \vec{n}) + \psi_{\rho_e} \sum_s (\delta \vec{J}_s \cdot \vec{n}) h_s^{int} + \psi_{\rho_e^{ve}} \sum_s (\delta \vec{J}_s \cdot \vec{n}) e_s^{ve}. \quad (\text{C.1})$$

The procedure to simplify Eqn. (C.1) can be applied identically on a term-by-term basis, therefore, consider a single, general term,

$$K = \psi (\delta \vec{J}_s \cdot \vec{n}) \xi, \quad (\text{C.2})$$

subject to the following linearized boundary condition,

$$\delta \vec{J}_s = -\partial_n \vec{J}_s \cdot \vec{n} \delta S + \vec{J}_s \cdot \nabla_S \delta S. \quad (\text{C.3})$$

After applying the linearized boundary condition,

$$\begin{aligned} K &= \psi \xi \left[ -\partial_n \vec{J}_s \cdot \vec{n} \delta S + \vec{J}_s \cdot \nabla_S \delta S \right] \\ &= -\psi \xi \nabla \cdot \vec{J}_s \delta S + \psi \xi \nabla_S \cdot \vec{J}_s \delta S + \psi \xi \vec{J}_s \cdot \nabla_S \delta S, \end{aligned} \quad (\text{C.4})$$

where the identity from Eqn. (3.6d),  $\nabla \cdot (\vec{\eta}) = \partial_n(\vec{\eta}) \cdot \vec{n} + \nabla_S \cdot (\vec{\eta}) - 2H_m \vec{\eta} \cdot \vec{n}$ , is used to rewrite the first term of the first line. Note, the application of the non-catalytic boundary condition eliminates the dependence on  $H_m$  from the substitution. The third term of Eqn. (C.4) may be manipulated using integration by parts such that,

$$\psi \xi \vec{J}_s \cdot \nabla_S \delta S = \nabla_S \cdot (\psi \xi \vec{J}_s \delta S) - \nabla_S \cdot (\psi \xi \vec{J}_s) \delta S. \quad (\text{C.5})$$

Note that  $K$  is integrated over  $S$  in the evaluation of the surface sensitivity, therefore the first term of Eqn. (C.5) is zero in accordance with Eqn. (3.6c) and is omitted from the subsequent analysis. Inserting Eqn. (C.5) into Eqn. (C.4),

$$K = -\psi\xi\nabla \cdot \vec{J}_s \delta S + \psi\xi\nabla_S \cdot \vec{J}_s \delta S - \nabla_S \cdot (\psi\xi\vec{J}_s) \delta S, \quad (\text{C.6})$$

The second and third terms of Eqn. (C.6) are combined using the product rule, such that,

$$K = -\psi\xi\nabla \cdot \vec{J}_s \delta S - \nabla_S (\psi\xi) \cdot \vec{J}_s \delta S. \quad (\text{C.7})$$

The first term of Eqn. (C.7) contains second order derivative terms, which are inconvenient to evaluate on unstructured mesh topologies. This term can be simplified by writing the species mass conservation equation on  $S$  and solving for  $\nabla \cdot \vec{J}_s$ ,

$$\begin{aligned} \frac{\partial \rho_s}{\partial t} + \nabla \cdot (\rho_s \vec{u}) - \nabla \cdot (-\vec{J}_s) &= \dot{w}_s \\ \nabla \cdot \vec{J}_s &= -\rho_s \nabla \cdot \vec{u} + \dot{w}_s, \end{aligned} \quad (\text{C.8})$$

where the no-slip and adiabatic wall boundary conditions have been applied. Inserting Eqn. (C.8) into Eqn. (C.7) leads to,

$$K = \psi\xi\rho_s(\nabla \cdot \vec{u})\delta S - \psi\xi\dot{w}_s - \nabla_S (\psi\xi) \cdot \vec{J}_s \delta S. \quad (\text{C.9})$$

Using Eqn. (3.6d) once more, noting that  $\nabla_S \cdot \vec{u} = 0$  and  $H_m \vec{u} \cdot \vec{n} = 0$  because of the enforcement of the no-slip boundary condition everywhere on  $S$ ,

$$K = \psi\xi\rho_s \partial_n \vec{u} \cdot \vec{n} \delta S - \psi\xi\dot{w}_s - \nabla_S (\psi\xi) \cdot \vec{J}_s \delta S. \quad (\text{C.10})$$

From the conclusion of Eqn. (C.9), it is now possible to return to the original surface sensitivity given by Eqn. (C.1),

$$\begin{aligned} &\sum_s \psi_{\rho_s} (\delta \vec{J}_s \cdot \vec{n}) + \psi_{\rho_e} \sum_s (\delta \vec{J}_s \cdot \vec{n}) h_s^{int} + \psi_{\rho_e^{ve}} \sum_s (\delta \vec{J}_s \cdot \vec{n}) e_s^{ve} \\ &= \left[ \sum_s \psi_{\rho_s} \rho_s + \psi_{\rho_e} \sum_s \rho_s h_s^{int} + \psi_{\rho_e^{ve}} \sum_s \rho_s e_s^{ve} \right] (\partial_n \vec{u} \cdot \vec{n} \delta S) \\ &\quad - \sum_s [\psi_{\rho_s} + \psi_{\rho_e} h_s^{int} + \psi_{\rho_e^{ve}} e_s^{ve}] \dot{w}_s \\ &\quad - \sum_s \nabla_S \psi_{\rho_s} \cdot \vec{J}_s \delta S - \sum_s \nabla_S (\psi_{\rho_e} h_s^{int}) \cdot \vec{J}_s \delta S - \sum_s \nabla_S (\psi_{\rho_e^{ve}} e_s^{ve}) \cdot \vec{J}_s \delta S \\ &= \vartheta(\partial_n \vec{u} \cdot \vec{n} \delta S) - \sum_s \nabla_S \psi_{\rho_s} \cdot \vec{J}_s \delta S - \sum_s \nabla_S (\psi_{\rho_e} h_s^{int}) \cdot \vec{J}_s \delta S - \sum_s \nabla_S (\psi_{\rho_e^{ve}} e_s^{ve}) \cdot \vec{J}_s \delta S \\ &\quad - \sum_s [\psi_{\rho_s} + \psi_{\rho_e} h_s^{int} + \psi_{\rho_e^{ve}} e_s^{ve}] \dot{w}_s, \end{aligned} \quad (\text{C.11})$$

where  $\vartheta$  is given by Eqn. (3.43). The substitution of  $\vartheta$  is made by recognizing the definitions of the mass-averaged vib.-el. energy-per-unit volume,  $\rho e^{ve}$ , and enthalpy,  $\rho h = \sum_s \rho_s [h_s^{int} + (1/2)(\vec{u} \cdot \vec{u})]$ .

## C.2 Variation of the Trans.-Rot. Thermal Conduction

This section provides a detailed explanation of the simplified form of  $\delta(\kappa^{tr}\nabla T)$  in the surface sensitivities corresponding to adiabatic wall boundary conditions. Specifically, the term in question is,

$$\psi_{pe}\delta(\kappa^{tr}\nabla T) \cdot \vec{n}, \quad (\text{C.12})$$

subject to the following linearized boundary condition,

$$\delta(\kappa^{tr}\nabla T) \cdot \vec{n} = -\partial_n(\kappa^{tr}\nabla T) \cdot \vec{n}\delta S + (\kappa^{tr}\nabla T) \cdot \nabla_S \delta S. \quad (\text{C.13})$$

After applying the linearized boundary condition,

$$\begin{aligned} \psi_{pe}\delta(\kappa^{tr}\nabla T) \cdot \vec{n} &= \psi_{pe} [\kappa^{tr}\nabla T \cdot \nabla_S \delta S - \partial_n(\kappa^{tr}\nabla T) \cdot \vec{n}\delta S] \\ &= \psi_{pe}(\kappa^{tr}\nabla T) \cdot \nabla_S \delta S - \psi_{pe}\nabla \cdot (\kappa^{tr}\nabla T)\delta S + \psi_{pe}\nabla_S \cdot (\kappa^{tr}\nabla T)\delta S, \end{aligned} \quad (\text{C.14})$$

where the identity from Eqn. (3.6d),  $\nabla \cdot (\vec{\xi}) = \partial_n(\vec{\xi}) \cdot \vec{n} + \nabla_S \cdot (\vec{\xi}) - 2H_m \vec{\xi} \cdot \vec{n}$ , is applied to the final term of the first line. Note that the term including  $H_m$  is zero by the application of the adiabatic boundary condition. The derivation continues by applying integration by parts to the third term of Eqn. (C.14),

$$\psi_{pe}\nabla_S \cdot (\kappa^{tr}\nabla T)\delta S = \nabla_S \cdot [\psi_{pe}(\kappa^{tr}\nabla T)\delta S] - \nabla_S(\psi_{pe}\delta S) \cdot (\kappa^{tr}\nabla T). \quad (\text{C.15})$$

Note that  $\psi_{pe}\delta(\kappa^{tr}\nabla T) \cdot \vec{n}$  is integrated over  $S$  in the evaluation of the surface sensitivity, therefore the first term of Eqn. (C.15) is zero in accordance with Eqn. (3.6c) and is omitted from the subsequent analysis.

$$\psi_{pe}\delta(\kappa^{tr}\nabla T) \cdot \vec{n} = \psi_{pe}(\kappa^{tr}\nabla T) \cdot \nabla_S \delta S - \psi_{pe}\nabla \cdot (\kappa^{tr}\nabla T)\delta S - \nabla_S(\psi_{pe}\delta S) \cdot (\kappa^{tr}\nabla T). \quad (\text{C.16})$$

The first and third terms of Eqn. (C.16) are combined using the product rule such that,

$$\psi_{pe}\delta(\kappa^{tr}\nabla T) \cdot \vec{n} = -(\nabla_S \psi_{pe}) \cdot (\kappa^{tr}\nabla T)\delta S - \psi_{pe}\nabla \cdot (\kappa^{tr}\nabla T)\delta S. \quad (\text{C.17})$$

The second term of Eqn. (C.17) contains second order derivative terms, which are inconvenient to evaluate on unstructured mesh topologies. This term can be simplified by writing the energy

equation on  $S$ ,

$$\begin{aligned} \frac{\partial \rho e}{\partial t} + \nabla \cdot [(\rho e + p)\vec{u}] - \nabla \cdot \left( \vec{u} \cdot \bar{\sigma} + \kappa^{tr} \nabla T + \kappa^{ve} \nabla T^{ve} - \sum_s \vec{J}_s h_s^{int} \right) &= 0 \\ \sum_s (\rho_s h_s^{int}) \nabla \cdot \vec{u} - \nabla \vec{u} : \bar{\sigma} - \nabla \cdot (\kappa^{tr} \nabla T) - \nabla \cdot (\kappa^{ve} \nabla T^{ve}) + \sum_s (\nabla \cdot \vec{J}_s) h_s^{int} + \sum_s \vec{J}_s \cdot \nabla h_s^{int} &= 0, \end{aligned} \quad (\text{C.18})$$

where the no-slip boundary condition and the relationship  $(\rho e + p) = \sum_s \rho_s (h_s^{int} + (1/2) \vec{u} \cdot \vec{u})$  has been applied. To further simplify, the species mass conservation on the surface is required,

$$\begin{aligned} \frac{\partial \rho_s}{\partial t} + \nabla \cdot (\rho_s \vec{u}) + \nabla \cdot (\vec{J}_s) &= \dot{w}_s \\ \nabla \cdot \vec{u} &= \frac{(\dot{w}_s - \nabla \cdot \vec{J}_s)}{\rho_s}. \end{aligned} \quad (\text{C.19})$$

Inserting Eqn. (C.19) into Eqn. (C.18),

$$\nabla \cdot (\kappa^{tr} \nabla T) = \sum_s h_s^{int} \dot{w}_s - \nabla \vec{u} : \bar{\sigma} - \nabla \cdot (\kappa^{ve} \nabla T^{ve}) + \sum_s \vec{J} \cdot \nabla h_s^{int}. \quad (\text{C.20})$$

Furthermore it can be shown [10],

$$\nabla \vec{u} : \bar{\sigma} = \bar{\sigma} \partial_n \vec{u} \cdot \vec{n} \quad (\text{C.21})$$

Therefore,  $\psi_{\rho e} \delta(\kappa^{tr} \nabla T) \cdot \vec{n}$  can be expressed as,

$$\begin{aligned} \psi_{\rho e} \delta(\kappa^{tr} \nabla T) \cdot \vec{n} &= -(\nabla_S \psi_{\rho e}) \cdot (\kappa^{tr} \nabla T) \delta S - \psi_{\rho e} \sum_s h_s^{int} \dot{w}_s \delta S + \psi_{\rho e} \bar{\sigma} \partial_n \vec{u} \cdot \vec{n} \delta S \\ &\quad + \psi_{\rho e} \nabla \cdot (\kappa^{ve} \nabla T^{ve}) \delta S - \psi_{\rho e} \sum_s \vec{J} \cdot \nabla h_s^{int} \delta S. \end{aligned} \quad (\text{C.22})$$

### C.3 Variation of the Vib.-El. Thermal Conduction

This section provides a detailed explanation of the simplified form of  $\delta(\kappa^{ve} \nabla T^{ve})$  in the surface sensitivities corresponding to the adiabatic wall boundary conditions. The simplification procedure of this section mirrors that in Section C.2. Specifically, the term in question is,

$$(\psi_{\rho e} + \psi_{\rho e^{ve}}) \delta(\kappa^{ve} \nabla T^{ve}) \cdot \vec{n} = K, \quad (\text{C.23})$$

where  $K$  has been introduced as a short-hand reference. For adiabatic walls, the corresponding linearized boundary condition is,

$$\delta(\kappa^{ve} \nabla T^{ve}) \cdot \vec{n} = -\partial_n (\kappa^{ve} \nabla T^{ve}) \cdot \vec{n} \delta S + (\kappa^{ve} \nabla T^{ve}) \cdot \nabla_S \delta S \quad (\text{C.24})$$

After applying the linearized boundary conditions,

$$\begin{aligned} K &= (\psi_{pe} + \psi_{pe^{ve}}) [\kappa^{ve} \nabla T^{ve} \cdot \nabla_S \delta S - \partial_n (\kappa^{ve} \nabla T^{ve}) \cdot \vec{n} \delta S] \\ &= (\psi_{pe} + \psi_{pe^{ve}}) [\kappa^{ve} \nabla T^{ve} \cdot \nabla_S \delta S - \nabla \cdot (\kappa^{ve} \nabla T^{ve}) \delta S + \nabla_S \cdot (\kappa^{ve} \nabla T^{ve}) \delta S], \end{aligned} \quad (\text{C.25})$$

where the identity of Eqn. (3.6d),  $\nabla \cdot (\vec{\xi}) = \partial_n (\vec{\xi}) \cdot \vec{n} + \nabla_S \cdot (\vec{\xi}) - 2H_m \vec{\xi} \cdot \vec{n}$  is used to rewrite the final term of the first line. Note that the term that depends on  $H_m$  is zero by the application of the adiabatic boundary condition. The derivation continues by applying integration by parts to the third term of Eqn. (C.25),

$$(\psi_{pe} + \psi_{pe^{ve}}) \nabla_S \cdot (\kappa^{ve} \nabla T^{ve}) \delta S = \nabla_S \cdot [(\psi_{pe} + \psi_{pe^{ve}}) (\kappa^{ve} \nabla T^{ve}) \delta S] - \nabla_S [(\psi_{pe} + \psi_{pe^{ve}}) \delta S] \cdot (\kappa^{ve} \nabla T^{ve}) \quad (\text{C.26})$$

Note that  $K$  is integrated over  $S$  in the evaluation of the surface sensitivity, therefore the first term of Eqn. (C.26) is zero in accordance with Eqn. (3.6c) and is omitted from the subsequent analysis.

$$\begin{aligned} K &= (\psi_{pe} + \psi_{pe^{ve}}) \kappa^{ve} \nabla T^{ve} \cdot \nabla_S \delta S - (\psi_{pe} + \psi_{pe^{ve}}) \nabla \cdot (\kappa^{ve} \nabla T^{ve}) \delta S \\ &\quad - \nabla_S [(\psi_{pe} + \psi_{pe^{ve}}) \delta S] \cdot (\kappa^{ve} \nabla T^{ve}). \end{aligned} \quad (\text{C.27})$$

The first and third terms of Eqn. (C.27) are combined using the product rule such that,

$$K = -\nabla_S (\psi_{pe} + \psi_{pe^{ve}}) \cdot (\kappa^{ve} \nabla T^{ve}) \delta S - (\psi_{pe} + \psi_{pe^{ve}}) \nabla \cdot (\kappa^{ve} \nabla T^{ve}) \delta S. \quad (\text{C.28})$$

The second term of Eqn. (C.28) contains second order derivative terms, which are inconvenient to evaluate on unstructured meshes. This term may be simplified by writing the vibrational-electronic energy equation on  $S$ .

$$\begin{aligned} \frac{\partial \rho e^{ve}}{\partial t} + \nabla \cdot (\rho e^{ve} \vec{u}) - \nabla \cdot \left( \kappa^{ve} \nabla T^{ve} - \sum_s \vec{J}_s e_s^{ve} \right) &= \sum_s \dot{w}_s e_s^{ve} + q^x \\ \sum_s \rho_s e_s^{ve} (\nabla \cdot \vec{u}) - \nabla \cdot (\kappa^{ve} \nabla T^{ve}) + \sum_s (\nabla \cdot \vec{J}_s) e_s^{ve} + \sum_s \vec{J}_s \cdot \nabla e_s^{ve} &= \sum_s \dot{w}_s e_s^{ve} + q^x, \end{aligned} \quad (\text{C.29})$$

where the no-slip boundary condition and  $\rho e^{ve} = \sum_s \rho_s e_s^{ve}$  have been applied to Eqn. (C.29). Inserting the mass conservation equation on  $S$  from Eqn. (C.19) into Eqn. (C.29),

$$\nabla \cdot (\kappa^{ve} \nabla T^{ve}) = \sum_s \vec{J}_s \cdot \nabla e_s^{ve} - q^x \quad (\text{C.30})$$

Therefore,  $K$  can be expressed as,

$$\begin{aligned} K &= (\psi_{\rho e} + \psi_{\rho e^{ve}}) \delta(\kappa^{ve} \nabla T^{ve}) \cdot \vec{n} \\ &= -\nabla_S (\psi_{\rho e} + \psi_{\rho e^{ve}}) \cdot (\kappa^{ve} \nabla T^{ve}) \delta S - (\psi_{\rho e} + \psi_{\rho e^{ve}}) \sum_s \vec{J}_s \cdot \nabla e_s^{ve} \delta S + (\psi_{\rho e} + \psi_{\rho e^{ve}}) q^x \delta S. \end{aligned} \quad (\text{C.31})$$

# Appendix D

## Solver Validation

This appendix contains a validation test of the unstructured FVM solver developed for this work. In this exercise, shock tube heat flux measurements are compared to the predicted heat flux from the solution of the governing equations presented in Chapter 2, discretized in accordance with the procedure of Chapter 4, for a blunt body in thermochemical nonequilibrium. Additional simulation results from Scalabrin [125] are included that provide a relevant comparison to other unstructured real-gas solvers.

**Background and Problem Setup** In the late 1990’s, an experimental campaign by Hollis and Perkins [55, 56] was launched to provide validation-quality experimental results for the purpose of verification and validation of hypersonic simulation tools. These tests, conducted at the NASA Hypersonic Pulse Facility (HYPULSE), were performed using both air and carbon-dioxide gas mixtures over a scale replica of a blunted cone Mars entry vehicle. Surface heat transfer rates were acquired using thin-film temperature resistance gauges along the forebody, afterbody, and along the sting that supported the model in the test chamber. Simulation results from this work, as well as from Scalabrin [125] are compared to these experimental readings.

In this validation exercise, the air test gas results are simulated using the free stream conditions in Tab. (D.1). Since the data acquisition time is small, and the experimental model is machined from a ceramic thermal insulator, Macor® (Corning, Inc.), wall conditions are assumed to be isothermal and non-catalytic at the laboratory ambient temperature.

**Geometry** The geometry of the test article is a standard 70° blunted cone, mounted to a sting for installation in the experimental facility. The shape of the lander alone is similar to the heritage Viking and MSL configurations that are common for Mars landers. Schematically, the geometry of the capsule and sting are shown in Fig. (D.1), with the corresponding parameter values listed in Tab. (D.2). In the axisymmetric projection of the geometry, all radius measurements  $R$  are given in millimeters, and angle measurements correspond to circular sectors, measured in degrees.

Parameter	Value
$T_\infty$	1113 K
$T_{wall}$	300 K
$p_\infty$	1829.48 Pa
$M_\infty$	7.70741
$Re_d$	$3.39 \times 10^4$
$\alpha$	0
$\beta$	0
$Y_{N_2}$	0.766
$Y_{O_2}$	0.231
$Y_{NO}$	0.001
$Y_N$	0.001
$Y_O$	0.001

Table D.1:  $70^\circ$  blunted cone free stream conditions.

Parameter	Value
$L_s$	116.84 mm
$R_b$	25.4 mm
$R_c$	1.27 mm
$R_f$	15.24 mm
$R_n$	12.7 mm
$R_s$	10.32 mm
$\alpha_n$	$70^\circ$
$\alpha_f$	$40^\circ$

Table D.2: Mars entry vehicle model geometry.

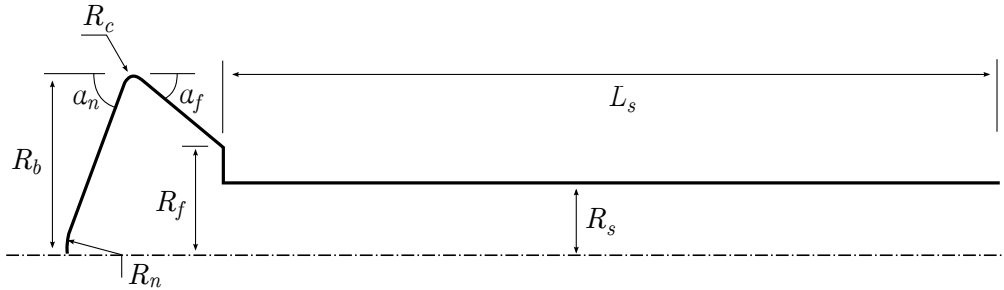


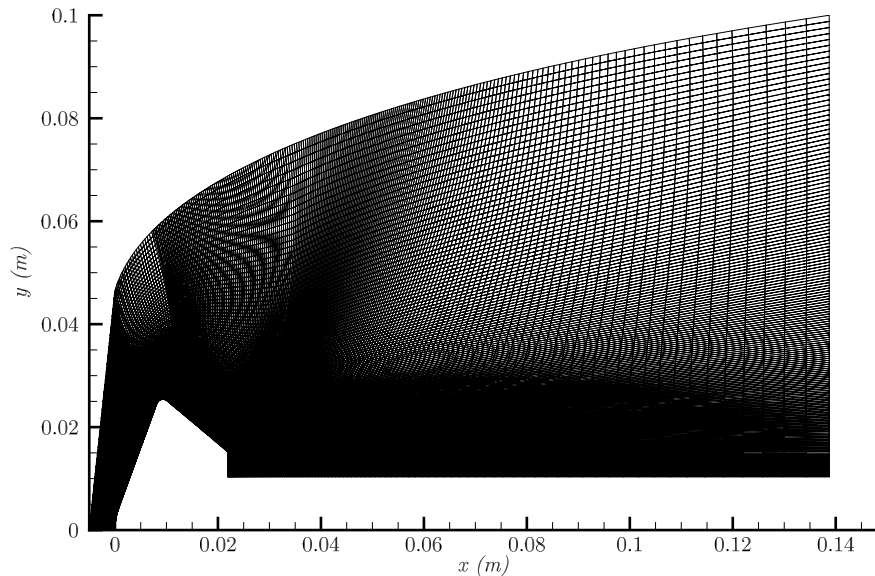
Figure D.1: Schematic of the Mars entry vehicle model geometry.

**Computational Mesh** The computational environment for this validation test case leverages the axisymmetry in the domain and uses a two-dimensional computational mesh. The mesh consists of a total of 47,146 quadrilateral elements, comprised of 47,616 nodes, with 151 nodes used in the wall-normal direction to resolve the shock and boundary layer in the domain. To preserve mesh quality, five patches are used on the forebody, shoulder, aft body frustum, and along the sting to ensure orthogonality, which are visible in Fig. (D.2).

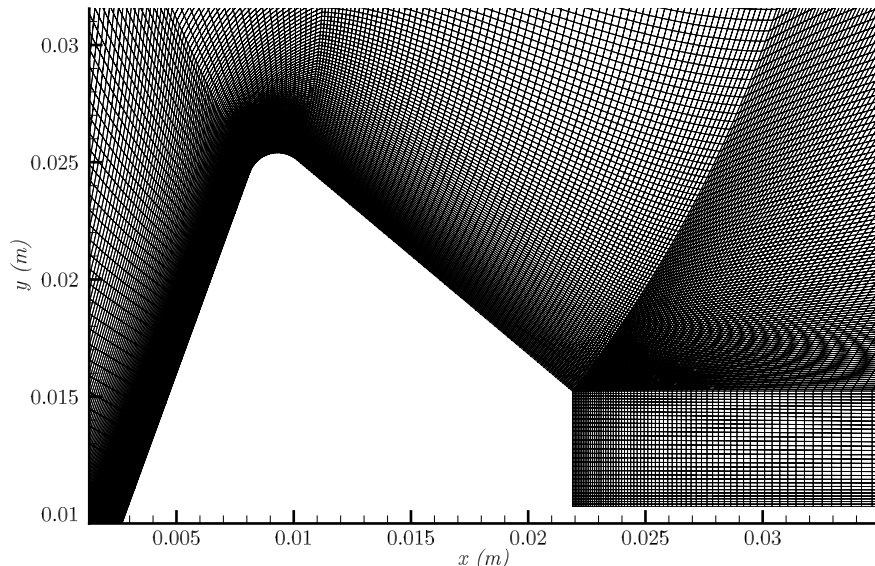
**Results** The simulated shock tube environment is solved using an axisymmetric formulation of the conservation equations. Far field conditions are applied to the inflow and outflow boundaries, a symmetry wall boundary conditions is applied along the stagnation line, and an isothermal, non-catalytic boundary is set for the model surface. The AUSM scheme is used, in conjunction with the corrected average gradient method to resolve the convective and viscous fluxes in the domain.

Fig. (D.3) shows the flow field solution around the model geometry. Mach contours show the rapid compression through the shock wave, expansion around the shoulder, and separation at the model base, near the sting. Far downstream, the recirculation bubble reattaches to the sting and a second compression wave is generated. In the wake, the recirculation zone shows complex, coherent vortex structures.

A comparison between the experimental and simulated heat transfer rates for the forebody and backshell of the model is shown in Fig. (D.4). In the plots, the  $x$ -axis is the surface distance from the stagnation point,  $S$ , non-dimensionalized by the model base radius,  $R_b$ , such that a value of  $S/R_b \approx 1$  roughly corresponds to the location of the vehicle shoulder. The  $y$ -axis is the surface heat flux,  $Q$ , in units of Watts per square centimeter. The first plot shows the forebody heat transfer rates for  $S/R_b \in [0, 1.15]$  and the second from  $S/R_b \in [1.15, 6]$ . Numerically simulated heat fluxes are compared against the experimental values collected by Hollis and Perkins, as well as the simulated values of Scalabrin, whose formulation and numerical implementation of the flow equations is similar to that of this work. In this way, an absolute measure of the accuracy of the model is achieved, and where shortcomings exist, a comparison to other state-of-the-art solvers is possible.

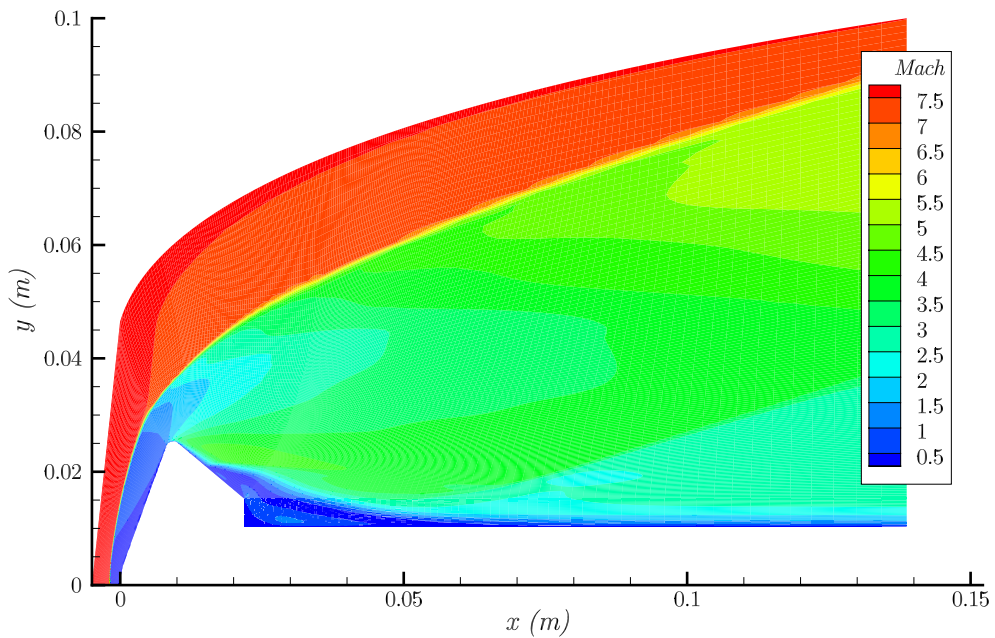


(a) Full mesh topology.

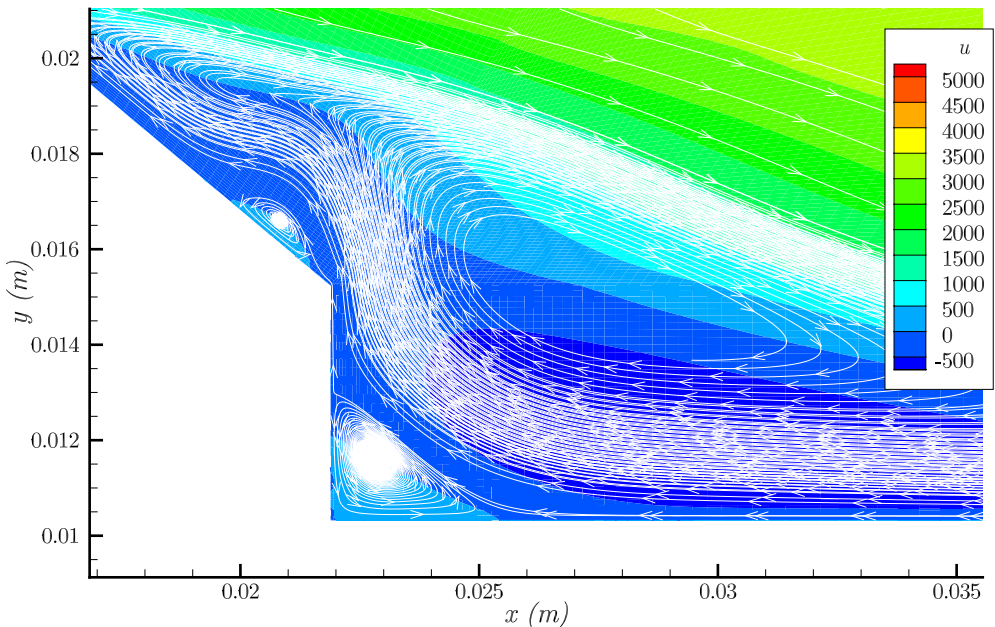


(b) Zoomed view showing patch structure along the capsule shoulder.

Figure D.2: Computational meshes for the Mars vehicle model.



(a) Mach number.



(b) X-velocity component with stream trace overlay, showing flow recirculation.

Figure D.3: Flow field solutions for the Mars vehicle model.

Generally, the computed heat transfer profiles on the forebody and backshell of the test article are in good agreement with the experimentally acquired heat fluxes of Hollis and Perkins and the numerical results from Scalabrin. Smooth, bell-shaped curves are expected for the forebody heat transfer, with the peak value at the stagnation point, corresponding to  $S/R_b = 0$ . Simulated heat transfer rates are over-predicted near the stagnation line, and the peak value lies off the axis of symmetry, due to the presence of the carbuncle phenomena [128, 116]. The carbuncle phenomena has been the subject of study for several decades, and is largely attributed to numerical errors in the computation of the shock-jump flow state across the shock wave [111, 73], and the alignment of the computational grid with the shock [43]. McCormack discusses [92] several additional contributors that include the presence of  $1/r$  factors in non-cartesian coordinate systems that tend to  $\infty$  near the stagnation line, unsteady flow in the subsonic region behind the shock, and preferential numerical dissipation in the stagnation region. MacCormack posits the inherent dissipation of the spatial integration, acting on surface areas of unequal size, preferentially draws radial momentum and energy toward the axis of symmetry, leading to the elevated heat transfer near the stagnation point shown in Fig. (D.4). The Dissipation Equal Area Rule [92] has been shown to be effective at eliminating the carbuncle phenomena for supersonic blunt-body flows, but requires additional development for deployment in unstructured solver architectures, which is beyond the scope of this work. The simulated heat transfer rates by Hollis and Perkins, as well as those by Scalabrin, utilize a Modified Steger-Warming spatial integration scheme, with more numerical dissipation than the AUSM scheme used in this work. The carbuncle phenomena has been shown to be sensitive to the dissipation near the stagnation line, which may explain the absence of carbuncle-like symptoms in those publications.

On the backshell and along the sting, heat transfer rates are in good agreement with the experimental results up to  $S/R_b \approx 3$ . After, the values are significantly under-predicted. This particular region lies within the large separation bubble that extends from the frustum of the model along the sting. Clearly the separation and reattachment of the flow is not well captured in the numerical solution. This is a known issue with laminar and RANS Navier-Stokes solutions, which may be remedied by the use of more sophisticated simulation techniques, such as Large-Eddy Simulation (LES) or Direct Numerical Simulation (DNS), which more accurately propagate eddies and vortices in turbulent and separated flows. The simulation of this work agrees closely with the second-order Scalabrin solution, which is representative of the state-of-the-art in numerical simulation, and since the objective of this thesis is not to advance the capabilities of the direct flow solver, the performance shown here is acceptable.

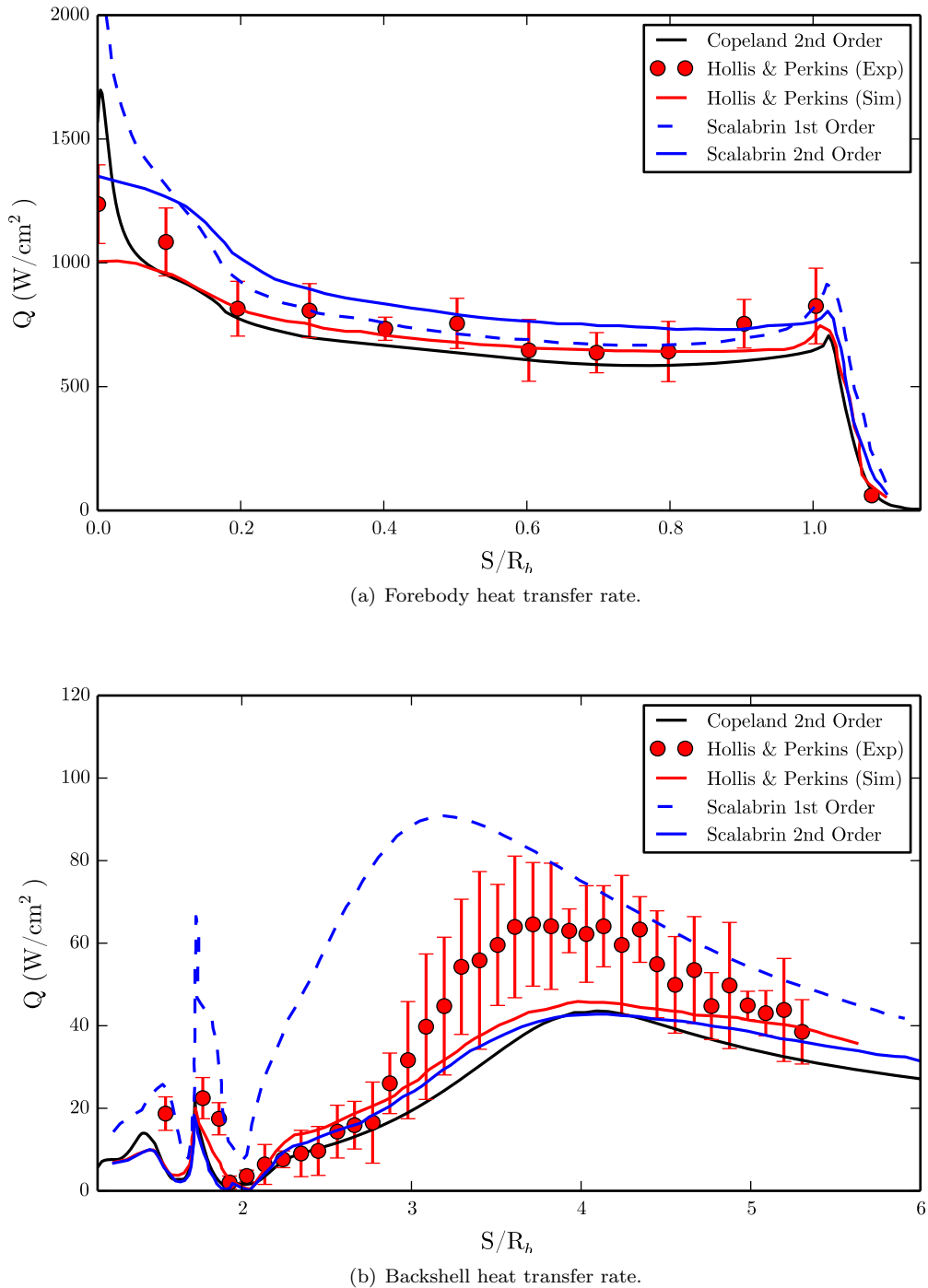


Figure D.4: Surface heat transfer rates for the Mars vehicle model.



# Bibliography

- [1] Michael J. Aftosmis and Marian Nemec. Cart3d simulations for the first aiaa sonic boom prediction workshop. In *52nd AIAA Aerospace Sciences Meeting*, National Harbor, MD, January 2014. AIAA Paper 2014-0558.
- [2] Kyle W. Anderson and V. Venkatakrishnan. Aerodynamic design optimization on unstructured grids with a continuous adjoint formulation. *Computers & Fluids*, 28:443–480, 1999.
- [3] W. K. Anderson and V. Venkatakrishnan. Aerodynamic design optimization on unstructured grids with a continuous adjoint formulation. In *35th AIAA Aerospace Science Meeting & Exhibit*, Reno, NV, 1997. AIAA Paper 97-0643.
- [4] John D. Anderson Jr. *Hypersonic and High-Temperature Gas Dynamics*. AIAA Education Series, 2006.
- [5] Eyal Arian and Manuel D. Salas. Admitting the inadmissible: Adjoint formulation for incomplete cost functionals in aerodynamic optimization. *AIAA Journal*, 37(1):37–43, 1999.
- [6] R. B. Bird, W. E. Stewart, and E. D. Lightfoot. *Transport Phenomena*. John Wiley & Sons, 1960.
- [7] F. G. Blottner, M. Johnson, and M. Ellis. Chemically reacting viscous flow program for multi-component gas mixtures. Sc-rr-70-754, Sandia Laboratories, Albuquerque, NM, December 1971.
- [8] Deepak Bose, Michael J. Wright, and Tahir Gökçen. Uncertainty and sensitivity analysis of thermochemical modeling for titan atmospheric entry. In *37th AIAA Thermophysics Conference*, Portland, OR, July 2004. AIAA Paper 2004-2455.
- [9] Stephen Boyd and Lieven Vandenberghe. *Convex Optimization*. Cambridge University Press, Cambridge, UK, 2004.
- [10] Alfonso Bueno-Orovio, Carlos Castro, Francisco Palacios, and Enrique Zuazua. Continuous adjoint approach for the spalart-allmaras model in aerodynamic optimization. *AIAA Journal*, 50(3):631–646, 2012.

- [11] Thomas R. A. Bussing and Earll M. Murman. Finite-volume method for the calculation of chemically reacting flows. *AIAA Journal*, 26(9):1070–1078, 1987.
- [12] Graham V. Candler. *The Computation of Weakly Ionized Hypersonic Flows in Thermochemical Nonequilibrium*. PhD thesis, Stanford University, 1988.
- [13] Graham V. Candler and Robert W. MacCormack. Computation of weakly ionized hypersonic flows in thermochemical nonequilibrium. *Journal of Thermophysics*, 5(3):266–273, September 1988.
- [14] Carlos Castro, Carlos Lozano, Francisco Palacios, and Enrique Zuazua. Systematic continuous adjoint approach to viscous aerodynamic design on unstructured grids. *AIAA Journal*, 45(9):2125–2139, 2007.
- [15] S. Chapman and T. G. Cowling. *The Mathematical Theory of Non-Uniform Gases*. Cambridge University Press, London, 1939.
- [16] S. R. Copeland, A. K. Lonkar, F. Palacios, and J. J. Alonso. Adjoint-based goal-oriented mesh adaptation for nonequilibrium hypersonic flows. In *51st AIAA Aerospace Science Meeting including the New Horizons Forum and Aerospace Exposition*, Grapevine, TX, January 2013. AIAA Paper 2013-0552.
- [17] Sean R. Copeland, Milad Mahzari, Ioana Cozmuta, and Juan J. Alonso. A statistics-based material property analysis to support ablation simulation uq efforts. In *14th AIAA Non-Deterministic Approaches Conference*, Honolulu, HI, April 2012. AIAA Paper 2012-1763.
- [18] R. Courant, K. Friedrichs, and H. Lewy. über die partiellen defferenzengleichungen der mathematischen physik. *Mathematische Annalen*, 100(1):32–74, 1928.
- [19] R. Courant, K. Friedrichs, and H. Lewy. On the partial difference equations of mathematical physics. *IBM Journal*, 11:215–234, 1967.
- [20] Charles F. Curtiss and Joseph O. Hirschfelder. Transport properties of multicomponent gas mixtures. *Journal of Chemical Physics*, 17(6):550–555, June 1949.
- [21] Boris Diskin and James Thomas. Accuracy of gradient reconstruction on grids with high aspect ratio. Report 12, National Institute of Aerospace, 2008.
- [22] Marie-Claude Druguet, Graham V. Candler, and Ioannis Nompelis. Effect of numerics on navier-stokes computations of hypersonic double-cone flows. *AIAA Journal*, 43(3):616–623, March 2005.
- [23] Karthikeyan Duraisamy, Juan J. Alonso, and Praveen Chandrashekhar. Goal-oriented uncertainty propagation using stochastic adjoints. In *20th AIAA Computational Fluid Dynamics Conference*, Honolulu, HI, June 2011. AIAA Paper 2011-3412.

- [24] Karthikeyan Duraisamy, Juan J. Alonso, Francisco Palacios, and Praveen Chandrashekhar. Error estimation for high speed flows using continuous and discrete adjoints. In *48th AIAA Aerospace Sciences Meeting Including the New Horizons Forum and Aerospace Exposition*, Orlando, FL, January 2010. AIAA Paper 2010-128.
- [25] Richard P. Dwight. *Efficiency Improvements of RANS-Based Analysis and Optimization using Implicit and Adjoint Methods on Unstructured Grids*. PhD thesis, University of Manchester, 2006.
- [26] Richard P. Dwight. Robust mesh deformation using the linear elasticity equations. In Herman Deconinck and E. Dick, editors, *Computational Fluid Dynamics 2006*, pages 401–406. Springer Berlin Heidelberg, 2009.
- [27] Scott Eberhardt and Kevin Brown. Shock-capturing technique for hypersonic, chemically relaxing flows. *Journal of Spacecraft*, 24(6):481–488, 1987.
- [28] Thomas D. Economon. *Optimal Shape Design Using an Unsteady Continuous Adjoint Approach*. PhD thesis, Stanford University, August 2014.
- [29] Bernd Einfeldt. On godunov-type methods for gas dynamics. *SIAM Journal on Numerical Analysis*, 25(2):294–318, 1988.
- [30] Alaa Elmiligui, Susan Cliff, Michael Aftosmis, Marian Nemec, Edward Parlette, Floyd Wilcox, and Linda Bangert. Sonic boom computations for a mach 1.6 cruise low boom configuration and comparisons with wind tunnel data. In *29th AIAA Applied Aerodynamics Conference*. AIAA Paper 2011-3496, 2011.
- [31] A. Eucken. *Physik. Z.*, 14:324, 1913.
- [32] J. A. Fay and F. R. Riddell. Theory of stagnation point heat transfer in dissociated air. *Journal of the Aeronautical Sciences*, 25(2):73–85, 1958.
- [33] James A. Fay and Nelson H. Kemp. Theory of stagnation-point heat transfer in a partially ionized diatomic gas. *AIAA Journal*, 1(12):2741–2751, 1963.
- [34] Krzysztof J. Fidkowski and David L. Darmofal. Review of output-based error estimation and mesh adaptation in computational fluid dynamics. *AIAA Journal*, 49(4):673–694, 2011.
- [35] Giovanni P. Galdi. *An Introduction to the Mathematical Theory of the Navier-Stokes Equations: Steady-State Problems*, volume 501. Springer, 2011.
- [36] M. B. Giles and N. A. Pierce. Adjoint equations in cfd: duality, boundary conditions and solution behavior. In *13th Computational Fluid Dynamics Conference*. AIAA Paper 1997-1850, 1997.
- [37] M. B. Giles and N. A. Pierce. Adjoint error correction for integral outputs. Error Estimation and Adaptive Discretization Methods in Computational Fluid Dynamics, 2002.

- [38] Michael B. Giles and Niles A. Pierce. An introduction to the adjoint approach to design. *Flow, Turbulence and Combustion*, 65:393–415, 2000.
- [39] P. A. Gnoffo and R. S. McCandless. Three-dimensional aotv flowfields in chemical nonequilibrium. In *24th AIAA Aerospace Sciences Meeting*, Reno, NV, January 1986. AIAA Paper 1986-0230.
- [40] Peter A. Gnoffo. Planetary-entry gas dynamics. *Annual Review of Fluid Mechanics*, 31:459–494, 1999.
- [41] Peter A. Gnoffo, Roop N. Gupta, and Judy L. Shinn. Conservation equations and physical models for hypersonic air flows in thermal and chemical nonequilibrium. Technical report, NASA Technical Paper 2867, February 1989.
- [42] Peter A. Gnoffo, K. James Weilmuenster, H. Harris II Hamilton, David R. Olynick, and Ethiraj Venkatapathy. Computational aerothermodynamic design issues for hypersonic vehicles. *Journal of Spacecraft and Rockets*, 36(1):21–43, February 1999.
- [43] Peter A. Gnoffo and Jeffery A. White. Computational aerothermodynamic simulation issues on unstructured grids. In *37th AIAA Thermophysics Conference*, Portland, OR, July 2004. AIAA Paper 2004-2371.
- [44] R. Goulard. On catalytic recombination rates in hypersonic stagnation heat transfer. *Journal of Jet Propulsion*, 28(11):737–745, 1958.
- [45] Michael J. Grant and Robert D. Braun. Analytic hypersonic aerodynamics for conceptual design of entry vehicles. In *48th AIAA Aerospace Sciences Meeting Including the New Horizons Forum and Aerospace Exposition*, Orlando, FL, January 2010. AIAA Paper 2010-1212.
- [46] Bertil Gustafsson and Arne Sundström. Incompletely parabolic problems in fluid dynamics. *SIAM Journal on Applied Mathematics*, 35(2):343–357, 1978.
- [47] W. L. Hankey and G. A. Elliott. Hypersonic lifting body optimization. *Journal of Spacecraft and Rockets*, 5(12):1463–1467, 1968.
- [48] L. C. Hartung and D. A. Throckmorton. Space shuttle entry heating data book: Vol i sts 2. Reference Publication 1191, National Aeronautics and Space Administration, May 1988.
- [49] L. C. Hartung and D. A. Throckmorton. Space shuttle entry heating data book: Vol ii sts 3. Reference Publication 1192, National Aeronautics and Space Administration, May 1988.
- [50] L. C. Hartung and D. A. Throckmorton. Space shuttle entry heating data book: Vol iii sts 5. Reference Publication 1193, National Aeronautics and Space Administration, May 1988.
- [51] Andreas Haselbacher, James J. McGuirk, and Gary J. Page. Finite volume discretization aspects for viscous flows on mixed unstructured grids. *AIAA Journal*, 37(2):177–184, February 1999.

- [52] C. Hirsch. *Numerical Computation of Internal and External Flows. Volume 2: Computation Methods for Inviscid and Viscous Flows.* Wiley, 1990.
- [53] Joseph O. Hirschfelder, Charles F. Curtiss, and R. Byron Bird. *Molecular Theory of Gases and Liquids.* John Wiley & Sons, 1954.
- [54] John H. Holland. *Adaptation in Natural and Artificial Systems.* MIT Press, 1975.
- [55] Brian R. Hollis and John N. Perkins. High-enthalpy aerothermodynamics of a mars entry vehicle part 1: Experimental results. *Journal of Spacecraft and Rockets*, 34(5):449–456, 1997.
- [56] Brian R. Hollis and John N. Perkins. High-enthalpy aerothermodynamics of a mars entry vehicle part 2: Computational results. *Journal of Spacecraft and Rockets*, 34(4):457–463, 1997.
- [57] Brian R. Hollis and Dinesh K. Prabhu. Assessment of laminar, convective aeroheating prediction uncertainties for mars entry vehicles. In *42nd AIAA Thermophysics Conference*, Honolulu, HI, June 2011. AIAA Paper 2011-3144.
- [58] R. L. Jaffe. Rate constants for chemical reactions in high-temperature nonequilibrium air. In Moss J. N. and C. D. Scott, editors, *Thermophysical Aspects of Re-Entry Flows: Progress in Astronautics and Aeronautics*, volume 103, pages 123–151. AIAA, 1986.
- [59] A. Jameson, L. Martinelli, and N. A. Pierce. Optimum aerodynamic design using the navier-stokes equations. *Theoretical and Computational Fluid Dynamics*, 10:213–237, 1998.
- [60] Antony Jameson. Aerodynamic design via control theory. *Journal of Scientific Computing*, 3(3):233–260, 1988.
- [61] Antony Jameson. Computational aerodynamics for aircraft design. *Science*, 245:361–371, 1989.
- [62] Antony Jameson. Optimum aerodynamic design using cfd and control theory. In *12th AIAA Computational Fluid Dynamics Conference*. AIAA Paper 1995-1729, 1995.
- [63] Antony Jameson and Sangho Kim. Reduction of the adjoint gradient formula for aerodynamic shape optimization problems. *AIAA Journal*, 41(11):2114–2129, 2003.
- [64] Antony Jameson and Luigi Martinelli. A continuous adjoint method for unstructured grids. In *16th AIAA CFD Conference*, Orlando, FL, June 2003. AIAA Paper 2003-3955.
- [65] Antony Jameson, Wolfgang Schmidt, and Eli Turkel. Numerical solution of the euler equations by finite volume methods using runge-kutta time-stepping schemes. In *14th AIAA Fluid and Plasma Dynamic Conference*, Palo Alto, CA, June 1981.
- [66] Antony Jameson and Seokkwan Yoon. Lower-upper implicit schemes with multiple grids for the euler equations. *AIAA Journal*, 25(7):929–935, July 1987.

- [67] W. Linwood Jr. Jones and Aubrey E. Cross. Electrostatic probe measurements of plasma parameters for two reentry flight experiments at 25,000 feet per second. Technical Note TN D-6617, NASA, Washington, DC, February 1972.
- [68] Kyu Hong Kim, Chongam Kim, and Oh-Hyun Rho. Methods for the accurate computations of hypersonic flows i. ausmpw+ scheme. *Journal of Computational Physics*, 174(1):38–80, January 2001.
- [69] Kyu Hong Kim, Joon Ho Lee, and Oh-Hyun Rho. An improvement of ausm schemes by introducing the pressure-based weight functions. *Computers & Fluids*, 27(3):311–346, 1998.
- [70] Sung-Eun Kim, Boris Makarov, and Doru Caraeni. A multi-dimensional linear reconstruction scheme for arbitrary unstructured grids. In *16th AIAA Computational Fluid Dynamics Conference*, Orlando, FL, June 2003. AIAA Paper 2003-3990.
- [71] David J. Kinney. Aero-thermodynamics for conceptual design. In *42nd AIAA Aerospace Sciences Meeting and Exhibit*, Reno, NV, 2004. AIAA Paper 2004-31.
- [72] David J. Kinney. Development of the orion crew exploration vehicle’s aerothermal database using a combination of high fidelity cfd and engineering level methods. In *47th AIAA Aerospace Sciences Meeting Including the New Horizons Forum and Aerospace Exposition*, Orlando, FL, January 2009. AIAA Paper 2009-1100.
- [73] Keiichi Kitamura, Philip Roe, and Farzad Ismail. Evaluation of euler fluxes for hypersonic flow computations. *AIAA Journal*, 47(1):44–53, January 2009.
- [74] William L. Kleb and K. James Weilmuenster. Characteristics of the shuttle orbiter leeside flow during a reentry condition. In *27th AIAA Thermophysics Conference*, Nashville, TN, July 1992. AIAA Paper 1992-2951.
- [75] Heinz-Otto Kreiss. Problems with different time scales for parital differential equations. *Communications on Pure and Applied Mathematics*, 33:399–439, 1980.
- [76] L. Landau and E. Teller. Zur theorie der schalldispersion. *Physik Z. Sowjetunion*, 10(1):34, 1936.
- [77] J. H. Lee. Basic governing equations for the flight regimes of aeroassisted orbital transfer vehicles. In H. F. Nelson, editor, *Thermal Design of Aeroassisted Orbital Transfer Vehicles*, volume 96, pages 3–53. AIAA, New York, 1985.
- [78] Randall J. LeVeque. *Finite Volume Methods for Hyperbolic Problems*. Cambridge University Press, 2002.
- [79] Lala Yi Li, Yves Allaneau, and Antony Jameson. Continuous adjoint approach for adaptive mesh refinement. In *20th AIAA Computational Fluid Dynamics Conference*, Honolulu, HI, June 2011. AIAA Paper 2011-3982.

- [80] Tony C. Lin, Wallis R. Grabowsky, and Kevin E. Yelmgren. The search for optimum configurations for re-entry vehicles. *Journal of Spacecraft and Rockets*, 2:142–149, 1984.
- [81] Jacques Louis Lions. *Optimal control of systems governed by partial differential equations*. Springer, Berlin, 1971.
- [82] Meng-Sing Liou. A sequel to ausm: Ausm+. *Journal of Computational Physics*, 129:364–382, 1996.
- [83] Meng-Sing Liou and Christopher J. Steffen. A new flux splitting scheme. *Journal of Computational Physics*, 107:23–39, 1993.
- [84] M. P. Loomis and G. A. Allen Jr. Demonstration of integrated trajectory/aerothermal/tps sizing design tools for mars smart lander. In *AIAA Atmospheric Flight Mechanics Conference and Exhibit*, Monterey, CA, 2002. AIAA Paper 2002-4508.
- [85] R. W. MacCormack and A. J. Paullay. Computational efficiency achieved by the splitting of finite difference operators. In *10th AIAA Aerospace Sciences Meeting*, San Diego, CA, January 1972. AIAA Paper 1972-0154.
- [86] R. W. MacCormack and A. J. Paullay. The influence of the computational mesh on accuracy for initial value problems with discontinuities or nonunique solutions. *Computers & Fluids*, 2(3-4):339–361, December 1974.
- [87] Robert MacCormack, D D. Ambrosio, Giordano, J. Lee, and T. Kim. Plasmadynamic simulations with strong shock waves. In *42nd AIAA Plasmadynamics and Lasers Conference*, Honolulu, HI, June 2011. AIAA Paper 2011-3921.
- [88] Robert W. MacCormack. Algorithm development for hypersonic flow. In *16th AIAA/DLR/DGLR International Space Planes and Hypersonic Systems and Technologies Conference*, Bremen, Germany, October 2009. AIAA Paper 2009-7320.
- [89] Robert W. MacCormack. Solution of maxwell’s equations coupled to the navier-stokes equations. In *40th AIAA Plasmadynamics and Lasers Conference*, San Antonio, TX, June 2009. AIAA Paper 2009-3911.
- [90] Robert W. MacCormack. Non-equilibrium ionized flow simulations within strong electromagnetic fields. In *48th AIAA Aerospace Sciences Meeting Including the New Horizons Forum and Aerospace Exposition*, Orlando, FL, January 2010. AIAA Paper 2010-0225.
- [91] Robert W. MacCormack. Solution of the equations of magneto-fluid dynamics with chemical reaction. In *41st AIAA Plasmadynamics and Lasers Conference*, Chicago, IL, July 2010. AIAA Paper 2010-4636.
- [92] Robert W. MacCormack. The carbuncle cfd problem. In *49th AIAA Aerospace Science Meeting including the New Horizons Forum and Aerospace Exposition*, Orlando, FL, January 2011. AIAA Paper 2011-381.

- [93] Robert W. MacCormack and Graham V. Candler. The solution of the navier-stokes equations using gauss-seidel line relaxation. *Computers & Fluids*, 17(1):135–150, 1989.
- [94] D. J. Mavriplis and A. Jameson. Multigrid solution of the navier-stokes equations on triangular meshes. *AIAA Journal*, 28(8):1415–1425, August 1990.
- [95] D. J. Mavriplis and V. Venkatakrishnan. A unified multigrid solver for the navier-stokes equations on mixed element meshes. *International Journal for Computational Fluid Dynamics*, 8:247–263, 1997.
- [96] Dimitri J. Mavriplis. On convergence acceleration techniques for unstructured meshes. In *29th AIAA Fluid Dynamics Conference*, Albuquerque, NM, 1998. AIAA Paper 1998-2966.
- [97] Dimitri J. Mavriplis. Revisiting the least squares procedure for gradient reconstruction on unstructured meshes. In *16th AIAA Computational Fluid Dynamics Conference*, Orlando, FL, June 2003. AIAA Paper 2003-3986.
- [98] John Melton, Marsha Berger, Michael Aftosmis, and Michael Wong. 3d applications of a cartesian grid euler method. In *33rd AIAA Aerospace Sciences Meeting and Exhibit*. AIAA Paper 1995-0853, January 1995.
- [99] Roger C. Millikan and Donald R. White. Systematics of vibrational relaxation. *Journal of Chemical Physics*, 39(12):3209–3213, December 1963.
- [100] Gino Moretti and Michael Abbott. A time-dependent computational method for blunt body flows. *AIAA Journal*, 4(12):2136–2141, 1966.
- [101] Scott M. Murman, Michael J. Aftosmis, and Marsha J. Berger. Numerical simulation of rolling-airframes using a multi-level cartesian method. In *20th AIAA Applied Aerodynamics Conference*, St. Louis, MO, June 2002. AIAA Paper 2002-2798.
- [102] Siva K. Nadarajah and Antony Jameson. A comparison of the continuous and discrete adjoint approach to automatic aerodynamic optimization. AIAA Paper 2000-0667.
- [103] J. A. Nelder and R. Mead. A simplex method for function minimization. *The Computer Journal*, 7(4):308–313, 1965.
- [104] Eric J. Nielsen and Kyle W. Anderson. Recent improvements in aerodynamic design optimization on unstructured meshes. *AIAA Journal*, 40(6):1155–1163, June 2002.
- [105] C. J. Nietubicz, T. H. Pulliam, and J. L. Steger. Numerical solution of the azimuthal-invariant thin-layer navier-stokes equations. *AIAA Journal*, 18(12):1411–1412, 1980.
- [106] Ioannis Nompelis, T. W. Drayna, and Graham V. Candler. A parallel unstructured implicit solver for hypersonic reacting flow simulation. In *17th AIAA Computational Fluid Dynamics Conference*, Toronto, Canada, June 2005. AIAA Paper 2010-4867.

- [107] F. Palacios, J. J. Alonso, K. Duraisamy, M. R. Colonno, A. C. Aranake, A. Campos, S. R. Copeland, T. D. Economou, A. K. Lonkar, T. W. Lukaczyk, and T. W. R. Taylor. Stanford university unstructured (su<sup>2</sup>): An open source integrated computational environment for multiphysics simulation and design. In *51<sup>st</sup> AIAA Aerospace Sciences Meeting Including the New Horizons Forum and Aerospace Exposition (Submitted)*, Grapevine, TX, 2013.
- [108] Francisco Palacios, Juan J. Alonso, Michael Colonno, Jason Hicken, and Trent Lukaczyk. Adjoint-based method for supersonic aircraft design using equivalent area distributions. In *50<sup>th</sup> AIAA Aerospace Sciences Meeting Including the New Horizons Forum and Aerospace Exposition*, Nashville, TN, January 2012. AIAA Paper 2012-0269.
- [109] Francisco Palacios, Karthik Duraisamy, Juan J. Alonso, and Enrique Zuazua. Robust grid adaptation for efficient uncertainty quantification. *AIAA Journal*, 50(7):1538–1546, 2012.
- [110] Francisco Palacios, Karthik Duraisamy, Aniket Aranake, Sean R. Copeland, Thomas D. Economou, Amrita K. Lonkar, Trent W. Lukaczyk, Kedar R. Naik, Santiago Padron, and Juan J. Alonso. Stanford university unstructured (su2): Analysis and design technology for turbulent flows. In *52<sup>nd</sup> AIAA Aerospace Sciences Meeting*, National Harbor, MD, January 2014. AIAA Paper 2014-0243.
- [111] Maurizio Pandolfi and Dominic D'Ambrosio. Numerical instabilities in upwind methods: Analysis and cures for the "carbuncle" phenomenon. *Journal of Computational Physics*, 166:271–301, 2001.
- [112] Chul Park. On convergence of computation of chemically reacting flows. In *23<sup>rd</sup> AIAA Aerospace Science Meeting*, Reno, NV, January 1985. AIAA Paper 1985-0247.
- [113] Chul Park. *Nonequilibrium Hypersonic Aerothermodynamics*. Wiley, New York, NY, 1990.
- [114] M. A. Park. Adjoint-based, three-dimensional error prediction and grid adaptation. In *32<sup>nd</sup> AIAA Fluid Dynamics Conference*, St. Louis, MO, June 2002. AIAA Paper 2002-3286.
- [115] S. V. Patankar and D. B. Spalding. A calculation procedure for heat, mass and momentum transfer in three-dimensional parabolic flows. *International Journal of Heat and Mass Transfer*, 15(10):1787–1806, October 1972.
- [116] K. M. Peery and S. T. Imlay. Blunt-body flow simulations. In *AIAA/SAE/ASME/ASEE 24<sup>th</sup> Joint Propulsion Conference*, Boston, MA, July 1988. AIAA Paper 1988-2904.
- [117] O. Pironneau. On optimum design in fluid mechanics. *Journal of Fluid Mechanics*, 64(1):97–110, 1974.
- [118] O. Pironneau. Optimal shape design for elliptic systems. In R. F. Drenick and F. Kozin, editors, *System Modeling and Optimization*, volume 38 of *Lecture Notes in Control and Information Sciences*, pages 42–66. Springer Berlin Heidelberg, 1982.

- [119] J. J. Reuther, D. K. Prabu, J. L. Brown, M. J. Wright, and D. A. Saunders. Computational fluid dynamics for winged re-entry vehicles at hypersonic conditions. In *34th AIAA Fluid Dynamics Conference and Exhibit*, Portland, OR, 2004. AIAA Paper 2004-2537.
- [120] P. L. Roe. Approximate riemann solvers, parameter vectors and difference schemes. *Journal of Computational Physics*, 43:357–372, 1981.
- [121] V. V. Rusanov. Calculation of intersection of non-steady shock waves with obstacles. *J. Comput. Math. Phys. USSR*, 1:267–279, 1961.
- [122] Youcef Saad and Martin H. Schultz. Gmres: A generalized minimal residual algorithm for solving nonsymmetric linear systems. *SIAM Journal on Scientific and Statistical Computing*, 7(3):856–869, 1986.
- [123] Manuel D. Salas. A review of hypersonics aerodynamics, aerothermodynamics and plasma-dynamics activities within nasa’s fundamental aeronautics program. In *39th AIAA Thermophysics Conference*, Miami, FL, June 2007. AIAA Paper 2007-4264.
- [124] J. A. Samareh. Aerodynamic shape optimization based on free-form deformation. In *10th AIAA/ISSMO Multidisciplinary Analysis and Optimization Conference*, volume AIAA Paper 2004-4630, August 2004.
- [125] L. Scalabrin. *Numerical Simulation of Weakly Ionized Hypersonic Flow over Reentry Capsules*. PhD thesis, University of Michigan, 2007.
- [126] Stephan Schmidt, Caslav Ilic, Volker Schulz, and Nicolas R. Gauger. Three-dimensional large-scale aerodynamic shape optimization based on shape calculus. *AIAA Journal*, 11:2615–2627, 2013.
- [127] T. W. Sederberg and S. R. Parry. Free-form deformation of solid geometric models. In *Proceedings of SIGGRAPH 89 (Computer Graphics)*, volume 20, pages 151–159, 1986.
- [128] J. S. Shang and Eswar Josyula. Numerical simulations of non-equilibrium hypersonic flow past blunt bodies. In *26th AIAA Aerospace Sciences Meeting*, Reno, NV, January 1988. AIAA Paper 1988-0512.
- [129] Scott G. Sheffer, Luigi Martinelli, and Antony Jameson. An efficient multigrid algorithm for compressible reactive flows. *Journal of Computational Physics*, 144:484–516, 1998.
- [130] J. Simon. Differentiation with respect to the domain in boundary value problems. *Numerical Functional Analysis and Optimization*, 2(7-8):649–687, 1980.
- [131] J. Sokolowski and J.-P. Zolesio. *Introduction to Shape Optimization*. Springer-Verlag, New York, NY, 1991.

- [132] Joseph L. Steger and R. F. Warming. Flux vector splitting of the inviscid gasdynamic equations with application to finite-difference methods. *Journal of Computational Physics*, 40:263–293, 1981.
- [133] George Walter Sutton and Arthur Sherman. *Engineering Magnetohydrodynamics*. McGraw-Hill, New York, NY, 1965.
- [134] Kenneth Sutton and Peter A. Gnoffo. Multi-component diffusion with application to computational aerothermodynamics. In *7th AIAA/ASME Joint Thermophysics and Heat Transfer Conference*. AIAA Paper 98-2575, 1998.
- [135] R. R. Thareja, J. R. Stewart, O. Hassan, K. Morgan, and J. Peraire. A point implicit unstructured grid solver for the euler and navier-stokes equations. In *26th AIAA Aerospace Sciences Meeting*, Reno, NV, January 1988. AIAA Paper 1988-0036.
- [136] John E. Theisinger and Robert D. Braun. Multi-objective hypersonic entry aeroshell shape optimization. *Journal of Spacecraft and Rockets*, 46(5):957–966, 2009.
- [137] Bram van Leer. Towards the ultimate conservative difference scheme i: The quest of monotonicity. In Henri Cabannes and Roger Temam, editors, *Proceedings of the Third International Conference on Numerical Methods in Fluid Mechanics*, volume 18 of *Lecture Notes in Physics*, pages 163–168. Springer Berlin Heidelberg, 1973.
- [138] Bram van Leer. Towards the ultimate conservative difference scheme ii: Monotonicity and conservation combined in a second-order scheme. *Journal of Computational Physics*, 14(4):361–370, March 1974.
- [139] Bram van Leer. Towards the ultimate conservative difference scheme iii: Upstream-centered finite-difference schemes for ideal compressible flow. *Journal of Computational Physics*, 23(3):263–275, March 1977.
- [140] Bram van Leer. Towards the ultimate conservative difference scheme iv: A new approach to numerical convection. *Journal of Computational Physics*, 23(3):276–299, March 1977.
- [141] Bram van Leer. *Flux-Vector Splitting for the Euler Equations*, volume 170 of *Lecture Notes in Physics*. Springer, Berlin, 1982.
- [142] V. Venkatakrishnan. Convergence to steady state solutions of the euler equations on unstructured grids with limiters. *Journal of Computational Physics*, 118:120–130, 1995.
- [143] J. G. Verwer and Sanz-Serna J. M. Convergence of method of lines approximations to partial differential equations. *Computing*, 33:297–313, 1984.
- [144] Walter Vincenti and Jr. Charles H. Kruger. *Introduction to Physical Gas Dynamics*. Krieger, 1965.

- [145] Qiqi Wang. *Uncertainty Quantification for Unsteady Fluid Flow Using Adjoint-Based Approaches*. PhD thesis, Stanford University, Stanford, CA, December 2008.
- [146] Jonathan M. Weiss, Joe P. Maruszewski, and Wayne A. Smith. Implicit solution of the navier-stokes equations on unstructured meshes. In *13th Computational Fluid Dynamics Conference*. AIAA Paper 1997-2103, 1997.
- [147] C. R. Wilke. A viscosity equation for gas mixtures. *Journal of Chemical Physics*, 18(4):517, 1950.
- [148] M. J. Wright, G. V. Candler, and D. Bose. Data-parallel line relaxation method for the navier-stokes equations. *AIAA Journal*, 36(0):1603–1609, 1998.
- [149] Michael J. Wright, Deepak Bose, and Yih-Kanq Chen. Probabilistic modeling of aerothermal and thermal protection material response uncertainties. *AIAA Journal*, 45(2):399–419, February 2007.
- [150] Michael J. Wright, Chun Y. Tang, Karl T. Edquist, Brian R. Hollis, Paul Krasa, and Charles A. Campbell. A review of aerothermal modeling for mars entry missions. In *48th AIAA Aerospace Sciences Meeting Including the New Horizons Forum and Aerospace Exposition*, Orlando, FL, January 2010. AIAA Paper 2010-0443.
- [151] H. C. Yee and Judy L. Shinn. Semi-implicit and fully implicit shock-capturing methods for nonequilibrium flows. *AIAA Journal*, 27(3):299–307, March 1989.
- [152] Seokkwan Yoon and Antony Jameson. Lower-upper symmetric-gauss-seidel method for the euler and navier-stokes equations. *AIAA Journal*, 26(9):1025–1026, September 1988.
- [153] A. Zafarullah. Application of the method of lines to parabolic parital differential equations with error estimates. *Journal of the Association for Computing Machinery*, 17(2):294–302, April 1970.

ProQuest Number: 28120144

INFORMATION TO ALL USERS

The quality and completeness of this reproduction is dependent on the quality  
and completeness of the copy made available to ProQuest.



Distributed by ProQuest LLC (2021).

Copyright of the Dissertation is held by the Author unless otherwise noted.

This work may be used in accordance with the terms of the Creative Commons license  
or other rights statement, as indicated in the copyright statement or in the metadata  
associated with this work. Unless otherwise specified in the copyright statement  
or the metadata, all rights are reserved by the copyright holder.

This work is protected against unauthorized copying under Title 17,  
United States Code and other applicable copyright laws.

Microform Edition where available © ProQuest LLC. No reproduction or digitization  
of the Microform Edition is authorized without permission of ProQuest LLC.

ProQuest LLC  
789 East Eisenhower Parkway  
P.O. Box 1346  
Ann Arbor, MI 48106 - 1346 USA